

# **LOW-POWER DUAL-BAND ON-BODY ANTENNA FOR WIRELESS BODY SENSOR NETWORKS**

**SHAIMAA MOHAMED FARGHALY SAYED**

**SCHOOL OF SCIENCE, ENGINEERING AND ENVIRONMENT  
UNIVERSITY OF SALFORD, MANCHESTER, UNITED KINGDOM**

Submitted in Partial Fulfilment of the Requirements of the Degree of  
Doctor of Philosophy

2020

## Table of Contents

---

Low-Power Dual-Band on-body Antenna for Wireless Body sensor networks.....	i
Shaimaa Mohamed Farghaly Sayed .....	i
School Of Science, Engineering and Environment .....	i
University of Salford, Manchester, United Kingdom.....	i
Table of Contents.....	ii
List of Figures .....	ix
List of Tables .....	xviii
ACKNOWLEDGMENT .....	xix
DEDICATION.....	xx
LIST OF ABBREVIATIONS.....	xxi
Abstract.....	xxiv
Chapter 1 .....	1
Introduction.....	1
1.1. Wireless Body Area Networks .....	1
1.2. Research Motivation.....	2
1.3. Research Problem .....	2
1.4. Research Aim and Objectives.....	3
1.4.1. Research Aim.....	3
1.4.2. Research Objectives.....	3
1.5. Thesis Contribution.....	4
1.6. Application.....	4
1.7. Thesis Organization .....	5

Chapter 2.....	7
On/Off-Body Antennas for Biosensor Network (Literature Review) .....	7
2.1. Introduction.....	7
2.2. Medical Implant Biosensor types .....	8
2.2.1. In-body Biosensors .....	8
2.2.2. On - body Biosensors .....	12
2.2.3. Off - body Biosensors.....	13
2.3. Importance of Biosensor Networks .....	13
2.4. WBAN Architecture .....	15
2.5. Biosensor Networks Problems and Design Considerations.....	16
2.5.1. Propagation Medium Losses .....	16
2.5.2. Data Rates Required for Specific Medical Application .....	17
2.5.3. Processor Operating Time .....	17
2.5.4 Power Consumption and Battery Life Time.....	17
2.6. Some Existing Wireless Communications Protocols for WBAN.....	18
2.6.1. WI-FI—IEEE 802.11ax.....	18
2.6.2. BLUETOOTH—IEEE 802.15.3.....	18
2.6.3. IEEE 802.15.4.....	19
2.7. Design Considerations for On/Off Body Antenna.....	20
2.7.1. Impedance Matching and Tuning .....	21
2.7.2. Radiation Pattern.....	21
2.7.3. Antenna Cost and Weight .....	22
2.7.4. Antenna Placement .....	22
2.7.5. Radiated Power Limitation .....	23

2.7.6. Antenna Communication Bands .....	23
2.7.7. Examples for on-off Body Antenna Design .....	24
2.8. Evaluation for Literature Findings and Previous Work for Proposed Helical Antennas	24
2.9. Conclusion .....	51
Chapter 3.....	52
Assessment of Radiation from Compact Helical Antennas Proposed for On-Body Biosensor Networks .....	52
3.1. Introduction.....	52
3.2. The Proposed Antennas System for On-Body Biosensor Communication .....	53
3.3. Propagation Model of EM Waves near the Surface of the Human Body.....	55
3.3.1. Geometry of the Problem.....	55
3.3.2. Mechanisms of Microwave Propagation near the Surface of the Human Body..	57
3.3.3. Polarization of the Radiated Field for Current Element above Lossy Medium...	59
3.3.4. Fresnel Reflection on the Human Body.....	60
3.4. Evaluation of the Electric Field Radiated from a Wire Antenna over the Human Body	61
3.4.1. Evaluation of the Magnetic and Scalar Potentials due to Current Element above Lossy Medium .....	61
3.4.3. Radiated Field due to Direct Path (Line-of-Sight).....	66
3.4.4. Radiated Field due to Indirect Path (Ground-Reflected Ray).....	67
3.4.5. Total Radiated Field.....	68
3.5. Evaluation of the Radiated Fields from Helical Wire Antennas Placed above the Human Body Surface for WBAN.....	71
3.5.1. Helical Antenna Proposed as Central Antenna for On-Body Biosensor Communications .....	71

3.5.2. Conical and Inverted Conical Helix as Central Antennas for On-Body Biosensor Communications .....	75
3.6. Switching Mechanism.....	77
3.7. Conclusion .....	77
Chapter 4.....	78
Electromagnetic Simulation and Experimental Study of the On-Body Helical Antennas Proposed for Biosensor Networks .....	78
4.1. Introduction.....	78
4.2. Near Field Distribution due to the Proposed On-Body Antennas .....	79
4.2.1. Near Field Distribution due to Cylindrical Helix Antenna on the Human Body	79
4.2.2. Far-Field Pattern due to Cylindrical Helix Antenna on the Human Body.....	81
4.2.3. Near Field Distribution due to Inverted Conical Helix Antenna on the Human Body	85
4.2.4. Far-Field Pattern due to Inverted Conical Helix Antenna on the Human Body..	86
4.2.5. Near Field Distribution due to Conical Helix Antenna on the Human Body..	90
4.2.6. Far-Field Pattern due to Conical Helix Antenna on the Human Body .....	91
4.3. Experimental Measurements and Discussions.....	95
4.3.1. Fabrication of the On-Body Helical Antenna Prototypes .....	95
4.3.2. Experimental Assessment of the Proposed Antenna Performance .....	103
4.4. Conclusion .....	113
Chapter 5.....	115
Performance Assessment of the Proposed On-Body Helical Antennas .....	115
5.1. Introduction.....	115
5.2. Calculation of SAR in the Human Tissues due to the Central On-Body Antenna...	116
5.3. Channel Modeling for WBAN communications and Assessment of Noise Power .	117

5.4. Assessment of Signal Strength and SNR over the Skin of the Human Body in Communication System of the WBAN.....	119
5.5. Assessment of the BER through Numerical Simulation.....	120
5.6. Results and Discussions.....	120
5.6.1. Experimental Measurement and Numerical Assessment of the Power Density Distribution on the Human Body Surface.....	121
5.6.3. SAR Distribution in the Skin, Fat and Muscle Tissues .....	124
5.6.4. Performance Analysis of the On-Body Communication System .....	126
5.6.5. Optimization of the Conical Helix Antenna for Higher Performance of the WBAN Communication System.....	134
5.7. Conclusion .....	139
Chapter 6.....	140
Low Power Dual-Band Conical-Helix/Monopole and Monopole/Spiral On-Body Antennas .....	140
6.1. Introduction.....	140
6.2. The Proposed Conical Helix/Monopole Dual-Band Antenna .....	141
6.3. Assessment of the WBAN Communication System Performance .....	144
6.4. Results of Electromagnetic Simulation and Experimental Measurements.....	144
6.4.1. Antenna-on-Body Model for Electromagnetic Simulation.....	144
6.5. Fabrication of the On-Body Conical-Helix/Monopole Antenna Prototype.....	146
6.5.1. Constructing the Conical-Helix and Monopole Wires .....	146
6.5.2. Mounting the Wire Structure on the Ground Plate and the Feeding Connector	147
6.5.3. Adding Impedance Matching Elements to the Antenna Structure .....	148
6.5.4. Covering the Wire Antenna with Hemispherical Radom for Mechanical Protection .....	149

6.6. Return Loss and Impedance Bandwidth of the Proposed On-Body Antenna.....	150
6.7. Simulation and Experimental Assessment of the Radiation Patterns of the Proposed On-Body Antenna.....	152
6.7.1. Radiation Patterns at <b>3.0 GHz</b> .....	154
6.7.2. Radiation Patterns at <b>5.8 GHz</b> .....	156
6.8. Power Density and SAR Distribution in the Human Tissues due to Radiation from the Proposed On-Body Antenna .....	159
6.8.1. Experimental Assessment of the Power Density Distribution on the Surface of the Human Body .....	159
6.8.2. Semi-Analytic Assessment of the Power Density and SAR Distribution in the Tissues of the Human Body .....	161
6.9. Assessment of the On/Off-Body Communication System Performance using the Proposed On-Body Antenna .....	164
6.9.1. Distribution of the SNR and BER on the Skin due to the Proposed On-Body Antenna	164
6.9.2. Dependence of the SNR and BER on the Height of the On-Body Antenna above the Skin.....	165
6.10. The Proposed Dual-Band Monopole/Spiral Antenna .....	166
6.11. Fabrication of the Monopole/spiral Antenna Prototype .....	171
6.11.1. Constructing the Single-Arm Spiral and Monopole Wires.....	171
6.11.2. Adding Impedance Matching Element to the Antenna Structure .....	172
6.11.3. Covering the Wire Antenna with Hemispherical Radom for Mechanical Protection .....	172
6.12. Results of Electromagnetic Simulation and Experimental Measurements.....	173
6.12.1. Return Loss and Impedance Bandwidth of the Proposed On-Body Antenna .	173

6.12.2. Simulation and Experimental Assessment of the Radiation Patterns of the Proposed On-Body Antenna .....	175
6.13. Power Density and SAR Distribution in the Human Tissues due to Radiation from the Proposed On-Body Antenna .....	182
6.14. Assessment of the WBAN Communication System Performance using the Proposed On-Body Antenna .....	185
6.14.1. Distribution of the SNR and BER on the Skin due to the Proposed On-Body Antenna	185
6.14.2. Dependence of the SNR and BER on the Height of the On-Body Antenna above the Skin.....	186
6.15. Conclusion .....	187
Chapter 7.....	189
Conclusions and Suggestions for Future Work .....	189
7.1. Conclusions.....	189
7.2. Suggestions for Future Work.....	192
7.3. Reflection.....	192
References.....	193



## List of Figures

---

Figure 2.1: Deep brain Stimulation using an in-body biosensor controlled by a neurostimulator. [26].....	9
Figure 2.2: EndoStim biosensor for the treatment of the GORD or LPR. [27].....	10
Figure 2.3: Implantable Cardioverter Defibrillator. [28].....	11
Figure 2.4: Conceptual illustration of the placement of the biosensor used for ICP monitoring. [28].....	12
Figure 2. 5: General architecture of body area networks.....	15
Figure 2. 6: WBAN Architecture. [38].....	16
Figure 2. 7: On- and Off- body Radiation Patterns. [64].....	22
Figure 2. 8: The antenna sensor with its simulated and measured results. [91] .....	29
Figure 2. 9: The octafilar helical antenna. [93].....	31
Figure 2. 10: The compared simulated results return loss and gain. [93].....	31
Figure 2. 11: The four-arm folded ellipsoidal helix antenna with variable ( $\alpha$ ). [94].....	32
Figure 2. 12: The effect of varying ( $\alpha$ ) on resonant frequency. [94].....	32
Figure 2. 13: The effect of varying ( $\alpha$ ) on resonant frequency. [95].....	33
Figure 2. 14: Bifilar Transverse Bilateral Helix Antenna. [96].....	34
Figure 2. 15: (a) Simulated Meander Antenna for Capsule Endoscopy. (b) Spiral Helix Antenna for outside application. [97] .....	34
Figure 2. 16: Proposed Helical Antenna (a) Top View. (b) Side view. [98].....	35
Figure 2. 17: Quarter-wave Monopole Antenna. [102] .....	36
Figure 2. 18: In-the-Ear Spiral Monopole Antenna. [102] .....	37
Figure 2. 19: Imbedded Spiral Antenna for Endoscope. [103].....	37

Figure 2. 20: Spiral MICS-Band Antenna. [104].....	38
Figure 2. 21: (a) Return Loss of Spiral Antenna on Human Breast. (b) Return Loss when tumors occupy from 2% to 46% of the breast. (c) Return Loss when tumors occupy from 50% to 100% of the breast. [104].....	39
Figure 2. 22: (a) Spiral Resonator for BGL monitoring. (b) Patch Resonator for BGL monitoring (top and side views). [105].....	40
Figure 2. 23: Simulated S11 for Both Resonators. [105].....	41
Figure 2. 24: Detailed Geometry of the UWB Antenna. [106].....	41
Figure 2. 25: Single-Arm Archimedean Spiral Antenna. [107].....	42
Figure 2. 26: (a) Spiral Antenna. (b) Embroidered Spiral Antenna Measurement on Human Chest. [109].....	43
Figure 2. 27: YZ – Plane Radiation for OFF-Body Communication. [113].....	45
Figure 3.1: The on-body antenna connects the biosensor network to the Wi-Fi. ....	53
Figure 3.2: The on-body central antenna communicates with the on-skin biosensor antennas via on-body microwave propagation, (a) Photograph showing one of the antennas proposed in the present thesis attached to clothes of the patient as wearable antenna, (b) Illustrative schematic showing the in-body sensors connected to the on-skin antennas.....	54
Figure 3.3: Propagation of microwave on the surface of the human body for on-body biosensor network communication [114].....	55
Figure 3.4: The radiation from the on-body antenna covers the chest-belly area occupied by the biosensor antennas. ....	56
Figure 3.5: Geometry used to develop the propagation model of electromagnetic waves on the human body.....	56
Figure 3.6: Definition of the vertical and horizontal polarization vectors for the incident ray of light. ....	60

Figure 3. 7: Unwrapped turn of a helix.....	63
Figure 3. 8: Geometry of the helical antenna (a) Three-dimensional view, (b) Elevation view, (c) Top view, (d) Side view.....	72
Figure 3. 9: Two types of helical wire antennas with conical external shape: (a) Conical helix, (b) Inverted conical helix.....	75
Figure 3. 10: Geometry of the conical helix antenna (a) Three-dimensional view, (b) Elevation view, (c) Top view, (d) Side view. ....	76
Figure 4.1: The radiation from the on-body antenna covers the chest-belly area surrounded by the blue dashed rectangle and occupied by the on-skin biosensor antennas.....	79
Figure 4.2: Geometry of the helical antenna in the Matlab, (a) Three-dimensional view, (b) Elevation view, (c) Top view, $NT = 4$ , $H = 20$ mm, $D = 20$ mm.....	80
Figure 4.3: Distribution of the electric field magnitude in the plane of the biosensor antennas (parallel to the skin of the human body) due to a central on-body cylindrical helix antenna, $HH = 20$ mm, and $DH = 20$ mm, $f = 2.45$ GHz, $Pin = 0$ dBm.....	81
Figure 4.4: Geometric model of the inverted helical antenna on a circular disc in the CST® simulator, (a) Top view, (b) Side view, (c) Elevation view, (d) Three-dimensional view, $NT = 4$ , $HH = 20$ mm, and $DH = 20$ mm.....	82
Figure 4.5: Three-dimensional far-field radiation pattern of a central on-body cylindrical helix antenna, $HH = 20$ mm, and $DH = 20$ mm, $f = 5.8$ GHz, $Pin = 10$ dBm.....	83
Figure 4.6: Far-field radiation patterns of the right-hand and left-hand polarized electric field for the proposed cylindrical helix antenna in the planes (a) $\phi = 0, 180^\circ$ and (b) $\phi = 90^\circ, 270^\circ$ , $NT = 4$ , $HH = 20$ mm, $DH = 20$ mm, $f = 5.8$ GHz.....	84
Figure 4.7: Frequency dependence of the axial ratio of the far-field radiated from the proposed cylindrical helix antenna in the direction $\theta = 0$ , $NT = 4$ , $HH = 20$ mm, $DH = 20$ mm.....	84

Figure 4.8: Geometry of the inverted conical helix antenna, (a) Three-dimensional view, (b) Elevation view, (c) Top view,  $NT = 4$ ,  $H = 20$  mm,  $\theta_0 = 26.5^\circ$ ,  $D = 20$  mm..... 85

Figure 4.9: Electric field distribution in the plane of the biosensor antennas (parallel to the skin of the human body) due to a central on-body inverted conical helix antenna,  $NT = 4$ ,  $H = 20$  mm, and  $D = 20$  mm,  $f = 2.45$  GHz,  $Pin = 0$  dBm.....86

Figure 4.10: Geometric model of the inverted conical helix antenna on a circular disc in the CST® simulator, (a) Top view, (b) Side view, (c) Elevation view, (d) Three-dimensional view,  $NT = 4$ ,  $HC = 20$  mm,  $\theta_0 = 26.5^\circ$ , and  $DC = 20$  mm..... 87

Figure 4.11: Three-dimensional far-field radiation pattern a central on-body conical helix antenna,  $HC = 20$  mm,  $\theta_0 = 26.5^\circ$ ,  $DC = 20$  mm,  $f = 5.8$  GHz,  $Pin = 10$  dBm.....88

Figure 4.12: Far-field radiation patterns of the right-hand and left-hand polarized electric field for the proposed conical helix antenna in the planes (a)  $\phi = 0, 180^\circ$  and (b)  $\phi = 90^\circ, 270^\circ$ ,  $NT = 4$ ,  $HC = 20$  mm,  $\theta_0 = 26.5^\circ$ ,  $DC = 20$  mm,  $f = 5.8$  GHz,  $Pin = 10$  dBm..... 89

Figure 4.13: Frequency dependence of the axial ratio of the far-field radiated from the proposed inverted conical helix antenna in the direction  $\theta = 0$ ,  $NT = 4$ ,  $HC = 20$  mm,  $\theta_0 = 26.5^\circ$ ,  $DC = 20$  mm,  $f = 5.8$  GHz,  $Pin = 10$  dBm. ....89

Figure 4.14: Geometry of the conical helix antenna, (a) Three-dimensional view, (b) Elevation view, (c) Top view,  $NT = 4$ ,  $H = 20$  mm,  $\theta_0 = 26.5^\circ$ ,  $D = 20$  mm..... 90

Figure 4.15: Electric field distribution in the plane of the biosensor antennas (parallel to the skin of the human body) due to a central on-body conical helix antenna,  $NT = 4$ ,  $HC = 20$  mm,  $\theta_0 = 26.5^\circ$ ,  $DC = 20$  mm. ....91

Figure 4.16: Geometric model of the inverted helical antenna on a circular disc in the CST® simulator, (a) Top view, (b) Side view, (c) Elevation view, (d) Three-dimensional view,  $NT = 4$ ,  $HH = 20$  mm, and  $DH = 20$  mm.....92

Figure 4.17: Three-dimensional far-field radiation pattern a central on-body conical helix antenna,  $HC = 20$  mm,  $\theta_0 = 26.5^\circ$ ,  $DC = 20$  mm,  $f = 5.8$  GHz,  $Pin = 10$  dBm..... 93

Figure 4.18: Far-field radiation patterns of the right-hand and left-hand polarized electric field for the proposed conical helix antenna in the planes (a)  $\phi = 0, 180^\circ$  and (b)  $\phi = 90^\circ, 270^\circ$ ,  $NT = 4$ ,  $HC = 20$  mm,  $\theta_0 = 26.5^\circ$ ,  $DC = 20$  mm,  $f = 5.8$  GHz,  $Pin = 10$  dBm..... 94

Figure 4.19: Frequency dependence of the axial ratio of the far-field radiated from the proposed inverted conical helix antenna in the direction  $\theta = 0$ ,  $NT = 4$ ,  $HC = 20$  mm,  $\theta_0 = 26.5^\circ$ ,  $DC = 20$  mm,  $f = 5.8$  GHz,  $Pin = 10$  dBm. ....94

Figure 4.20: The conical helix antenna proposed to play the role of a central on-body antenna for on-body biosensor antenna network (a) Shape and relative size of the wire antenna, (b) The antenna mounted on a circular copper disc and connected to an SMA connector and an impedance matching element is added, (c) The wire antenna is covered with a microwave-transparent hemispherical radome. ....95

Figure 4.21: Fabricated wires for the three types of medical antennas. The upper antennas are Left-hand circularly polarized whereas the lower antennas are right-hand circularly polarized, (a) Helical antenna, (b) Conical helix antenna, (c) Inverted conical helix antenna..... 96

Figure 4.22: Fabricated copper circular disc to act as a ground base for the three types of helical antennas with a mounted SMA connector, (a) Bottom view, (b) Top view. ....97

Figure 4.23: The fabricated prototypes of the three proposed helical antennas mounted on a circular copper disc with SMA connector for feeding (without being covered by the radome)... 98

Figure 4.24: The cylindrical helix antenna mounted on a circular copper disc and connected to the inner conductor of an SMA connector (a) without impedance matching, (b) with a strip patch connected near the feed point for impedance matching. ....99

Figure 4.25: The inverted conical helix antenna mounted on a circular copper disc and connected to the inner conductor of an SMA connector (a) without impedance matching, (b) with a triangular patch connected near the feed point for impedance matching. ....99

Figure 4.26: The conical helix antenna mounted on a circular copper disc and connected to the inner conductor of an SMA connector (a) without impedance matching, (b) with a triangular patch connected near the feed point for impedance matching..... 100

Figure 4.27: The fabricated prototypes of the three proposed helical antennas mounted on a circular copper disc and covered by hemispherical radome with SMA feeding connector.....101

Figure 4.28: The matched cylindrical helix antenna on a copper circular disc with SMA connector is being covered with hemispherical radome. ....101

Figure 4.29: The matched inverted conical helix antenna on a copper circular disc with SMA connector is being covered with hemispherical radome.....102

Figure 4.30: The matched conical helix antenna on a copper circular disc with SMA connector is being covered with hemispherical radome. ....102

Figure 4.31: The final form of the proposed on-body medical antenna connected to a coaxial cable for the purpose of experimental measurements.....103

Figure 4.32: Measurement of the reflection coefficient  $S_{11}$  of the helical antenna using the VNA of the Agilent Field Fox N9918A, (a) The uncovered antenna, (b) The antenna covered with the hemispherical radome. ....104

Figure 4.33: Measured frequency response of the reflection coefficient  $S_{11}$  of the cylindrical helix antenna showing the effect of adding the matching element and the placement of the antenna on the human body. ....105

Figure 4.34: Measurement of the reflection coefficient  $S_{11}$  of the inverted conical helix antenna using the VNA of the Agilent Field Fox N9918A (a) The uncovered antenna, (b) The antenna covered with the hemispherical radome.....106

Figure 4.35: Measured frequency response of the reflection coefficient  $S_{11}$  of the inverted conical helix antenna showing the effect of adding the matching element and the placement of the antenna on the human body. ....107

Figure 4.36: Measurement of the reflection coefficient  $S_{11}$  of the conical helix antenna using the VNA of the Agilent Field Fox N9918A, (a) The uncovered antenna, (b) The antenna covered with the hemispherical radome..... 108

Figure 4.37: Measured frequency response of the reflection coefficient  $S_{11}$  of the conical helix antenna showing the effect of adding the matching element and the placement of the antenna on the human body. ....109

Figure 4.38: Experimental setup for measuring the radiation pattern of the proposed on-body helical antennas using the VNA of the Agilent Field Fox N9918A..... 110

Figure 4.39: Comparison between the simulated and measured far-field radiation patterns of the right-hand circular polarization for the cylindrical helix antenna in the planes (a)  $\phi = 0, 180^\circ$  and (b)  $\phi = 90^\circ, 270^\circ, f = 5.8 \text{ GHz}$ .....111

Figure 4.40: Comparison between the simulated and measured far-field radiation patterns of the right-hand circular polarization for the inverted conical helix antenna in the planes (a)  $\phi = 0, 180^\circ$  and (b)  $\phi = 90^\circ, 270^\circ, f = 5.8 \text{ GHz}$ .....112

Figure 4.41: Comparison between the simulated and measured far-field radiation patterns of the right-hand circular polarization for the conical helix antenna in the planes (a)  $\phi = 0, 180^\circ$  and (b)  $\phi = 90^\circ, 270^\circ, f = 5.8 \text{ GHz}$ . ....113

Figure 5.1: Representation of the received signal,  $rx e^{j\phi x}$ , for a specific transmitted symbol,  $rse^{j\phi s}$ , after adding the AWGN  $rne^{j\phi n}$ .....119

Figure 5.2: Wi-Fi Antenna operating at 5.8 GHz is mounted on the ceil of the room and directed downwards.....121

Figure 5.3: Measurement of the power density distribution near the skin of the body using the radiation hazard meter Extech® model 480846 due to, (a) Ambient radiation from the Wi-Fi antenna mounted on the ceil as shown in Figure 5.2, (b) Radiation by the proposed conical helix antenna without the radome (input power  $P_{in} = 0 \text{ dBm}$  at  $f = 2.45 \text{ GHz}$ ).....122

Figure 5.4: Measurement of the power density distribution near the skin of the body using the radiation hazard meter Extech® model 480846 when the conical helix antenna is excited with input power  $P_{in} = 0 \text{ dBm}$  at  $f = 2.45 \text{ GHz}$ , (a) The antenna is oriented with tip pointing to the power density meter , (b) The antenna is oriented with tip pointing to the room ceil (normal operation). ....123

**Figure 5.5:** Distribution of the power density just on the surface of the body due to conical helix antenna fed with input power  $P_{in} = 4 \text{ dBm}$  at  $f = 2.45 \text{ GHz}$ ..... 124

**Figure 5.6:** SAR distribution in the skin tissues due to conical helix antenna fed with input power,  $P_{in} = 4 \text{ dBm}$  at  $f = 2.45 \text{ GHz}$ . .....125

**Figure 5.7:** SAR distribution in the fat tissues due to conical helix antenna fed with input power,  $P_{in} = 4 \text{ dBm}$  at  $f = 2.45 \text{ GHz}$ . .....126

**Figure 5.8:** SAR distribution in the muscle tissues due to conical helix antenna fed with input power,  $P_{in} = 4 \text{ dBm}$  at  $f = 2.45 \text{ GHz}$ . .....126

**Figure 5.9:** Constellation diagram for 8-PSK modulation system with 50% spectral efficiency after adding the AGWN for different values of  $E_b/N_o$  (a) Reference symbols (c)  $E_b/N_o = 25 \text{ dB}$ , (d)  $E_b/N_o = 20 \text{ dB}$ , (e)  $E_b/N_o = 15 \text{ dB}$ , (f)  $E_b/N_o = 10 \text{ dB}$ .....128

**Figure 5.10:** BER and SER versus the  $E_b/N_o$  for BSN that implements  $M$ -ary PSK modulation with different number of symbols. (a)  $M = 4$ , (b)  $M = 8$ , (c)  $M = 16$ , (d)  $M = 32$ . .....129

**Figure 5.11:** Distribution of the received power and SNR over the area within which the (isotropic) biosensor antennas are allocated due to a central on-body cylindrical helix antenna fed with input power,  $P_{in} = 4 \text{ dBm}$  at  $f = 2.45 \text{ GHz}$ , (a) Power received by isotropic biosensor antennas, (b) SNR at the receiving biosensor antennas..... 131

**Figure 5.12:** Distribution of the BER over the area within which the (isotropic) biosensor antennas are allocated due to a central on-body cylindrical helix antenna fed with input power,  $P_{in} = 4 \text{ dBm}$  at  $f = 2.45 \text{ GHz}$ , (a) BER for 8-symbol PSK, (b) BER for 16-symbol PSK... 132

**Figure 5.13:** Distribution of the received power and SNR over the area within which the (isotropic) biosensor antennas are allocated due to a central on-body conical helix antenna fed with input power,  $P_{in} = 4 \text{ dBm}$  at  $f = 2.45 \text{ GHz}$ , (a) Power received by isotropic biosensor antennas, (b) SNR..... 133

**Figure 5.14:** Distribution of the BER over the area within which the (isotropic) biosensor antennas are allocated due to a central on-body conical helix antenna fed with input power,  $P_{in} = 4 \text{ dBm}$  at  $f = 2.45 \text{ GHz}$ , (a) BER for 8-symbol PSK, (b) BER for 16-symbol PSK...134



**Figure 5.15:** Dependence of the minimum resulting SNR on the height of the conical helix when used in WBAN as a central on-body antenna fed with different values of the input power at  $f = 2.45 \text{ GHz}$ . .....135

**Figure 5.16:** Dependence of the maximum resulting BER on the height of the conical helix when used in WBAN as a central on-body antenna fed with different values of the input power at  $f = 2.45 \text{ GHz}$ . .....135

**Figure 5.17:** Dependence of the minimum resulting SNR on the half apex-angle of the conical helix when used in WBAN as a central on-body antenna fed with input power,  $P_{in} = 4 \text{ dBm}$  at  $f = 2.45 \text{ GHz}$ . .....136

**Figure 5.18:** Dependence of the maximum resulting BER on the half apex-angle of the conical helix when used in WBAN as a central on-body antenna fed with input power,  $P_{in} = 4 \text{ dBm}$  at  $f = 2.45 \text{ GHz}$ . .....137

**Figure 5.19:** Dependence of the minimum resulting SNR on the location of the conical helix above the surface of the human body when used in WBAN as a central on-body antenna fed with different values of the input power at  $f = 2.45 \text{ GHz}$ . .....138

**Figure 5.20:** Dependence of the maximum resulting BER on the location of the conical helix above the surface of the human body when used in WBAN as a central on-body antenna fed with different values of the input power at  $f = 2.45 \text{ GHz}$ . .....138

## List of Tables

---

Table 2.1: Comparison Between Uniform and Radius Varying Helices. [92].	30
Table 2.2: Summarizing Previous Related Work.	46
Table 5.1: Average mass density of the concerned types of human tissues.	117
Table 5.2: Electric properties of concerned types of human tissues at 2.45 GHz.	117
Table 6.1: Electric properties of the concerned types of the human tissues at 3.0 GHz and 5.8 GHz.	145

## **ACKNOWLEDGMENT**

I am thankful and grateful to Almighty Allah for giving me power to complete this work. I offer sincere thanks to my supervisor Dr. Omar Alani for the encouragement, advice provided, and guidance in the preparation of this thesis. Dr. Omar played a major role in this thesis; I passed through severe family problems which lead to prohibiting me from travelling and an interruption of study but, he supported me all the way through pulling myself together and helped me to continue my PhD.

I would like to acknowledge the role of the Arab Academy for Science, Technology and Maritime Transport which supported and sponsored me during my Ph.D. study.

I owe my deep gratefulness to my father, Prof. Mohamed Farghaly for his endless support and help by all means for me to reach this point. I am who I am because of him. I am proud to be the daughter of this genius man and having the chance to fulfil his dream by studying PhD.

I also owe everything to my supporting mother and my daughters, although they are too young, but they gave me an endless love and support.

Finally, I would like to express my gratitude to Prof. Khalid Fawzy and Dr. Asmaa El-Sayed in the National Institute of Research in Cairo, Egypt for their dedication, guidance, long teaching hours of this work.

## **DEDICATION**

I dedicate this thesis to my father, mother and my daughters.

## LIST OF ABBREVIATIONS

WBAN	Wireless Body Area Network
SAR	Specific Absorption Rate
Wi-Fi	Wireless Fidelity
SNR	Signal-to-Noise Ratio
BER	Bit Error Rate
CST	Computer Simulation Technology
AWGN	Additive White Gaussian Noise
BSN	Body Sensor Network
PSK	Phase Shift Keying
IMDs	Implantable Medical Devices
DBS	Deep Brain Stimulation
FDA	Food and Drug Administration
GORD	Gastro – Oesophageal Reflux Disease
LOS	Lower – Oesophageal Sphincter
IPG	Implantable Pulse Generator
ICD	Implantable Cardioverter Defibrillator
ICP	Intracranial Pressure
TBIs	Traumatic Brain Injuries
MEMS	Microelectromechanical Systems
RF	Radio Frequency
CSF	Cerebral Spinal Fluid

EES	Epidermal Electronics Systems
IoT	Internet of Things
IBC	Intra-Body Communication
Kbps	Kilobits per seconds
Mbps	Megabits per seconds
BLE	Bluetooth Low Energy
IEEE	Institute of Electrical and Electronics Engineers
MAC	Medium Access Control
ZigBEE	Zonal Intercommunication Global Standard with battery life Economical and Efficient
WLAN	Wireless Local Area Network
ERP	Effective Radiated Power
ZOR	Zeroth- Order Resonance
MICS	Medical Implant Communication System
FCC	Federal Communication System
MBAN	Medical Body Area Network
ISM	Industrial, Scientific and Medical
EM	Electromagnetic
MATlab	Matrix Laboratory
SMA	Sub Miniature version A
VNA	Vector Network Analyzer
BCWC	Body Centric Wireless Communication

BCC	Body Centric Communication
B.W.	Band Width
BAN	Body Area Network
CBSA	Cavity Back Slot Antenna
CMOS	Complementary Metal Oxide Semiconductor
ECG	Electrocardiogram
EEG	Electroencephalogram
RF	Radio Frequency
RFID	Radio Frequency Identification
SN	Sensor Node
UWB	Ultra-Wide Band
IB2IB	In-Body 2 In-Body
IB2OB	In-Body 2 On-Body
IB2OFFB	In-Body 2 OFF-Body
ITEA	In The Ear Antenna
OFHA	Octafilar Helical Antenna

## Abstract

---

In Wireless Body Area Network (WBAN), the implanted biosensor collects various physiological data and wirelessly transmits the information to external medical devices in real time. The antenna design for this application faces great challenges as the microwave propagation medium is not the free space as the human tissues constitute part of the transmission channel. The effects of the human body should be taken into consideration during the antenna design.

The present thesis aims to arrive at the optimum design of the on-body antenna to operate as a central antenna for WBAN. Five types of helical antennas are proposed in the present thesis having a dual-frequency operation at 2.45 GHz and 5.8 GHz. The proposed antennas are optimized to maximize the Signal-to-Noise-Ratio (SNR) and, hence, to minimize the BER and the Specific Absorption Rate (SAR) in the human tissues.

In this thesis, a semi-analytic rigorous technique for the assessment of microwave propagation on the medium equivalent to the human body is developed and the radiated fields from the proposed on-body antennas in the near zone are evaluated.

The commercially available CST® simulator is used and experimental measurements are done for the five fabricated prototypes. The near-field distribution over the surface of human body is evaluated at 2.45 GHz using a Matlab® program, while the far-field radiation patterns obtained by experimental measurements showing good agreement with those obtained by the CST® simulator. It is shown that the radiation patterns produced by the more compact antennas; the conical-helix monopole and the monopole-spiral antennas show better performance and more appropriate for the intended application.

It is clear from the obtained results that the conical-helix/monopole and the monopole-spiral antennas have the highest performance. These antennas are shown to achieve the minimum BER of  $5.3 \times 10^{-5}$  and  $6 \times 10^{-8}$  for both antennas respectively. In addition, the minimum average of the SAR that does not exceed 0.3 W/Kg in the human tissues while consuming the minimum value of the input power when compared with the other antenna types.



# Chapter 1

## Introduction

---

### 1.1. Wireless Body Area Networks

Medical implant biosensors are an integral part of the Wireless Body Area Network (WBAN), where wearable devices and implants are interconnected with wearable or implanted link sensor nodes. The general architecture of body area networks is that a link node wearable on the surface talks to and listens from the implanted and other surface mounted devices. It then combines and relays the signal to devices external to the body – mainly a monitoring or controlling device on the surface or a few meters away from the body.

Biosensors are mainly designed for the purpose of diagnostic, therapeutic and assistive applications in health-care, active living and sports technology. In WBAN, to monitor a patient's health status, the implanted device collects various physiological data and wirelessly transmits the information to external medical devices in real time. The antenna design for this purpose faces great difficulties as the wireless communication medium is not through-the-air but uses the human tissues as part of the transmission channel. The human body is lossy in nature and also has higher permittivity, so the designer needs to consider the human body effects in the antenna design. Thus, the placement of antenna over the body can significantly contribute to its performance. The factors affecting the antenna design include antenna impedance matching, radiation pattern, Specific Absorption Rate (SAR), size compactness, space constraints, desired radiation characteristics, low cost, light weight, multi-band operation, interference mitigation, reconfigurability, positioning, bending and stable performance with the variation of the gap between the antenna and the human body. To comply with the safety guide lines, a limitation is applied to the effective power radiated from the antenna. This power limitation added extra challenge to the antenna design in the human body lossy medium.

For wearable antennas intended for on/off-body wireless communications, the challenge is to design an antenna with dual operation modes, each mode has its specific radiation characteristics, and to make the antenna input impedance matching less sensitive to potentially

varying distance between the antenna and the human body. For the first mode the antenna is used for on-body communications to collect vital information from the human body (i.e. from the in-body and on-body biosensors). This requires the antenna to have wide-beam or omnidirectional radiations in the plane parallel to the human body surface to provide maximum coverage over the body. This can be achieved by minimizing the radiations that are away from the human body (i.e. off-body). By introducing a null in the direction normal to the body, we can suppress off-body radiations and can enhance the on-body radiations. In the second mode of operation the antenna is used to transmit the collected information towards the outside Wi-Fi for example. In this case, the radiated beam can be directed towards the receiving device placed away of the patient's body.

## **1.2. Research Motivation**

Lower energy consumption of each biosensor antenna and reliable transmission of biomedical data are of critical priority in WBANs. The patient needs on-body antennas to collect the monitored medical data; which represents emergency situation or normal medical data that needs more reliability for transmission from on-body antennas to the sensor node and then to an external device in addition to increasing the lifetime for biosensor nodes. Therefore, designing a dual-antenna that can perform in both on- and off- body communication while decreasing the specific absorption rate (SAR) and reducing the harmful effects on the human body will support this motivation.

## **1.3. Research Problem**

The antenna design for this application faces great challenges as the microwave propagation medium is not the free space as the human tissues constitute part of the transmission channel. The human body has high permittivity and conductivity, so the effects of the human body should be taken into consideration during the antenna design. The factors affecting the antenna design include antenna impedance matching, multi-band operation, radiation pattern, and the constraints on the Specific Absorption Rate (SAR) in the human tissues. To comply with the safety limits of microwave exposure, a limitation is applied to the effective power radiated from the on-body

antenna. This power limitation adds extra challenge to the antenna design in the presence of the human body lossy medium.

## **1.4. Research Aim and Objectives**

### **1.4.1. Research Aim**

The aim of this research is to arrive at the optimum design of the on-body antenna to operate as a central antenna for WBAN.

Each antenna should have dual-frequency operation at 2.45 GHz for the on-body communications (WBAN) and 5.8 GHz for the off-body communications (Wi-Fi). The aim is to maximize the Signal-to-Noise-Ratio (SNR) and the SAR in the human tissues, hence, to minimize the Bit-Error-Rate (BER) for efficient on-body communications of the WBAN at the two frequencies of operation.

### **1.4.2. Research Objectives**

The present thesis aims to arrive at the optimum design of the on-body antenna to operate as a central antenna for WBAN. This antenna should fulfill the following requirements:

- Dual-frequency operation 2.45 GHz for the on-body communications (WBAN) and 5.8 GHz for the off-body communications (Wi-Fi).
- Broadside radiation pattern at 2.45 GHz for on-body communications.
- End-fire radiation pattern at 5.8 GHz for off-body communications.
- Maximization of the frequency bandwidth for the off-body communications to achieve high bit rate for transferring the data records from the WBAN to the external storage devices through the Wi-Fi in short time to minimize the electromagnetic doze in the human body.
- Minimization of the input power of the biosensor antennas to achieve long life time of the difficult-to-replace batteries of the biosensors.
- Maximizing the Signal-to-Noise-Ratio (SNR) and, hence, minimizing the Bit-Error-Rate (BER) for efficient on-body communications of the WBAN.

- Minimization of the SAR in the human tissues at the two frequencies of operation, especially at the lower frequency of the WBAN (2.45 GHz.) as the microwave at this frequency is much more penetrable into the human tissues than the case at the higher frequency (5.8 GHz).

The on-body central antenna design has considerable challenges as some of the above design objectives are contradicting. For example, to reduce the BER in the communication system WBAN, the input power of the antennas should be increased, which leads to increase the SAR in the human tissues. Thus, some of the on-body antenna design objectives are contradicting. Consequently, a compromise should be made to realize threshold values of some performance measures such as the maximum BER and the minimum SAR.

## **1.5. Thesis Contribution**

This thesis proposes five novel on-body antennas to operate for WBAN. Each antenna performs in dual-frequency mode. These antennas were designed using the de-embedding technique and optimized to minimize the input power as well as the SAR.

A mathematical model is done for the designed on-body antennas to develop a propagation model of electromagnetic waves on the human body which is a lossy medium. The propagation model provides description of the electric field components in order to get the total radiated field from the on-body helical antennas placed above the human body.

Furthermore, several studies were made to develop the dependence of the SNR and BER on the height and the apex angle of the conical helix antenna. These studies resulted in that with increasing the height of the conical helix, the SNR is increased and the BER is decreased, while when increasing the apex angle the SNR and BER stay constant.

## **1.6. Application**

The proposed dual on-body antennas in this thesis are designed to perform for WBAN in medical applications where the patient is being monitored in the hospital. The data are collected and sent to an external device through Wi-Fi to the doctor to be analyzed.

## 1.7. Thesis Organization

In addition to this chapter of introduction, the thesis contains other six chapters which are organized as follows;

**Chapter 2:** An overview of the types of the medical implant biosensors is presented showing the difference between the in-body, on-body, and off-body biosensors and the uses of each type. The WBAN architecture is illustrated with the associated network problems and design considerations. The wireless communication protocols used in the WBAN is reviewed. Finally, the antenna design considerations for the on/off body biosensor are investigated. The most important factors affecting the antenna design include antenna detuning, impedance matching, radiation pattern, SAR, size compactness, space constraints, low cost, light weight, multi-band operation, interference mitigation, configurability, positioning, bending and stable performance with the variation of the gap between the antenna and the human body. The details of each design parameter is presented with some examples for antennas designed to work as an on/off body biosensor.

**Chapter 3:** A semi-analytic rigorous technique for the assessment of microwave propagation on the medium equivalent to the human body is developed to evaluate the near field radiated from arbitrarily shaped wire antennas at the possible locations of on-skin antennas connected to implantable (in-body) biosensors. Three types of helical antennas are proposed to be employed as central antennas for WBAN. Each of the proposed antennas is a dual-band of the helical wire type. It is designed to operate in the end-fire (axial) mode to communicate with the Wi-Fi communication system (5.0 – 6.0 GHz). Also, it is designed to operate in the broad-side (normal) mode to communicate with the on-skin biosensor antennas at 2.45 GHz [. The radiated fields from the proposed on-body antenna helical antenna types in the near zone are evaluated using the proposed semi-analytic technique.

**Chapter 4:** The cylindrical helix, conical helix, and inverted conical helix antennas proposed to operate as central antennas for WBAN are investigated through semi-analytic technique, CST® simulator, and experimental measurements. Each of the proposed helical antennas is a dual-band that is designed to produce in the end-fire radiation to communicate (through its far-field) with

the Wi-Fi antenna at 5.8 GHz, and to produce broad-side radiation to communicate (through its near field) with the on-skin biosensor antennas at 2.45 GHz. Three prototypes of the proposed helical antennas are fabricated. Each antenna is matched with  $50\Omega$  coaxial feeder over a wide frequency band, mounted on a copper circular disc, and covered with a very thin dielectric radom for protecting the wire antenna. Such an antenna when covered by the radom is shaped like a hemispherical button that can be attached to the patient clothes and, hence, it can be considered as wearable antenna. The near-field distribution over the surface of human body is presented at 2.45 GHz. The radiation patterns obtained by experimental measurements for the three fabricated prototypes show good agreement with those obtained by the CST® simulator and are shown to be appropriate for communication with the Wi-Fi antennas at 5.8 GHz.

**Chapter 5 & 6:** Quantitative assessment of the WBAN communication system performance is achieved when each of the five proposed helix antennas is employed as on-body central antenna for the WBAN. For its high immunity to noise, the utilized modulation system is assumed to be  $M$ -ary Phase-Shift Keying (PSK), with  $M = 8$  and  $M = 16$ . A channel modeling is performed for such a communication system by considering Additive White Gaussian Noise (AWGN) to evaluate the SNR and, hence, the corresponding BER can be calculated. This enables the calculation of the minimum input power of the proposed on-body WBAN central antenna that achieves the required BER for a specific data rate. On the other hand, the distribution of the microwave power density near the body surface is evaluated by simulation and experimental measurements to ensure the realization of the electromagnetic exposure safety limits. Also, the SAR distribution inside the human tissues of concern is evaluated. It is shown that the conical-helix/monopole and monopole-spiral antenna have higher performance than that of the other three proposed helix antennas. The effects of the on-body conical helix antenna dimensional parameters and the antenna height above the human body surface on such performance measures and electromagnetic doze level are numerically studied for the purpose of arriving at the optimum design of the proposed on-body wearable conical helix antenna. It is shown that SNR is increased and, hence, the BER is decreased with increasing the height of the helix while being constant and independent of the apex angle of the conical helix.

**Chapter Seven:** The conclusions of the present thesis are summarized and some extensions suggested as future work for more complete design of the antenna system for WBAN.

## Chapter 2

### On/Off-Body Antennas for Biosensor Network (Literature Review)

---

#### 2.1. Introduction

Technological advancement, miniaturization of electronic devices and progress in ad-hoc network routing protocols and embedded systems have facilitated developments in the field of biosensors and biosensor networks. Biosensor networks are a collection of biosensor units that collect information about biological responses and process it in order to make a decision for a desired outcome. Medical implant biosensors communications have achieved great progress over the past six decades. Low power communications and long term operation of medical implants have been the sought of research since 1950 [1]. Reliable communications, high degree of miniaturization, and sustainable power sources, are the primary target of implanted medical devices (IMDs) design, while maintaining bio-compatibility to surrounding tissues adhering to the human safety limits set by appropriate guidelines.

IMDs are designed mainly for the purpose of diagnostic, therapeutic and assistive applications in health-care, active living and sports technology. Diagnostic implants measure vital health signs and include devices such as intra-cranial pressure monitors [2], [3], glucose sensors [4], deep brain activity sensors [5], oximeters [6], pH sensors [7], and gastrointestinal imagery pills [8]. The second category, therapeutic IMDs, have been used to treat some form of ailment via electromagnetic stimulation or targeted biochemical intervention according to a pre-calibrated stimulus or controlled closed loop feedback generated by another implanted sensory unit. These IMDs are used in applications such as pacemakers, nerve and muscle stimulator, deep brain stimulator [9], gastric defibrillators [10], targeted drug delivery systems [11]. Finally, assistive IMDs assist sick or even healthy people in improving anatomical and physiological functions. Some examples include cochlear implants [12], bionic vision implants [13], brain computer interfaces for prosthetic limbs [14], and athletic performance monitors.

## **2.2. Medical Implant Biosensor types**

### **2.2.1. In-body Biosensors**

Important application of biosensors is monitoring and measuring activity inside the human body. This kind of sensors are denominated as implantable biosensors when partially or fully introduced into the human body aiming to remain there for long periods of time in a minimally invasive way. Implantable devices are another viable alternative for a continuous monitoring, minimizing the pain and discomfort of the person. In the near future, these implanted electronics will be an important tool in biomedicine, since it can provide a clearer picture of the cascade of events occurring inside the body in a certain period of time, helping monitoring chronic diseases, or progress after treatment and/or surgery. They can be found in the body, heart, eyes, blood and brain. Implantable biosensors have several advantages over other monitoring devices, since they can monitor biological metabolites, nerve electrical stimulation, the detection of electric signals, restoring body functions, and be used for drug delivery, between others directly from inside the biological body [15]. A good example is monitoring blood pressure, an essential parameter in all organs of the human body. A change in the pressure may result in a deteriorating or injury of the physiological function. Hypertension and infarction are usual and serious health problems associated with the function or dysfunction of the cardiac muscle. Investigations of implantable and miniaturized blood pressure biosensors for continuous monitoring of hypertension and consequent efficient treatment are being made [16].

Developing a fully implantable biosensor requires the integration of heterogeneous elements, including electrodes for the recognition/sensing of the target vital signals, a circuit capable of performing measurements and transmitting the data, and a power source. The final shape and dimensions of the implantable biosensor must be biocompatible and well tolerated by the host, in order to avoid toxicity and chronic inflammation [17]. Hence, one of the highest obstacles on the development of implantable devices delays on the challenges associated with the mismatch between the hard, planar surfaces of semiconductor wafers and the soft, curvilinear tissues of biological systems. They tend to easily damage the surrounding tissues during insertion and exert chronic stress onto the adjacent biological environment, due to their sharp edges, steepness, design and size [18, 19]. So, clearly, conventional sensors, partially or fully rigid



implants based on silicon wafer substrates, are more likely to be rejected and fouled. These materials are described as causing formation of fibrous capsules around the system diminishing the in vivo sensor performance, resulting in sensor failure [20–22]. Thus, for medical applications, it is mandatory to promote a replacement of silicon wafers by biocompatible, soft and flexible substrates, like biopolymer-based substrates, in order to alleviate that body-foreign issue and suppress fibrotic tissue encapsulation [16, 20]. Commonly used polymeric substrates are polyethylene naphthalate, polyethylene terephthalate and polyimide [23]. These polymer substrates are essential for devices to overcome the mismatch between the hard, planar surfaces of semiconductor wafers and the soft, curvilinear tissues of biological systems [24-25].

One of the most common processes that employ an in-body sensor is the Deep brain stimulation (DBS). DBS is an elective surgical procedure in which electrodes are implanted into certain brain areas as shown in Figure 2.1. These electrodes, or leads, generate electrical impulses that control abnormal brain activity. The electrical impulses can also adjust for the chemical imbalances within the brain that cause various conditions. Stimulation of brain areas is controlled by a programmable generator that is placed under the skin in the upper chest.

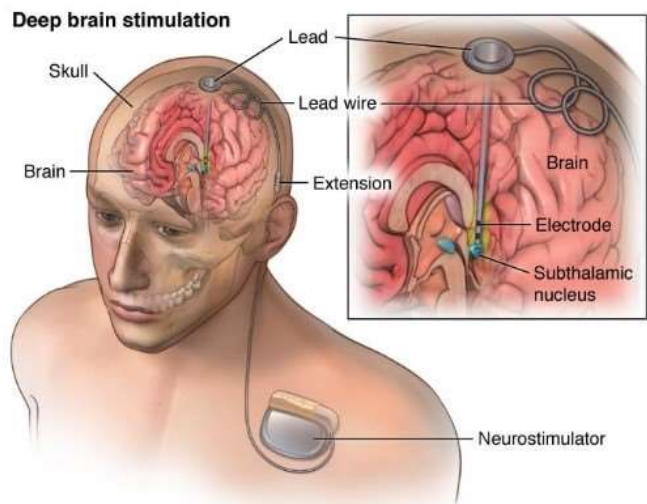


**Figure 2.1:** Deep brain Stimulation using an in-body biosensor controlled by a neurostimulator. [26]

In this therapy, electrodes are surgically placed deep into the brain where they electrically stimulate specific structures in an effort reduce the symptoms of various brain-based disorders. The U.S. Food and Drug Administration (FDA) first approved the use of DBS in 1997 for essential tremor. Since then, the FDA or other global regulators have approved DBS for

Parkinson's disease, dystonia, tinnitus, epilepsy, obsessive-compulsive disorder, and neuropathic pain. DBS is also being investigated as a treatment for Tourette syndrome and psychiatric disorders such as depression. It is estimated that more than 150,000 people globally have received a DBS implant [26]. Researchers have also put a great deal of time into manipulating the vagus nerve using neural implants. The vagus nerve connects most of our key organs to the brain stem, and researchers are hacking this communication superhighway in an effort to treat heart failure, stroke, rheumatoid arthritis, Crohn's disease, epilepsy, type 2 diabetes, obesity, depression, migraine, and other ailments.

Another example of the in-body biosensor is the one used for the EndoStim [27] for the treatment of the gastro-oesophageal reflux disease (GORD) or laryngopharyngeal reflux (LPR). EndoStim involves applying electric current to the nerves around the lower oesophageal sphincter (LOS) to increase its effectiveness, a technology known as neuro-stimulation. The EndoStim system consists of a bipolar lead (electrical wire) that delivers low energy electrical pulses to the lower oesophageal sphincter and an Implantable Pulse Generator (IPG) – a small device similar to a pacemaker – which is wirelessly programmed and can be adjusted to suit each patient's needs. By stimulating the LOS valve, it is expected to stay closed to prevent reflux and open to allow for food and drink to pass into the stomach. A diagram showing the EndoStim is shown in Figure 2.2.

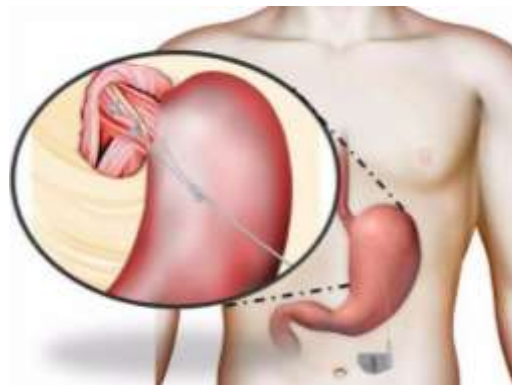


**Figure 2.2:** EndoStim biosensor for the treatment of the GORD or LPR. [27]

The Implantable Cardioverter Defibrillator (ICD) is another example for the implantable in-body biosensor. It is a small battery-powered device placed in your chest to monitor your heart rhythm and detect irregular heartbeats. An ICD can deliver electric shocks via one or more wires connected to your heart to fix an abnormal heart rhythm as shown in Figure 2.3.

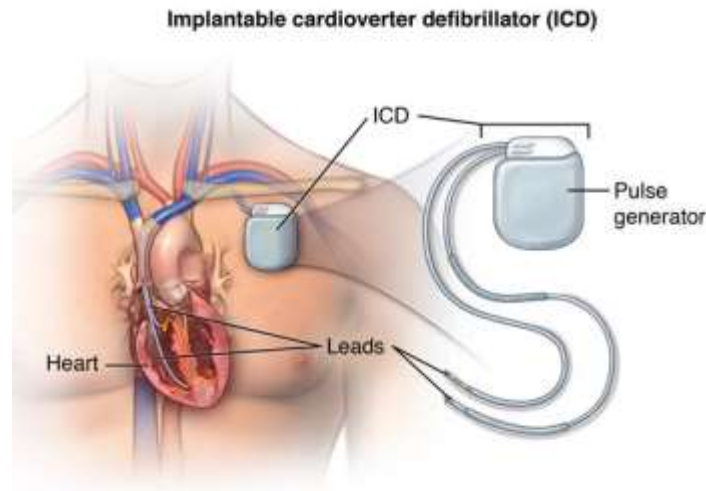


**Figure 2.3:** Implantable Cardioverter Defibrillator. [28]

Assessment of intracranial pressure (ICP) is of great importance in management of traumatic brain injuries (TBIs). An invasive implantable sensor for continuous ICP monitoring of the ICP can be used for this purpose. The implant comprises ultrathin ( $50 \mu\text{m}$ ) flexible spiral coils connected in parallel to a capacitive microelectromechanical systems (MEMS) pressure sensor. The implantable sensors are inductively coupled to an external on-body reader antenna. The ICP variation can be detected wirelessly through measuring the reader antenna's input impedance [28]. A conceptual illustration of the implant placement is shown in Figure 2.4.

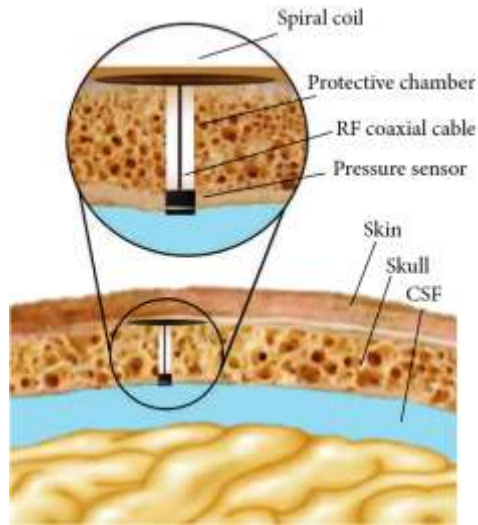


**Figure 2.4:** Conceptual illustration of the placement of the biosensor used for ICP monitoring. [28]

As shown in Figure 2.4, the flexible spiral coil lies between the skull and skin and is connected to the MEMS sensor through an ultrathin RF coaxial cable. The deformable diaphragm of the MEMS sensor is in contact with CSF for subdural ICP measurement. Both the MEMS sensor and coaxial cable are placed in a protective chamber which improves the mechanical attachment of the implant to the skull and facilitates the implant removal in case of rejection. The protective chamber should be a biocompatible, nonmetallic cylindrical chamber to protect the MEMS sensor and cable in physiological environment after implantation. However, since the coaxial cable itself is shielded, presence of the chamber does not affect the telemetry operation.

### 2.2.2. On - body Biosensors

A strategy to perfectly integrate electronics with the human body is the approach of skin-mounted epidermal electronics systems (EES) which provides a route to non-invasive continuous monitoring of clinically important physiological signals, such as skin temperature, heart rate, blood pressure, pulse and respiration rate, and transmits that information to the patient and the physician [29]. In addition to the assessment of these clinically relevant physiological parameters, sweat, saliva and tears also contain multiple physiology chemical constituents [30]. The use of this type of sensors holds considerable promise for maintaining and improving quality of life and consequently overrates the traditional systems. These traditional systems are known to possess wires or cables, point-contact electrodes affixed to the skin with adhesive pads,

mechanical clamps or straps, or penetrating needles, mostly mediated by conductive gels. Besides that, they are also poorly suited for practical applications outside of clinical settings, because they can cause discomfort, irritation and inflammation to the user, lose adhesion over time, lack mobility, be generally very bulky due to their robust, plan and hard formats and components and only allow the monitoring of one physiological signal [29].

### **2.2.3. Off - body Biosensors**

Post implant monitoring is an essential factor for the implantable devices and patient care. Remote monitoring fills the gap of the lack of information resultant from the conventional follow-up visits, providing large prospective trials, automatic daily transmissions and long-term support at a distance, allowing the patient to be at home [31]. Advances on implantable medical devices are demanding, since the methods to translate the follow-up observations are time consuming and complex. Better methods to transmit the collected data obtained are urging for further developments in implantable devices. A considerable increasing in the density of analysis and interpretation/processing algorithms is also required [32]. The devices are equipped with a micro-antenna for communication and thereby the sensed data are remotely transmitted to an external system, such as a computer, smartphone or tablet and network, like wireless body area networks (WBAN). The antenna may be built up by flexible materials and consequently, flexible coils, to improve the biocompatibility and conform to the inner body and organs.

Wireless communication can be achieved by using radio frequency (RF), optical, sound, or infrared media, although RF is the most common [33]. Wireless RF telemetry also depends upon a considerable power and can experience poor transmission through biological tissue. Wireless data transmissions through electromagnetic induction, or light were developed, but they have troubles transmitting the data when the external data transmission unit alters from its proper position; therefore, other methods are being developed [34].

## **2.3. Importance of Biosensor Networks**

Medical implant biosensors are an integral part of the Wireless Body Area Network (WBAN), where wearable devices and implants are interconnected with wearable or implanted link sensor nodes as shown in Figure 2.5. Implants can also communicate with each other, as an

example is the implanted glucose sensor which communicates with an insulin pump. The general architecture of body area networks, as shown in Figure 2.5, is that a link node wearable on the surface talks to and listens from the implanted and other surface mounted devices. It then combines and relays the signal to devices external to the body – mainly a monitoring or controlling device on the surface or a few meters away from the body. Another likely scenario is the possibility of two implants talking to each other; for example, a glucose sensor and an insulin pump. To reduce complexity and power consumption it is better to implement advanced security features at the link node rather than each individual implanted or on-body device.

So far, IMDs are designed for singular applications where communication is restricted between the IMD and external monitoring station either on-body or indoors. However, IMDs could be integrated into a wireless network of implants for more holistic and efficient data transmission. As such, the network of implants can be envisioned as an integral part of internet of things (IoT) for mainly two applications. On one hand, critical medical information could be passed on to patients' physicians and/or next of kin for immediate medical intervention irrespective of where the patient is. On the other hand, diagnostic information from individual patients could be compiled and analyzed over time to assist in medical research. However, the later should be done in such way that patient privacy is protected. Although some IMD designs consider privacy and secrecy of medical data, this calls for a rigorous inclusion of physical and application layers of the implant communication network which increases transmission overhead and reduces bandwidth efficiency.

Many different communication mechanisms have been employed and studied which include antenna enabled RF communication [35], inductive coupling between surfaces mounted and implanted coils [36]-[37], and recently the galvanically and capacitively coupled intra-body communication (IBC) [38]. Other emerging technologies such as ultrasonic [39]-[40], optical [41-43] and molecular intra-body communications [44-46] are also being investigated.

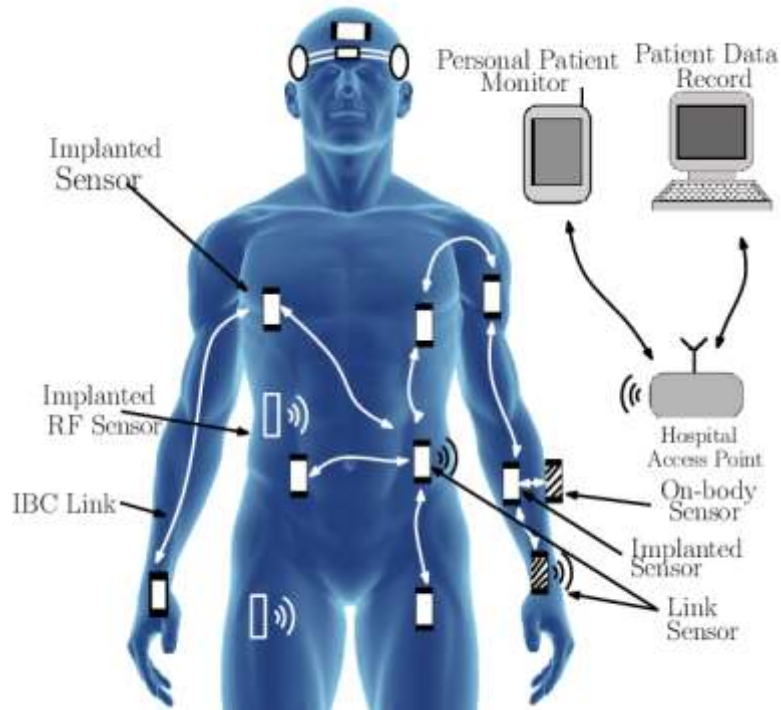


**Figure 2.5:** General architecture of body area networks. [35]

## 2.4. WBAN Architecture

Most of the IBC modalities considered in literature are based on the on-body (surface-to-surface) communication where both the transmitter and receiver are worn on the surface of the skin. This modality, for example, enables ubiquitous communication for wire-free patient vital sign monitoring setups in hospitals. For implant communication as part of the WBAN architecture, two modalities are possible. The first modality is the implant-to-implant communication where both the transmitter and receiver are inside the human body. This modality can be used to communicate implants that operate in a closed loop control setting. Besides, implant to implant communication can also serve as information relaying mechanism to cover a long communication distance by chaining implants. The second assumes communication between a transceiver on the surface of the skin and an implant inside human body of given electrical characteristics (implant-to-surface) and (surface-to-implant). The implant-to-surface implants are used in diagnostic application where a sensed quantity is transmitted to outside the human body as shown in figure 2.6. On the other hand, the surface-to-implant modality can be used with therapeutic and assistive implants to pass stimulation or control signals from the

outside to the implant. This modality is also extensively used in wireless powering techniques to transfer power from external sources.

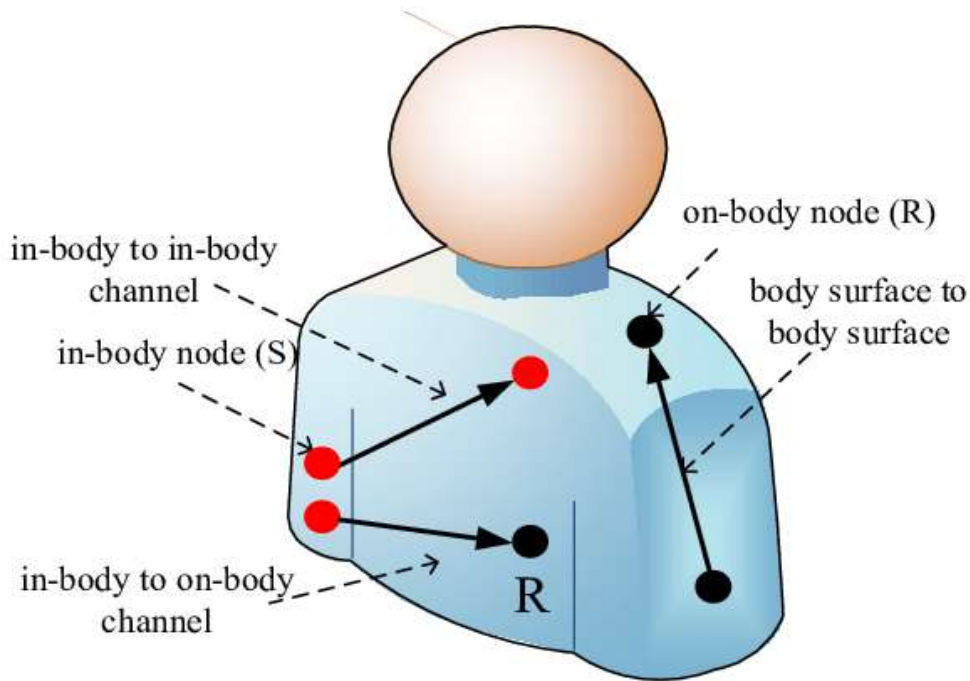


**Figure 2.6:** WBAN Architecture. [38]

## 2.5. Biosensor Networks Problems and Design Considerations

### 2.5.1. Propagation Medium Losses

Implant communication doesn't only use the through-the-air wireless radio frequency communication, but also uses the human tissues as part of the transmission channel which adds extra challenges. Several researches have been conducted to study the effect of the human body on the electromagnetic signals based on analytic work, simulations, and experimental measurements. In [47], the dielectric properties of the different biological tissue types are characterized as a function of frequency which enabled the researchers to test the hypothesis and theories on how the tissues affect the RF signals at different frequencies.



### **2.5.2. Data Rates Required for Specific Medical Application**

The invasive nature of implantation surgeries places a stringent miniaturization requirement and sustainable powering regime for implants, especially for long term duration. The use of electronic medical implants and its proper design need to take into account the specific application of the device. The required data rate dictates the bandwidth and even the implant communication mechanism. For example, subcutaneous glucose sensor transmitter is implanted just under the skin (depth of 4 mm) with low data rate (of less than 10 kbps) and intermittent transmission while a cochlear implant requires a deeper implantation depth of 2.5 cm with a high data rate of up to 500 kbps in a continuous transmission mode [48].

### **2.5.3. Processor Operating Time**

When a WBAN is controlled by the main processor of a mobile platform (i.e., personal server), the entire system cannot operate for long periods of time because this type of processor is not designed for continuous operation [49]. This problem can be mitigated by making the WBAN self-organizing so that the individual sensor nodes can operate without constant interventions from the personal server. In that case, the personal server would assume a more secondary role as a simple repository for the information collected locally as opposed to that of the coordinator of the network.

### **2.5.4 Power Consumption and Battery Life Time**

The main obstacle for wider adoption of wearable health monitoring is current battery technology [49]. Long-life batteries for WBAN sensors are highly desirable, especially when the replacement of the battery needs to be done surgically. To resolve this problem there are new developments in the market for WBAN's batteries. One of these is the case of printed batteries, which are especially suited for thin and flexible products like medical sensors in which they can be easily integrated [50].

Recently, the Interuniversity Microelectronic Centre has developed an economical radio chip for WBANs. The transceiver has ultralow-power consumption (0.687mW in receive mode and 2.5mW in transmit mode), data rates between 64 kilobits per second (Kbps) and 1 megabits per

second (Mbps), and transmission range of up to 30 m. Moreover, there are already WBAN applications that use sophisticated energy harvesting mechanisms. Some common energy sources are the human body, from which vibrational or thermal energy is collected [51] or the surrounding environment, where ambient electromagnetic fields may provide the necessary energy [52]. These technologies enable wireless sensor users to collect more data over time and offer more opportunities to operate autonomously in diverse environments.

In a WBAN, most energy-saving operations use duty-cycling approaches that periodically turn off the nodes so that they can operate in ultra-low-power modes for prolonged periods of time and be in active mode only when necessary, thereby achieving great energy savings [53, 54]. Evidently, such techniques strongly depend on time synchronization mechanisms. For this reason it is also important to evaluate in every communication protocol which mechanisms it uses to achieve the synchronization between sensors and how effectively its wake-up and turnoff cycles are implemented.

## **2.6. Some Existing Wireless Communications Protocols for WBAN**

### **2.6.1. WI-FI—IEEE 802.11ax**

This standard provides secure, reliable, and fast connectivity and can be used to connect electronic devices to each other, to the Internet, and to wired networks that use Ethernet technology. It is indicated for applications such as wireless local area network connectivity, broadband Internet access, and healthcare, being currently the most widely used protocol in private households [55]. Wi-Fi can operate in the 2.4- and 5-GHz radio bands and is able to deliver data rates of up to 10 Gbps.

### **2.6.2. BLUETOOTH—IEEE 802.15.3**

Bluetooth operates at 2.4 GHz, using a spread spectrum, full duplex signal at a high data rate of (11 to 55) Mbit/s. This frequency hopping adds protection against eavesdropping. The key features of the protocol are robustness, relatively high bandwidth, low latency, low cost, short range (10 m), and support for many mobile platforms [49]. This technology is indicated to provide connectivity among devices such as phones, personal data assistants, headsets, and

laptop computers and is currently in widespread use in hospitals, medical offices, assisted-living facilities, and homes. However, its high power consumption, its limitation of only up to eight devices in a personal area network, its inefficient idle modes, and the long start-up times make Bluetooth an unattractive option for wearable long-term health monitoring applications [49]. The Bluetooth version 4.0, Bluetooth Low Energy (BLE) technology, provides ultra-low power consumption, a data rate of up to 1 Mbps, a range of 10 m, and a fast start-up time (few milliseconds compared to Bluetooth's seconds) [56]. It consumes only 10% of the power consumed by Bluetooth, extending its battery life by sleeping and waking up when it needs to send data [57]. Time needed for connection setup and data transfer is less than 3ms (classic Bluetooth needs 100 ms) [58]. These features make it particularly suitable for latency-critical WBAN applications [56]. Although a promising technology, it is not yet supported by many devices and hence cannot yet be used in MSNs [57].

### **2.6.3. IEEE 802.15.4**

The IEEE 802.15.4 standard defines robust radio physical and medium access control (MAC) layers, and the ZigBee alliance defines the network, security, and application frameworks. The protocol operates at 2.4 GHz, 950 MHz, 915 MHz, 868 MHz, 780 MHz, 500 MHz, and 3.1–10.6 GHz frequency bands [59]. The capacity is 250 Kbps at 2.4 GHz, 40 Kbps at 915 MHz, and 20 Kbps at 868 MHz. Some modern devices have an indoor communication range of 50m and an outdoor range of more than 500 m [60]. The basic framework conceives a 10-meter communications range with a transfer rate of 250 kbit/s. Tradeoffs are possible to favor more radically embedded devices with even lower power requirements, through the definition of not one, but several physical layers. Lower transfer rates of 20 and 40 kbit/s were initially defined, with the 100 kbit/s rate.

IEEE standard 802.15.4 intends to offer the fundamental lower network layers of a type of wireless personal area network (WPAN) which focuses on low-cost, low-speed ubiquitous communication between devices. It can be contrasted with other approaches, such as Wi-Fi, which offer more bandwidth and requires more power. The emphasis is on very low cost communication of nearby devices with little to no underlying infrastructure, intending to exploit this to lower power consumption even more.

Even lower rates can be used, which results in lower power consumption. As already mentioned, the main goal of IEEE 802.15.4 regarding WPANs is the emphasis on achieving low manufacturing and operating costs through the use of relatively simple transceivers, while enabling application flexibility and adaptability.

ZigBee allows the formation of mesh networks, which let all participating devices communicate with one or many others, acting as routers transferring data between devices. When measurements obtained by multiple sensors must be accurately synchronized, as is the case, for example, with multichannel electrocardiogram sensors, we can use the IEEE 802.15.4 beacon enabled mode. In this mode, the personal area network coordinator of the network broadcasts beacons periodically to synchronize devices and specify the structure of the super frame. When a device receives a beacon, it synchronizes with the super frame structure and transmits its data [61].

## **2.7. Design Considerations for On/Off Body Antenna**

Several important factors need to be taken into consideration when designing on/off biosensor in a WBAN system. The most critical part of the WBAN communication system is the antenna. The antenna is a vital front-end component in any wireless system. Although many narrow- and wide-band antennas have been designed over the past decades, still there are several challenges when designing such antennas for modern systems. The most important factors affecting the antenna design include antenna detuning, impedance matching, radiation pattern, Specific Absorption Rate (SAR), size compactness, space constraints, desired radiation characteristics, low cost, light weight, multi-band operation, interference mitigation, reconfigurability, positioning, bending and stable performance with the variation of the gap between the antenna and the human body. For wearable antennas intended for on-body communications, the challenge is to achieve a wide beamwidth over the body and around, and to make the antenna input matching less sensitive to potentially varying distance between the antenna and the human body [62, 63].

### **2.7.1. Impedance Matching and Tuning**

Wearable devices operating in 2.4GHz Industrial, Scientific and Medical (ISM) band and 4.9 GHz public safety Wireless Local Area Network (WLAN)/5GHz IEEE 802.11 WLAN bands often require single or dual band operations. The operating frequency bands are narrow-band and can detune due to the human body loading effect. Therefore, the designer needs to consider the shift in operational frequency band due to the human body effect. The human body is lossy in nature and also has higher permittivity. When antenna designed in free space operates in near-body scenario, the impedance mismatch can occur and can also detune the antenna. In [64, 65], single- and dual-band antennas with full ground plane have been reported and antenna performance has been investigated. These antennas have stable performance and are less sensitive to changing near-body conditions.

### **2.7.2. Radiation Pattern**

On-body communications desire wide-beam or omnidirectional radiations in the plane parallel to the human body surface to provide maximum coverage over the body. This can be achieved by minimizing the radiations that are away from the human body (i.e. off-body). By introducing a null in the direction normal to the body, we can suppress off-body radiations and can enhance the on-body radiations. Printed antennas have radiations in the direction normal to the plane that are not suitable for on-body communications. By adjusting the current flow and introducing a full ground plane, desired radiation characteristics can be achieved that are suitable for on-body communications [64-66]. Moreover, the full ground plane also acts as a metallic reflector to minimize the radiations towards the body that can potentially be harmful. This also results in reduced SAR. The off-body radiation pattern should be directive beam in the direction away from the body and minimum in the direction parallel to the body to prevent the radiated electric field to induce SAR in the human body during transmitting the data to the central control station (patient mobile or doctor's device) as shown in figure 2.7.

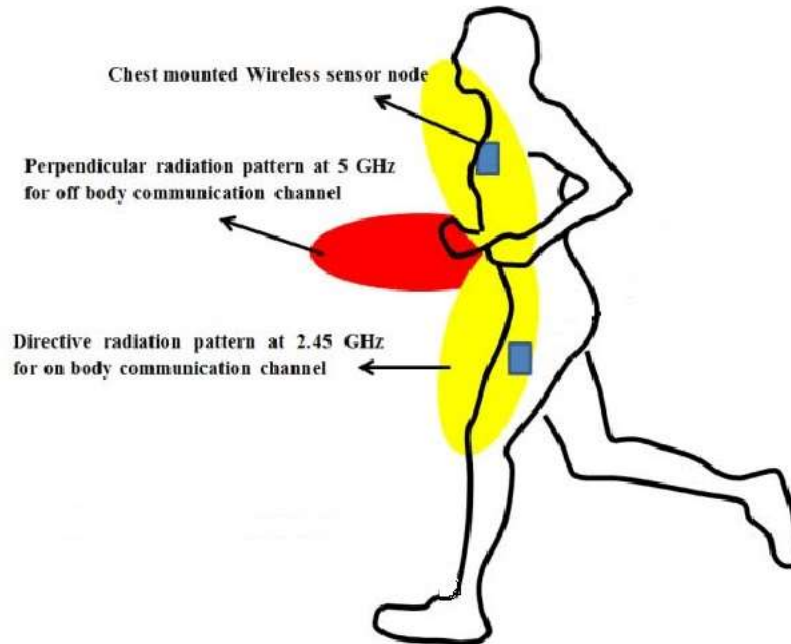


**Figure 2.7:** On- and Off- body Radiation Patterns. [64]

### 2.7.3. Antenna Cost and Weight

In wearable applications, communication devices are desired to be light weight and compact for ease of mobility. The other important factor is cost that need to be considered. From a commercial point of view, low cost solution can attract large number of customers. Therefore, it is critical to take care of size, cost and weight factors in addition to antenna performance.

### 2.7.4. Antenna Placement

The placement of antenna over the body (i.e. positioning) can significantly contribute to its performance. Bending limitations and scenarios can be determined based on the antenna placement and need to be investigated. The other challenge is to make the antenna insensitive to the variation of gap between the antenna and the human body. In [67], antenna placement options have been investigated and sensitivity analysis for wearable antenna has been carried out. Due to the full ground plane, this antenna performance is very insensitive to the separation between the antenna and the human arm. Moreover, small width of the antenna makes it a suitable candidate for on-body wearable devices and its placement along the arm length can avoid bending and hence possible detuning. It is important to consider the bending effects for

antennas in wearable communication devices, as this can impact the antenna performance. In [66], an armband wearable printed antenna has been presented. It has wide beam radiation pattern and has stable performance with the changing bending radius. In some wearable applications, crumpling is another factor that needs to be taken into account [68].

### **2.7.5. Radiated Power Limitation**

In WBAN, to monitor a patient's health status, the implanted device collects various physiological data and wirelessly transmits the information to external medical devices in real time [69]. However, they have a short transmission range due to the low radiation efficiency and the effective radiated power (ERP) regulation of  $25 \mu\text{W}$  [70]. This limitation demonstrates the necessity of a dual-band on-body repeater antenna to deliver weak signals from implanted devices to external devices. In addition, antenna performance is significantly affected by body tissues due to the high dielectric constant and conductivity at the microwave frequency band. Also, the input impedance and resonance frequency cannot be changed, but the gain and radiation efficiency of an antenna can also be deteriorated when an antenna is operated on or in a body. In order to be insensitive to the human body effect, compact zeroth-order resonance (ZOR) antennas for implantable and wearable WBAN systems were proposed in [71, 72]. Additionally, to protect the human body from radio wave exposure, the structure of the antennas for WBAN must have a low specific absorption rate (SAR) [73].

### **2.7.6. Antenna Communication Bands**

The Medical Implant Communication System (MICS) is a low-power, short-range (2 m), high-data-rate, 401–406 MHz (the core band is 402–405 MHz) communication network that has been accepted worldwide for transmitting data to support the diagnostic or therapeutic functions associated with medical implant devices [74]. The Federal Communications Commission (FCC) allocated additional spectrum (2360-2400 MHz) specifically for medical body area network (MBAN) devices in May 2012, effective on October 10 [74]. The off-body antenna that transmits data towards outside the body can either use the MICS band or the industrial, scientific and medical (ISM) band WLAN 802.11a (5.725–5.85GHz).

### **2.7.7. Examples for on-off Body Antenna Design**

In [74], a dual-band on-body antenna for a wireless body area network repeater system is proposed. The designed dual-band antenna has the maximum radiation directed toward the inside of the human body in the medical implantable communication service (MICS) band in order to collect vital information from the human body and directed toward the outside in the industrial, scientific, and medical (ISM) band to transmit that information to a monitoring system. In addition, the return loss property of the antenna is insensitive to human body effects by utilizing the epsilon negative zeroth-order resonance property. In [75-80], a reconfigurable beam-steering antenna was designed and fabricated in the WLAN 802.11a band (5.725–5.85GHz). The antenna is able to steer the maximum beam direction according to the mode of operation.

## **2.8. Evaluation for Literature Findings and Previous Work for Proposed Helical Antennas**

An additional overview of previous related work in BSNs is clearly highlighted in this section. Some papers focused on the sensor node design and the traditional antenna design requirements in specific. On the other hand, other researchers focused on the application and was not restricted with certain antenna parameters' constraints as long as the design satisfied their goal.

Body centric wireless communication (BCWC) has drawn the attention in the past years. Since the antenna design as a wireless communication module in a BSN is difficult as it depends on the wearer's age, posture and weight gain or loss. Therefore, the antenna specifications and design requirements are the most important and challenging issues in this field. Antennas used for BSNs can be divided into wearable and implantable antennas as mentioned before, therefore, the communication can be considered either as in-body, on-body or off-body each according to the location of the antenna.

Therefore, the authors have proposed in [81], an electrical model for the human body that allows implants to use body centric communication (BCC). It defined BCC and stated its



properties that made it attractive to form a BAN over the e-Textiles embedded with wires. These properties are the flexibility of sensor locations and the attenuation of signals with distance, which gives more security as it needs to be close to the body to be connected to the network. Besides, this rapid attenuation reduces the interference with other BCC networks and allows for reusable bandwidth. The authors also clarified how BCC works by creating a potential difference in one area of the body and sensing the attenuated potential difference in another area. In addition, it discussed how the receiver architecture affects the channel gain.

On the other hand, there are some drawbacks for using BCC such as the high attenuation in the channel, which will result in high power dissipation for data transmission. It was also obvious from the explanation in this paper that BCC can only use the conductive tissues – lying beneath the epidermis and acting as a spreading resistance from about 10 kHz to 10 MHz – as a network channel. At last, it was shown that the transmitter and receiver have to be electrically isolated in order to measure the BCC channel precisely. The authors have implemented their work here experimentally.

Moreover, the authors have proposed in [82], a robust and energy-efficient wideband BCC transceiver.

It is well known that BCC offers limited data rates up to 10 Mb/s which is insufficient to transfer multimedia data for wearable smart devices. However, the proposed BCC achieved high data rate of 60 Mb/s by employing more than one factor. The high data rate achieved in this work was a result of using high input impedance at the receiver, digital direct transmission.

Finally, the proposed BCC was fabricated; the performance of the transceiver was measured, and then compared with other designs.

While in [83], gave an overview for the BANs challenges for applications to achieve energy efficiency and sustainability. The authors addressed several topics in this study as applications, services, security, privacy issues, node and network architecture ...etc. This work mainly

focused on the core position of radio channel on the overall system as well as the influence on the human body. Furthermore, a classification for BANs depending on the application was presented. The approach proposed is called true cross-layer protocol which focused on different problems such as mobility, delay and packet losses. Although BANs are dealing with short communication distance, the human body introduces strong shadowing and antenna misalignment.

A survey was made in [84] to give an overview on the advantages and importance of WSNs for healthcare applications especially elderly people, chronically ill and children. In this study, the examples of how people could benefit from living in homes that have wireless sensor technologies for improved quality of life were evaluated. Several researches discussed the usage of large-scale wireless telecommunication technologies such as 3G, WiFi Mesh ...etc. and others the usage of small-scale personal area technologies such as Bluetooth, RFID, ZigBee ...etc. The link combining all the above technologies is the application. Then the authors have overviewed briefly the previous studies for healthcare applications. They observed that other studies either focused only on smart home perspective or had limited information about the design issues and challenges, while this survey provided different research approach not only from smart home perspective but also from a more healthcare perspective. Moreover, the benefits and considerations for healthcare monitoring systems were mentioned.

A smart mobile system that collects, analyses, displays and streams multiple sensor data to centralized computing server was presented in [85]. The introduced smart phone uses Android system which provides the ability to communicate with sensor nodes (SNs) on demand and acquires real-time multiple sensor data simultaneously. The benefits of the proposed work are mobility, operating with low power to process, collect, and transmit the desired data wirelessly.

In addition, a comprehensive approach in BSNs in [86] explained that BSNs work on improving the quality of life through improving their efficiency in various applications. The authors clarified that the requirements for any BSN device should be the wearability and the

limited power budget. Therefore, reducing the form factor and extending the time between battery recharges are very important issues. This paper proposed a solution for reducing energy consumption by implementing an ultralow-power BSN platform, exploiting periodic or predictable wireless channels, using adaptable sensing, coding and signal processing.

Since power optimization is the major concern in the design of the BSN systems, therefore, proposed a novel signal processing approach to minimize power consumption of node localization is proposed in [87]. The problem that the authors introduced is that to recharge multiple sensor nodes puts so much burden on the end users. While the proposed solution is to develop an efficient signal, processing algorithms that reduce the computation load. Furthermore, introducing a compromise between accuracy and power consumption of node localization minimized sensing and computation power.

A mobile monitoring system for epileptic patients is introduced in [88]. After explaining what epilepsy and its percentage is worldwide, the authors clarified that their motivation is to overcome the shortcomings in previous clinical video EEG monitoring of the targeted patients. These systems were either expensive, did not include other monitoring parameters like ECG ...etc or of low availability. The proposed system is reconfigurable, mobile, and acquires multi-parametric data. This system uses Bluetooth technology to transmit signals after collecting from sensors to a computer.

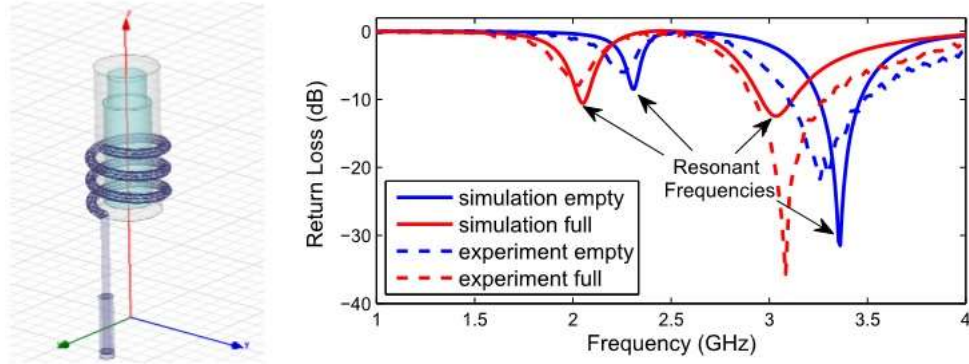
In addition, a microstrip antenna designed for implantable BSN was presented in [89]. The challenging medium when implanting a sensor inside the human body is the tissues. The proposed antenna is designed to fit and adjust to the human tissues environment as well as to provide a reliable transmission. The challenges in designing the antenna are concerning the size, safety constraints and the power transmissions relative to the SAR. Afterwards the permittivity and conductivity of each body part were studied which are essential for determining the signal propagation characteristics. This work was experimentally tested on a human arm model of three layers (skin, fat and muscle), then compared to the simulation results. The simulation results

showed that the antenna provided a return loss of -18.3 dB, maximum gain of -35.1 dB and an omni-directional pattern.

Another design was introduced in [90] as a tuneable antenna using a cavity backed slot antenna (CBSA) for biomedical sensing applications. The novelty of this approach is the design of the antenna by isolating the feed currents from the body and providing frequency tuning of as a function of probe length. After explaining the antenna-body effects, there was an observation that the size of aperture is directly proportional to the directivity, while inversely proportional to the resonant frequency. The resonant frequency is the factor that determines the sensing depth, which means there will be a trade-off between both of them.

Furthermore, the antenna design was explained and then the simulation results were obtained. The CBSA was fabricated and the measurements were obtained under three conditions: 1) In close proximity to a skin tissue phantom. 2) In free space. 3) In close proximity to a human core. The results showed that the proposed antenna is broadband (+400MHz) and efficient (88%).

Another application the authors were interested in was the wireless drug dosage monitoring as in [91]. The proposed design is a helix antenna wrapped around a dielectric material core that acts as drug reservoir. The authors explained the need of drug dosage monitoring to provide feedback, medical tracking, and disease management also to avoid leakage. As shown in figure 2.8, the drug dosage monitoring is done by tracking the resonant frequency of the helix antenna shifting between 2.4 – 2.5 GHz.

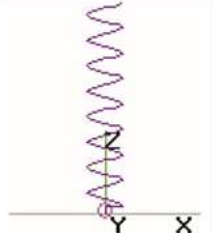
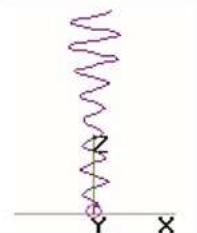


**Figure 2.8:** The antenna sensor with its simulated and measured results. [91]

Therefore, the target is to increase the sensitivity over the required band as well as to make sure that the resonant frequency shifts within a certain range with the variation of the drug volume inside the reservoir. Finally, the proposed design did not focus on the size of the antenna as long as it acts as a good sensor with acceptable performance.

On the other hand, some authors were interested in wire antennas' size reduction. As in the case of wire antennas, the wire length is inversely proportion to the resonant frequency. Therefore, a proposed strategy to optimize helical windings with continuously varying the radii is presented in [92]. The previously introduced techniques to achieve resonance with shorter antenna such as inductive loading can be at the cost of degradation in bandwidth and efficiency. This paper introduced another way, which is adding wire length through helical windings and varying the radius in each turn. Changing the radius in each turn of the helical antenna can be explained one turn per time, but this will add complexity in the analysis. Finally, a comparison was done between an optimized uniform helix and a helix with continuously varying radii as shown in table 2.1.

**Table 1.1:** Comparison Between Uniform and Radius Varying Helices. [92]

Parameter	Uniform Helix	Radii Varying RBF
Pitch	30 mm	
Radius	24.2 mm	N/A
$\omega_1$	N/A	20.7 mm
$\omega_2$		10 mm
$\omega_3$		10 mm
$\omega_4$		15.3 mm
$\omega_5$		30 mm
$\omega_6$		28.7 mm
L in Matching	-75.2 nH / 33.7 pF	-43nH* / 58.9 pF
C in Matching	62.9 pF	62 pF
Efficiency	91.3 %	92.39 %
Bandwidth	1.21 MHz	1.51 MHz
$f_{center}$	99.6 MHz	99.9 MHz
Configurations		

It can be seen from the table above that the helix with varying the radius provides a wider operating bandwidth and a slightly higher total efficiency.

Furthermore, an octafilar helical antenna (OFHA) for ultra-high frequency (UHF) – RFID for portable reader was presented in [93]. The antenna is designed to resonate at 915 MHz and was placed on reader device in the presence of human hand model. The authors also mentioned that the proposed antenna for RFID technology is of circular polarization and small size, high gain and high front to back ratio. The QFHA consists of four arms with 45° shift between each of them, while the OFHA consists of eight arms having no ground plane as shown in figure 2.9.

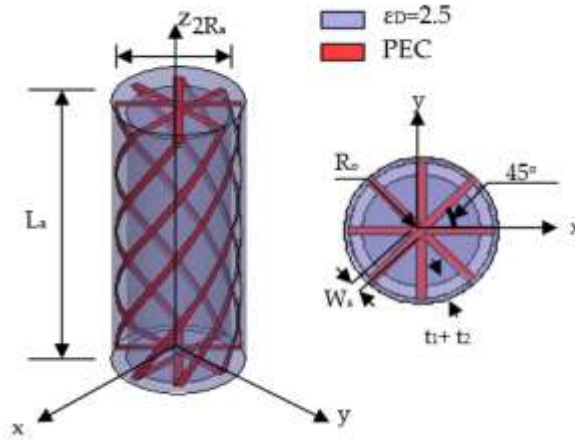


**Figure 2.9:** The octafilar helical antenna. [93]

A comparison between an OFHA and quadrifilar helical antenna (QFHA) was investigated under same environmental conditions. Results in figure 2.10 show that the comparison between both OFHA and QFHA according to return loss and gain.

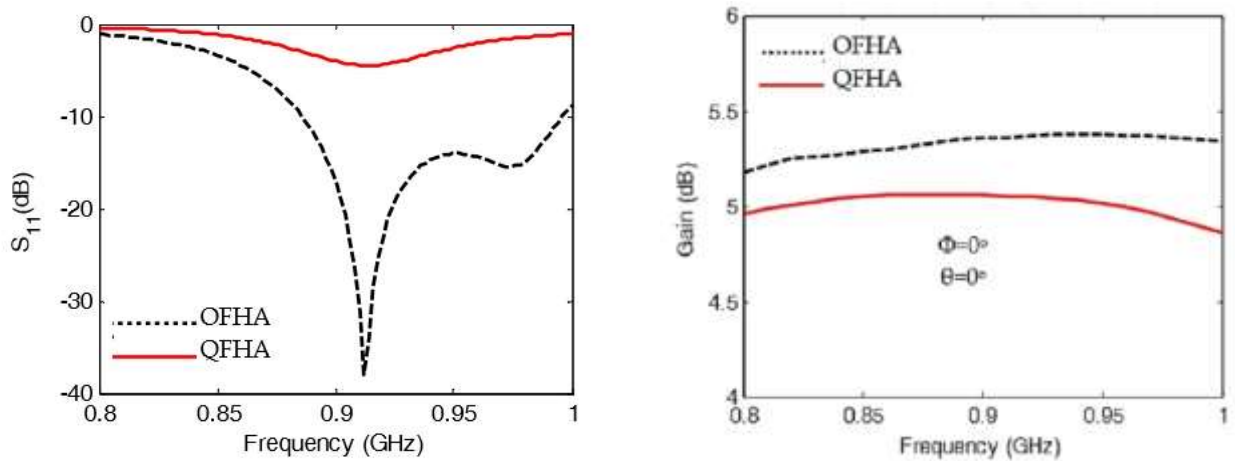


**Figure 2.10:** The compared simulated results return loss and gain. [93]

Finally, it was obvious that the OFHA has better performance than the QFHA as it is clear that the gain is varied from 5.317 dB to 5.439 dB at frequency of 915 MHz.

Moreover, a dual-band multi-arm folded ellipsoidal helix antenna is designed in [94] for the wireless data communication and wireless power transferring functions of an artificial cardiac pacemaker. The antenna is designed to tune the dual resonant frequencies to the desired bands at 900 MHz and 2.4 GHz by varying the pitch angle ( $\alpha$ ). Figures 2.11 and 2.12, show the antenna design and results when ( $\alpha$ ) have two values 0 and 0.6 and the impact on the return loss curve achieving a bandwidth of 10% at each band.

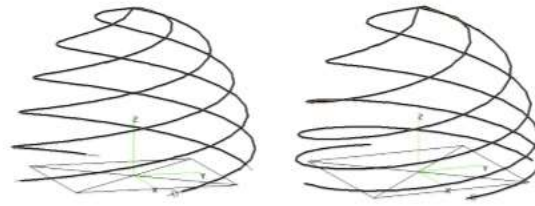


**Figure 2.11:** The four-arm folded ellipsoidal helix antenna with variable ( $\alpha$ ). [94]

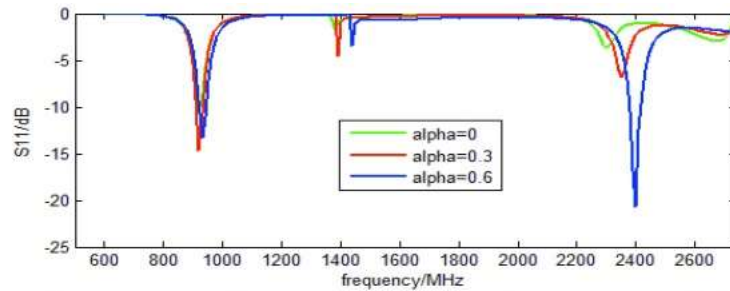


**Figure 2.12:** The effect of varying ( $\alpha$ ) on resonant frequency. [94]

Finally, the radiation pattern for the higher band at 2.4 GHz showed some distortion on the vertical plane compared to that of the lower band at 930 MHz. The other problem the authors faced at the 2.4 GHz band was its sensitivity to the fabrication imperfection, so they had to fine-tune it manually.

Another essential need for BSNs' applications are biomedical implanted sensors that could achieve the target they were designed for as in [95]. The majority of the in-body sensors



communicate in frequencies less than 1 GHz. Although these sensors have low propagation losses, but on the expense of bandwidth and size in comparison with the frequencies higher than 1 GHz. working above 1 GHz will reduce in size and provide wider band but with higher propagation losses. Then the authors discussed the three scenarios for In-Body path loss channel. These scenarios are In-Body to In-Body (IB2IB), In-Body to On-Body (IB2OB) and In-Body to Off-Body (IB2OFF) where each is explained clearly. Figure 2.13 (a and b), shows the two types of antennas used to be tested for the path loss in the three channel scenarios as previously mentioned.

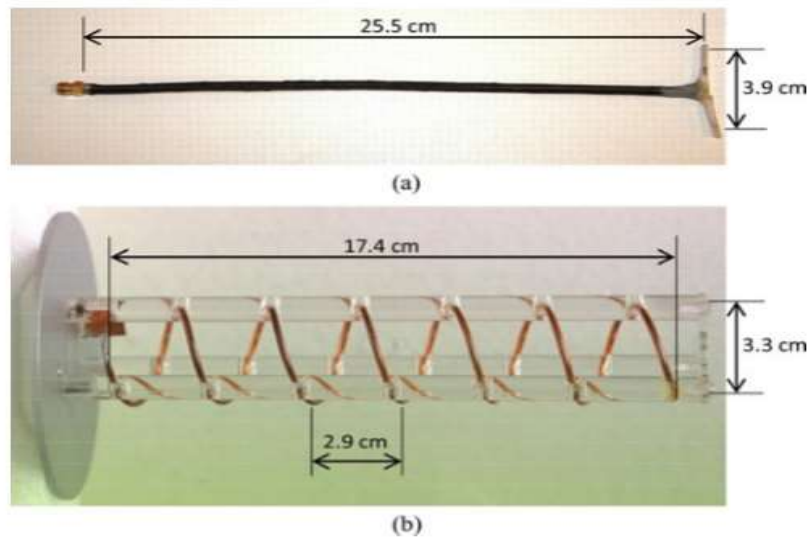


**Figure 2.13:** The effect of varying ( $\alpha$ ) on resonant frequency. [95]

Two parallel helical antennas joined at the central feed point and then attached to a monopole are presented in [96] as shown in figure 2.14.

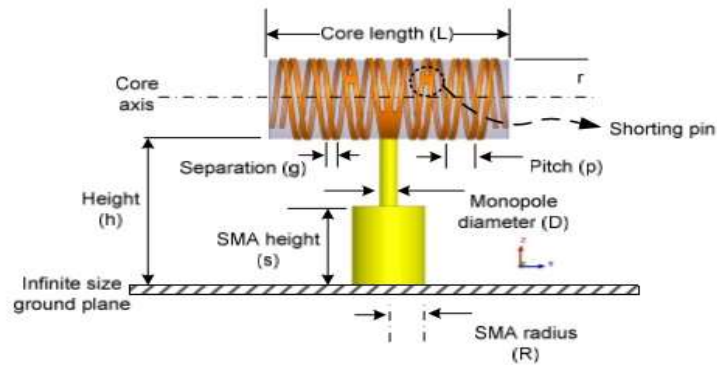


**Figure 2.14:** Bifilar Transverse Bilateral Helix Antenna. [96]

This design is to achieve a second resonance to be close to the first resonance which leads to increase the B.W. The dimensions were briefly stated and the results showed that the B.W. was improved by 22% at 615 MHz with radiation efficiency of 63%.

Moreover, a wireless communication link for a capsule endoscopy is presented in [97] for monitoring of small intestine in humans. The communication link includes both capsule inside-body transmitting antenna and an outside-body receiving antenna as shown in figure 2.15.



**Figure 2.15:** (a) Simulated Meander Antenna for Capsule Endoscopy. (b) Spiral Helix Antenna for outside application. [97]

The transmitting capsule antenna operates at 600 MHz with bandwidth 10 MHz, while the outside antenna is a double spiral helix that has circular polarization to provide a communication link regardless the orientation of the capsule. The authors clarified the design limitations of both antennas. The communication link was tested for path loss detection with the variation of the capsule orientation. The results showed that there was a frequency shift of 10 MHz for different

positions of the antenna inside the intestine. Besides, the link quality is affected by the antenna mismatch and orientation during the operation.

Another ingestible capsule endoscope multi-layer helical antenna is presented in [98] and operates at the ISM band (2.4 – 2.48) GHz. The proposed antenna is composed of three open loops at different layers connected via holes to form an axial-mode helical structure as shown in figure 2.16.



**Figure 2.16:** Proposed Helical Antenna (a) Top View. (b) Side view. [98]

The authors tested three positions that a swallowed capsule would pass through which are the stomach, the small intestine and the colon. The results showed that the radiation performance is affected by the three positions tested in this paper. Finally, compared to previous work in capsule systems this structure is less complex design and has wider impedance and axial ratio bandwidths.

Previous related work concerning helices used for dual bands or tuning such as in [99], a helical antenna is printed on 10-layer ferrite package to achieve compactness. The target is to connect the antenna the bias coil in one structure to replace the need of large external magnets or coils, since antennas act as bias winding that provides frequency tuning.

Moreover, in [100 and 101] dual frequency helices was presented. The first design dual band is done by combining two helical antennas (cylindrical and conical). One of them resonates at 860 MHz while the other at 1800 MHz, taking into consideration that both helices were normal modes. The target was to isolate between the transmitted and received signals using a four-port circulator as well as amplifying the gain using an amplifier. On the other hand, the second proposed dual band design was by testing three different configurations in order to reduce the size to be used for dual-mode cellular phones operating at two different frequencies.

In addition, hearing-aid instruments are significantly important commercial products to those who suffer from this problem. A quarter wave spiral monopole mounted on a ground plane is presented in [102] as shown in figure 2.17. It works at 2.4 GHz and is designed to be placed in the ear.

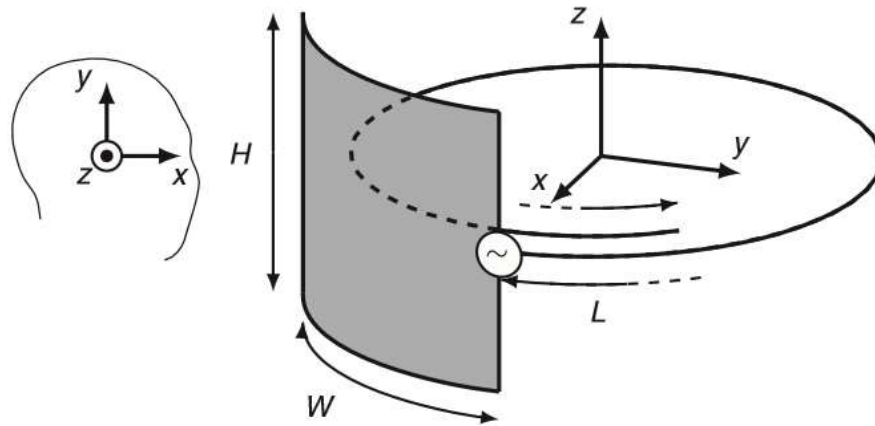


**Figure 2.17:** Quarter-wave Monopole Antenna. [102]

The proposed In-The-Ear (ITE) antenna is considered a solution for ear-to-ear link through a Bluetooth chip. This antenna is placed inside the ear as shown in figure 2.18, while most of the previous designs were mounted behind or on the outer part of the ear.



**Figure 2.18:** In-the-Ear Spiral Monopole Antenna. [102]

An imbedded spiral antenna for endoscope was proposed as well in [103] as shown in figure 2.19. The authors analysed a dual-spiral antenna with varying the length providing an omnidirectional radiation pattern and an UWB for short distance communication. Spiral antennas are well known with their wide band but of low gain. Then the antenna characteristics were explained and how it would overcome the drawbacks of the old conventional endoscope methods.

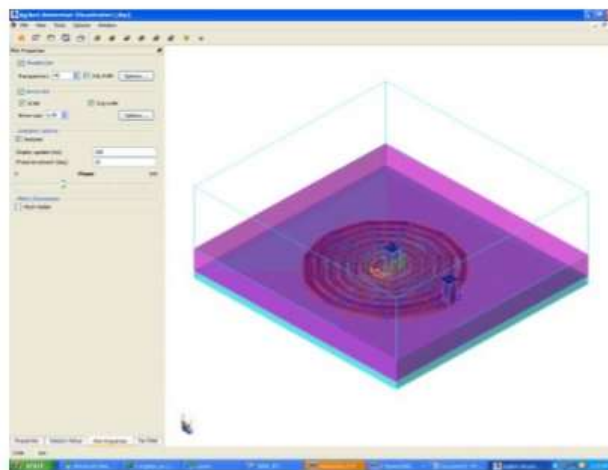


**Figure 2.19:** Imbedded Spiral Antenna for Endoscope. [103]

Results showed that the omnidirectional radiation produced helps to transmit signals regardless the orientation or the location of the capsule. The obtained bandwidth is of 27.7% with operational frequency between 560 MHz and 740 MHz.

Furthermore, another spiral antenna is designed and fabricated operates in the MICS band in [104] as shown in figure 2.20.

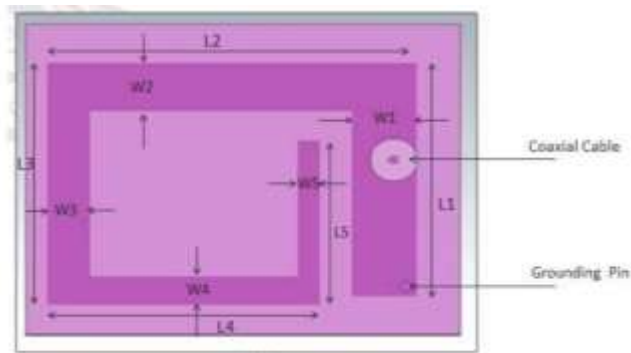
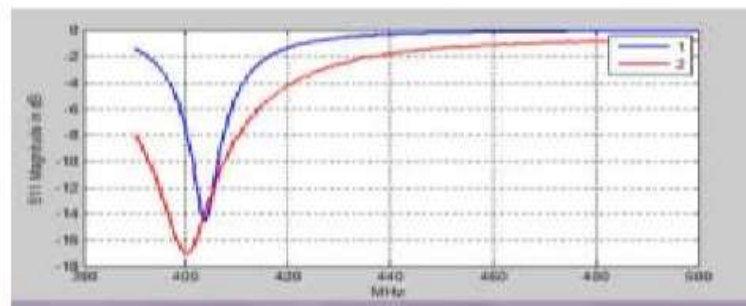
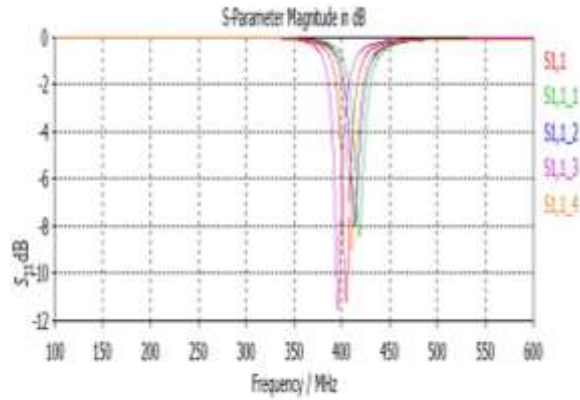


**Figure 2.20:** Spiral MICS-Band Antenna. [104]

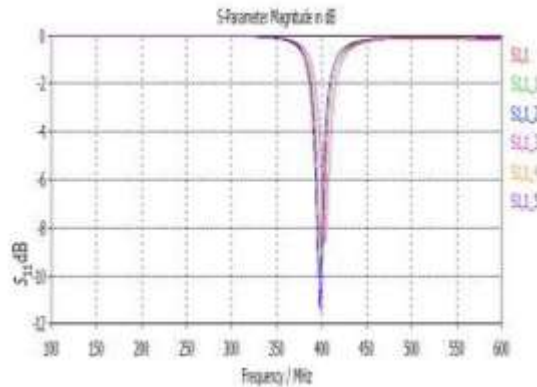
The authors tested the effect of the existence of tumors in breast on the return loss as shown in figures 2.21 (a, b and C). It is used as a tool to detect the presence of cancer cells and its stage.



(a)



(b)



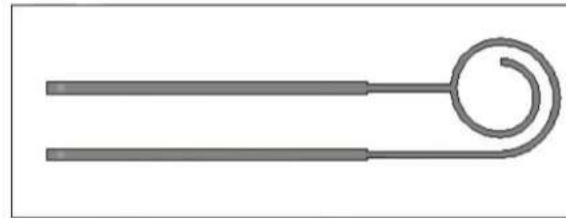
(c)

**Figure 2.21:** (a) Return Loss of Spiral Antenna on Human Breast. (b) Return Loss when tumors occupy from 2% to 46% of the breast. (c) Return Loss when tumors occupy from 50% to 100% of the breast. [104]

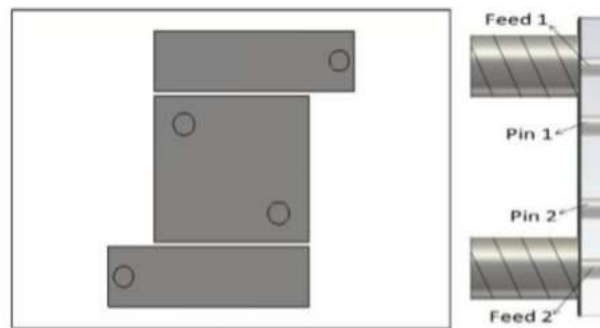
The results showed that according to the percentage the tumor occupies from the breast volume, the resonance frequency increases or decreases.

Many researchers focused on developing non-invasive techniques to monitor blood glucose levels for diabetes patients. The previous non-invasive methods used and stated in literature were mentioned briefly. The authors proposed a non-invasive radio-based blood glucose monitoring using two microstrip resonators operating in the 2.40 – 2.48 GHz band in [105]. The two

resonators are placed to face a four-layered phantom where one of the resonators is a patch resonator as shown in figure 2.22 (a), while the other is a spiral resonator as shown in 2.22 (b).



(a)



(b)

**Figure 2.22:** (a) Spiral Resonator for BGL monitoring. (b) Patch Resonator for BGL monitoring (top and side views). [105]

The two resonators were compared with respect to their ability to detect small changes in blood glucose level as well as, the ability to maintain the on-body channel during different physical activities was tested using simple received signal strength measurements.

The phantom size is kept constant for both resonators' simulations and by decreasing the blood permittivity; the results of  $S_{11}$  were obtained as shown in figure 2.23.



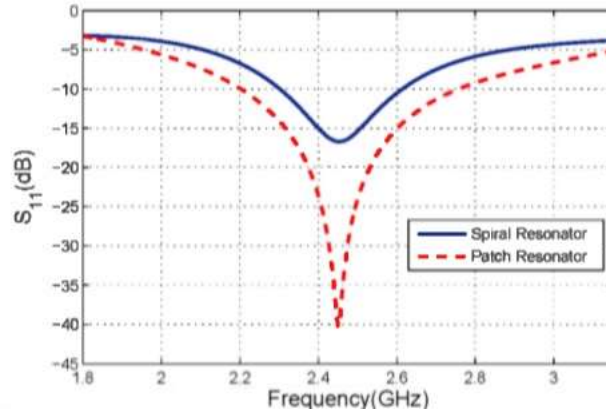


**Figure 2.23:** Simulated S11 for Both Resonators. [105]

Finally, the results showed that the resonators were capable of detecting small changes in blood glucose level, but the system sensitivity must be optimized.

In addition, a printed UWB antenna is proposed in [106] to overcome the band limitations of the patch antenna. After stating the unique advantages of UWB technology, it was also important to mention that antennas with a high degree of isolation from human body are required. The authors tested the effect of the human body on the performance of the antenna. The geometry of the proposed antenna as shown in figure 2.24. consists of three arc-shaped radiator patches on the top surface and a ground plane printed on the opposite side of a dielectric sheet.

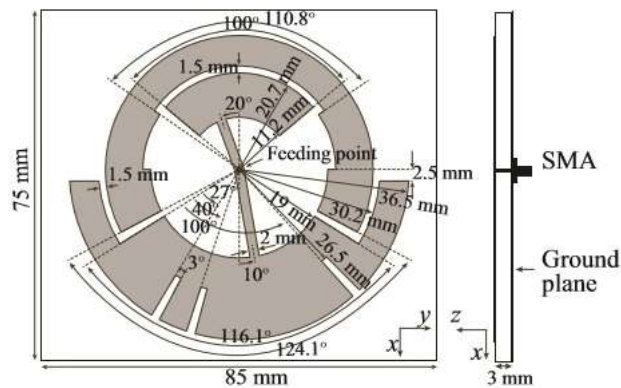


**Figure 2.24:** Detailed Geometry of the UWB Antenna. [106]

Since the antenna is fixed on clothes, therefore, the size of the antenna was not the concern of the authors due to the availability of large cloth area. Results showed that the bandwidth achieved from 4 GHz to 9.5 GHz – which is 75% - is suitable for off-body communication with maximum gain about 7.4 dBi.

A single arm Archimedean spiral for radiometric temperature measurement inside human body is proposed in [107]. Measuring the temperature of tissues using non-invasive methods has many useful applications in medical fields. These applications such as breast cancer early diagnosis, controlling temperature during hyperthermia and monitoring of brain temperature of new born infant. The design parameters and dimensions were mentioned as shown in figure 2.25.

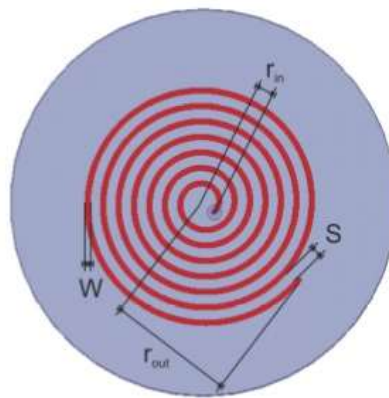
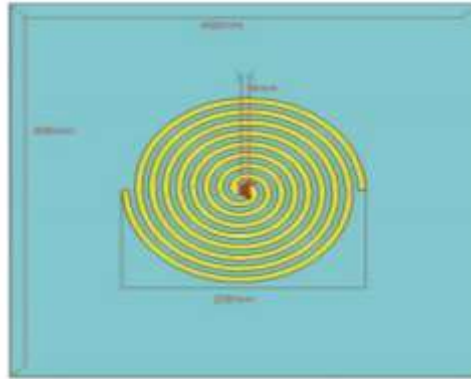


**Figure 2.25:** Single-Arm Archimedean Spiral Antenna. [107]

As it is known from [108] that temperature of any object if exceeded the  $0^{\circ}\text{K}$  will radiate an electromagnetic noise (thermal noise) over the whole frequency spectrum. Therefore, the specific absorption rate (SAR) of the antenna can be determined by measuring the rise in the temperature of the antenna's load during a certain time interval.

Another compact and flexible embroidered spiral antenna used for wearable applications is proposed in [109]. Although, wide band antennas are suitable for wearable communications as on-body antennas, they often suffer from the detuning due to the presence human body. However, spiral antennas are well known for their wide bandwidth and low-profile qualities.

Therefore, the authors developed an embroidered spiral antenna and compared its performance once on a phantom and another time on a real human chest as shown in figures 2.26 (a, b).



(a)



(b)

**Figure 2.26:** (a) Spiral Antenna. (b) Embroidered Spiral Antenna Measurement on Human Chest. [109]

The fabrication of the antenna showed that it has light weight, flexible and easily integrated into clothing. Finally, the results showed that the return loss of the antenna when placed on a phantom chest was better than 6 dB from 0.5 to 3 GHz.

The field of wireless body area networks (WBAN) has witnessed huge progress recently. Flexible wearable devices are applied for monitoring and diagnosing patients to perform with low power consumption. WBAN can be categorized into ON, OFF and IN body communication depending upon the position of transmitting and receiving antennas.

For ON body communication, an omnidirectional field parallel to the surface of the body is preferred. However, many wearable health care systems employ multiple bio-sensors for monitoring different vital signs at the same time. Therefore, flexible, compact and multiband antennas are in great demand. Dual-band antennas are considered a hot topic in solving this issue. A dual band dual polarized wearable antenna covering the lower and higher ISM bands is presented for ON body communication in [110]. The antenna has merit of small size, light weight, and flexibility but, it is only suitable for ON body applications.

An interesting topic which is the RF switching system that can provide a wideband performance over high ranges of frequencies as in [111]. The switching system was controlled by a Bluetooth connection using an Android mobile phone. This system was connected to an array of eight testing. Head imaging is used for detecting deadly diseases such as stroke, cancer and internal brain bleeding.

Another switching technique using the PIN diodes and a patch frequency reconfigurable antenna as in [112]. Depending on the switching state (ON/OFF), different operating frequencies were obtained. The proposed antenna can be controlled to operate either in a single or a dual band without changing its dimensions but by changing the state of the Pin diodes.

Moreover, since this research is concerned with dual-mode antennas as mentioned earlier, there were two dual-mode patch antennas designed in [113]. The first paper presented a patch attached to the waist with two slots in order to enhance bandwidth and reduce the size, while the second was also a patch attached to the chest with signal electrode and a ground electrode. Both antennas were placed on body phantoms with a plastic layer between the antenna and the body. In addition, both designs were proposed for same reasons, which are checking the received voltage in the on-body mode and test simulated results (return loss and radiation pattern) for off-

body mode. Although, the two designs are small in size, but they both have some drawbacks as well. The first design for example does not have a ground plane, which prevents the back radiation that affects the human body with the existence of the two slots as shown in figure 2.27.

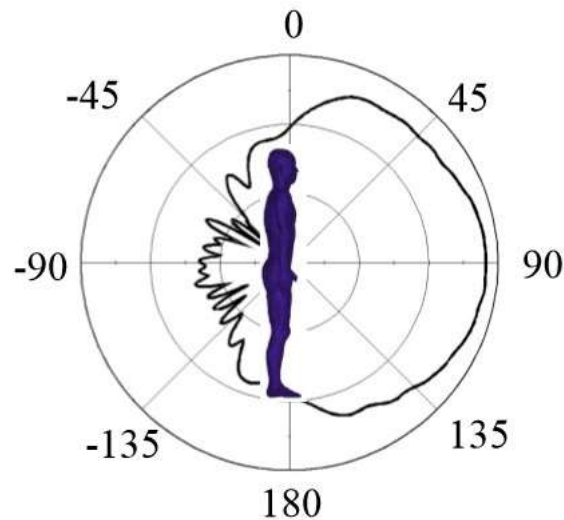


**Figure 2.27:** YZ – Plane Radiation for OFF-Body Communication. [113]

Moreover, both designs have narrow bandwidths as well as the omnidirectional pattern in the off-body mode lead to waste of power, as the omnidirectional pattern is needed in the on-body mode to offer more coverage to body parts.

Briefly, as mentioned earlier in the related work of BSNs in this chapter, the challenges concerning sensor nodes were developing in many aspects. The main challenges facing the design of antennas for BSNs were illustrated as well. These challenges include the save of power, the design requirements such as high gain, efficiency, directivity, size and high wearability. Furthermore, the designed antenna must be of high transmission reliability to deliver the collected data accurately to the desired node or gateway.

The requirements and limitations are set according to the application they were designed for in the first place. As the application of a BSN may require long-term real-time monitoring, therefore, the size of sensors should be reduced and any possible physical or chemical harm to the user should be

eliminated. Other applications may require large bandwidth or high gain and radiation efficiency regardless the size of the antenna. Previous studies as mentioned in this chapter aimed to improve and overcome many shortcomings by various means. However, many drawbacks are still hot topic research areas that could be useful for other researchers.

Finally, in this chapter to sum almost everything up concerning previous related work, the following table 2.2 is summarizing the mentioned work earlier.

**Table 2.2:** Summarizing Previous Related Work

REFERENCES	ANTENNA DESIGN TYPE	PURPOSE OF THE PAPER
[81, 87]	Survey	<ul style="list-style-type: none"> <li>• BCC Implants</li> <li>• Enhancing Channel Gain.</li> </ul>
[82-84]	Survey	<ul style="list-style-type: none"> <li>• Healthcare monitoring issues (security, privacy ...etc.)</li> <li>• Wearable and Implantable applications.</li> </ul>
[85]	Survey	<ul style="list-style-type: none"> <li>• Low-power</li> <li>• BSN Architecture</li> <li>• Biosensor design</li> </ul>
[86, 88 and 89]	Survey	<ul style="list-style-type: none"> <li>• Main constraints for sensors and antennas' design.</li> <li>• Vital sign data</li> <li>• Challenges for BANs Applications</li> </ul>
[90]		<ul style="list-style-type: none"> <li>• Smart mobile for collecting, analysing, displaying and streaming data to an external server</li> <li>• Low-power system</li> <li>• Data analysis</li> <li>• Uses Bluetooth</li> </ul>

[91]	Survey	<ul style="list-style-type: none"> <li>• BSN Challenges</li> <li>• Reducing energy consumption by a novel circuit design</li> <li>• Reduce cost</li> </ul>
[92]	Wearable motion sensors	<ul style="list-style-type: none"> <li>• Minimizing power consumption via real data collection.</li> </ul>
[93]	EEG and ECG sensors	<ul style="list-style-type: none"> <li>• Reducing hardware by minimizing number of sensors placed for a patient.</li> </ul>
[94]	Microstrip Patch Antenna	<ul style="list-style-type: none"> <li>• Miniaturization</li> <li>• Omnidirectional pattern</li> </ul>
[95]	Tunable Cavity Backed-slot Antenna	<ul style="list-style-type: none"> <li>• Biomedical sensor</li> <li>• Parameters variation's effect on B.W. and frequency</li> </ul>
[96]	Helical Antenna (Implanted)	<ul style="list-style-type: none"> <li>• Reducing Size for drug delivery</li> <li>• Reducing cost</li> </ul>
[97]	Helical Antenna	<ul style="list-style-type: none"> <li>• Adding wire length to the helix (via radius variation) to resonate at certain frequency</li> <li>• Obtained B.W. is a little bit wider than of uniform helix</li> </ul>

[98]	Helical Antenna	<ul style="list-style-type: none"> <li>• Comparison between two helical antennas (OFHA and QFHA)</li> <li>Proposed OFHA is of:</li> <li>• Higher gain about 5.4 dB</li> <li>• Higher front-to-back ratio</li> <li>• Good Axial Ratio</li> <li>• Omnidirectional coverage</li> </ul>
[99]	Helical Antenna	<ul style="list-style-type: none"> <li>• Small folded ellipsoidal helices with different pitch angle</li> <li>• Deigned to be implanted for cardiac pacemakers</li> <li>• Wireless data communication</li> <li>• Wireless power transfer</li> <li>• Dual-band antenna at 900 MHz and 2.4 GHz</li> </ul>
[100]	Monopole and Helix antennas	<ul style="list-style-type: none"> <li>• Testing path loss for In-Body channel Scenarios: <ul style="list-style-type: none"> <li>– IB2IB</li> <li>– IB2OB</li> <li>– IB2OFF</li> </ul> </li> </ul>
[101]	Two parallel Helical Antennas	<ul style="list-style-type: none"> <li>• B.W. Enhancement by resonating at close frequencies so leading to a wider band</li> </ul>
[102]	<ol style="list-style-type: none"> <li>1. Meander antenna implanted capsule</li> <li>2. Spiral-Helical outside-body</li> </ol>	<ul style="list-style-type: none"> <li>• Implanted capsule with omnidirectional pattern</li> <li>• Outside antenna with directive pattern and circular polarization</li> <li>• Testing communication link quality between both with different capsule orientations.</li> <li>• Not concerned with size in case of outside helix as its total length is 4.18 cm</li> </ul>



	antenna	
[103]	Helical Antenna (Implanted)	<ul style="list-style-type: none"> <li>• Reducing helical size</li> <li>• Reducing design complexity by using three-open loops on top of each other to get axial mode</li> <li>• B.W. achieved is 33.3%</li> </ul>
[104]	Spiral Antenna	<ul style="list-style-type: none"> <li>• Reducing size to be placed inside the ear</li> <li>• Facilitate Ear-to-Ear link using Bluetooth chip</li> </ul>
[105]	Spiral Antenna (Implanted)	<ul style="list-style-type: none"> <li>• To achieve omnidirectional pattern</li> <li>• Low power consumption at low frequency range</li> <li>• Wide B.W. to transmit high resolution images and large amount of data in real-time</li> </ul>
[106]	Spiral Antenna (Implanted)	<ul style="list-style-type: none"> <li>• To study effect of changing the tumor's percentage occupying the human breast on the resonance frequency.</li> <li>• Miniaturized</li> </ul>
[107]	<ol style="list-style-type: none"> <li>1. Patch resonator</li> <li>2. Spiral resonator</li> </ol>	<ul style="list-style-type: none"> <li>• Compare their ability to detect small changes in BGL through simulations on body phantom</li> <li>• High data rate for ECG waveforms</li> </ul>

[108]	Three-Arc shaped radiators printed on a patch antenna	<ul style="list-style-type: none"> <li>• Wide B.W. of about 75%</li> <li>• Average gain of 7.4 dBi</li> <li>• Size is not the concern</li> <li>• Presence of full-ground plane to reduce effect on body tissues</li> </ul>
[109]	Archimedean Spiral Antenna	<ul style="list-style-type: none"> <li>• Wide band</li> <li>• Directive beam</li> <li>• Circular polarization</li> <li>• Radiometric temperature measurement inside human body (using thermal camera)</li> </ul>
	Spiral Antenna (wearable)	<ul style="list-style-type: none"> <li>• Compact and flexible to be placed on human chest</li> <li>• Designed to replace antennas on conventional portable wireless devices</li> </ul>
	Embroidered Spiral Antenna (wearable)	<ul style="list-style-type: none"> <li>• Compact and flexible</li> <li>• Wide band to overcome detuning due to presence of human body</li> </ul>
[110 and 111]		<ul style="list-style-type: none"> <li>• BGL monitoring</li> <li>• Testing glucose level on the dielectric properties of the antenna</li> </ul>
[112]		<ul style="list-style-type: none"> <li>• Reducing size for implants</li> </ul>

[113]	Patch Antennas	<ul style="list-style-type: none"> <li>• Dual-mode for On- and Off-body communication</li> <li>• Miniaturized</li> <li>• Introducing slots to enhance B.W.</li> <li>• Low gain</li> </ul>
-------	----------------	---

## 2.9. Conclusion

In this chapter an overview for the types of the medical implant biosensors is presented showing the difference between the in-body, on-body, and off-body biosensors and the uses of each type. The WBAN architecture is illustrated with the associated network problems and design considerations. The wireless communication protocols used in the WBAN is reviewed. Finally, the antenna design considerations for the on/off body biosensor is investigated. The most important factors affecting the antenna design include antenna detuning, impedance matching, radiation pattern, SAR, size compactness, space constraints, low cost, light weight, multi-band operation, interference mitigation, reconfigurability, positioning, bending and stable performance with the variation of the gap between the antenna and the human body. The details of each design parameter is presented with some examples for antennas designed to work as an on/off body biosensor.

## Chapter 3

# Assessment of Radiation from Compact Helical Antennas Proposed for On-Body Biosensor Networks

---

### 3.1. Introduction

This chapter has two main objectives; the first one is to develop a semi-analytic model for assessment of microwave propagation on the medium equivalent to the human body. The second objective is to provide designs of three types of helical antennas proposed to operate as central on-body antennas in Wireless Body Area Networks (WBANs) and to evaluate the near field radiated from the proposed antennas at the possible location of the on-skin antennas for implantable (in-body) biosensors.

This chapter highlights the considerations and challenges when designing antennas suitable for on-body communication in WBANs. Designing antennas that are required to operate near the human body surface is challenging as several important factors need to be taken into consideration along with the human body effects. These factors include antenna detuning, impedance matching, radiation pattern, Specific Absorption Rate (SAR), size, cost, weight, positioning, bending and stable performance with the variation of the gap between the antenna and the human body. An antenna designed to overcome the addressed challenges and to achieve the operational requirements is suitable for on-body communication as human-body wearable antenna.

The antenna design, location and performance depend on the medium of propagation. Antenna parameters are massively changing when it is in free space than in any other medium. Therefore, when designing an antenna for body sensor networks with proximity to the human body, the performance will change in a very noticed way. It is hard to apply the traditional theory of the antenna and channel to observe their normal characteristics separately. The antenna when mounted on a lossy, dispersive medium (e.g. human body) it acts as a radiator that is affected by this propagation medium. Therefore, the concept of the antenna de-embedding is the solution for

dealing with the antenna on its own, modelling it and taking into consideration the effect of the surrounding medium.

### 3.2. The Proposed Antennas System for On-Body Biosensor Communication

Each of the proposed antennas is a dual-band of the helical wire type. It is designed to operate in the end-fire (axial) mode to communicate with the Wi-Fi communication system (5.0 – 6.0 GHz). Also, it is designed to operate in the broad-side mode to communicate with the on-skin biosensor antennas at 2.45 GHz. This configuration is illustrated in Figure 3.1.

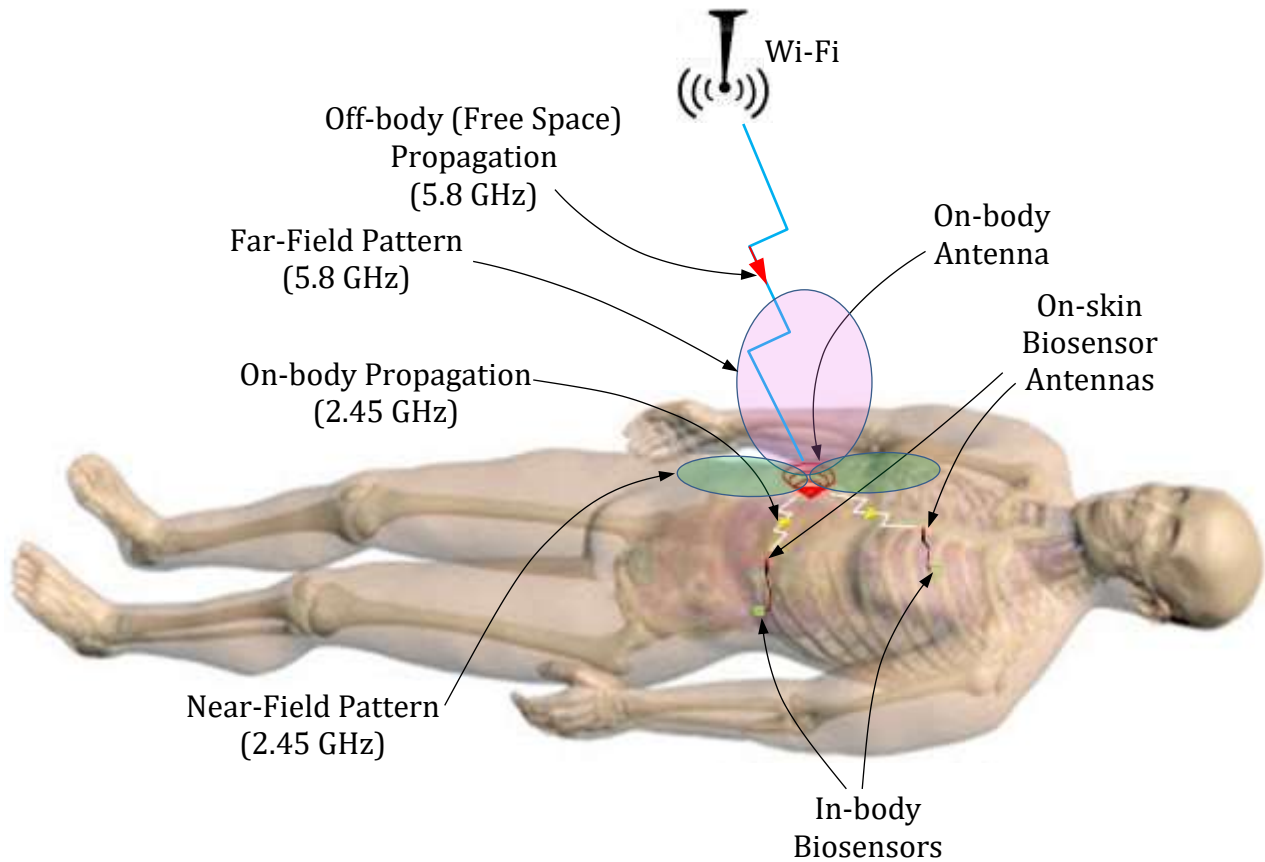


**Figure 3.1:** The on-body antenna connects the biosensor network to the Wi-Fi.

The microwave propagation model developed in the present chapter is based on the assumption that the on-body central antenna communicates with the on-skin biosensor antennas via on-body microwave propagation as shown in Figure 3.2. A photograph showing one of the antennas proposed in the present thesis (conical helix antenna) attached to the clothes of the

patient as wearable antenna is shown in Figure 3.2(a). An illustrative schematic showing the in-body sensors connected to the on-skin antennas is shown in Figure 3.2(b). On-skin antennas connected to the implanted (in-body) sensors through implanted RF coaxial electrodes are preferable to in-body antennas that are directly mounted on the implanted biosensors as they require much less power and thus avoiding high level of the SAR localized in some tissues and enabling long life-time of the batteries.

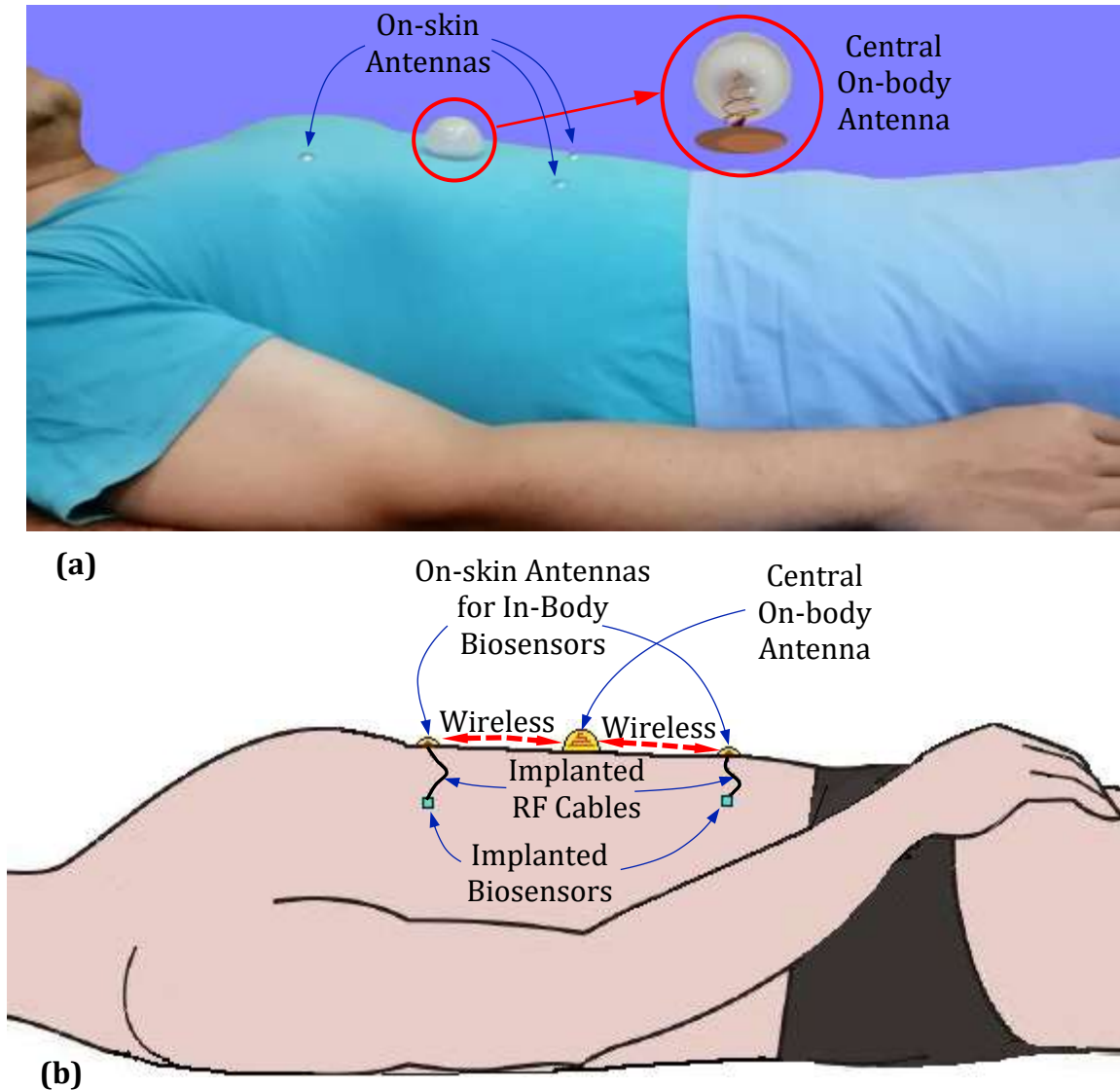


**Figure 3.2:** The on-body central antenna communicates with the on-skin biosensor antennas via on-body microwave propagation, (a) Photograph showing one of the antennas proposed in the present thesis attached to clothes of the patient as wearable antenna, (b) Illustrative schematic showing the in-body sensors connected to the on-skin antennas.

### 3.3. Propagation Model of EM Waves near the Surface of the Human Body

The propagation of the microwave near the surface of the human body in a WBAN, see Figure 3.3., is strongly dependent on the geometry and electric properties of the human body and the positions of the transmitting and receiving antennas. A special model should be developed for the assessment of the radiated field distribution on the body surface and the field inside the human tissues [114]. The present section is dedicated for this purpose.

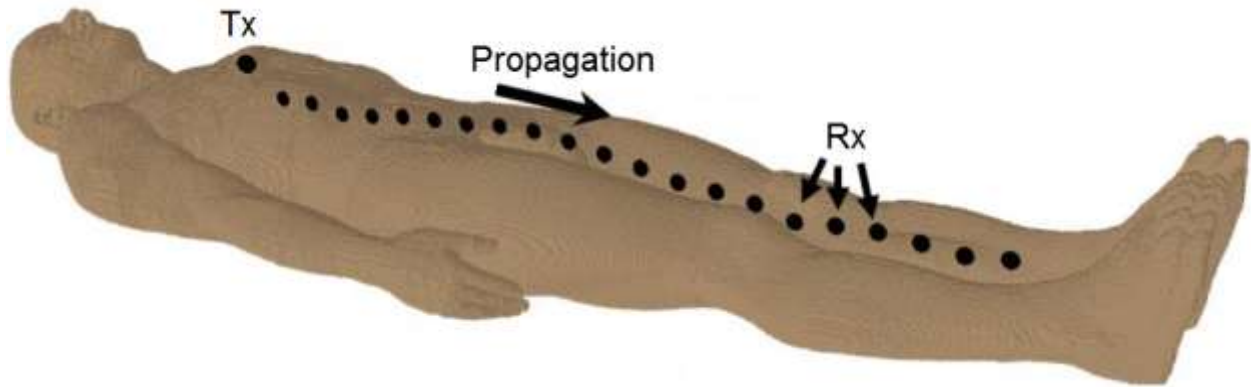


**Figure 3.3:** Propagation of microwave on the surface of the human body for on-body biosensor network communication [114].

#### 3.3.1. Geometry of the Problem

A mathematical model is done for the designed on-body antennas to develop a propagation model of electromagnetic waves on the human body which is a lossy medium. The propagation model provides description of the electric field components in order to get the total radiated field from the on-body helical antennas placed above the human body. This mathematical model is considered one of the main contributions of this work.

Assuming a flat surface model for the human chest-belly area over which the on-body antennas are located, see Figure 3.4, the electric field due to a transmitting isotropic radiator located at a height  $h_t$  above the body surface and received by an isotropic receiver located at a height  $h_r$  above the body can be calculated with the aid of the geometry shown in Figure 3.5.

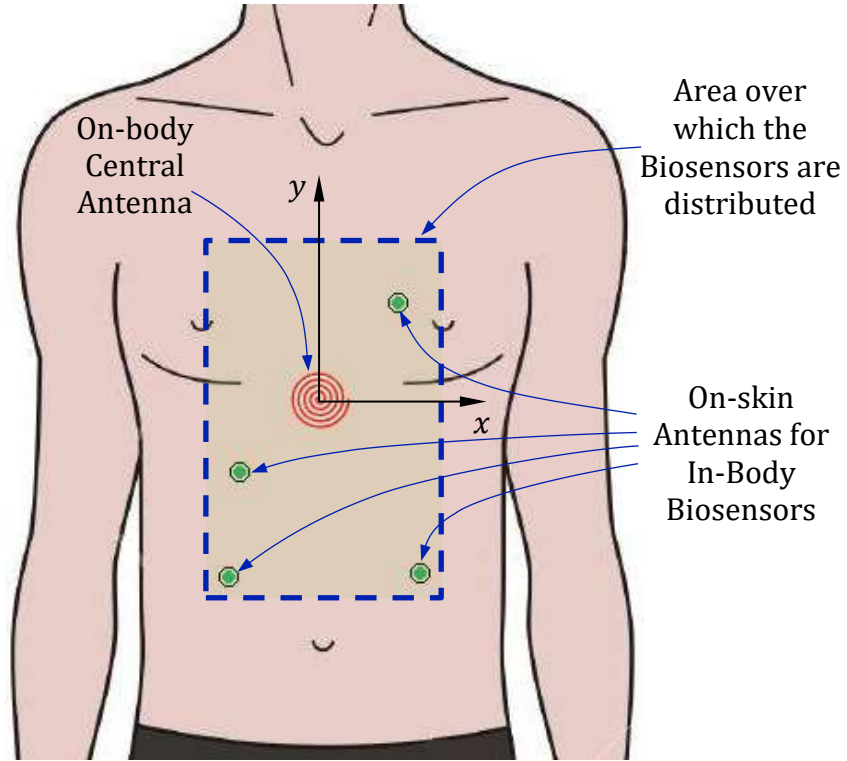


**Figure 3.4:** The radiation from the on-body antenna covers the chest-belly area occupied by the biosensor antennas.

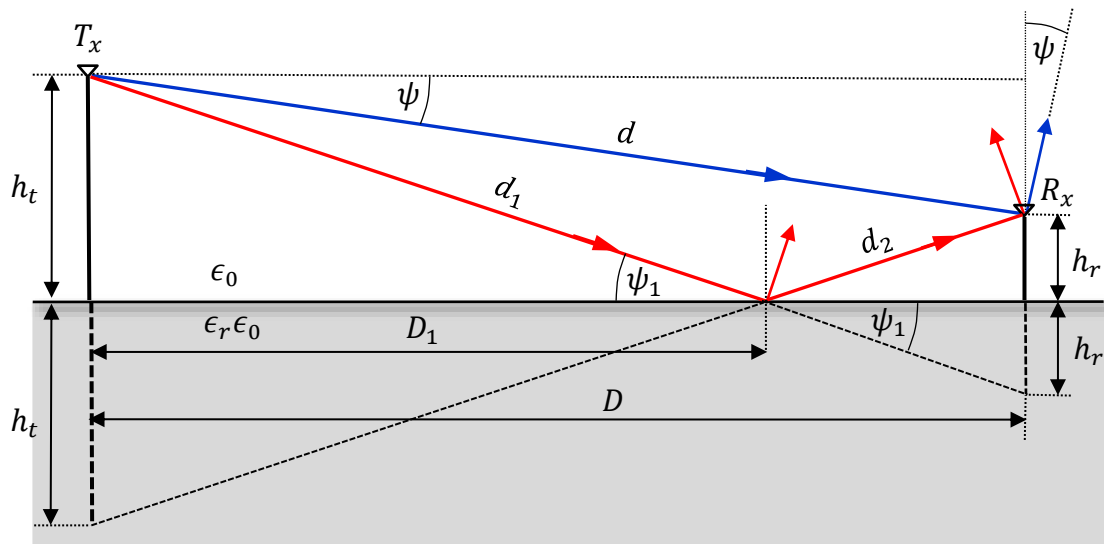


**Figure 3.5:** Geometry used to develop the propagation model of electromagnetic waves on the human body.



The length of the direct path from the transmitting to the receiving antennas is expressed as follows.

$$d = \frac{D}{\cos \psi} \quad (3-1)$$

where  $D$  is the horizontal distance between the transmitting and receiving antennas and  $\psi$  is the elevation angle of the receiving antenna relative to the transmitting.

$$\psi = \tan^{-1} \left( \frac{h_t - h_r}{D} \right) \quad (3-2)$$

The distance between the projection point of the transmitting antenna on the body surface and the point of reflection of the incident ray on this surface can be calculated as follows.

$$D_1 = D \frac{h_t}{h_t + h_r} \quad (3-3)$$

The total length of the distance travelled by the indirect ray (incident and reflected) to arrive at receiving antenna

$$d_{in} = d_1 + d_2 = \frac{D}{\cos \psi_1} \quad (3-4)$$

where the angle  $\psi_1$ , the distance  $d_1$ , and the distance  $d_2$  can, respectively, be evaluated as follows,

$$\psi_1 = \tan^{-1} \left( \frac{h_t + h_r}{D} \right) \quad (3-5)$$

$$d_1 = \frac{D_1}{\cos \psi_1} \quad (3-6)$$

$$d_2 = \frac{D - D_1}{\cos \psi_1} \quad (3-7)$$

### 3.3.2. Mechanisms of Microwave Propagation near the Surface of the Human Body

The propagation mechanisms shown in Figure 3.5 provide descriptions of the electric field components. The electric field of the propagating wave can be divided into three parts; direct

wave  $E_d$ , reflected wave on the dissipated medium (human body surface)  $E_g$  and the surface wave  $E_s$ .

$$E = E_d + E_g + E_s \quad (3-8)$$

### 3.3.2.1. Direct Wave

The direct wave travels a distance  $d$  until it reaches the receiver therefore the field component will be normal on the direction of propagation multiplied by the factor  $\cos \psi$  and then multiplied by the Green's function that is clarified in (3-20) where the phase must be taken into consideration as follows.

$$E_d = \frac{1}{d} e^{(-j\frac{2\pi d}{\lambda})} \cos \psi \quad (3-9)$$

### 3.3.2.2. Reflected Wave

The ground reflected wave travels two distances, from the transmitting antenna to the ground reflecting point (on the human body surface) and then to the receiver. The reflection coefficient  $\Gamma$  is multiplied due to the reflection of the wave and since the wave first hits the ground point therefore, its normal component is multiplied once by  $\cos \psi$  and then once more when it is delivered at the receiver point.

$$E_g = \frac{\Gamma}{d_{in}} e^{(-j\frac{2\pi d_{in}}{\lambda})} \cos^2 \psi_1 \quad (3-10)$$

### 3.3.2.3. Surface Wave

The surface wave is transmitted along the human body surface and travels a distance  $d_{in}$ . This wave suffers from high attenuation due to the lossy dispersive medium (human body) therefore,  $\alpha_s$  is taken into consideration.

$$E_s = \frac{T}{d_{in}} e^{(-\alpha_s d_2 \cos \psi_1)} e^{-j2\pi(\frac{d_1}{\lambda} + \frac{d_2}{\lambda_s})} \cos \psi_1 \quad (3-11)$$

where,  $\alpha_s$  is the attenuation of the surface waves.

### 3.3.3. Polarization of the Radiated Field for Current Element above Lossy Medium

This section is concerned with the definition of the polarization designations. The incident electric field is decomposed as shown in Figure 3.6. The unit vectors defining the orientation of the horizontal and vertical components of electric field can be, respectively, obtained as follows,

$$\hat{\mathbf{a}}_h = \frac{\hat{\mathbf{a}}_z \times \hat{\mathbf{k}}_i}{\sin \theta_i} \quad (3-12)$$

$$\hat{\mathbf{a}}_v = \hat{\mathbf{a}}_{ki} \times \hat{\mathbf{a}}_h \quad (3-13)$$

The angle of polarization ( $\psi$ ) is the angle between the incident electric field vector  $\mathbf{E}_i$  and the horizontal direction defined by  $\hat{\mathbf{a}}_h$ . This angle can be calculated as follows.

$$\psi = \cos^{-1} \left( \frac{\mathbf{E}_i \cdot \hat{\mathbf{h}}}{E_i} \right) \quad (3-14)$$

The horizontally polarized electric field vector of the incident plane wave can be expressed as follows

$$\mathbf{E}_{i_h} = \hat{\mathbf{a}}_h E_i \cos \psi_i \quad (3-15)$$

The vertically polarized electric field vector of the incident plane wave can be expressed as

$$\mathbf{E}_{i_v} = \hat{\mathbf{a}}_v E_i \sin \psi_i \quad (3-16)$$

According to the geometry shown in Figure 3.6, it can be shown that

$$\hat{\mathbf{a}}_h = -\hat{\mathbf{a}}_x \sin \phi_i + \hat{\mathbf{a}}_y \cos \phi_i, \quad (3-17)$$

and,

$$\hat{\mathbf{a}}_v = -\hat{\mathbf{a}}_x \cos \theta_i \cos \phi_i - \hat{\mathbf{a}}_y \cos \theta_i \sin \phi_i + \hat{\mathbf{a}}_z \sin \theta_i \quad (3-18)$$

In terms of  $\hat{\mathbf{h}}$  and  $\hat{\mathbf{v}}$ , the incident electric field vector can be expressed as

$$\mathbf{E}_i = E_i (\hat{\mathbf{a}}_h \cos \psi_i + \hat{\mathbf{a}}_v \sin \psi_i) \quad (3-19)$$

In terms of the angles  $\theta_i$ ,  $\phi_i$  and  $\psi_i$ , the incident electric field vector can be expressed as

$$\begin{aligned} \mathbf{E}_i = E_0 e^{-jk_0 \hat{\mathbf{a}}_{ki} \cdot \mathbf{r}} & (\hat{\mathbf{a}}_x (\sin \phi_i \cos \psi_i - \cos \theta_i \cos \phi_i \sin \psi_i) \\ & - \hat{\mathbf{a}}_y (\cos \phi_i \cos \psi_i + \cos \theta_i \sin \phi_i \sin \psi_i) + \hat{\mathbf{a}}_z \sin \theta_i \sin \psi_i) \end{aligned} \quad (3-20)$$

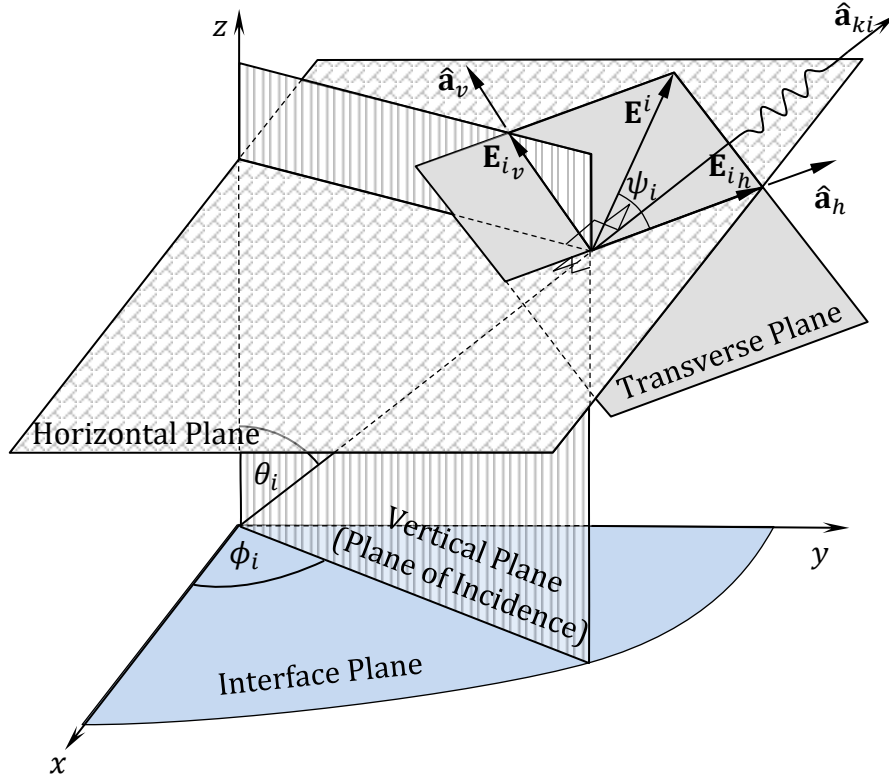


**Figure 3.6:** Definition of the vertical and horizontal polarization vectors for the incident ray of light.

### 3.3.4. Fresnel Reflection on the Human Body

The propagating wave in free space has its vertical and horizontal polarizations. However, when considering a lossy medium such as the human body; the horizontal and vertical components of the field incident on the interface plane between the free space and the lossy medium are subjected to different values of the reflection and transmission coefficients. The reflection coefficient of the vertically polarized wave can be expressed as follows.

$$\Gamma_v = \frac{\cos \theta_t - \sqrt{\epsilon_r} \cos \theta_i}{\cos \theta_t + \sqrt{\epsilon_r} \cos \theta_i} \quad (3-21)$$

The reflection coefficient of the horizontally polarized wave can be expressed as follows.

$$\Gamma_h = \frac{\cos \theta_i - \sqrt{\epsilon_r} \cos \theta_t}{\cos \theta_i + \sqrt{\epsilon_r} \cos \theta_t} \quad (3-22)$$

The transmission coefficient of the vertically polarized wave can be expressed as follows.

$$T_v = \frac{2 \cos \theta_i}{\cos \theta_t + \sqrt{\epsilon_r} \cos \theta_i} \quad (3-23)$$

The transmission coefficient of the horizontally polarized wave can be expressed as follows.

$$T_h = \frac{2 \cos \theta_i}{\cos \theta_i + \sqrt{\epsilon_r} \cos \theta_t} \quad (3-24)$$

where, where  $\theta_i$  is the angle of incidence and  $\theta_t$  is the angle of refraction (transmission into the lossy medium). These angles can be expressed as follows.

$$\theta_i = \frac{\pi}{2} - \psi_1 \quad (3-25-a)$$

$$\theta_t = \sin^{-1} \left( \frac{\sin \theta_i}{\sqrt{\epsilon_r}} \right) \quad (3-25-b)$$

As shown in the equations above,  $\Gamma_v, \Gamma_h, T_v, T_h$  the reflection and transmission coefficients for both vertical and horizontal components, respectively are calculated for the human body tissues, given  $\epsilon_r$ .

### **3.4. Evaluation of the Electric Field Radiated from a Wire Antenna over the Human Body**

#### **3.4.1. Evaluation of the Magnetic and Scalar Potentials due to Current Element above Lossy Medium**

For a dual-mode helical antenna, it will act in an on-body communication mode to receive from the sensor antenna mounted on the human body and transmits in an off-body communication mode to an external wireless system. The current distribution  $\mathbf{J}$  flowing on the antenna's surface will be integrated on the helical surface in order to obtain the radiated electric field by calculating the magnetic vector potential  $\mathbf{A}$  as follows,

$$\mathbf{E} = -j\omega\mathbf{A} - \nabla\Phi \quad (3-26)$$

where,  $\mathbf{A}$  is the magnetic vector potential and  $\Phi$  is the scalar electric potential. For a wire antenna of arbitrary shape,  $\mathbf{A}$  and  $\Phi$  can, respectively, be expressed as follows.

$$\mathbf{A} = \frac{\mu}{4\pi} \int_{\text{Antenna Length}} G J(x_s, y_s, z_s) \mathbf{dl} \quad (3-27)$$

$$\Phi = \frac{j}{4\pi\epsilon\omega} \int_{\text{Antenna Length}} G \nabla_l \cdot [J(x_s, y_s, z_s) \mathbf{dl}] \quad (3-28)$$

where,  $J(x_s, y_s, z_s)$  is the current at a point  $(x_s, y_s, z_s)$  on the wire antenna,  $\mathbf{dl}$  is the infinitesimal length vector (of the wire) at the point  $(x_s, y_s, z_s)$ , and  $G$  is the Green's function of free space corresponding to the direct wave. This function can be defined as follows.

$$G_d = \frac{e^{-jkR_d}}{R_d}, \quad R_d = |\mathbf{r}_f - \mathbf{r}_s| \quad (3-29-a)$$

$$G_{ind} = \frac{e^{-jkR_{ind}}}{R_{ind}}, \quad R_{ind} = |\mathbf{r}_g - \mathbf{r}_s| + |\mathbf{r}_f - \mathbf{r}_g| \quad (3-29-b)$$

where  $\mathbf{r}_f = (x_f, y_f, z_f)$  is the position vector of a point in radiation zone (near or far) and  $\mathbf{r}_s = (x_s, y_s, z_s)$  is the position vector of a point on the wire antenna.

### 3.4.2. Geometric Models of the Helical Wire Antennas

#### 3.4.2.1. Infinitesimal Length on Wire Antennas

In the Cartesian coordinates, the infinitesimal length vector can be expressed as

$$\mathbf{dl} = dx \hat{\mathbf{a}}_x + dy \hat{\mathbf{a}}_y + dz \hat{\mathbf{a}}_z \quad (3-30)$$

In the cylindrical coordinates, the infinitesimal length vector can be expressed as

$$\mathbf{dl} = dr \hat{\mathbf{a}}_r + r d\phi \hat{\mathbf{a}}_\phi + dz \hat{\mathbf{a}}_z \quad (3-31)$$

In the spherical coordinates, the infinitesimal length vector can be expressed as

$$\mathbf{dl} = dr \hat{\mathbf{a}}_r + r d\theta \hat{\mathbf{a}}_\theta + r \sin \theta d\phi \hat{\mathbf{a}}_\phi \quad (3-32)$$

The  $d\mathbf{l}$  vector can be transformed from cylindrical to Cartesian coordinates as follows,

$$\begin{pmatrix} dx \\ dy \\ dz \end{pmatrix} = \begin{pmatrix} \cos \phi & -\sin \phi & 0 \\ \sin \phi & \cos \phi & 0 \\ 0 & 0 & 1 \end{pmatrix} \begin{pmatrix} dr \\ r d\phi \\ dz \end{pmatrix} \quad (3-33)$$

If the wire antenna is segmented into  $N$  equal length segments; each with a length  $L/N$ , the length-element vectors representing wire segments can be expressed as follows.

$$\Delta \mathbf{l}_n = \Delta x_n \hat{\mathbf{a}}_x + \Delta y_n \hat{\mathbf{a}}_y + \Delta z_n \hat{\mathbf{a}}_z \quad (3-34)$$

### 3.4.2.2. Infinitesimal Length on Helical Wire Antenna

The parametric equations for the coordinates of a point on the helix can be expressed as follows.

$$r = a, \quad z = a \phi_s \tan \psi_p \quad (3-35)$$

where,  $a$  is the helix radius and  $\psi_p$  is the pitch angle of the helix. It should be noted that  $\phi_s$  is the angular coordinate of the cylindrical system which is a free parameter that takes a value to identify a specific point on the helical wire.

As shown in Figure 3.7, for unwrapped infinitesimal length element on the helical wire, one has

$$dr = 0, \quad dz = a d\phi_s \tan \psi_p \quad (3-36)$$

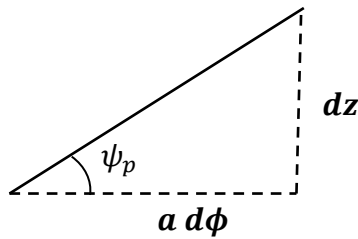


**Figure 3. 7:** Unwrapped turn of a helix

Thus, the infinitesimal length vector on a helical wire can be expressed as

$$d\mathbf{l} = a d\phi_s (\hat{\mathbf{a}}_\phi + \tan \psi_p \hat{\mathbf{a}}_z) \quad (3-37)$$

Substituting from (3-37) into (3-33), one gets

$$\begin{pmatrix} dx \\ dy \\ dz \end{pmatrix} = \begin{pmatrix} \cos \phi_s & -\sin \phi_s & 0 \\ \sin \phi_s & \cos \phi_s & 0 \\ 0 & 0 & 1 \end{pmatrix} \begin{pmatrix} 0 \\ a d\phi_s \\ a \tan \psi_p d\phi_s \end{pmatrix} \quad (3-38)$$

Let the cylindrical coordinates of a point on the wire antenna be  $(r_s, \phi_s, z_s)$ ; thus, according to (3-38), the Cartesian components of the length element vectors on the wire antenna can be expressed as follows.

$$dx = -a \sin \phi_s d\phi_s \quad (3-39-a)$$

$$dy = a \cos \phi_s d\phi_s \quad (3-39-b)$$

$$dz = a \tan \psi_p d\phi_s \quad (3-39-c)$$

The length-element vector in the Cartesian coordinates can be expressed as follows.

$$d\mathbf{l} = a d\phi_s (-\sin \phi_s \hat{\mathbf{a}}_x + \cos \phi_s \hat{\mathbf{a}}_y + \tan \psi_p \hat{\mathbf{a}}_z) \quad (3-40)$$

### 3.4.2.3. Infinitesimal Length on the Conical Helix Wire Antenna

The parametric equations for the coordinates of a point on the helix can be expressed as follows.

$$r = c_r \phi_s, \quad z = \frac{c_r}{\tan \theta_0} \phi_s \quad (3-41)$$

where,  $c_r$  is a constant equal to the rate of increase of the conical helix radius with the angle  $\phi_s$  and  $\theta_0$  is half the apex angle. It should be noted that  $\phi_s$  is the free parameter that takes a value to identify a specific point on the helical wire.

For the conical helix antenna, one has

$$dr = c_r d\phi_s, \quad dz = \frac{c_r}{\tan \theta_0} d\phi_s \quad (3-42)$$

Thus, the infinitesimal length vector on a conical helix wire can be expressed as

$$d\mathbf{l} = c_r d\phi_s \left( \hat{\mathbf{a}}_r + \phi_s \hat{\mathbf{a}}_\phi + \frac{1}{\tan \theta_0} \hat{\mathbf{a}}_z \right) \quad (3-43)$$

Substituting from (3-43) into (3-33), one gets



$$\begin{pmatrix} dx \\ dy \\ dz \end{pmatrix} = \begin{pmatrix} \cos \phi_s & -\sin \phi_s & 0 \\ \sin \phi_s & \cos \phi_s & 0 \\ 0 & 0 & 1 \end{pmatrix} \begin{pmatrix} c_r d\phi_s \\ c_r \phi_s d\phi_s \\ \frac{c_r}{\tan \theta_0} d\phi_s \end{pmatrix} \quad (3-44)$$

Let the cylindrical coordinates of a point on the wire antenna be  $(r_s, \phi_s, z_s)$ ; thus, according to (3-44), the Cartesian components of the length element vectors on the conical-helix wire antenna can be expressed as follows.

$$dx = c_r (\cos \phi_s - \phi_s \sin \phi_s) d\phi_s \quad (3-45-a)$$

$$dy = c_r (\sin \phi_s + \phi_s \cos \phi_s) d\phi_s \quad (3-45-b)$$

$$dz = \frac{c_r}{\tan \theta_0} d\phi_s \quad (3-45-c)$$

The length-element vector in the Cartesian coordinates can be expressed as follows.

$$d\mathbf{l} = c_r d\phi_s \left[ (\cos \phi_s - \phi_s \sin \phi_s) \hat{\mathbf{a}}_x + (\sin \phi_s + \phi_s \cos \phi_s) \hat{\mathbf{a}}_y + \frac{1}{\tan \theta_0} \hat{\mathbf{a}}_z \right] \quad (3-46)$$

#### 3.4.2.4. Segmentation of the Helical Wire Antenna

The components of the length-element vector can be expressed as

$$\Delta x_n = -a \sin \phi_{s_n} \Delta \phi_s \quad (3-47-a)$$

$$\Delta y_n = a \cos \phi_{s_n} \Delta \phi_s \quad (3-47-b)$$

$$\Delta z_n = a \tan \psi_p \Delta \phi_s \quad (3-47-c)$$

where  $\Delta \phi_s$  is the azimuth angle subtended by the length element  $\Delta \mathbf{l}_n$ ; for a helix of  $T$  turns, it can be expressed as follows.

$$\Delta \phi_s = \frac{2T\pi}{N} \quad (3-48)$$

The discrete angular coordinate on the helical wire can be expressed as follows.

$$\phi_{s_n} = n \Delta \phi_s = \frac{2nT\pi}{N} \quad (3-49)$$

Thus, all the segments on the helical wire have the same length, which can be calculated as follows.

$$\Delta l_n = \frac{T}{N} 2\pi a \sqrt{1 + \tan^2 \psi_p}, \quad n = 1, 2, \dots, N \quad (3-50-I)$$

$$\Delta l_n = \frac{T}{N} 2\pi a \sqrt{\sec^2 \psi_p}, \quad n = 1, 2, \dots, N \quad (3-50-II)$$

$$\Delta l_n = \frac{T}{N} \frac{2\pi a}{\cos \psi_p}, \quad n = 1, 2, \dots, N \quad (3-50-III)$$

Thus, the length element vector can be expressed as follows.

$$\Delta \mathbf{l}_n = a \Delta \phi_s (-\sin \phi_s \hat{\mathbf{a}}_x + \cos \phi_s \hat{\mathbf{a}}_y + \tan \psi_p \hat{\mathbf{a}}_z) \quad (3-51)$$

Substituting from (3-30) of the appendix into (3-27), the components of the vector magnetic potential at a point far from the antenna can be expressed as follows.

$$A_x = \frac{\mu}{4\pi} \int_{\text{Antenna Length}} J_x G_d dx \quad (3-52-a)$$

$$A_y = \frac{\mu}{4\pi} \int_{\text{Antenna Length}} J_y G_d dy \quad (3-52-b)$$

$$A_z = \frac{\mu}{4\pi} \int_{\text{Antenna Length}} J_z G_d dz \quad (3-52-c)$$

### 3.4.3. Radiated Field due to Direct Path (Line-of-Sight)

The integral (3-27) can be discretized over the wire length to be expressed as follows.

$$\mathbf{A}_d = \frac{\mu}{4\pi} \sum_{n=1}^N J_n G_{d_n} \Delta \mathbf{l}_n, \quad n = 1, 2, \dots, N \quad (3-53)$$

where  $G_{d_n}$  is the discrete analog of  $G_d$  and can be expressed as follows

$$G_{d_n} = \frac{e^{-jkR_{d_n}}}{R_{d_n}}, \quad R_{d_n} = |\mathbf{r}_f - \mathbf{r}_{s_n}| \quad (3-54)$$

The components of the vector magnetic potential can be expressed as follows.

$$A_{d_x} = \frac{\mu}{4\pi} \sum_{n=1}^N J_{n_x} G_{d_n} \Delta x_n, \quad n = 1, 2, \dots, N \quad (3-55-a)$$

$$A_{d_y} = \frac{\mu}{4\pi} \sum_{n=1}^N J_{n_y} G_{d_n} \Delta y_n, \quad n = 1, 2, \dots, N \quad (3-55-b)$$

$$A_{d_z} = \frac{\mu}{4\pi} \sum_{n=1}^N J_{n_z} G_{d_n} \Delta z_n, \quad n = 1, 2, \dots, N \quad (3-55-c)$$

Thus, the electric field radiated by the wire antenna in the direct path (line-of-sight) at a relatively far point can be expressed using (3-27) to get the following expression.

$$\mathbf{E}_d = -j\omega \frac{\mu}{4\pi} \sum_{n=1}^N J_n G_{d_n} \Delta \mathbf{l}_n, \quad n = 1, 2, \dots, N \quad (3-56)$$

#### 3.4.4. Radiated Field due to Indirect Path (Ground-Reflected Ray)

It can be shown that, for the ground reflected wave, the Greens function has the following components.

$$G_{h_{ind_n}} = \frac{e^{-jkR_{ind_n}}}{R_{ind_n}} \Gamma_h, \quad R_{ind_n} = |\mathbf{r}_g - \mathbf{r}_{s_n}| + |\mathbf{r}_f - \mathbf{r}_g| \quad (3-57-a)$$

$$G_{v_{\parallel ind_n}} = -\frac{e^{-jkR_{ind_n}}}{R_{ind_n}} \Gamma_v, \quad R_{ind_n} = |\mathbf{r}_g - \mathbf{r}_{s_n}| + |\mathbf{r}_f - \mathbf{r}_g| \quad (3-57-b)$$

$$G_{v_{\perp ind_n}} = \frac{e^{-jkR_{ind_n}}}{R_{ind_n}} \Gamma_v, \quad R_{ind_n} = |\mathbf{r}_g - \mathbf{r}_{s_n}| + |\mathbf{r}_f - \mathbf{r}_g| \quad (3-57-c)$$

where the subscript  $h$  indicates the direction of horizontal polarization,  $v_{\parallel}$  indicates the direction normal to the horizontal plane, and  $v_{\perp}$  indicates the direction of the component of the vertical polarization parallel to the horizontal plane.

Thus, the ground-reflected electric field due to the current on the  $n^{th}$  segment of the wire antenna can be expressed as follows

$$\begin{aligned} \Delta \mathbf{e}_{ind_n} = & -j\omega \frac{\mu}{4\pi} J_n \frac{e^{-jkR_{ind_n}}}{R_{ind_n}} \left[ \Gamma_h \Delta l_{n_h} \hat{\mathbf{a}}_h \right. \\ & \left. + \Gamma_v (\Delta l_{n_v} \cos \psi \hat{\mathbf{a}}_{v_\perp} - \Delta l_{n_v} \sin \psi \hat{\mathbf{a}}_{v_\parallel}) \right], \quad n = 1, 2, \dots, N \end{aligned} \quad (3-58)$$

The last expression (3-36) can be rewritten as follows.

$$\begin{aligned} \Delta \mathbf{e}_{ind_n} = & -j\omega \frac{\mu}{4\pi} J_n \frac{e^{-jkR_{ind_n}}}{R_{ind_n}} \left[ \Gamma_h \Delta l_{n_h} \hat{\mathbf{a}}_h + \Gamma_v (\Delta l_{n_{v_\perp}} \hat{\mathbf{a}}_{v_\perp} - \Delta l_{n_{v_\parallel}} \hat{\mathbf{a}}_{v_\parallel}) \right], \\ & n = 1, 2, \dots, N \end{aligned} \quad (3-59)$$

Making use of (3-35), the last expression (3-37) can be rewritten as follows.

$$\begin{aligned} \Delta \mathbf{e}_{ind_n} = & -j\omega \frac{\mu}{4\pi} J_n \left[ G_{h_{ind_n}} \Delta l_{n_h} \hat{\mathbf{a}}_h + G_{v_\parallel_{ind_n}} \Delta l_{n_{v_\parallel}} \hat{\mathbf{a}}_{v_\parallel} + G_{v_\perp_{ind_n}} \Delta l_{n_{v_\perp}} \hat{\mathbf{a}}_{v_\perp} \right], \\ & n = 1, 2, \dots, N \end{aligned} \quad (3-60)$$

### 3.4.5. Total Radiated Field

The direct (line-of-sight) electric field due to the current flowing in the length element  $\Delta \mathbf{l}_n$  can be expressed as follows

$$\Delta \mathbf{e}_{d_n} = -j\omega \frac{\mu}{4\pi} J_n \bar{\mathbf{G}}_{d_n} \Delta \mathbf{l}_n, \quad n = 1, 2, \dots, N \quad (3-61)$$

where

$$\bar{\mathbf{G}}_{d_n} = \begin{pmatrix} G_{d_n} & 0 & 0 \\ 0 & G_{d_n} & 0 \\ 0 & 0 & G_{d_n} \end{pmatrix}, \quad n = 1, 2, \dots, N \quad (3-62)$$

The indirect (ground-reflected) electric field due to the current flowing in the length element  $\Delta \mathbf{l}_n$  can be expressed as

$$\Delta \mathbf{e}_{ind_n} = -j\omega \frac{\mu}{4\pi} J_n \bar{\mathbf{G}}_{ind_n} \Delta \mathbf{l}_n, \quad n = 1, 2, \dots, N \quad (3-63)$$

where

$$\bar{\bar{\mathbf{G}}}_{ind_n} = \begin{pmatrix} G_{h_{ind_n}} & 0 & 0 \\ 0 & G_{v_{\parallel ind_n}} & 0 \\ 0 & 0 & G_{v_{\perp ind_n}} \end{pmatrix}, \quad n = 1, 2, \dots, N \quad (3-64)$$

Thus, the total radiated field due to the current flowing in the length element  $\Delta \mathbf{l}_n$  can be expressed as

$$\Delta \mathbf{e}_n = \Delta \mathbf{e}_{d_n} + \Delta \mathbf{e}_{ind_n}, \quad n = 1, 2, \dots, N \quad (3-65)$$

The last expression can be written as follows.

$$\Delta \mathbf{e}_n = -j\omega \frac{\mu}{4\pi} J_n \bar{\bar{\mathbf{G}}}_n \Delta \mathbf{l}_n, \quad n = 1, 2, \dots, N \quad (3-66)$$

where,

$$\bar{\bar{\mathbf{G}}}_n = G_{d_n} \bar{\bar{\mathbf{U}}} + \bar{\bar{\mathbf{G}}}_{ind_n} \quad (3-67)$$

where  $\bar{\bar{\mathbf{U}}}$  is  $3 \times 3$  unity matrix,

$$\bar{\bar{\mathbf{U}}} = \begin{pmatrix} 1 & 0 & 0 \\ 0 & 1 & 0 \\ 0 & 0 & 1 \end{pmatrix}$$

From (3-40) and (3-42) the total dyadic Green's function can be expressed as follows.

$$\bar{\bar{\mathbf{G}}}_n = \begin{pmatrix} G_{n_{xx}} & 0 & 0 \\ 0 & G_{n_{yy}} & 0 \\ 0 & 0 & G_{n_{zz}} \end{pmatrix}, \quad n = 1, 2, \dots, N \quad (3-68-a)$$

where,

$$\begin{aligned} G_{n_{xx}} &= G_{d_n} + G_{h_{ind_n}} \\ G_{n_{yy}} &= G_{d_n} + G_{v_{\parallel ind_n}} \\ G_{n_{zz}} &= G_{d_n} + G_{v_{\perp ind_n}} \end{aligned} \quad (3-68-b)$$

The total radiated field due to the current flowing along the wire antenna can be expressed as follows.

$$\mathbf{E} = \sum_{n=1}^N \Delta \mathbf{e}_n \quad (3-69)$$

Substituting form (4-35) into (3-38), the following expression is obtained for the radiated electric field.

$$\mathbf{E} = -j\omega \frac{\mu}{4\pi} \sum_{n=1}^N J_n \bar{\bar{\mathbf{G}}}_n \Delta \mathbf{l}_n \quad (3-70)$$

Alternative Derivation:

The vector magnetic potential due to the direct path can be expressed as follows.

$$\mathbf{A}_d = \frac{\mu}{4\pi} \sum_{n=1}^N J_n \bar{\bar{\mathbf{G}}}_{d_n} \Delta \mathbf{l}_n, \quad n = 1, 2, \dots, N \quad (3-71)$$

The vector magnetic potential due to the indirect (ground-reflected) path can be expressed as follows.

$$\mathbf{A}_{ind} = \frac{\mu}{4\pi} \sum_{n=1}^N J_n \bar{\bar{\mathbf{G}}}_{ind_n} \Delta \mathbf{l}_n, \quad n = 1, 2, \dots, N \quad (3-72)$$

The total vector magnetic potential can be expressed as

$$\mathbf{A} = \mathbf{A}_d + \mathbf{A}_{ind} \quad (3-73)$$

Therefore, substituting from (3-49) and (3-50) into (3-51) the total magnetic potential vector can be calculated as follows.

$$\mathbf{A} = \frac{\mu}{4\pi} \sum_{n=1}^N J_n \bar{\bar{\mathbf{G}}}_n \Delta \mathbf{l}_n, \quad n = 1, 2, \dots, N \quad (3-74)$$

Thus, the total radiated electric field can be expressed as follows.

$$\mathbf{E} = -j\omega \mathbf{A} = -j\omega \frac{\mu}{4\pi} \sum_{n=1}^N J_n \bar{\bar{\mathbf{G}}}_n \Delta \mathbf{l}_n, \quad n = 1, 2, \dots, N \quad (3-75)$$

The final expression (3-53) is the same as (3-48).

### **3.5. Evaluation of the Radiated Fields from Helical Wire Antennas Placed above the Human Body Surface for WBAN**

The radiated electric field from a wire antenna of arbitrary shape can be evaluated from the vector magnetic potential and scalar electric potentials as described in Section 3.4. The geometrical models of the helical wire antennas are usually described in the cylindrical coordinate system. The vector magnetic potential  $\mathbf{A}$  and, hence, the radiated electric field cannot be evaluated directly in the cylindrical coordinates, and since the length elements of the helical wire antennas is expressed in the cylindrical coordinates (as explained the above) a transformation to the Cartesian coordinates is needed. The  $d\mathbf{l}$  vector can be transformed from cylindrical to Cartesian coordinates as described above.

#### **3.5.1. Helical Antenna Proposed as Central Antenna for On-Body Biosensor Communications**

##### **3.5.1. 1. Geometry of the Helical Wire Antenna**

The geometry of the helix is described in Section 3.4.2.2 of the thesis appendix. The geometry of helical antenna is modeled in a Matlab® program written for this purpose and the resulting geometrical model is presented in Figure 3.8 for a right-hand wrapped helix. The helix diameter is  $D_H$ , the height is  $H_H$  and the number of turns is  $N_T$ . The pitch angle of the helix can be calculated as follows.

$$\psi_p = \tan^{-1} \left( \frac{H_H}{N_T \pi D_H} \right) \quad (3-76)$$

This model of the helical antenna is segmented as described in Section 3.4.2.4 and then equation (3-48) can be applied to evaluate the radiated electric field.

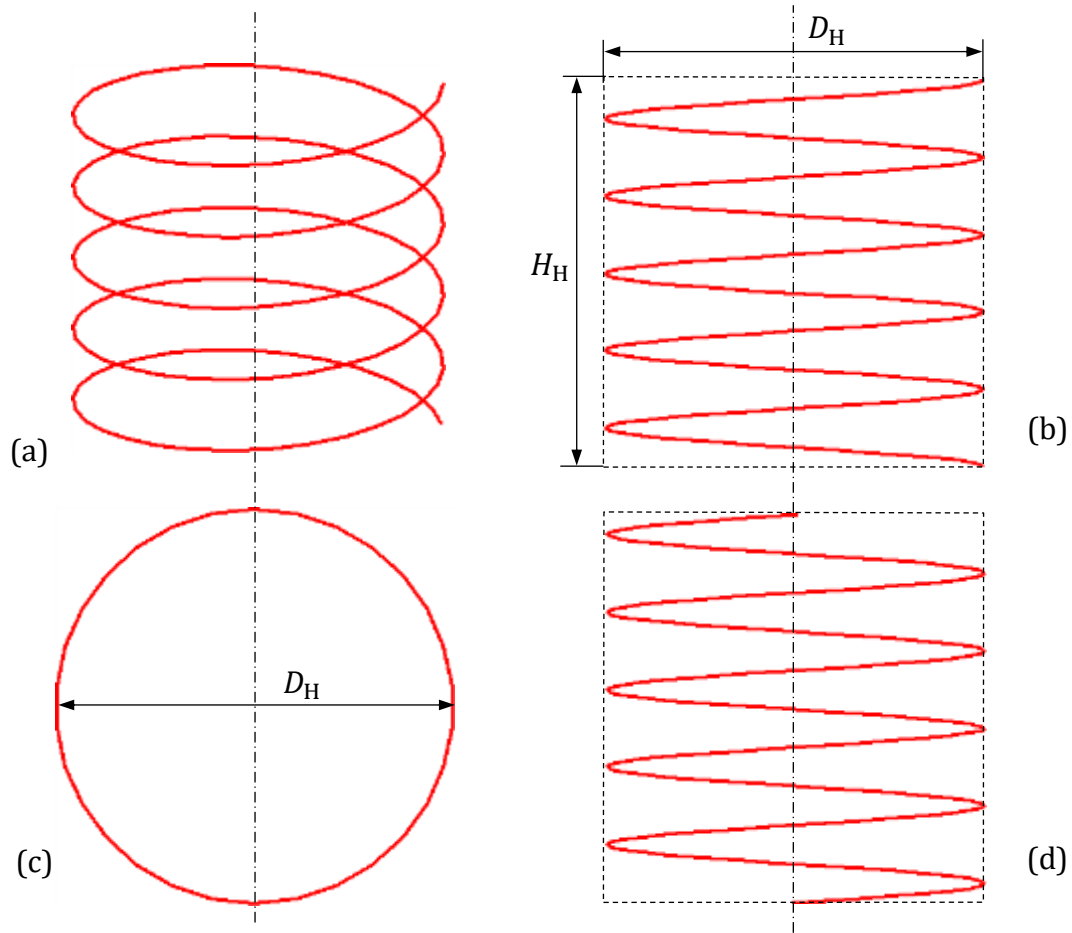


**Figure 3. 8:** Geometry of the helical antenna (a) Three-dimensional view, (b) Elevation view, (c) Top view, (d) Side view.

### 3.5.1.2. Radiated Fields due to Helical Wire Antenna

The components of the electric field radiated from the helical wire with the geometry described in Section 3.5.1 can be obtained by substitution from (3-51) into (3-48). Thus, the total radiated electric field can be expressed as follows.

$$E_x = j\omega \frac{\mu a T}{2N} \sum_{n=1}^N J_n G_{n_{xx}} \sin\left(\frac{2nT\pi}{N}\right), \quad (3-77-a)$$

$$E_y = -j\omega \frac{\mu a T}{2N} \sum_{n=1}^N J_n G_{n_{yy}} \cos\left(\frac{2nT\pi}{N}\right), \quad (3-77-b)$$



$$E_z = -j\omega \frac{\mu a T}{2N} \tan \psi_p \sum_{n=1}^N J_n G_{n_{zz}}, \quad (3-77-c)$$

### 3.5.1.3. Current Distribution on Long-Wire Helical Antennas

Assuming a long wire antenna ( $L \gg \lambda$ ) therefore, the current distribution along the wire length is supposed to be sinusoidal with period  $\lambda$  and linearly decaying amplitude. Thus, the current distribution can be expressed as follows.

$$J(l) = \alpha(l) \cos \frac{2\pi l}{\lambda} \quad (3-78)$$

where  $l$  is a variable representing the distance along wire length relative to the feeding point, and  $\alpha(l)$  describes the decay of the current amplitude while moving along the helix wire away from the feed point. The linear decay of the sinusoidal current amplitude is appropriate and can be described as follows.

$$\alpha(l) = c_1 l + c_2 \quad (3-79)$$

where  $c_1$  and  $c_2$  are constants that can be determined as follows.

The current is maximum and equal to  $J_o$  at the input port of the antenna ( $l = 0$ );

$$J(0) = J_o \quad (3-80)$$

This follows, from (3-56) and (3-57) that,

$$c_2 = J_o \quad (3-81)$$

The current vanishes at the end of the wire;

$$J(L) = 0 \quad (3-82)$$

It follows, from (3-56), (3-57), and (3-60) that,

$$0 = c_1 L + J_o \quad (3-83)$$

Thus, one has

$$c_1 = -\frac{J_o}{L} = -\frac{J_o}{2\pi a T} \quad (3-84)$$

Thus, the linearly decaying amplitude of the current along the wire can be expressed as,

$$\alpha(l) = J_o \left(1 - \frac{l}{2\pi aT}\right) \quad (3-85)$$

Substituting from (3-63) into (3-56), the current distribution along the wire of a helical antenna can be expressed as follows.

$$J(l) = J_o \left(1 - \frac{l}{2\pi aT}\right) \cos \frac{2\pi l}{\lambda} \quad (3-86)$$

As the length variable can be expressed in terms of the angle  $\phi_s$  as  $l = a\phi_s$ , the current distribution can be expressed as,

$$J(\phi_s) = J_o \left(1 - \frac{a\phi_s}{2\pi aT}\right) \cos \left(\frac{2\pi a\phi_s}{\lambda}\right) \quad (3-87)$$

Considering the segmentation of the helical wire according to (3-49), the discrete distribution of the current can be given as follows.

$$J_n = J_o \left(1 - \frac{a\phi_{s_n}}{2\pi aT}\right) \cos \left(\frac{2\pi a\phi_{s_n}}{\lambda}\right) \quad (3-88)$$

Substituting for  $\phi_{s_n}$  from (A-20) into (5-12), one gets

$$J_n = J_o \left(1 - \frac{n}{N}\right) \cos \left(\frac{4nT\pi^2 a}{\lambda N}\right) \quad (3-89)$$

Substituting from (3-67) into (3-48), one gets the following expression of the electric field at a point near the surface of the human body.

$$\mathbf{E} = -j\omega \frac{\mu J_o}{4\pi} \sum_{n=1}^N \left(1 - \frac{n}{N}\right) \cos \left(\frac{4nT\pi^2 a}{\lambda N}\right) \bar{\bar{\mathbf{G}}}_n \Delta \mathbf{l}_n \quad (3-90)$$

The electric field given by (5-67) can be expressed in terms of its components as follows.

$$E_x = j\omega \frac{\mu a T J_o}{2N} \sum_{n=1}^N \left(1 - \frac{n}{N}\right) \cos \left(\frac{4nT\pi^2 a}{\lambda N}\right) \sin \left(\frac{2nT\pi}{N}\right) G_{n_{xx}} \quad (3-91-a)$$

$$E_y = -j\omega \frac{\mu a T J_o}{2N} \sum_{n=1}^N \left(1 - \frac{n}{N}\right) \cos\left(\frac{4nT\pi^2 a}{\lambda N}\right) \cos\left(\frac{2nT\pi}{N}\right) G_{n_{yy}} \quad (3-91-b)$$

$$E_z = -j\omega \frac{\mu a T J_o}{2N} \tan \psi_p \sum_{n=1}^N \left(1 - \frac{n}{N}\right) \cos\left(\frac{4nT\pi^2 a}{\lambda N}\right) G_{n_{zz}} \quad (3-91-c)$$

### 3.5.2. Conical and Inverted Conical Helix as Central Antennas for On-Body Biosensor Communications

The conical helix antenna is a wire antenna wrapped like a helix with its radius decaying (or increasing) linearly with increasing the angular coordinate as the wire is further wrapped. Two types of conical helix antennas are considered in the present thesis as shown in Figure 3.9; the conical helix antenna is placed with its base near to the ground plane, whereas the inverted conical helix is paced with its tip (apex) near to the ground plane where the feed points are shown in the figure. In this section, the fields radiated form the two types of these conical helix antennas are evaluated.

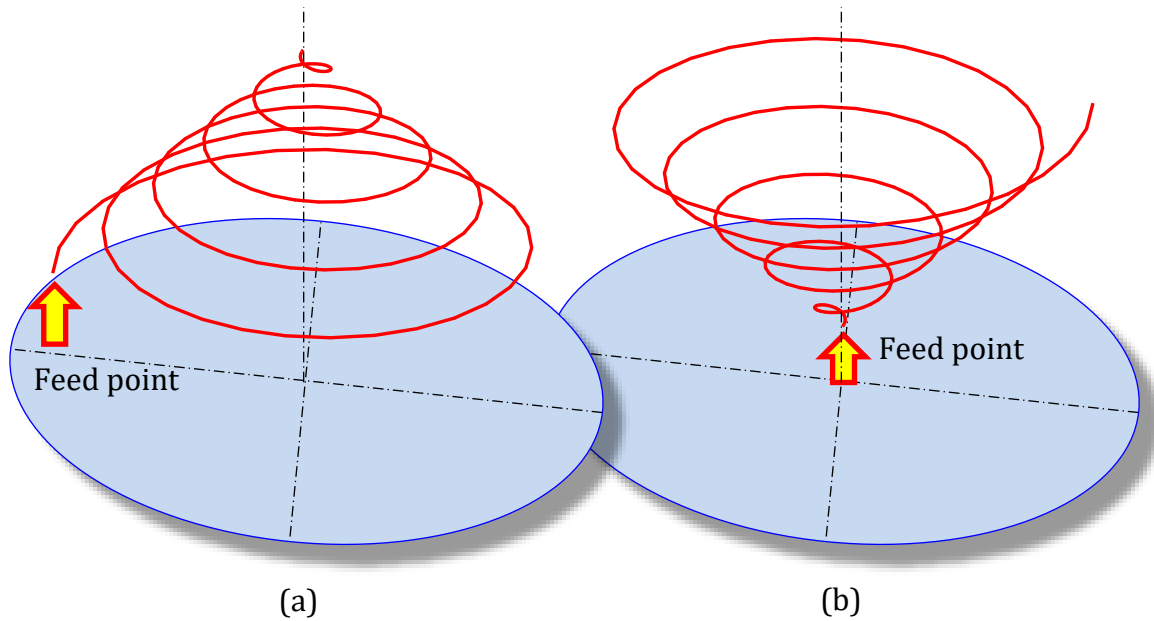


**Figure 3. 9:** Two types of helical wire antennas with conical external shape: (a) Conical helix, (b) Inverted conical helix.

The geometry of the conical helix is described in Section 3.4.2.3. The geometry of this type of helical antenna is modeled in a Matlab® program written for this purpose and the resulting geometrical model is presented in Figure 3.10 for a right-hand wrapped conical helix. The diameter of the largest turn on the helix is  $D_C$ , the height is  $H_C$  and the number of turns is  $N_T$ . The half apex angle of this conical helix can be calculated as follows.

$$\vartheta_0 = \tan^{-1} \left( \frac{D_C}{2H_C} \right) \quad (3-92)$$

In a way similar to that followed with the helical antenna described above, this model of the conical helix antenna is segmented as described in Section 3.4.2.4 and then equation (4-36) can be applied to evaluate the radiated electric field.

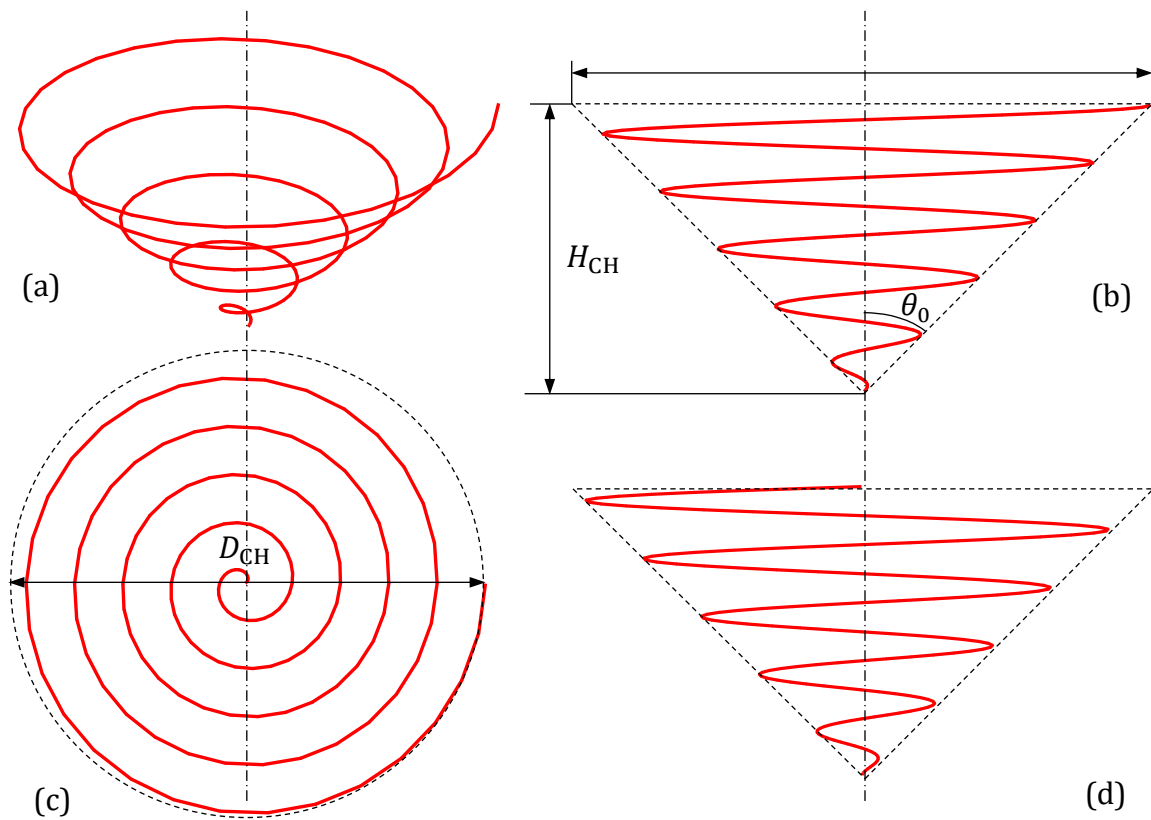


**Figure 3. 10:** Geometry of the conical helix antenna (a) Three-dimensional view, (b) Elevation view, (c) Top view, (d) Side view.

### **3.6. Switching Mechanism**

The proposed on-body antennas are designed to operate in dual-band mode 2.45 GHz and (5.0 – 6.0) GHz. The on-body antenna is collecting data from sensors mounted on the patient's body all the time when operating in the broadside mode to communicate with the biosensor antennas. The on-body proposed antennas will switch to the axial mode to communicate with an external device through Wi-Fi when the doctor demands the data of a certain patient.

### **3.7. Conclusion**

The present chapter proposes three types of helical antennas to be employed as central antenna for WBAN. Each of the proposed antennas is a dual-band of the helical wire type. It is designed to operate in the end-fire (axial) mode to communicate with the Wi-Fi communication system (5.0 – 6.0 GHz). Also, it is designed to operate in the broad-side mode to communicate with the on-skin biosensor antennas at 2.45 GHz. A rigorous technique for the assessment of microwave propagation on the medium equivalent to the human body is developed to evaluate the near field radiated from arbitrarily shaped wire antennas at the possible locations of on-skin antennas connected to implantable (in-body) biosensors. The radiated fields from the proposed on-body antenna helical antenna types in the near zone are evaluated using the proposed semi-analytic technique.

## Chapter 4

# Electromagnetic Simulation and Experimental Study of the On-Body Helical Antennas Proposed for Biosensor Networks

---

### 4.1. Introduction

This chapter is concerned with the quantitative studies of the three types of helical wire antennas proposed for being employed as on-body central antennas in WBANs. As explained in Chapter 3, each of the proposed helical antennas is a dual-band that is designed to operate in the end-fire (axial) mode to communicate (through its far-field) with the ceil-mounted Wi-Fi antenna at 5.8 GHz, and to operate in the broad-side mode to communicate (through its near field) with the on-skin biosensor antennas at 2.45 GHz. Three types of wire helical antennas are investigated in this chapter; these are the cylindrical helix, conical helix, and inverted conical helix antennas. Each antenna is matched with  $50\Omega$  coaxial feeder over a wide frequency band, mounted on a copper circular disc (representing the ground plane and the board on which the electronic circuit can be embedded), and covered with a very thin dielectric radome (almost transparent the microwave frequencies) for protecting the wire antenna. Such an antenna when covered by the radome is shaped like a hemispherical button that can be attached to the patient clothes and, hence, it can be considered as wearable antennas.

The design of the proposed antennas permits the use of low power (few milli-Watts) while communicating (at 2.45 GHz) with the on-skin antennas which are connected to in-body biosensors and allows the use of higher level of power while communicating with the Wi-Fi antenna (at 5.8 GHz). The power consumption is, thus, optimized leading to low level of the SAR in the human tissues and long life-time of the battery.

Three techniques are used for this purpose: (i) the semi-analytic technique developed in Chapter 4 for the assessment of the near-field distribution near the body surface (at the frequency 2.45 GHz), (ii) the commercially available CST® simulation package for the assessment of the far-field and radiation patterns (in the band around the Wi-Fi frequency 5.8 GHz), and (iii) experimental measurements of the three fabricated prototypes of the proposed helical antennas.

## 4.2. Near Field Distribution due to the Proposed On-Body Antennas

The evaluation of the near field just over the skin is a necessary requirement for the performance assessment of the on-body communication between the proposed central antenna and distributed on-skin biosensor antennas (investigated later on in Chapter 5). Also, the calculation of the electric field penetrating the human tissues namely the skin, fat, and muscle tissues is necessary for the evaluation of the SAR in these tissues. It should be noted that the human body area of concern in the present study is that rectangular area surrounded by the blue dashed rectangle shown in Figure 4.1. The near field is evaluated using the semi-analytic method explained, in detail, in Chapter 3 under the assumption of a flat surface of this region of the body. It should be noted that this rectangular area has the dimensions  $L_x = 20$  cm and  $L_y = 30$  cm in the following presentations and discussions of numerical results unless otherwise indicated.

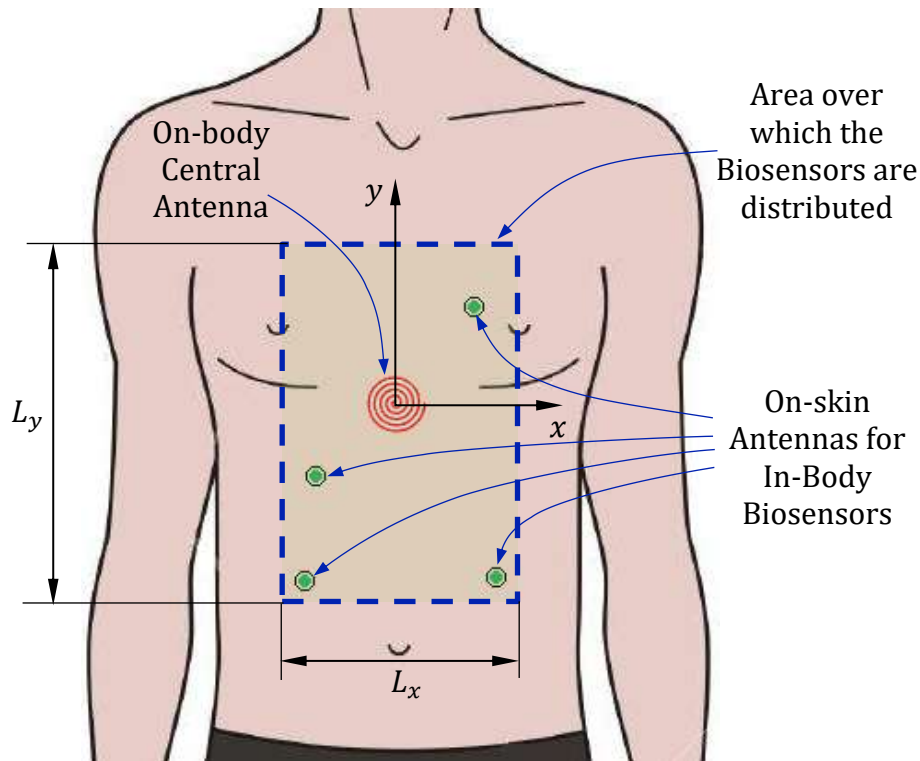


**Figure 4.1:** The radiation from the on-body antenna covers the chest-belly area surrounded by the blue dashed rectangle and occupied by the on-skin biosensor antennas.

### 4.2.1. Near Field Distribution due to Cylindrical Helix Antenna on the Human Body

The proposed cylindrical helix antenna has the geometric model shown in Figure 4.2 that is generated by a Matlab ® program for this purpose. This program applies the semi-analytic technique described in Chapter 4 to evaluate the near field over the body surface within the rectangular area bounded by the dashed rectangle shown in Figure 4.1. The proposed wire helix has a height  $H_H = 2\text{cm}$ , a diameter  $D_H = 2\text{cm}$ , and a number of turns  $N_T = 4$ .

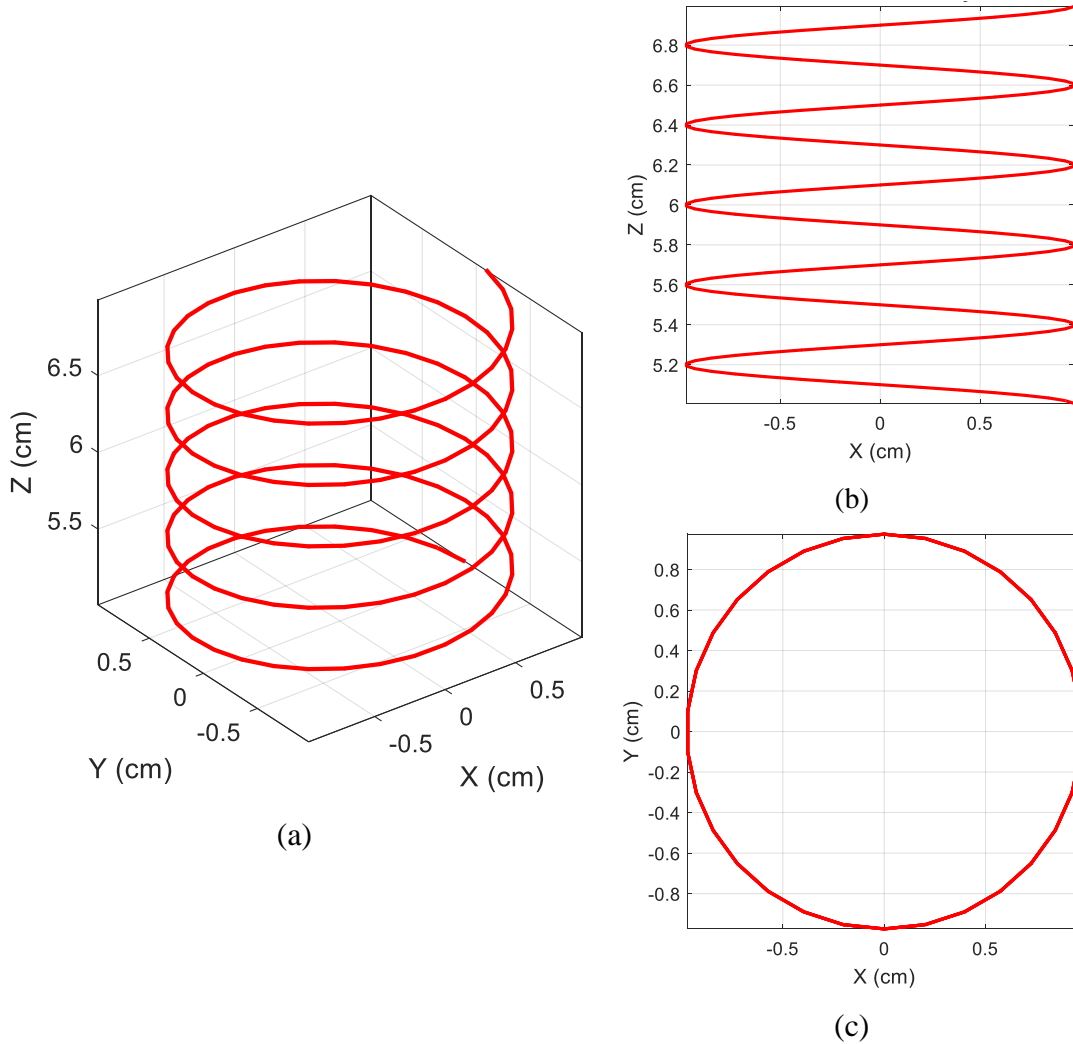


**Figure 4.2:** Geometry of the helical antenna in the Matlab, (a) Three-dimensional view, (b) Elevation view, (c) Top view,  $N_T = 4$ ,  $H = 20\text{ mm}$ ,  $D = 20\text{ mm}$ .

The electric field intensity distribution on the skin surface over the rectangular area (indicated by the dashed rectangle in Figure 4.1) is presented in Figure 4.3 using the shown color code when the operating frequency is 2.45 GHz and the input power to the helical antenna is 0 dBm. It is shown that the electric field magnitude does not exceed 7 V/m. The corresponding



power density distribution in the skin and SAR distribution in the different tissues are evaluated later on in Chapter 5. However, the calculated magnitude of the electric field on the skin is obviously low, which means low level of the SAR in the human tissues.

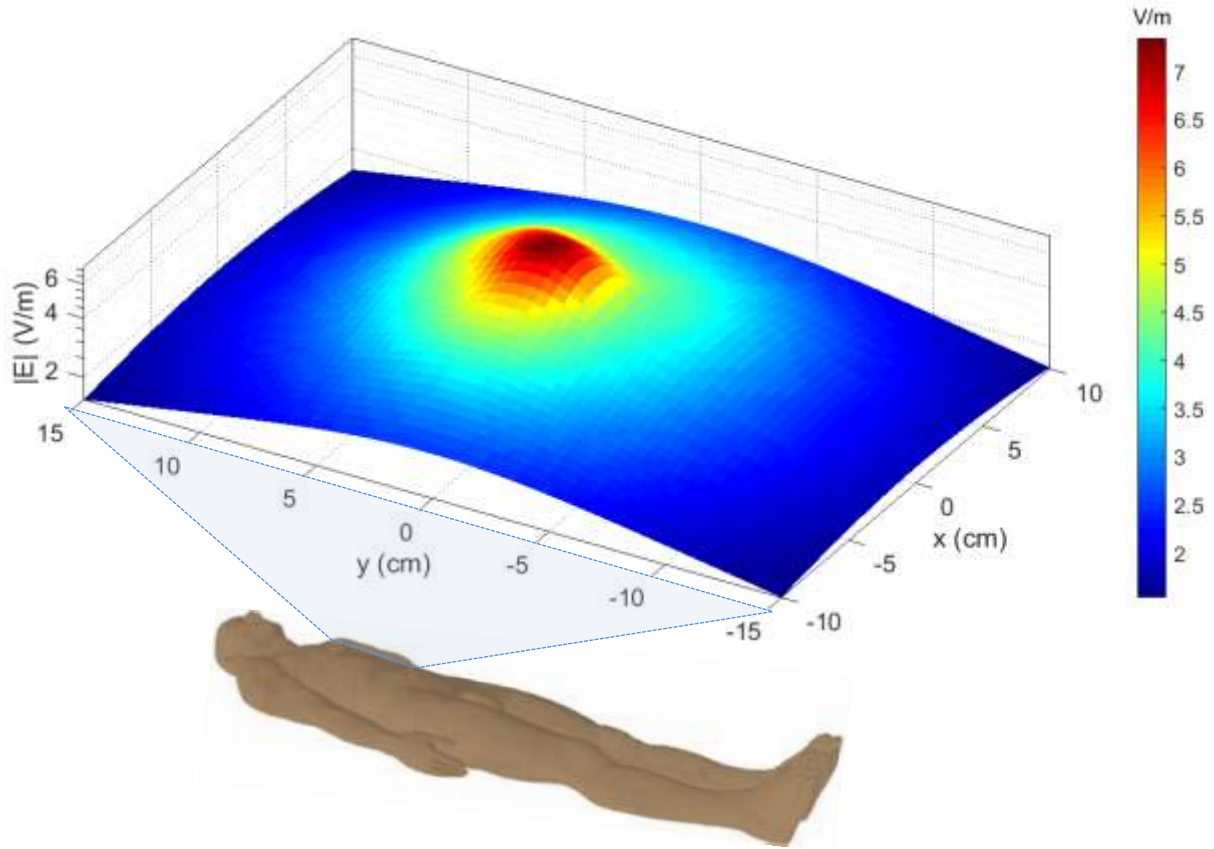


**Figure 4.3:** Distribution of the electric field magnitude in the plane of the biosensor antennas (parallel to the skin of the human body) due to a central on-body cylindrical helix antenna,  $H_H = 20 \text{ mm}$ , and  $D_H = 20 \text{ mm}$ ,  $f = 2.45 \text{ GHz}$ ,  $P_{in} = 0 \text{ dBm}$ .

#### 4.2.2. Far-Field Pattern due to Cylindrical Helix Antenna on the Human Body

The geometric model of the same cylindrical helix antenna in the CST® simulator is presented in Figure 4.4. The diameter of the circular copper plate is 4 cm. The CST simulator is used to evaluate the far-field pattern at 5.8 GHz when the input power to the antenna is 10 dBm.

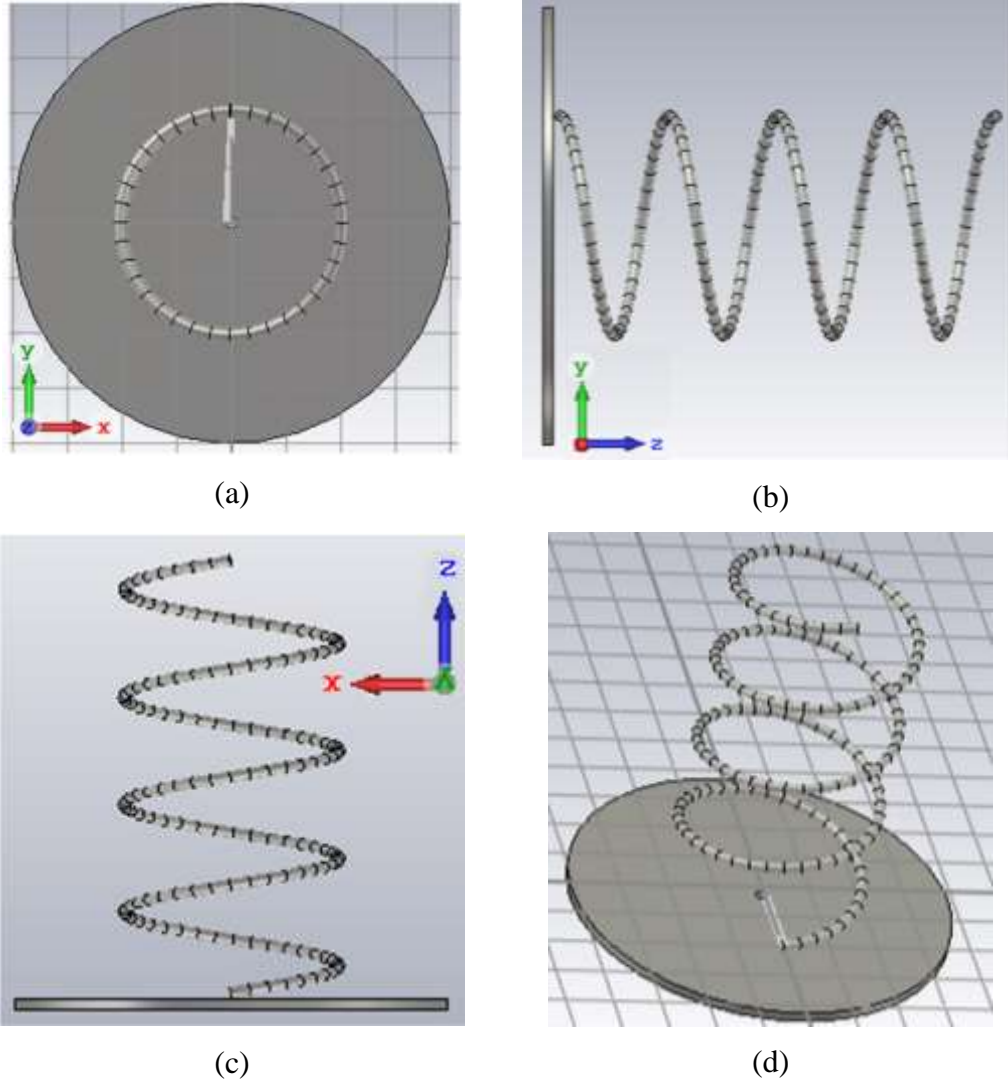


**Figure 4.4:** Geometric model of the inverted helical antenna on a circular disc in the CST® simulator, (a) Top view, (b) Side view, (c) Elevation view, (d) Three-dimensional view,  $N_T = 4$ ,  $H_H = 20 \text{ mm}$ , and  $D_H = 20 \text{ mm}$ .

The three-dimensional far-field radiation pattern of the on-body cylindrical helix antenna is presented in Figure 4.5 at 5.8 GHz for input power of 10 dBm. It is clear that the radiation pattern is directive and can be oriented towards the room ceil where the Wi-Fi antenna is mounted.

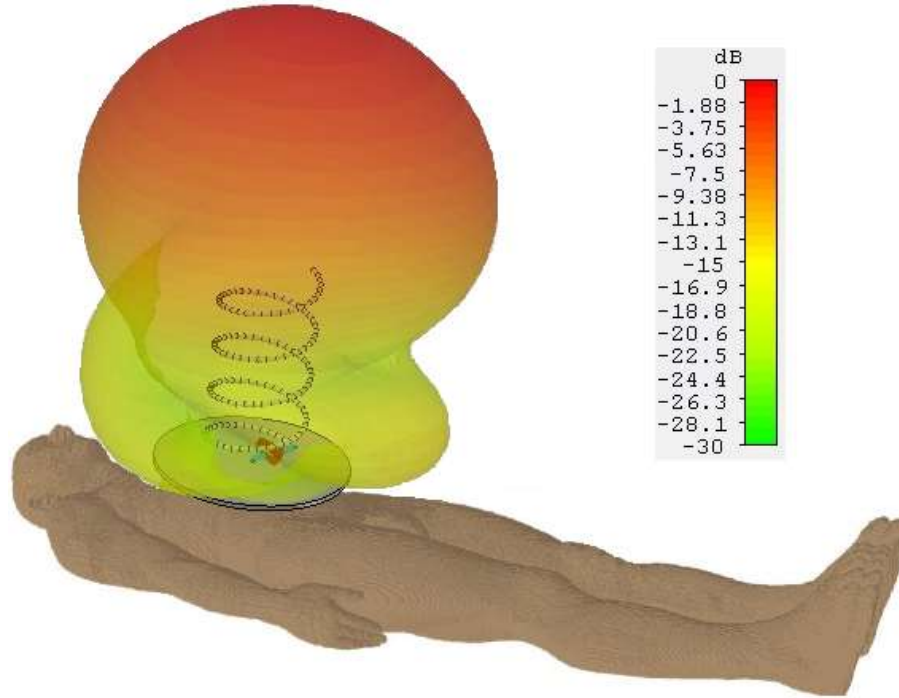


**Figure 4.5:** Three-dimensional far-field radiation pattern of a central on-body cylindrical helix antenna,  $H_H = 20 \text{ mm}$ , and  $D_H = 20 \text{ mm}$ ,  $f = 5.8 \text{ GHz}$ ,  $P_{in} = 10 \text{ dBm}$ .

The far-field radiation patterns of the right-hand and left-hand polarized electric field for the proposed on-body cylindrical helix antenna at  $f = 5.8 \text{ GHz}$  is presented in Figure 4.6 in the planes  $\phi = 0, 180^\circ$  and  $\phi = 90^\circ, 270^\circ$ . It is shown that the radiation patterns are directive and dominated by right-hand circular polarization. The dependence of the axial ratio on the frequency is presented in Figure 4.7. This antenna has a wide frequency band of the acceptable axial ratio, which is maintained below 3dB over the frequency band (3.8 – 7.8 GHz).

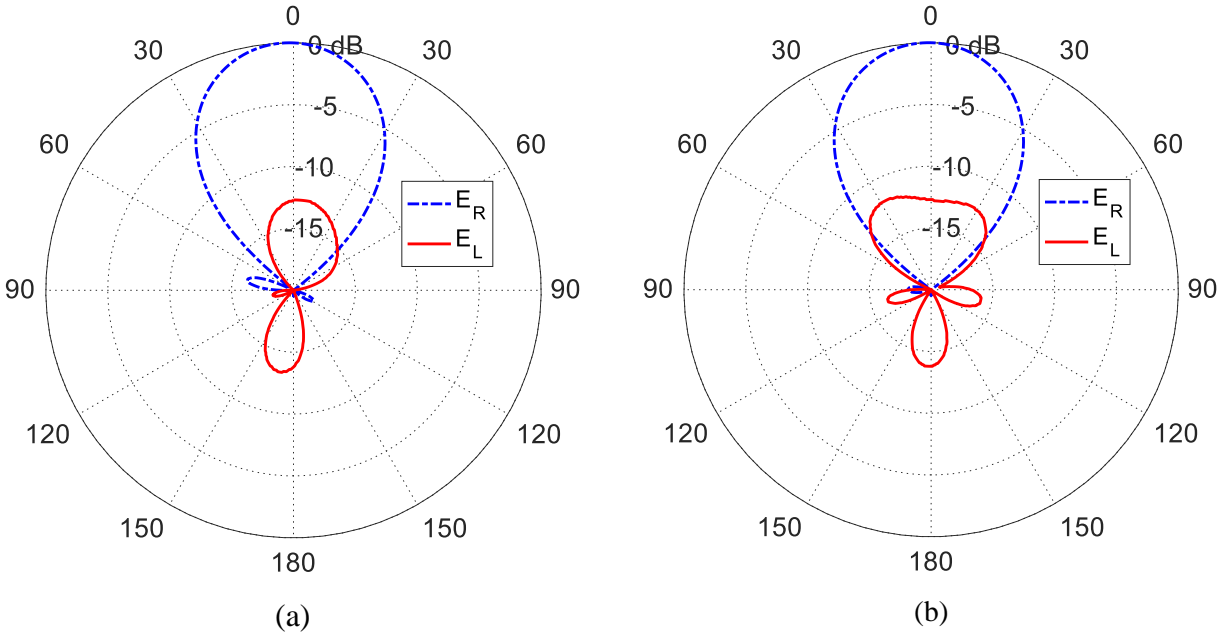


**Figure 4.6:** Far-field radiation patterns of the right-hand and left-hand polarized electric field for the proposed cylindrical helix antenna in the planes (a)  $\phi = 0, 180^\circ$  and (b)  $\phi = 90^\circ, 270^\circ$ ,  $N_T = 4$ ,  $H_H = 20$  mm,  $D_H = 20$  mm,  $f = 5.8$  GHz.

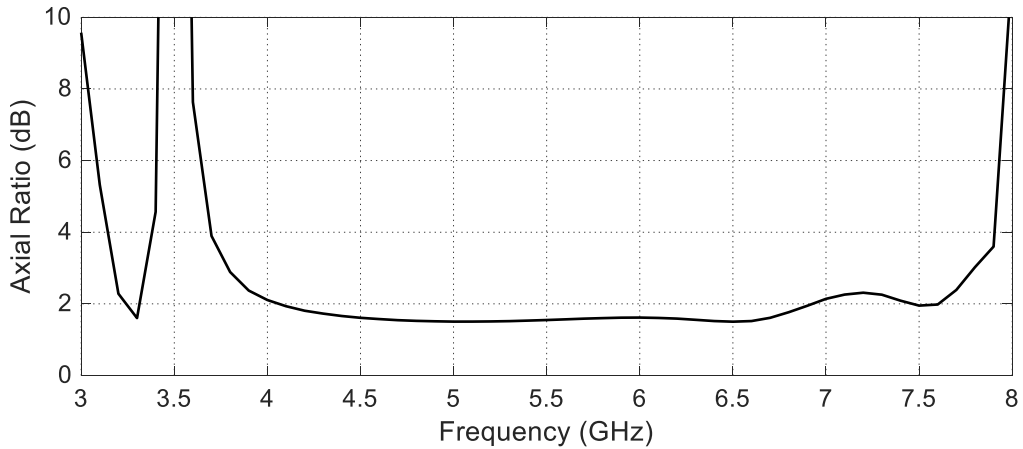


**Figure 4.7:** Frequency dependence of the axial ratio of the far-field radiated from the proposed cylindrical helix antenna in the direction  $\theta = 0$ ,  $N_T = 4$ ,  $H_H = 20$  mm,  $D_H = 20$  mm.

### 4.2.3. Near Field Distribution due to Inverted Conical Helix Antenna on the Human Body

The proposed inverted conical helix antenna has the geometric model shown in Figure 4.8 that is generated by a Matlab ® program for this purpose. This program applies the semi-analytic technique described in Chapter 4 to evaluate the near field over the body surface within the rectangular area bounded by the dashed rectangle shown in Figure 4.1. The proposed inverted conical helix has a height  $H_C = 2\text{cm}$ , half cone-angle  $\theta_0 = 26.5^\circ$ , and a diameter  $D_C = 2\text{cm}$ .

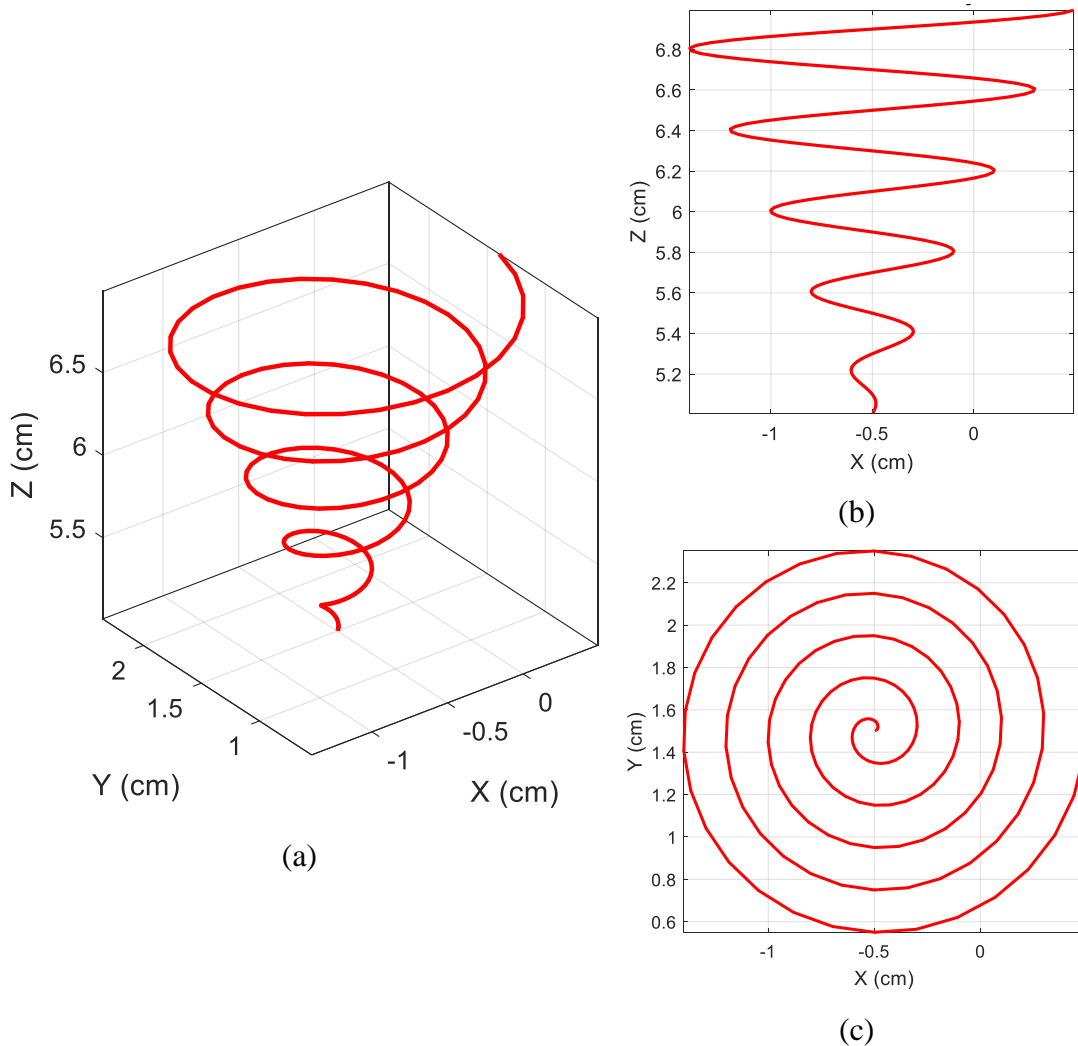


**Figure 4.8:** Geometry of the inverted conical helix antenna, (a) Three-dimensional view, (b) Elevation view, (c) Top view,  $N_T = 4$ ,  $H = 20\text{ mm}$ ,  $\theta_0 = 26.5^\circ$ ,  $D = 20\text{ mm}$ .

The electric field intensity distribution on the skin surface over the rectangular area of concern is presented in Figure 4.9 when the operating frequency is 2.45 GHz and the input power to the inverted conical helix antenna is 0 dBm. It is shown that the electric field magnitude does not exceed 5 V/m. The corresponding power density distribution on the skin and SAR distribution in the different tissues are evaluated later on in Chapter 5. However, the calculated magnitude of the electric field on the skin is obviously low, which means low level of the SAR in the human tissues.

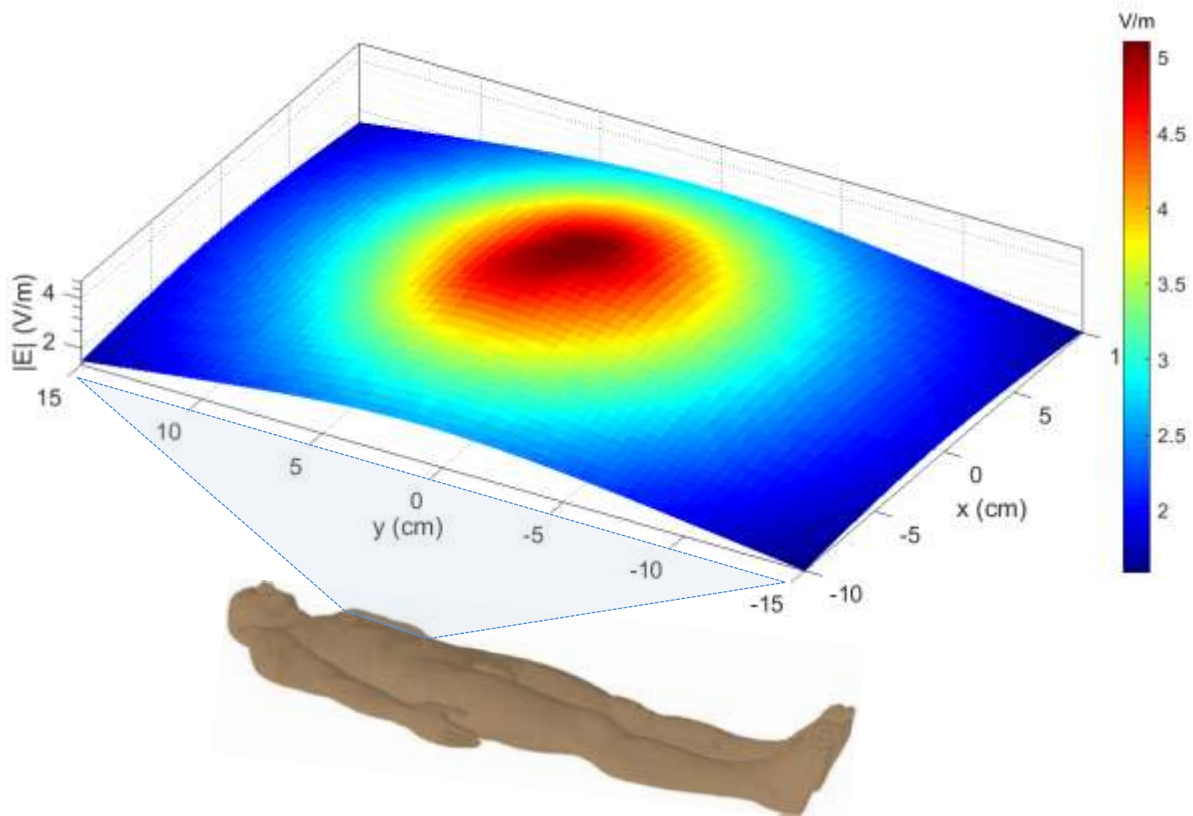


**Figure 4.9:** Electric field distribution in the plane of the biosensor antennas (parallel to the skin of the human body) due to a central on-body inverted conical helix antenna,  $N_T = 4$ ,  $H = 20$  mm, and  $D = 20$  mm,  $f = 2.45$  GHz,  $P_{in} = 0$  dBm.

#### 4.2.4. Far-Field Pattern due to Inverted Conical Helix Antenna on the Human Body

The geometric model of the same inverted conical helix antenna in the CST® simulator is presented in Figure 4.10. The diameter of the circular copper plate is 4 cm. The CST simulator is used to evaluate the far-field pattern at 5.8 GHz when the input power to the antenna is 10 dBm.

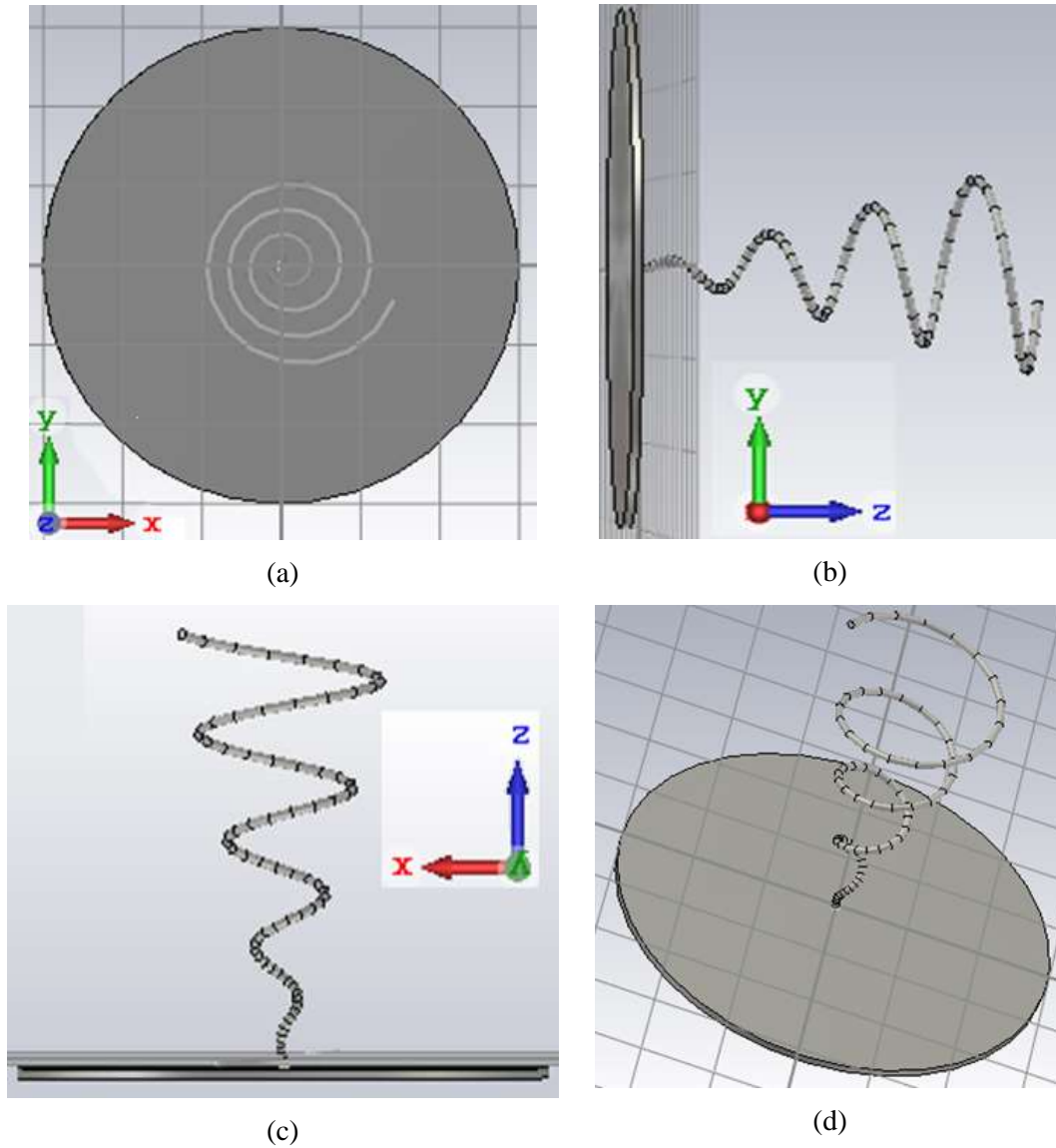


**Figure 4.10:** Geometric model of the inverted conical helix antenna on a circular disc in the CST® simulator, (a) Top view, (b) Side view, (c) Elevation view, (d) Three-dimensional view,  $N_T = 4$ ,  $H_C = 20$  mm,  $\theta_0 = 26.5^\circ$ , and  $D_C = 20$  mm.

The three-dimensional far-field radiation pattern of the on-body inverted conical helix antenna is presented in Figure 4.11 at 5.8 GHz for input power of 10 dBm. It is clear that the radiation pattern is directive and can be oriented towards the room ceil where the Wi-Fi antenna is mounted.



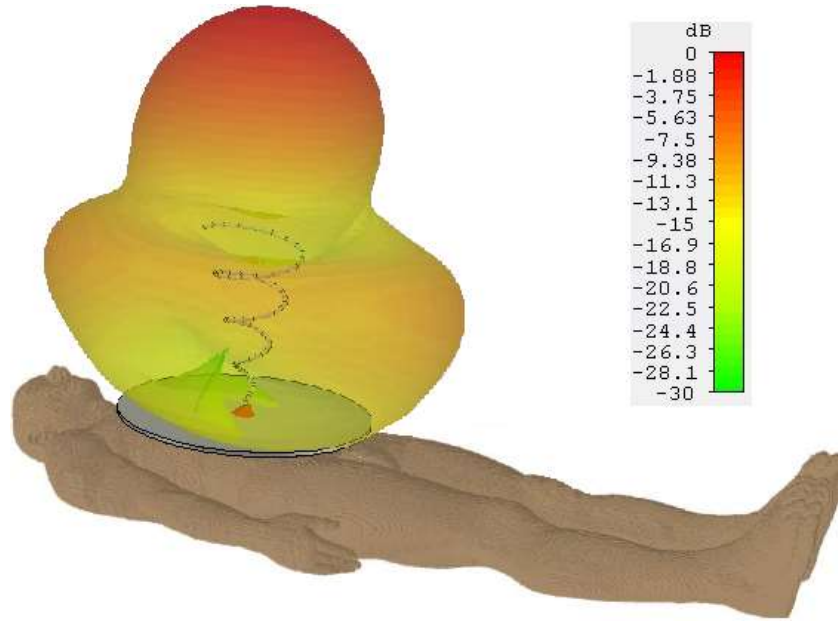


**Figure 4.11:** Three-dimensional far-field radiation pattern a central on-body conical helix antenna,  $H_C = 20 \text{ mm}$ ,  $\theta_0 = 26.5^\circ$ ,  $D_C = 20 \text{ mm}$ ,  $f = 5.8 \text{ GHz}$ ,  $P_{in} = 10 \text{ dBm}$ .

The far-field radiation patterns of the right-hand and left-hand polarized electric field for the proposed on-body inverted conical helix antenna at  $f = 5.8 \text{ GHz}$  is presented in Figure 4.12 in the planes  $\phi = 0, 180^\circ$  and  $\phi = 90^\circ, 270^\circ$ . It is shown that the radiation patterns are directive and dominated by right-hand circular polarization. The dependence of the axial ratio on the frequency is presented in Figure 4.13. This antenna has a wide frequency band of the acceptable axial ratio, which is maintained below 3dB over the frequency band (4.2 – 8.0 GHz).



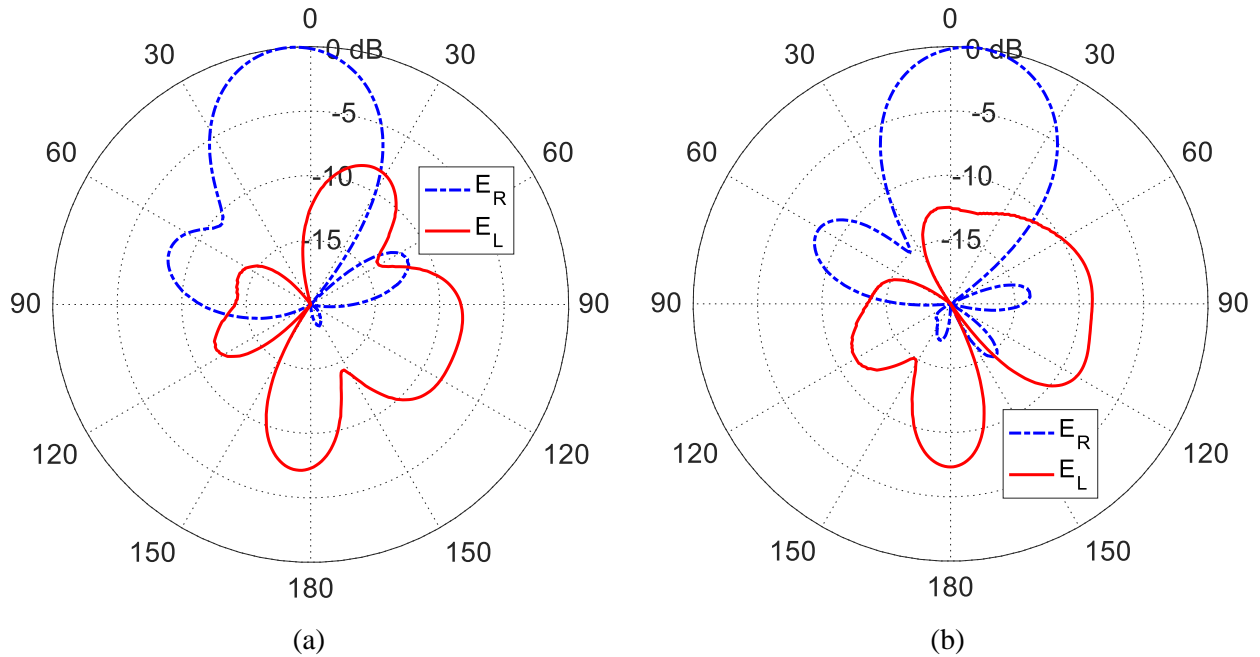


**Figure 4.12:** Far-field radiation patterns of the right-hand and left-hand polarized electric field for the proposed conical helix antenna in the planes (a)  $\phi = 0, 180^\circ$  and (b)  $\phi = 90^\circ, 270^\circ$ ,  $N_T = 4$ ,  $H_C = 20 \text{ mm}$ ,  $\theta_0 = 26.5^\circ$ ,  $D_C = 20 \text{ mm}$ ,  $f = 5.8 \text{ GHz}$ ,  $P_{in} = 10 \text{ dBm}$ .

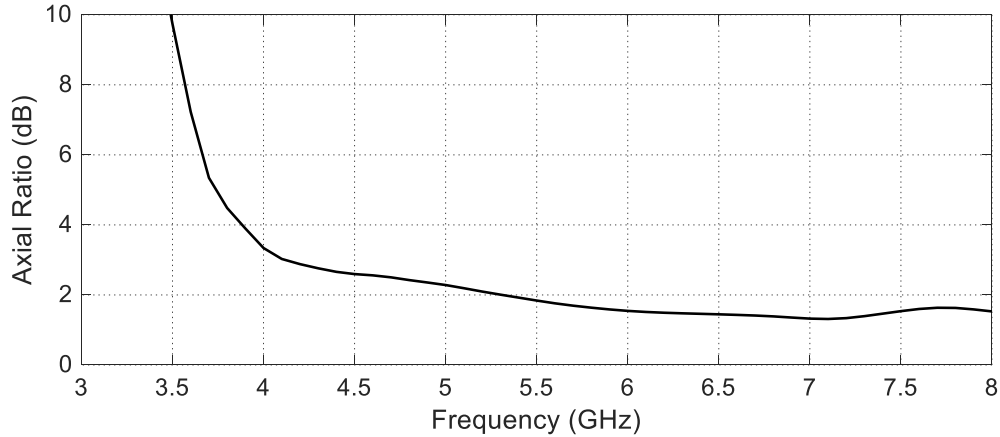


**Figure 4.13:** Frequency dependence of the axial ratio of the far-field radiated from the proposed inverted conical helix antenna in the direction  $\theta = 0$ ,  $N_T = 4$ ,  $H_C = 20 \text{ mm}$ ,  $\theta_0 = 26.5^\circ$ ,  $D_C = 20 \text{ mm}$ ,  $f = 5.8 \text{ GHz}$ ,  $P_{in} = 10 \text{ dBm}$ .

### 4.2.5. Near Field Distribution due to Conical Helix Antenna on the Human Body

The proposed conical helix antenna has the geometric model shown in Figure 4.14 that is generated by a Matlab ® program for this purpose. This program applies the semi-analytic technique described in Chapter 4 to evaluate the near field over the body surface within the rectangular area bounded by the dashed rectangle shown in Figure 4.1. The proposed conical helix has a height  $H_C = 2\text{cm}$ , half cone-angle  $\theta_0 = 26.5^\circ$ , and a diameter  $D_C = 2\text{cm}$ .

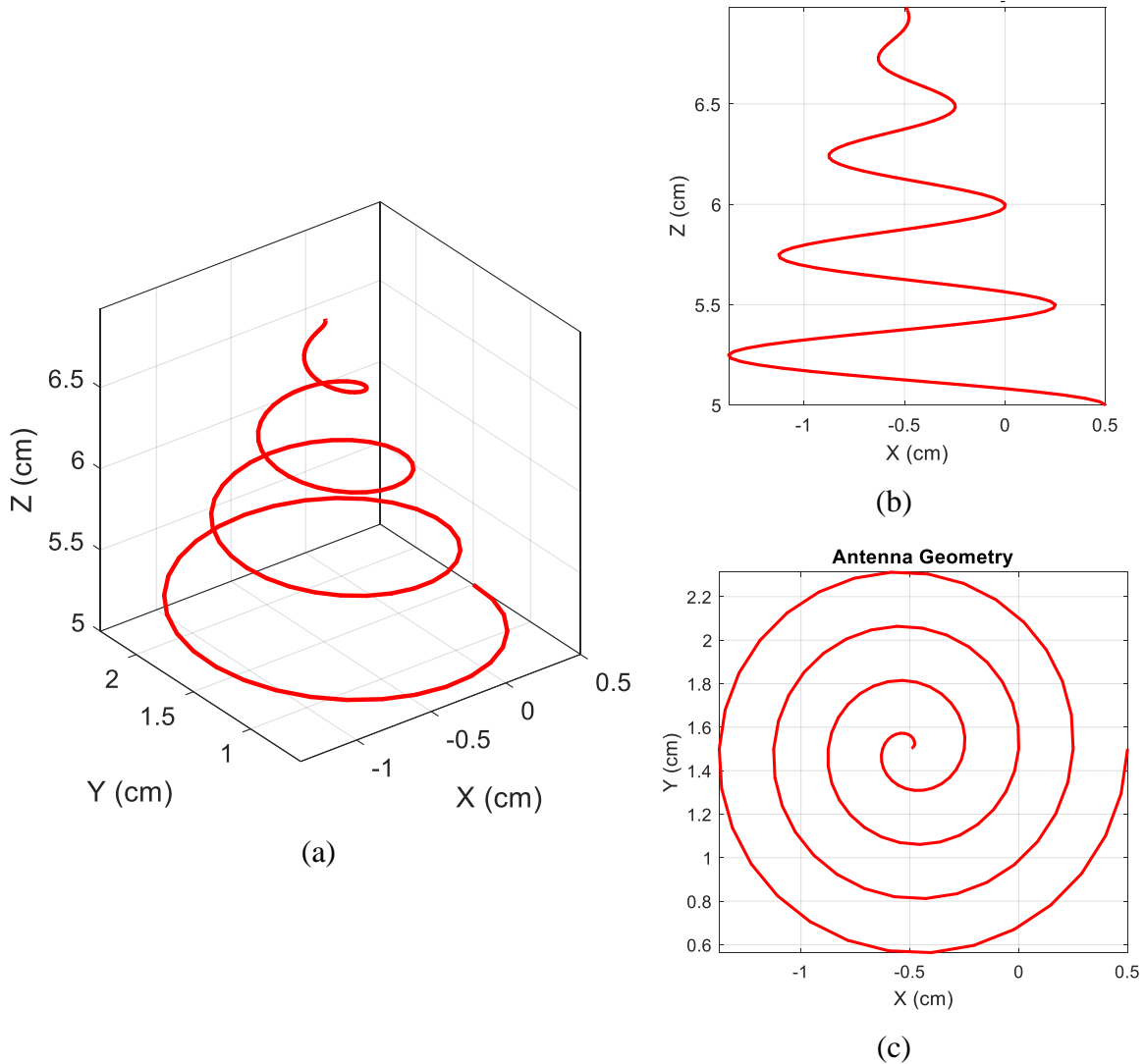


**Figure 4.14:** Geometry of the conical helix antenna, (a) Three-dimensional view, (b) Elevation view, (c) Top view,  $N_T = 4$ ,  $H = 20\text{ mm}$ ,  $\theta_0 = 26.5^\circ$ ,  $D = 20\text{ mm}$ .

The electric field intensity distribution on the skin surface over the rectangular area of concern is presented in Figure 4.15 when the operating frequency is 2.45 GHz and the input power to the conical helix antenna is 0 dBm. It is shown that the electric field magnitude does not exceed 5.5 V/m. The corresponding power density distribution on the skin and SAR distribution in the different tissues are evaluated later on in Chapter 5. However, the calculated magnitude of the electric field on the skin is obviously low, which means low level of the SAR in the human tissues.

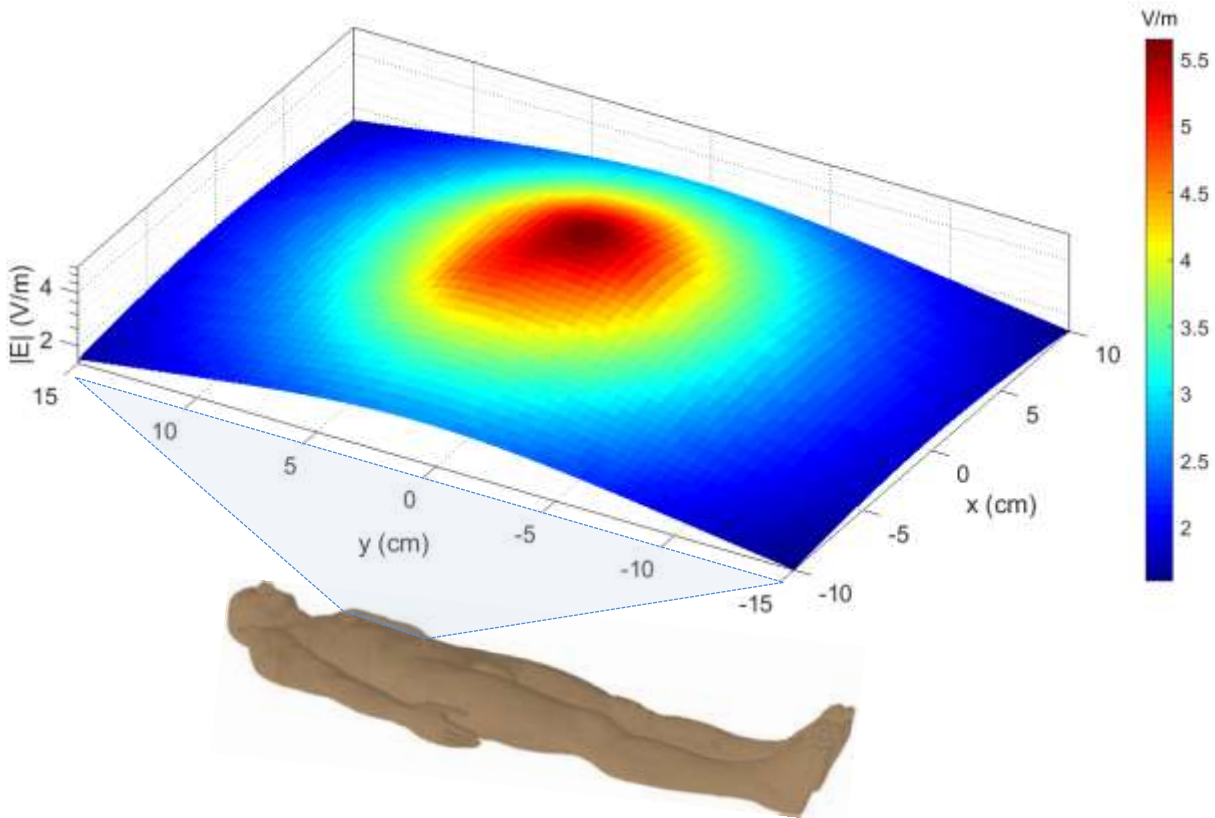


**Figure 4.15:** Electric field distribution in the plane of the biosensor antennas (parallel to the skin of the human body) due to a central on-body conical helix antenna,  $N_T = 4$ ,  $H_C = 20$  mm,  $\theta_0 = 26.5^\circ$ ,  $D_C = 20$  mm.

#### 4.2.6. Far-Field Pattern due to Conical Helix Antenna on the Human Body

The geometric model of the same conical helix antenna in the CST® simulator is presented in Figure 4.16. The diameter of the circular copper plate is 4 cm. The CST simulator is used to evaluate the far-field pattern at 5.8 GHz when the input power to the antenna is 10 dBm.

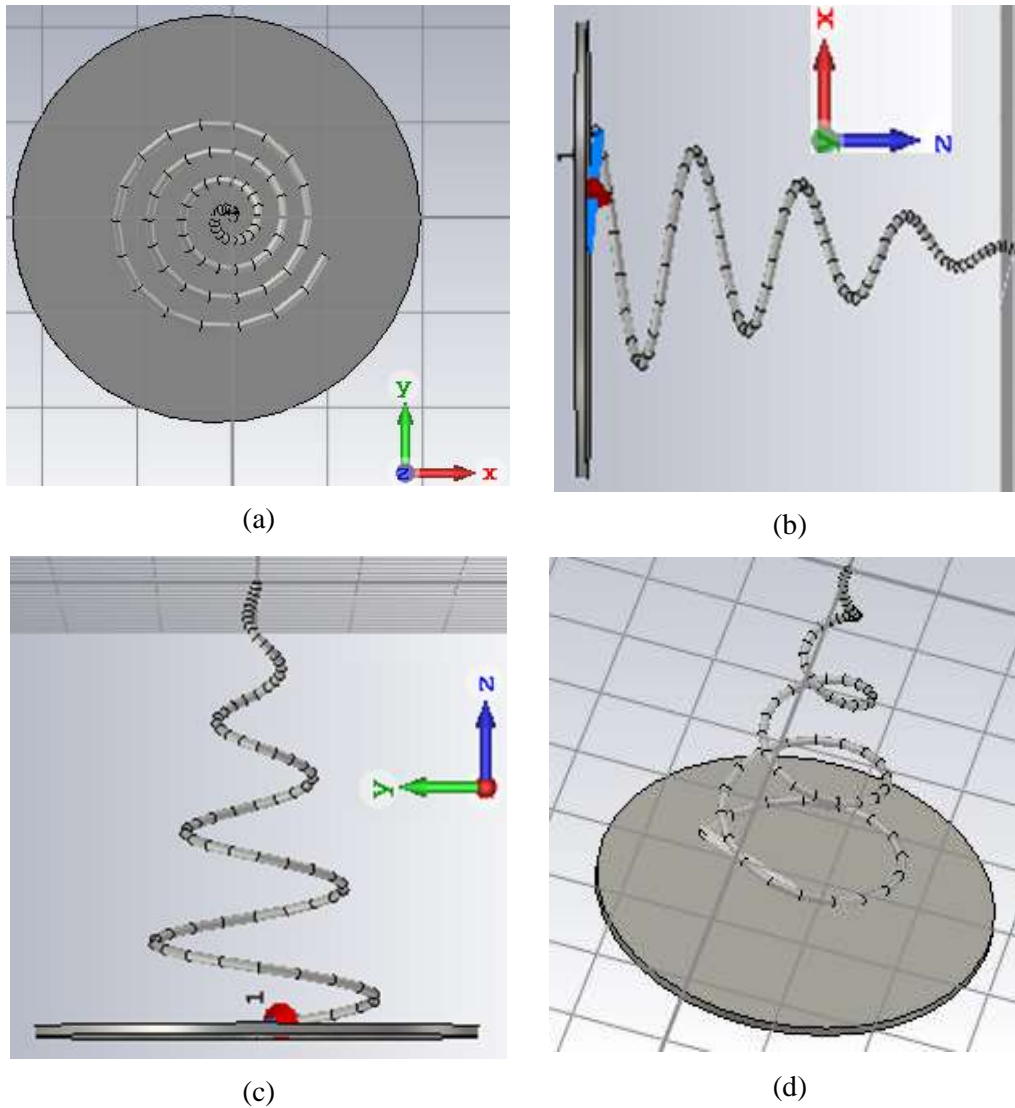


**Figure 4.16:** Geometric model of the inverted helical antenna on a circular disc in the CST® simulator, (a) Top view, (b) Side view, (c) Elevation view, (d) Three-dimensional view,  $N_T = 4$ ,  $H_H = 20$  mm, and  $D_H = 20$  mm.

The three-dimensional far-field radiation pattern of the on-body cylindrical helix antenna is presented in Figure 4.5 at 5.8 GHz for input power of 10 dBm. It is clear that the radiation pattern is directive and can be oriented towards the room ceil where the Wi-Fi antenna is mounted.

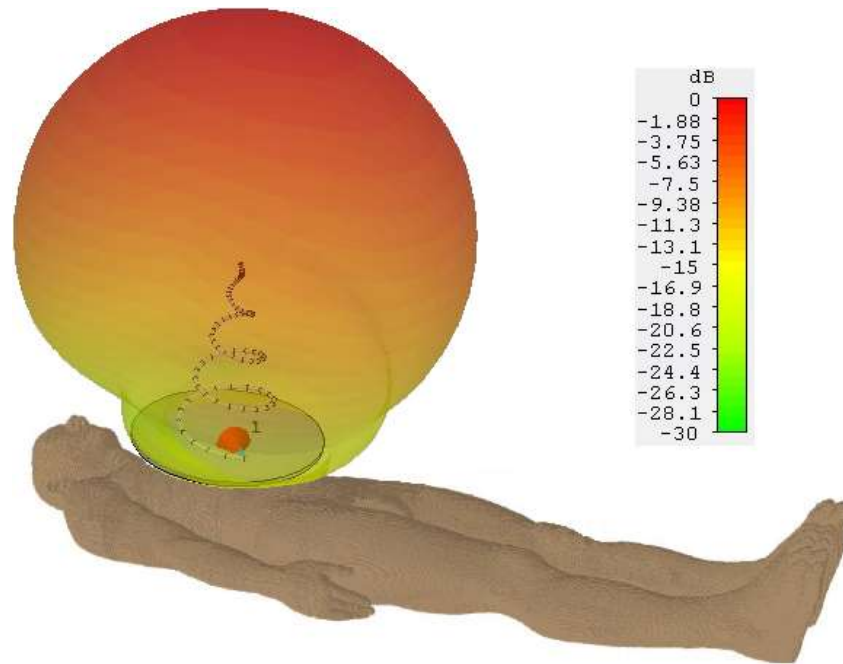


**Figure 4.17:** Three-dimensional far-field radiation pattern a central on-body conical helix antenna,  $H_c = 20 \text{ mm}$ ,  $\theta_0 = 26.5^\circ$ ,  $D_c = 20 \text{ mm}$ ,  $f = 5.8 \text{ GHz}$ ,  $P_{in} = 10 \text{ dBm}$ .

The far-field radiation patterns of the right-hand and left-hand polarized electric field for the proposed on-body conical helix antenna at  $f = 5.8 \text{ GHz}$  is presented in Figure 4.18 in the planes  $\phi = 0, 180^\circ$  and  $\phi = 90^\circ, 270^\circ$ . It is shown that the radiation patterns are directive and dominated by right-hand circular polarization. The dependence of the axial ratio on the frequency is presented in Figure 4.19. This antenna has a wide frequency band of the acceptable axial ratio, which is maintained below 3dB over the frequency band (4.2 – 8.0 GHz).

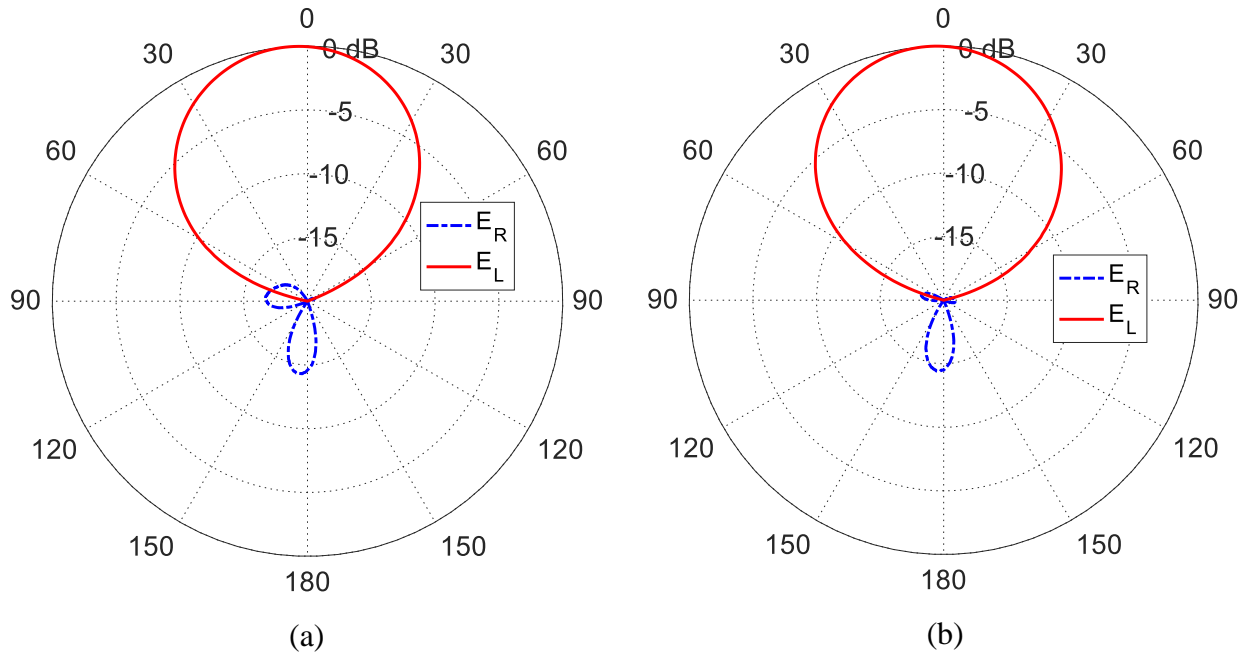


**Figure 4.18:** Far-field radiation patterns of the right-hand and left-hand polarized electric field for the proposed conical helix antenna in the planes (a)  $\phi = 0, 180^\circ$  and (b)  $\phi = 90^\circ, 270^\circ$ ,  $N_T = 4$ ,  $H_C = 20$  mm,  $\theta_0 = 26.5^\circ$ ,  $D_C = 20$  mm,  $f = 5.8$  GHz,  $P_{in} = 10$  dBm.

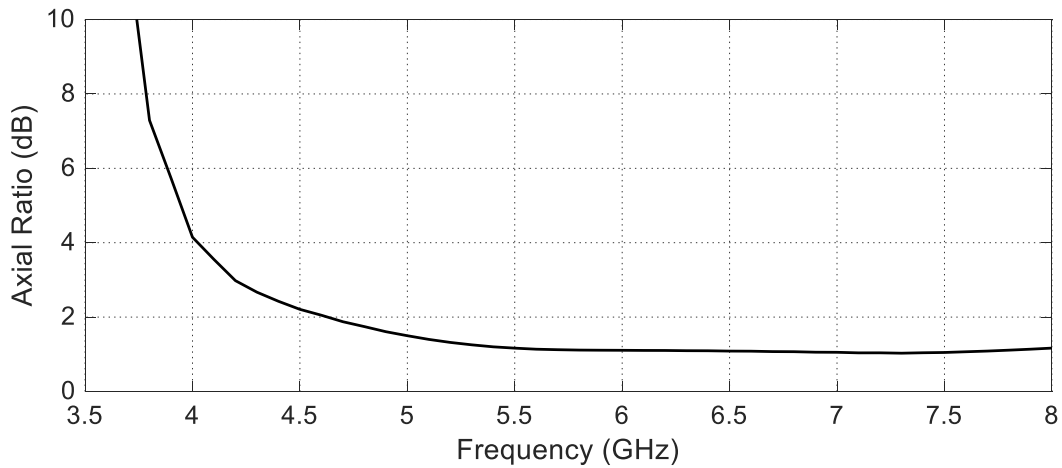


**Figure 4.19:** Frequency dependence of the axial ratio of the far-field radiated from the proposed inverted conical helix antenna in the direction  $\theta = 0$ ,  $N_T = 4$ ,  $H_C = 20$  mm,  $\theta_0 = 26.5^\circ$ ,  $D_C = 20$  mm,  $f = 5.8$  GHz,  $P_{in} = 10$  dBm.

### 4.3. Experimental Measurements and Discussions

For experimental assessment of the proposed types of on-body helical antennas, a prototype is fabricated for each type. The reflection coefficient at the antenna port is measured using vector network analyzer (VNA) of the Agilent Field Fox N9918A. The far-field radiation patterns are measured using the same VNA and a reference right-hand circularly polarized horn antenna.

#### 4.3.1. Fabrication of the On-Body Helical Antenna Prototypes

For the fabrication of each antenna, a copper wire is wrapped, mounted on a circular copper plate, connected to an SMA connector, an impedance matching element is added, and finally the wire antenna is covered with a hemispherical radome of very thin dielectric which is almost transparent to microwaves. An example is shown in Figure 4.20.

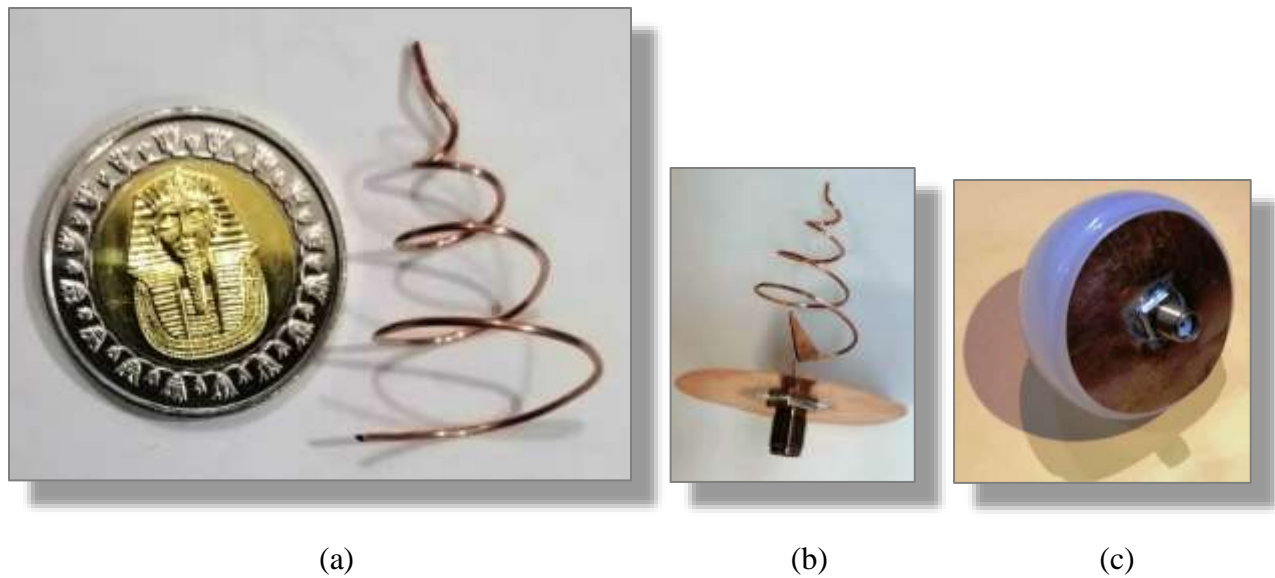


**Figure 4.20:** The conical helix antenna proposed to play the role of a central on-body antenna for on-body biosensor antenna network (a) Shape and relative size of the wire antenna, (b) The antenna mounted on a circular copper disc and connected to an SMA connector and an impedance matching element is added, (c) The wire antenna is covered with a microwave-transparent hemispherical radome.

##### 4.3.1.1. Wrapping the Wire of the Proposed Helical Antennas

The first stage of fabricating each of the proposed helical antennas is to wrap the wire as shown in Figure 4.21. A wire wrapped in the right-hand sense as the wires at the bottom of



Figure 4.21 produces right-hand circularly polarized field whereas a wire wrapped in the left-hand sense as the wires at the top of Figure 4.21 produces left-hand circularly polarized field.

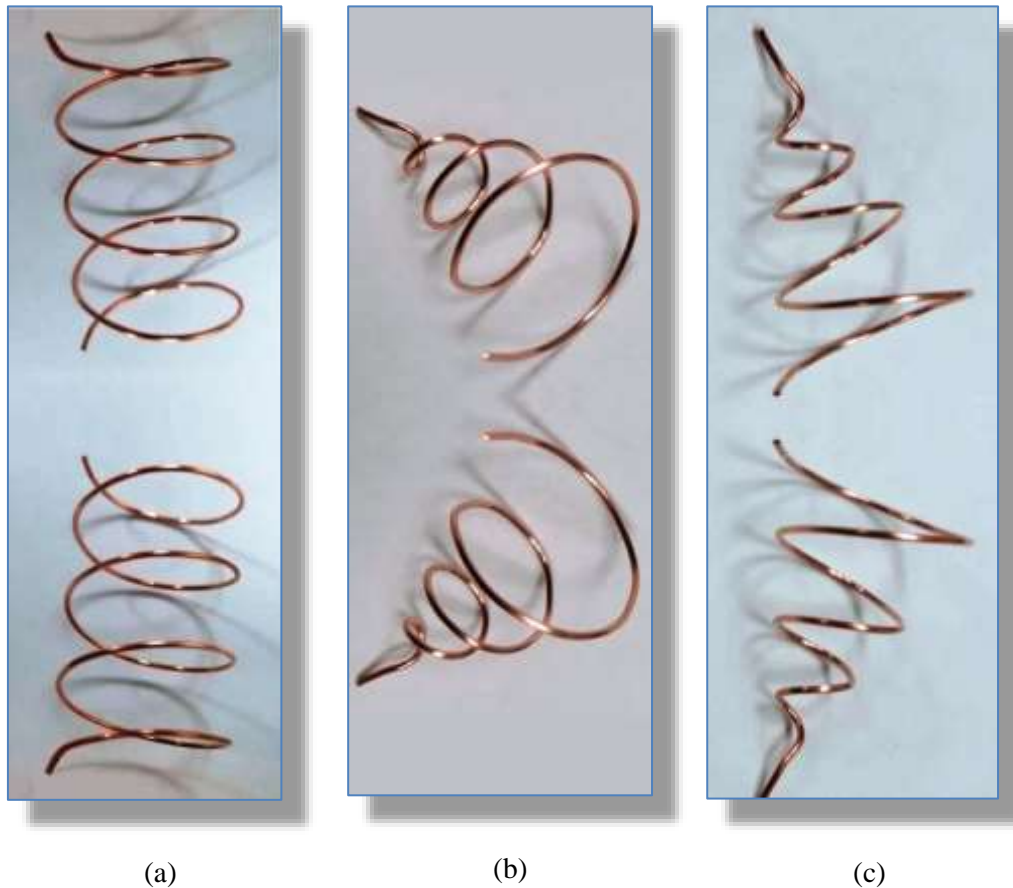


**Figure 4.21:** Fabricated wires for the three types of medical antennas. The upper antennas are Left-hand circularly polarized whereas the lower antennas are right-hand circularly polarized, (a) Helical antenna, (b) Conical helix antenna, (c) Inverted conical helix antenna.

#### 4.3.1.2. Mounting the Wrapped Wire antenna on a Circular Conducting Plate

A ground plane and a feeding coaxial connector are necessary for the operation of such monopole helical antennas. A circular copper disc of 4 cm diameter is prepared for this purpose and an SMA coaxial connector is mounted with its outer conductor welded to the circular disc as shown in Figure 4.22.

One of the terminals of the wrapped helical wire is welded to the inner conductor the SMA connector shown in Figure 4.22(b). The three types of the wrapped helical wires after being



mounted on the circular copper disc and welded to the SMA inner conductor are shown in Figure 4.23.

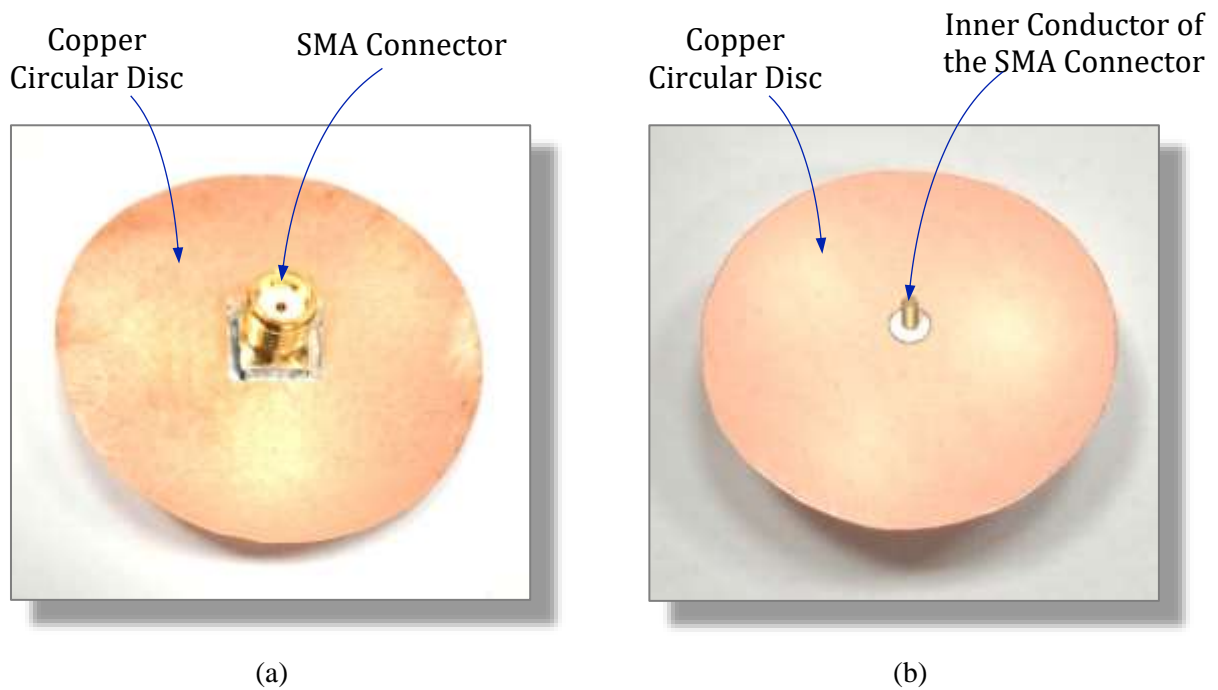


**Figure 4.22:** Fabricated copper circular disc to act as a ground base for the three types of helical antennas with a mounted SMA connector, (a) Bottom view, (b) Top view.



**Figure 4.23:** The fabricated prototypes of the three proposed helical antennas mounted on a circular copper disc with SMA connector for feeding (without being covered by the radome).

#### 4.3.1.3. Adding Impedance Matching Elements to the Antenna Structure

The wire antenna should be matched with the  $50\Omega$  SMA coaxial connector. The wire helix antennas are characterized by an advantage of low imaginary part of the input impedance at the design frequency for end-fire radiations. Unfortunately, they are, also, characterized by a resistive part of the impedance that is much smaller than  $50\Omega$ . The real part of the impedance can be increased to  $50\Omega$  by attaching a small conductive patch of rectangular or triangular shape to the wire of the antenna near the feed point as shown in Figures 4.24, 4.25, and 4.26 for the three types of helical antennas. The shape, size and location of such a patch for impedance matching can be properly attached to the helical wire with the aid of a VNA.



(a)



(b)

**Figure 4.24:** The cylindrical helix antenna mounted on a circular copper disc and connected to the inner conductor of an SMA connector (a) without impedance matching, (b) with a strip patch connected near the feed point for impedance matching.



(a)



(b)

**Figure 4.25:** The inverted conical helix antenna mounted on a circular copper disc and connected to the inner conductor of an SMA connector (a) without impedance matching, (b) with a triangular patch connected near the feed point for impedance matching.

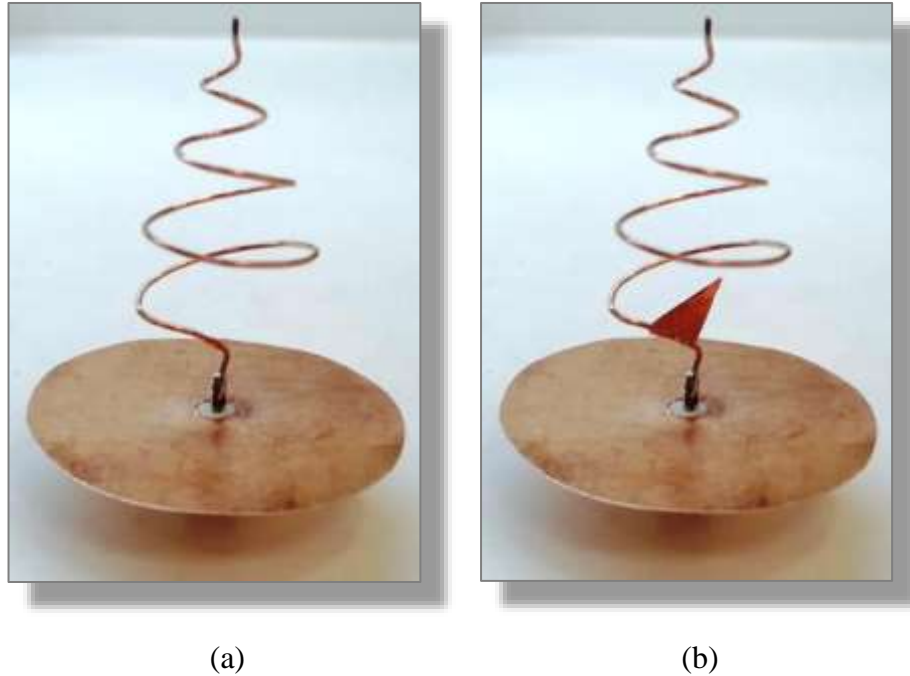


**Figure 4.26:** The conical helix antenna mounted on a circular copper disc and connected to the inner conductor of an SMA connector (a) without impedance matching, (b) with a triangular patch connected near the feed point for impedance matching.

#### 4.3.1.4. Covering the Wire Antennas with Radoms

For protecting the wrapped wires of the fabricated helical antennas from deformation due to unavoidable mechanical stresses, a hemispherical Radom of very thin dielectric material is used to cover each antenna as shown in Figure 4.27. As this radome is very thin, it is almost electromagnetically transparent at the microwave frequencies and, consequently, has no effect on the helical antenna characteristics. The wire antennas for the three fabricated prototypes are partially uncovered and connected to coaxial cables as shown in Figures 4.28, 4.29, and 4.30.



**Figure 4.27:** The fabricated prototypes of the three proposed helical antennas mounted on a circular copper disc and covered by hemispherical radome with SMA feeding connector.



**Figure 4.28:** The matched cylindrical helix antenna on a copper circular disc with SMA connector is being covered with hemispherical radome.



**Figure 4.29:** The matched inverted conical helix antenna on a copper circular disc with SMA connector is being covered with hemispherical radome.



**Figure 4.30:** The matched conical helix antenna on a copper circular disc with SMA connector is being covered with hemispherical radome.

Finally, for measurement purposes, the antenna prototypes are connected to flexible 50Ω coaxial cables as shown in Figure 4.31.



**Figure 4.31:** The final form of the proposed on-body medical antenna connected to a coaxial cable for the purpose of experimental measurements.

### **4.3.2. Experimental Assessment of the Proposed Antenna Performance**

The three fabricated prototypes of the proposed helical antennas are experimentally characterized. For each antenna type, the frequency response of the reflection coefficient  $|S_{11}|$  is measured over a wide range of the frequency. Also, the far-field radiation patterns are measured and compared to the radiation patterns obtained by electromagnetic simulation using the commercially available CST microwave studio suite.

#### **4.3.2.1. Measurement of the Reflection Coefficient of the Cylindrical Helix Antenna**

The experimental setup for measuring the frequency response of the reflection coefficient  $|S_{11}|$  of the cylindrical helix antenna is shown in Figure 4.32. As shown when comparing Figure 4.32(a) to 4.32(b), the reflection coefficient seems to be almost unaffected by the placement of the radome to cover the cylindrical helix antenna.





(a)

(b)

**Figure 4.32:** Measurement of the reflection coefficient  $|S_{11}|$  of the helical antenna using the VNA of the Agilent Field Fox N9918A, (a) The uncovered antenna, (b) The antenna covered with the hemispherical radome.

Figure 4.33 presents the measured frequency responses of the reflection coefficient  $|S_{11}|$  of the cylindrical helix antenna to show the improvement of the return loss over the operational frequency band due to the addition of the matching strip patch element to the wrapped wire near the feeding port. Also, it is shown that the placement of the antenna on the human body leads to a significant shift of the frequency band of matched impedance of the cylindrical helix antenna towards the higher frequencies, which makes it more appropriate for the frequency band of the Wi-Fi.



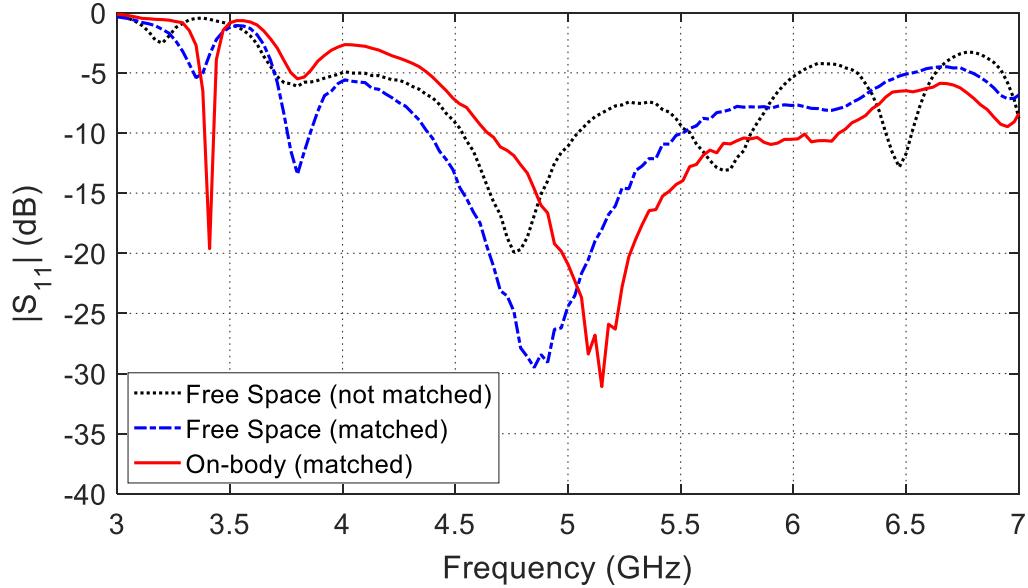


**Figure 4.33:** Measured frequency response of the reflection coefficient  $|S_{11}|$  of the cylindrical helix antenna showing the effect of adding the matching element and the placement of the antenna on the human body.

#### 4.3.2.2. Measurement of the Reflection Coefficient of the Inverted Conical Helix Antenna

The experimental setup for measuring the frequency response of the reflection coefficient  $|S_{11}|$  of the inverted conical helix antenna is shown in Figure 4.34. When comparing Figure 4.34(a) to 4.34(b), it becomes clear that the reflection coefficient of the inverted conical helix antenna is almost unaffected by the placement of the radome over the entire frequency range.

Figure 4.35 presents the measured frequency responses of the reflection coefficient  $|S_{11}|$  of the inverted conical helix antenna to show the improvement of the return loss over the operational frequency band due to the addition of the matching triangular patch element to the wrapped wire near the feeding port. Also, it is shown that the placement of the antenna on the human body leads to improve the return loss of the inverted conical helix antenna with a slight shift of the frequency band of matched impedance.



(a)



(b)

**Figure 4.34:** Measurement of the reflection coefficient  $|S_{11}|$  of the inverted conical helix antenna using the VNA of the Agilent Field Fox N9918A (a) The uncovered antenna, (b) The antenna covered with the hemispherical radome.

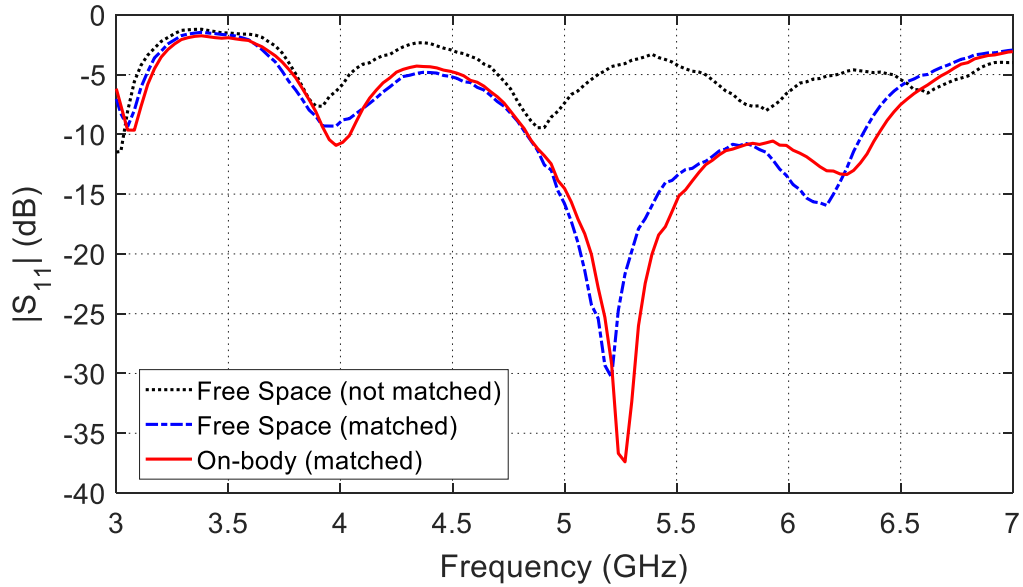


**Figure 4.35:** Measured frequency response of the reflection coefficient  $|S_{11}|$  of the inverted conical helix antenna showing the effect of adding the matching element and the placement of the antenna on the human body.

#### 4.3.2.3. Measurement of the Reflection Coefficient of the Conical Helix Antenna

The experimental setup for measuring the frequency response of the return loss  $|S_{11}|$  of the conical helix antenna is shown in Figure 4.36. When comparing Figure 4.36(a) to 4.36(b), it becomes clear that the return loss of the conical helix antenna over the entire frequency range is almost unaffected by the placement of the radome.



(a)



(b)

**Figure 4.36:** Measurement of the reflection coefficient  $|S_{11}|$  of the conical helix antenna using the VNA of the Agilent Field Fox N9918A, (a) The uncovered antenna, (b) The antenna covered with the hemispherical radome.

Figure 4.37 presents the measured frequency responses of the reflection coefficient  $|S_{11}|$  of the conical helix antenna to show the improvement of the return loss over the operational frequency band due to the addition of the matching triangular patch element to the wrapped wire near the feeding port. Also, it is shown that the placement of the antenna on the human body leads to improve the return loss of the inverted conical helix antenna with a slight shift of the frequency band of matched impedance.

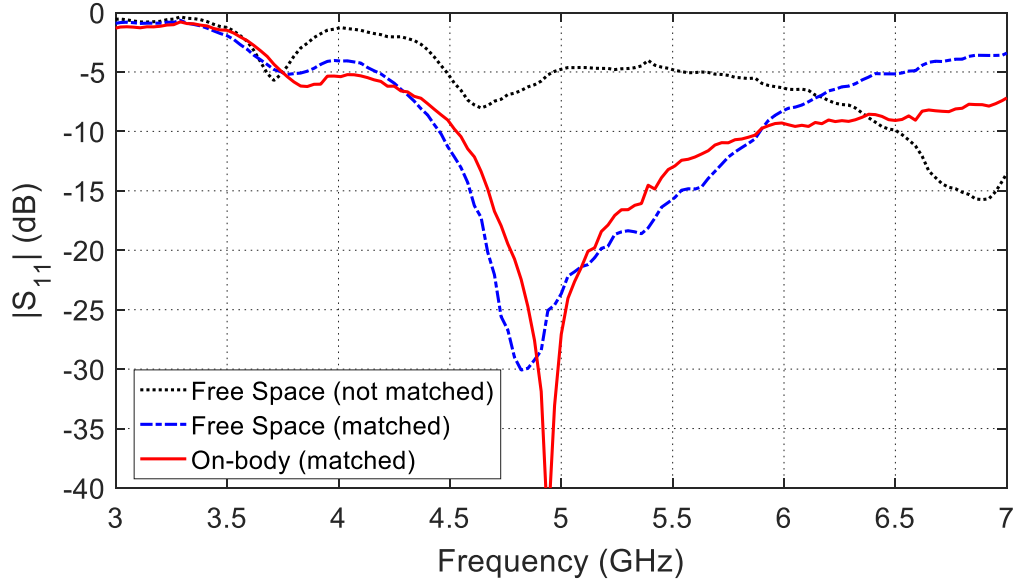


**Figure 4.37:** Measured frequency response of the reflection coefficient  $|S_{11}|$  of the conical helix antenna showing the effect of adding the matching element and the placement of the antenna on the human body.

#### 4.3.2.4. Measurement of the Radiation Pattern of the Cylindrical Helix Antenna

The experimental setup for measuring the radiation patterns of the proposed on-body helical antennas using the VNA of the Agilent Field Fox N9918A is shown in Figure 4.38. A reference right-hand circularly polarized helical antenna is connected to port ‘2’ of the VNA whereas the helical antenna under test is connected to port ‘1’ to obtain its radiation pattern by measuring the transmission coefficient  $|S_{21}|$  at 5.8 GHz.

The measured radiation patterns of right-hand circularly polarized field of the cylindrical helix antenna in the elevation planes  $\phi = 0, 180^\circ$  and  $\phi = 90^\circ, 270^\circ$  are presented in Figure 4.39 in comparison to the radiation pattern obtained by the CST simulator for the same antenna model. The measured radiation patterns of the cylindrical helix antenna show good agreement with those obtained by simulation.



**Figure 4.38:** Experimental setup for measuring the radiation pattern of the proposed on-body helical antennas using the VNA of the Agilent Field Fox N9918A.

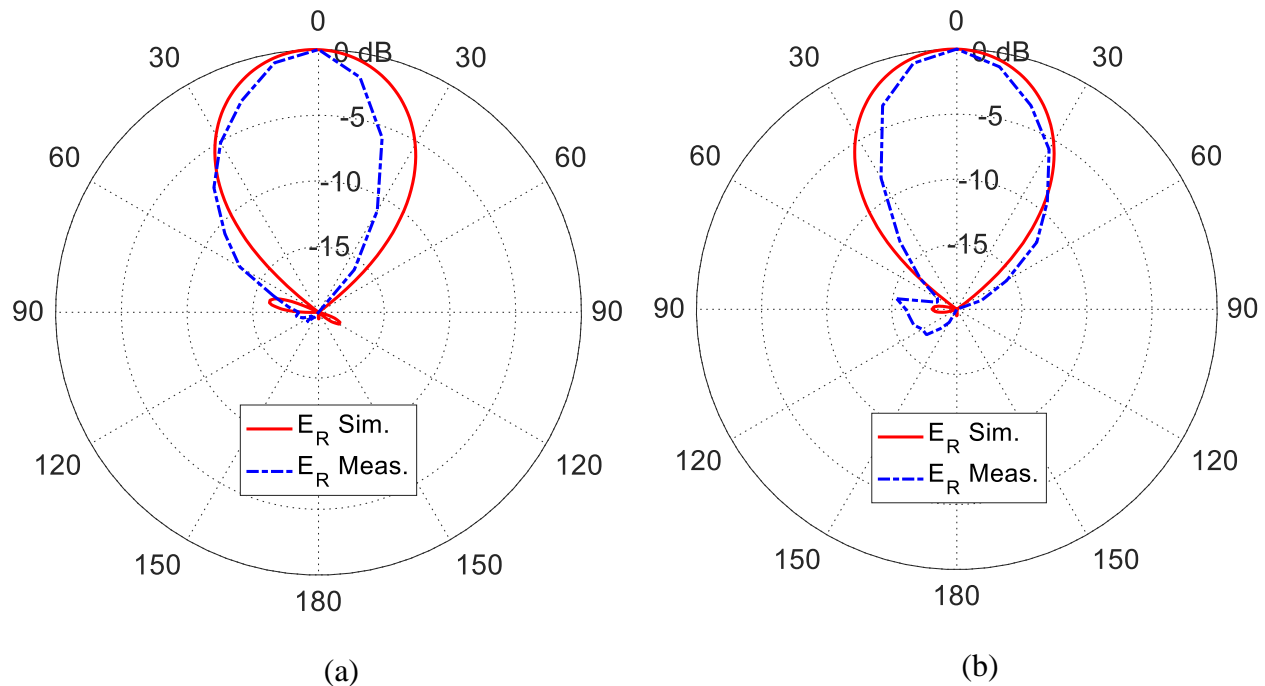


**Figure 4.39:** Comparison between the simulated and measured far-field radiation patterns of the right-hand circular polarization for the cylindrical helix antenna in the planes (a)  $\phi = 0, 180^\circ$  and (b)  $\phi = 90^\circ, 270^\circ$ ,  $f = 5.8 \text{ GHz}$ .

#### 4.3.2.5. Measurement of the Radiation Pattern of the Inverted Conical Helix Antenna

The measured radiation patterns of right-hand circularly polarized field of the inverted conical helix antenna in the elevation planes  $\phi = 0, 180^\circ$  and  $\phi = 90^\circ, 270^\circ$  are presented in Figure 4.40 in comparison to the radiation pattern obtained by the CST simulator for the same antenna model. The measured radiation patterns of the inverted conical helix antenna seem to be in good agreement with those obtained by simulation.

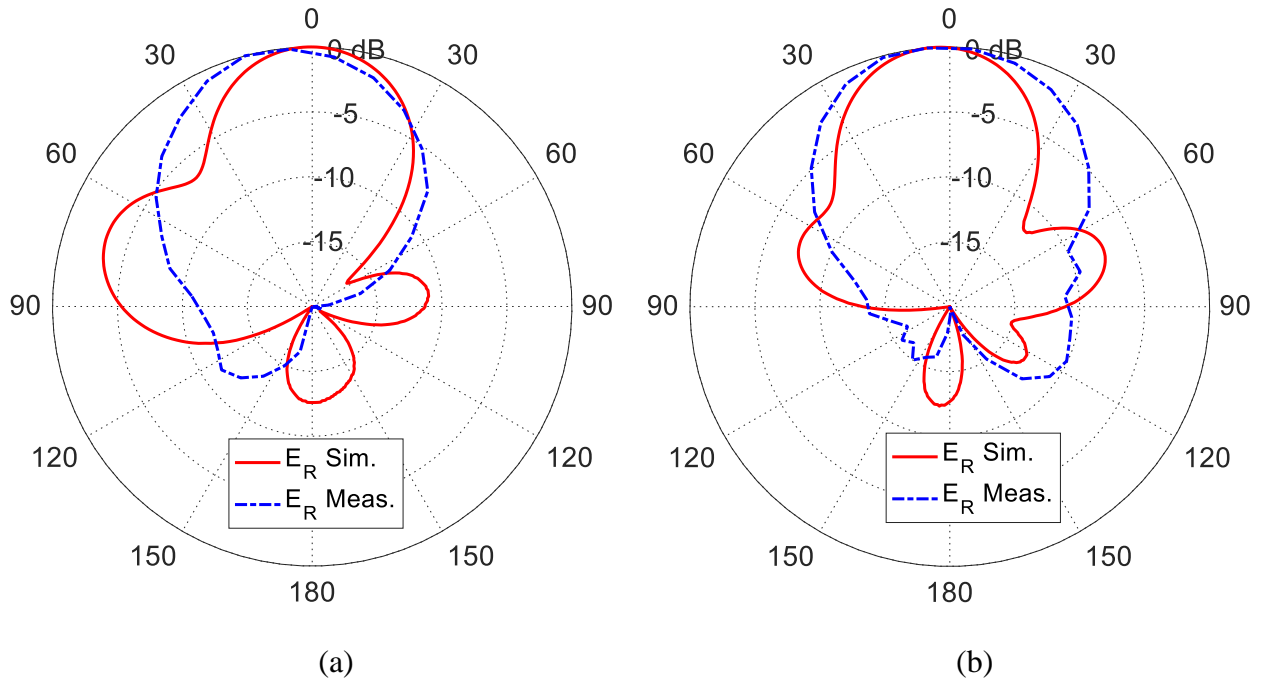


**Figure 4.40:** Comparison between the simulated and measured far-field radiation patterns of the right-hand circular polarization for the inverted conical helix antenna in the planes (a)  $\phi = 0, 180^\circ$  and (b)  $\phi = 90^\circ, 270^\circ$ ,  $f = 5.8 \text{ GHz}$ .

#### 4.3.2.6. Measurement of the Radiation Pattern of the Conical Helix Antenna

The measured radiation patterns of right-hand circularly polarized field of the conical helix antenna in the elevation planes  $\phi = 0, 180^\circ$  and  $\phi = 90^\circ, 270^\circ$  are presented in Figure 4.41 in comparison to the radiation patterns obtained by the CST simulator for the same antenna model. The measured radiation patterns of the conical helix antenna come in good agreement with those obtained by simulation.



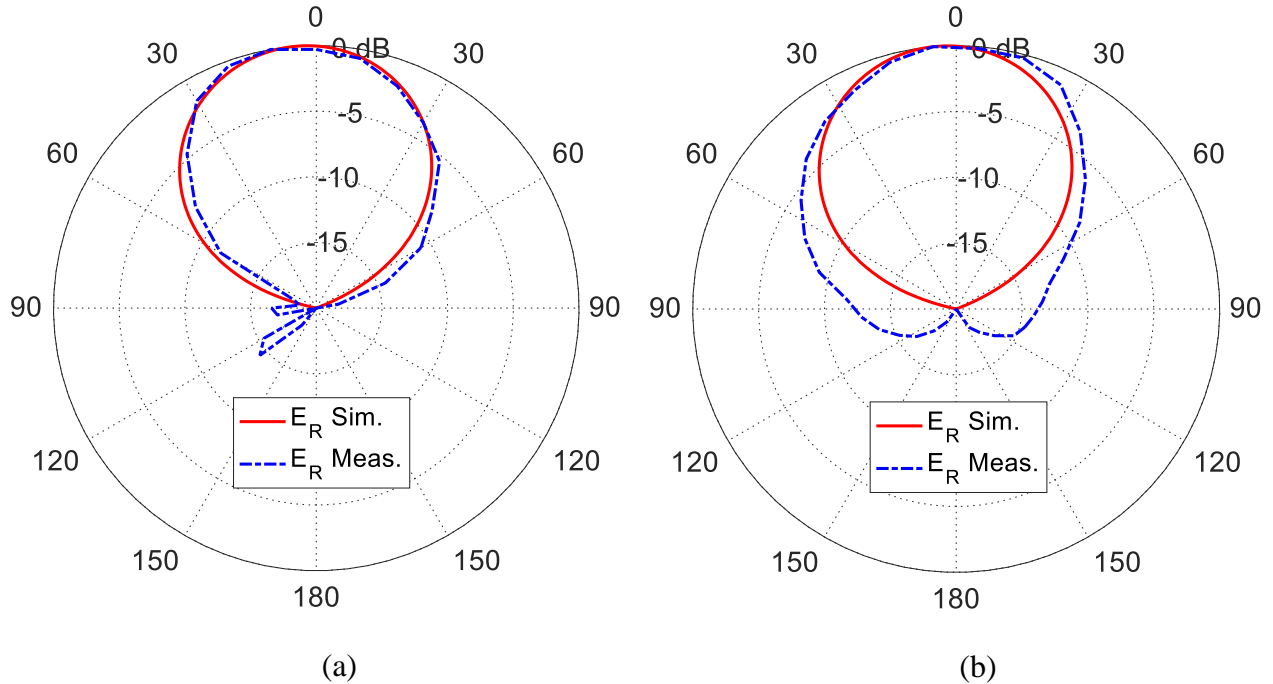


**Figure 4.41:** Comparison between the simulated and measured far-field radiation patterns of the right-hand circular polarization for the conical helix antenna in the planes (a)  $\phi = 0, 180^\circ$  and (b)  $\phi = 90^\circ, 270^\circ$ ,  $f = 5.8$  GHz.

#### 4.4. Conclusion

The cylindrical helix, conical helix, and inverted conical helix antennas proposed to operate as central antennas for WBAN are investigated through semi-analytic technique, CST simulator, and experimental measurements. Each of the proposed helical antennas is a dual-band that is designed to produce in the end-fire radiation to communicate (through its far-field) with the Wi-Fi antenna at 5.8 GHz, and to produce broad-side radiation to communicate (through its near field) with the on-skin biosensor antennas at 2.45 GHz. Three prototypes of the proposed helical antennas are fabricated. Each antenna is matched with  $50\Omega$  coaxial feeder over a wide frequency band, mounted on a copper circular disc, and covered with a very thin dielectric radome for protecting the wire antenna. Such an antenna when covered by the radome is shaped like a hemispherical button that can be attached to the patient clothes and, hence, it can be considered as wearable antenna. The near-field distribution over the surface of human body is presented at 2.45 GHz. The radiation patterns obtained by experimental measurements for the three fabricated

prototypes show good agreement with those obtained by the CST simulator and are shown to be appropriate for communication with the Wi-Fi antennas at 5.8 GHz. These experiments were done according to the semi-analytic model mentioned in chapter three and optimized to obtain the desired results. The laboratory these experiments took place had different sources of interference when testing the noise effect such as mobile phones. However, the readings of the power density distribution, SAR and radiation patterns was taken in an anechoic chamber.

## Chapter 5

### Performance Assessment of the Proposed On-Body Helical Antennas

#### 5.1. Introduction

This chapter aims to arrive at the optimum design of the on-body central helix antenna that fulfills the following requirements:

- (i) Dual-frequency operation 2.45 GHz for the on-body communications (WBAN) and 5.8 GHz for the off-body communications (Wi-Fi).
- (ii) Broadside radiation pattern at 2.45 GHz.
- (iii) End-fire radiation pattern at 5.8 GHz.
- (iv) Maximization of the frequency bandwidth for the off-body communications to achieve high bit rate for transferring the data records from the WBAN to the external storage devices through the Wi-Fi in short time to minimize the electromagnetic dose in the human body.
- (v) Minimization of the input power of the biosensor antennas to achieve long lifetime of the difficult-to-replace batteries of the biosensors.
- (vi) Maximizing the SNR and, hence, minimizing the BER for efficient on-body communications of the WBAN.
- (vii) Minimization of the SAR in the human tissues at the two frequencies of operation, especially at the lower frequency of the WBAN (2.45 GHz.) as the microwave at this frequency is much more penetrable into the human tissues than the case at the higher frequency (5.8 GHz).

The on-body central antenna design has considerable challenges as some of the above design objectives are contradicting. For example, to reduce the BER in the communication system WBAN to fulfill the objective (vi), the input power of the antennas should be increased, which leads to increase the SAR in the human tissues. Thus, the fulfillment of the antenna design objective (iv) contradicts with the design objectives (v) and (vii). Consequently, a compromise should be made to realize threshold values of some performance measures such as the maximum BER and the maximum SAR.

For these purposes the present chapter is concerned with the quantitative assessment of the WBAN communication system performance when each of the proposed helix and conical helix antennas is employed as on-body central antenna for the WBAN. For its high immunity to noise, the utilized modulation system is assumed to be  $M$ -ary PSK, with  $M = 8$  and  $M = 16$ . A channel modeling is performed for such a communication system by considering AWGN to evaluate the SNR and, hence, the corresponding BER can be calculated. This enables the calculation of the minimum input power of the proposed on-body WBAN central antenna that achieves the required BER for a specific data rate. On the other hand, the distribution of the microwave power density near the body surface is evaluated by simulation and experimental measurements to ensure the realization of the electromagnetic exposure safety limits. Also, the SAR distribution inside the human tissues of concern is evaluated. The effects of the on-body antenna dimensional parameters and, also, the antenna height above the human body surface on such performance measures and electromagnetic dose level are numerically studied for the purpose of arriving at the optimum design of the proposed on-body wearable conical helix antenna.

## 5.2. Calculation of SAR in the Human Tissues due to the Central On-Body Antenna

The semi analytic technique developed in Chapter 3 can be applied to calculate the electric field in the free space region near the body surface and inside the human tissues near the skin layer. If the electric field in the tissue is known the SAR can be calculated as follows.

$$\text{SAR} = \frac{\sigma |E|^2}{\rho} \quad (5-1)$$

where  $\sigma$  and  $\rho$  are the conductivity and mass density of the tissue and  $|E|$  is the magnitude of the electric field inside the tissue.

The microwave propagation on the surface of the human body is mainly at the frequency 2.45 GHz proposed for the WBAN. Hence, it is expected that the study of the SAR distribution in the human tissues due to the on body communications at 2.45 GHz is more important. According to (5-1), the mass density and the electric properties of the human tissues should be

known to calculate the SAR. The mass density, dielectric constant, and conductivity of the human tissues of concern at 2.45 GHz are listed in Tables 5.1 and 5.2, respectively.

**Table 5.1: Average mass density of the concerned types of human tissues [115].**

Tissue Type	Mass Density, $\rho(\text{kg/m}^3)$
Skin	1109
Fat	911
Muscle	1090

**Table 5.2: Electric properties of concerned types of human tissues at 2.45 GHz [115].**

Tissue Type	Dielectric Constant, $\epsilon_r$	Conductivity, $\sigma(\text{S/m})$
Skin	38	1.46
Fat	5.3	0.11
Muscle	52.7	1.77

### 5.3. Channel Modeling for WBAN communications and Assessment of Noise Power

For transmitting information through physical channels in the communication systems, the design of these systems requires to construct mathematical models which show the most important features of the transmission media. It is assumed that the unavoidable ambient light interfering with the signal carried by the diffused optical beam can be modeled as Additive White Gaussian Noise (AWGN) with power spectral density  $N_0/2$  (W/Hz). In such a model, the transmitted signal  $s(t)$  is distorted by such type of noise  $n(t)$  and consequently, the signal received at the optical detector,  $x(t)$ , can be expressed in the time-domain as follows.

$$x(t) = s(t) + n(t) \quad (5-2)$$

The discrete time samples of the noise function can be expressed as follows.

$$n_p = n(t_p), \quad t_p = (p - 1)\Delta t, \quad p = 1, 2, \dots, P \quad (5-3)$$

where  $P$  is total number of time samples that covers the time period required for simulation of the transmission/reception process of large enough number of symbols.

For such a simulation, the values of  $n_p$ , for  $p = 1, 2, \dots, P$ , can be generated using a Gaussian probability distribution function of the following form.

$$g_n = \frac{1}{\sigma_n \sqrt{2\pi}} e^{-\frac{n^2}{2\sigma_n^2}} = \frac{1}{\sqrt{2\pi N_0}} e^{-\frac{n^2}{N_0}} \quad (5-4)$$

with  $\sigma_n^2 = N_0/2$ .

In the frequency-domain, the received signal can be expressed, in a complex (phasor) diagram, as follows.

$$r_x e^{j\varphi_x} = r_s e^{j\varphi_s} + r_n e^{j\varphi_n} \quad (5-5)$$

where  $r_x$ ,  $r_s$ , and  $r_n$  are the magnitudes of the received, transmitted, and noise signals, respectively, whereas  $\varphi_x$ ,  $\varphi_s$ , and  $\varphi_n$  are the associated phases for these signals, respectively.

Assuming that the optical bandwidth is  $B_W = 2R_b$ , where  $R_b$  is the bit rate, the noise power can be evaluated as:

$$P_N = \frac{1}{2} N_0 B_W \quad (5-6)$$

where  $P_N$  is the noise power.

To model the AWGN numerically, the phase,  $\varphi_n$ , associated with the noise can be generated using a uniformly distributed probability distribution function over the interval  $0 \leq \varphi_n \leq 2\pi$ , whereas it may be convenient to set the magnitude of the noise,  $r_n$ , to a constant value as follows.

$$r_n = \sqrt{P_N} \quad (5-7)$$

Thus, the representation of the received signal in the complex plane (for a constellation diagram) due to the addition of the AWGN can be described as shown in Figure 5.1.

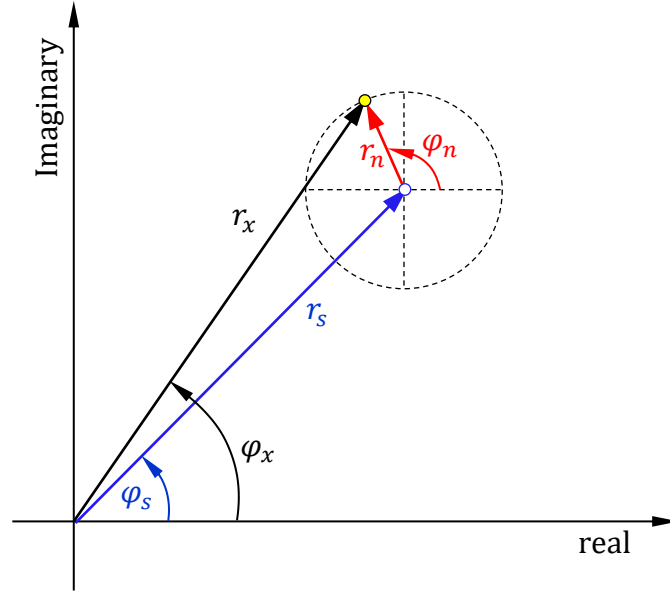


**Figure 5.1:** Representation of the received signal,  $\mathbf{r}_x e^{j\varphi_x}$ , for a specific transmitted symbol,  $\mathbf{r}_s e^{j\varphi_s}$ , after adding the AWGN  $\mathbf{r}_n e^{j\varphi_n}$ .

#### 5.4. Assessment of Signal Strength and SNR over the Skin of the Human Body in Communication System of the WBAN

The angular distribution of the transmitted signal strength (power) due to the on-body central antenna can be evaluated as:

$$P_s(R, \theta, \phi) = P_{Rx}(R) S(\theta, \phi) \quad (5-8)$$

where,  $S(\theta, \phi)$  is the power radiation pattern of the central on-body antenna and  $P_{Rx}(R)$  is the level of the signal at a distance  $R$  from this antenna. If the propagation were only in free space, the received power would be expressed as follows.

$$P_{Rx}(R) = P_{Tx} \left( \frac{\lambda}{4\pi R} \right)^2 \quad (5-9)$$

For more accurate results, the received power level,  $P_{Rx}(R)$ , is assessed using the on-body antenna de-embedding method proposed in Chapter 3. The SNR for an on-body sensor antenna located at  $(R, \theta, \phi)$  can be calculated as follows.

$$SNR = \frac{P_s}{P_N} = \frac{P_{Rx}(R) S(\theta, \phi)}{\frac{1}{2} N_o B_W} \quad (5-10)$$

## 5.5. Assessment of the BER through Numerical Simulation

The following expression gives the relation between the SNR and the ratio  $E_b/N_o$ .

$$SNR = \frac{P_s}{P_N} = \frac{E_b R_b}{\frac{1}{2} N_o B_W} \quad (5-11)$$

In another form, the relation (5-11) can be expressed as

$$(E_b/N_o)_{dB} = SNR_{dB} - (R_b/B_W)_{dB} - 3 \quad (5-12)$$

It should be noted that the quantity  $(R_b/B_W)$  is defined as the spectral efficiency of the communication system.

In the present chapter, the dependence of the BER on the SNR (or  $E_b/N_o$ ) is assessed through numerical simulation by generating random symbols (uniformly distribution) associated with noise samples (Gaussian distribution). Also, the calculation of the BER depends on the modulation technique implemented in the communication system of the Body Sensor Network (BSN). The *M*-ary-PSK is used for performance assessment of a BSN employing the central on-body antennas proposed in the present work. In digital modulation scheme, the modulated signal is characterized by constellation diagram.

## 5.6. Results and Discussions

This section is concerned with the presentation and discussion of some numerical and experimental results concerned with the assessment of electromagnetic exposure, SAR distribution in the human tissues, and the performance assessment of communication system of the WBAN employing the on-body conical helix antennas proposed in the present thesis. The on-body communications is performed between the on-body central antenna and the distributed on-skin antennas that are attached to the in-body (implantable) biosensors. Some important performance measures for the proposed WBAN systems such as the power density distribution, SNR, and BER are evaluated. The AWGN is modeled and the dependence of the performance of such WBAN implementing *M*-ary PSK modulation technique, with  $M = 8$  and  $M = 16$ , on the



various design parameters of the proposed on-body central antennas is investigated and discussed.

### **5.6.1. Experimental Measurement and Numerical Assessment of the Power Density Distribution on the Human Body Surface**

It is proposed, in the present thesis, that the Wi-Fi antenna with which the on-body central antenna of the WBAN communicates at 5.8 GHz is mounted on the room ceil as illustrated in Figure 3.1 (Chapter 3). For realistic situation while measuring the microwave power density distribution near the human body surface, the experimental measurements are performed while the patient is laid as shown in Figure 3.2 (Chapter 3) while the Wi-Fi antenna operating at 5.8 GHz is mounted on the room ceil and oriented downwards as shown in Figure 5.2.



**Figure 5.2:** Wi-Fi Antenna operating at **5.8 GHz** is mounted on the ceil of the room and directed downwards.

Under this situation, the measurement of the power density distribution near the skin of the body using the radiation hazard meter Extech® model 480846 as shown in Figure 5.3. In the

absence of the on-body conical helix antenna, the radiation hazard meter displays an average power density of  $0.008 \mu\text{W}/\text{cm}^2$  as shown in Figure 5.3(a). This very low level of the power density is caused by the ambient radiation from the Wi-Fi antenna that is mounted on the room ceil as shown in Figure 5.2. When placing the prototype of the conical helix antenna (without the Radom and being excited with input power  $P_{in} = 0 \text{ dBm}$  at  $f = 2.45 \text{ GHz}$ ) with random orientation on the patient chest and placing radiation hazard meter close to this antenna as shown in Figure 5.3 (b), the measured power density is  $0.200 \mu\text{W}/\text{cm}^2$ . Thus, even when the on-body conical helix antenna is excited the maximum value of the measured power density on the human body surface is very low which indicates that the electromagnetic exposure is quite below the safety limit. Thus the maximum SAR inside the human tissues is expected to be very low.



(a)



(b)

**Figure 5.3:** Measurement of the power density distribution near the skin of the body using the radiation hazard meter Exttech® model 480846 due to, (a) Ambient radiation from the Wi-Fi antenna mounted on the ceil as shown in Figure 5.2, (b) Radiation by the proposed conical helix antenna without the radome (input power  $P_{in} = 0 \text{ dBm}$  at  $f = 2.45 \text{ GHz}$ ).

The power density distribution near the skin of the body is measured using the radiation hazard meter when the conical helix antenna (covered with the radome) is placed on the patient chest and excited with input power  $P_{in} = 0$  dBm at  $f = 2.45$  GHz. The power density meter shows a reading of  $0.041 \mu\text{W}/\text{cm}^2$  when antenna is oriented with tip pointing to the power density meter as shown in Figure 5.4(a). When the antenna is oriented with tip pointing to the room ceil (normal operation) the reading of the power density meter is  $0.276 \mu\text{W}/\text{cm}^2$ . Comparing the two readings of the power density meter taking the orientations of the antenna into consideration indicates that the radiation of the conical helix antenna has mainly broadside radiation at this frequency. However, the power density still ensures safe values of the electromagnetic exposure.



(a)



(b)

**Figure 5.4:** Measurement of the power density distribution near the skin of the body using the radiation hazard meter Exttech® model 480846 when the conical helix antenna is excited with input power  $P_{in} = 0$  dBm at  $f = 2.45$  GHz, (a) The antenna is oriented with tip pointing

to the power density meter , (b) The antenna is oriented with tip pointing to the room ceil (normal operation).

Figure 5.5 presents the distribution of the microwave power density just on the skin surface over the rectangular area surrounded by the blue dashed rectangle shown in Figure 3.1 (Chapter 3) due to the placement of the conical helix antenna during normal operation with input power  $P_{in} = 4$  dBm at  $f = 2.45$  GHz. It should be noted that the power density distribution is evaluated using the semi-analytic technique developed in Chapter 3. It is shown that the maximum power density on the skin doesn't exceed  $0.035$  mW/cm<sup>2</sup>, which ensures safe level of electromagnetic exposure.

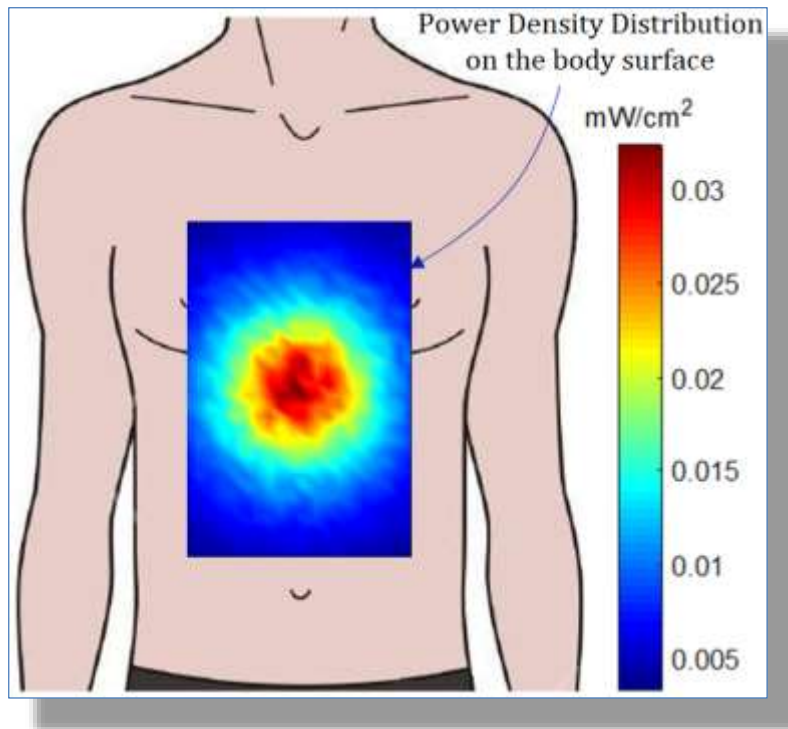


**Figure 5.5:** Distribution of the power density just on the surface of the body due to conical helix antenna fed with input power  $P_{in} = 4$  dBm at  $f = 2.45$  GHz

### 5.6.3. SAR Distribution in the Skin, Fat and Muscle Tissues

The SAR distributions in the tissues of skin, fat, and muscle due to the placement of the conical helix antenna on the patient chest as shown in Figure 3.2 (Chapter 3) with input power

$P_{in} = 4$  dBm at  $f = 2.45$  GHz are presented in Figures 5.6, 5.7, and 5.8. The SAR is evaluated using (5.1), where the magnitude of the electric field in the human tissues is evaluated using the semi-analytic technique developed in Chapter 3. It is shown that the maximum value of the SAR occurs in the skin tissues whereas the fat tissues has the minimum value of the SAR due to the higher conductivity of the skin tissue and larger depth of the fat tissues inside the human body. The maximum SAR in all the tissues doesn't exceed  $0.3$  W/kg, which ensures safe level of electromagnetic exposure.

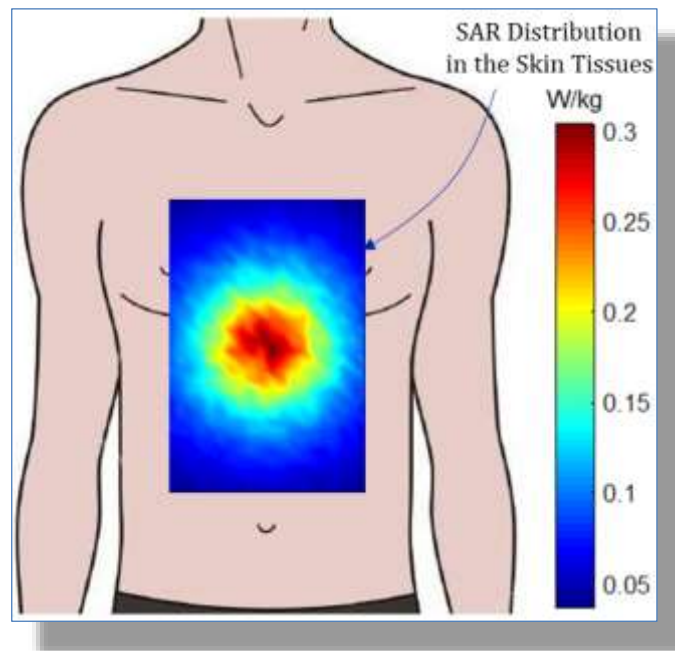


**Figure 5.6:** SAR distribution in the skin tissues due to conical helix antenna fed with input power,  $P_{in} = 4$  dBm at  $f = 2.45$  GHz.

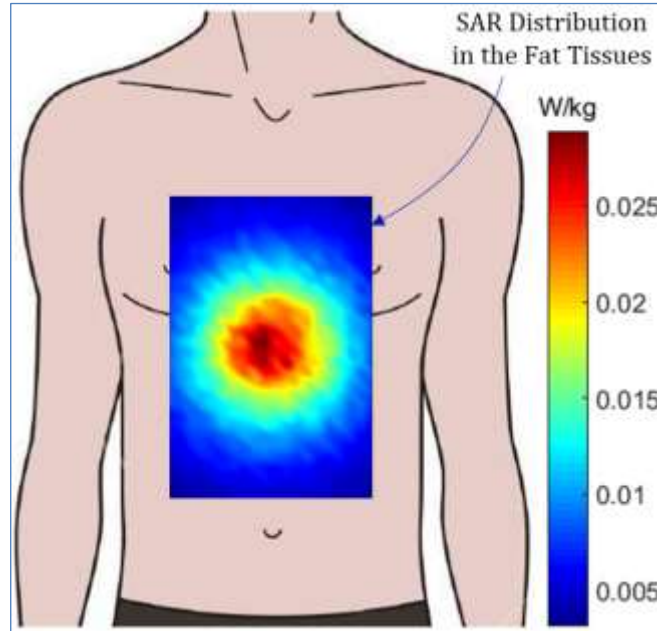


**Figure 5.7:** SAR distribution in the fat tissues due to conical helix antenna fed with input power,  $P_{in} = 4 \text{ dBm}$  at  $f = 2.45 \text{ GHz}$ .

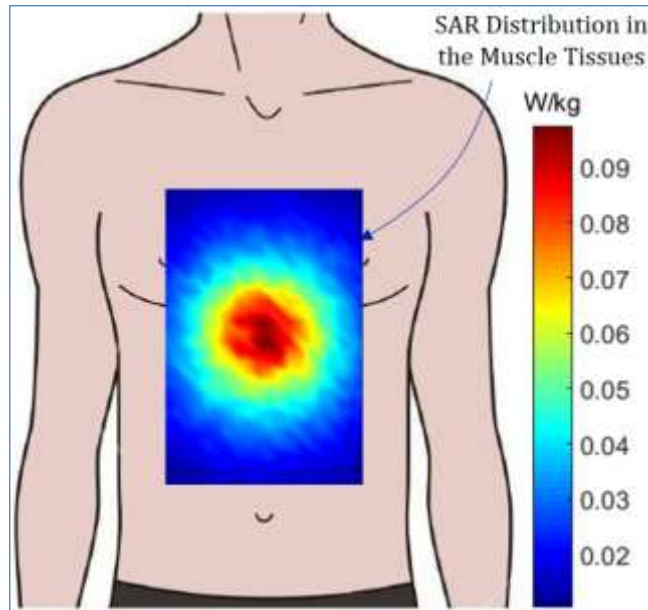


**Figure 5.8:** SAR distribution in the muscle tissues due to conical helix antenna fed with input power,  $P_{in} = 4 \text{ dBm}$  at  $f = 2.45 \text{ GHz}$ .

#### 5.6.4. Performance Analysis of the On-Body Communication System

In any communication system, data rates are required to be high enough to transfer the data records within acceptable time intervals according to the specific application requirements. Also, the BER should be below a specific (threshold) maximum value for reliable communications. However, increasing the data transfer rate has the effect of increasing the noise and, hence, increasing the BER unless the input power of the transmitted antenna is increased. This section provides a model for the assessment of the communication system of the WBAN employing the proposed conical helix as a central antenna for on-body communications with the on-skin biosensor network.

#### **5.6.4.1. Modeling the AWGN and the Received Signal in the Constellation Diagram**

The constellation diagram for *M*-PSK, with  $M = 8$ , is presented in Figure 5.9 for the eight transmitted (reference) symbols before and after the addition of AWGN with different values of the  $E_b/N_o$ . It should be mentioned that the AWGN is modeled as described in Section 5.3 and Figure 5.1. It is clear, in Figure 5.9, that the phase error associated with the received signal increases with decreasing the  $E_b/N_o$ , which may lead to an increasing BER.



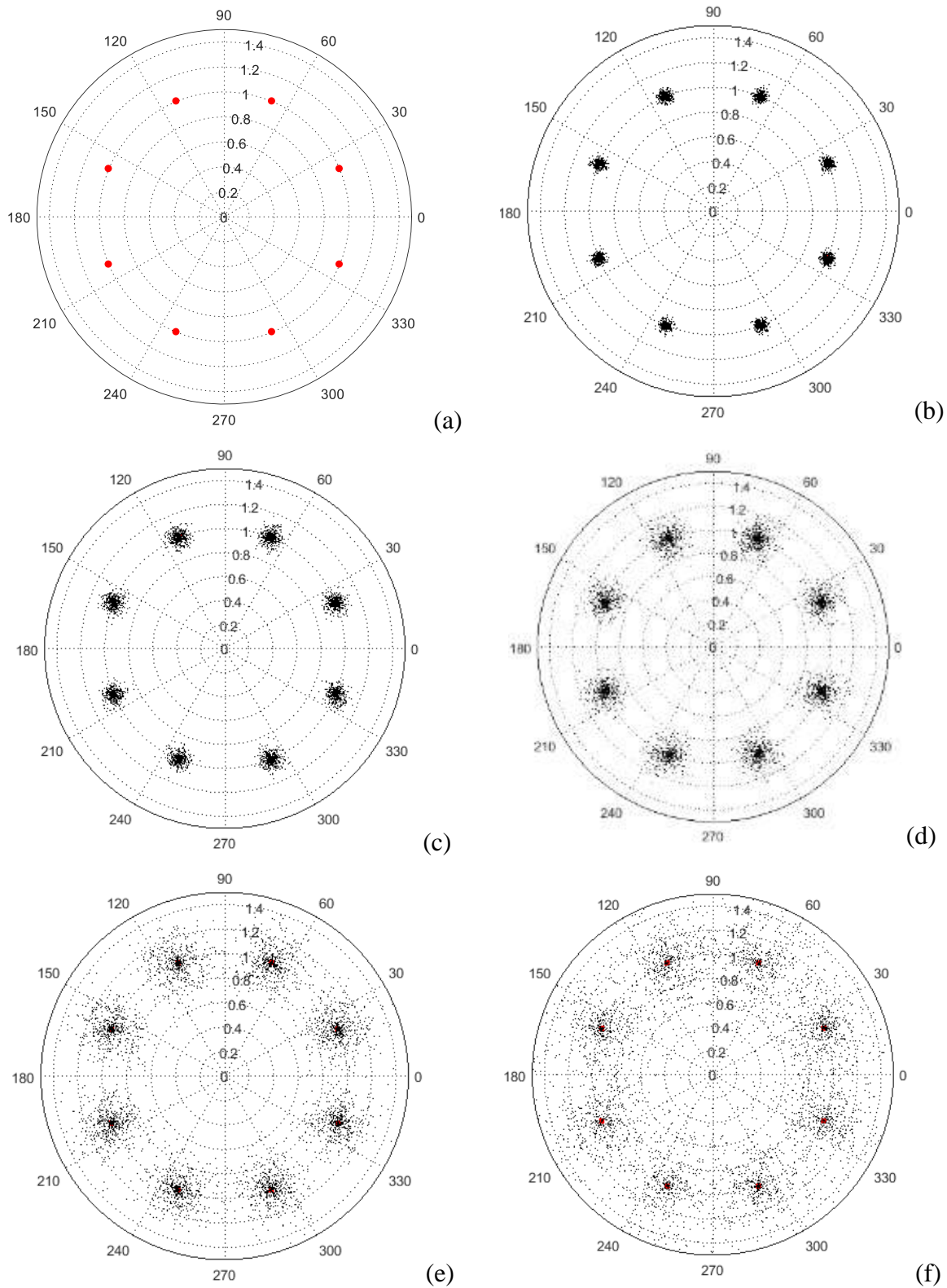
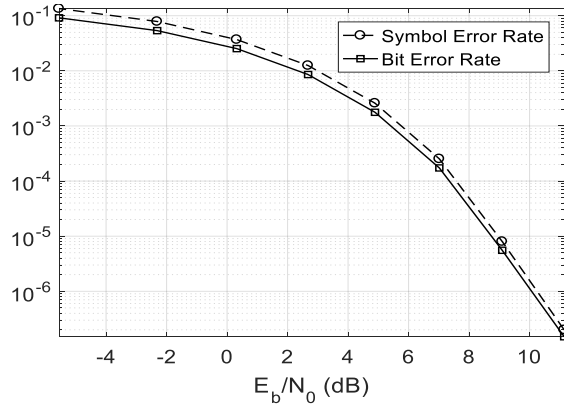


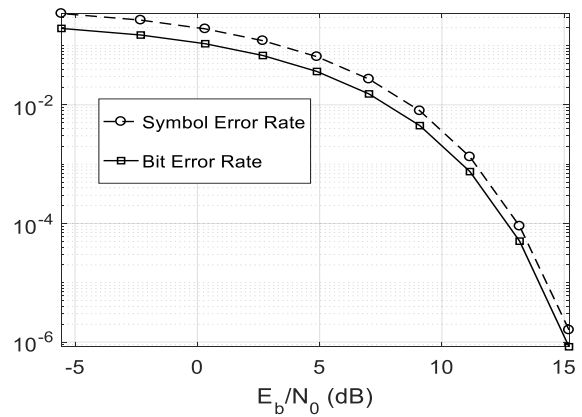
**Figure 5.9:** Constellation diagram for 8-PSK modulation system with 50% spectral efficiency after adding the AGWN for different values of  $E_b/N_o$  (a) Reference symbols (c)  $E_b/N_o = 25$  dB, (d)  $E_b/N_o = 20$  dB, (e)  $E_b/N_o = 15$  dB, (f)  $E_b/N_o = 10$  dB.



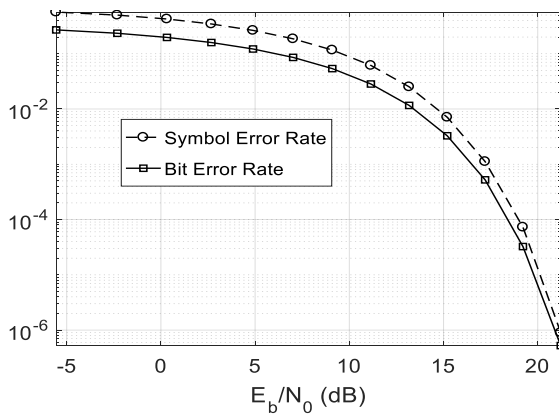
For a given value of the SNR or, equivalently,  $E_b/N_0$ , the BER can be evaluated for a specific digital modulation technique. Some curves for the BER and SER versus  $E_b/N_0$  for WBAN communication system that implements  $M$ -ary PSK modulation with different number of symbols,  $M$  are presented in Figure 5.10. It should be noted that these curves are obtained by simulation of the communication process employing  $M$ -ary PSK using the AGW as described in Section 5.3, 5.4, and 5.5.



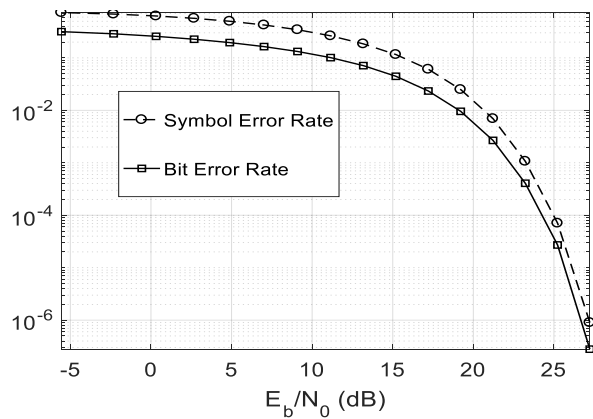
(a)



(b)



(c)



(d)

**Figure 5.10:** BER and SER versus the  $E_b/N_0$  for BSN that implements  $M$ -ary PSK modulation with different number of symbols. (a)  $M = 4$ , (b)  $M = 8$ , (c)  $M = 16$ , (d)  $M = 32$ .

#### 5.6.4.2. Distribution of the Received Power, SNR and BER due to Cylindrical Helix Antenna

Assuming isotropic receiving biosensor antennas allocated on the patient body within the area indicated in Figure 4.1 (Chapter 4), the distributions of the received power and SNR over the area of concern on the human body surface due to a central on-body cylindrical helix antenna placed as shown in Figure 3.2 (Chapter 3) and fed with input power,  $P_{in} = 4$  dBm at  $f = 2.45$  GHz, are presented in Figure 5.11. It is shown that SNR over the area of concern on the surface of the human body is high enough for reliable communications despite the on-body cylindrical helix antenna is fed with relatively low power (4 dBm).

The corresponding distributions of the BER over the same area on the body surface are presented in Figure 5.12 assuming that the WBAN is employing  $M$ -ary PSK modulation technique for  $M = 8$ , and  $M = 16$ . Obviously the BER obtained for  $M = 16$  is higher than that obtained for  $M = 8$ . However, the achieved BER seems to acceptable in the two cases, which indicates that the proposed cylindrical helix antenna is quite efficient for reliable on-body communications of the WBAN as it results in acceptable BER even when it is fed with low value of the input power.

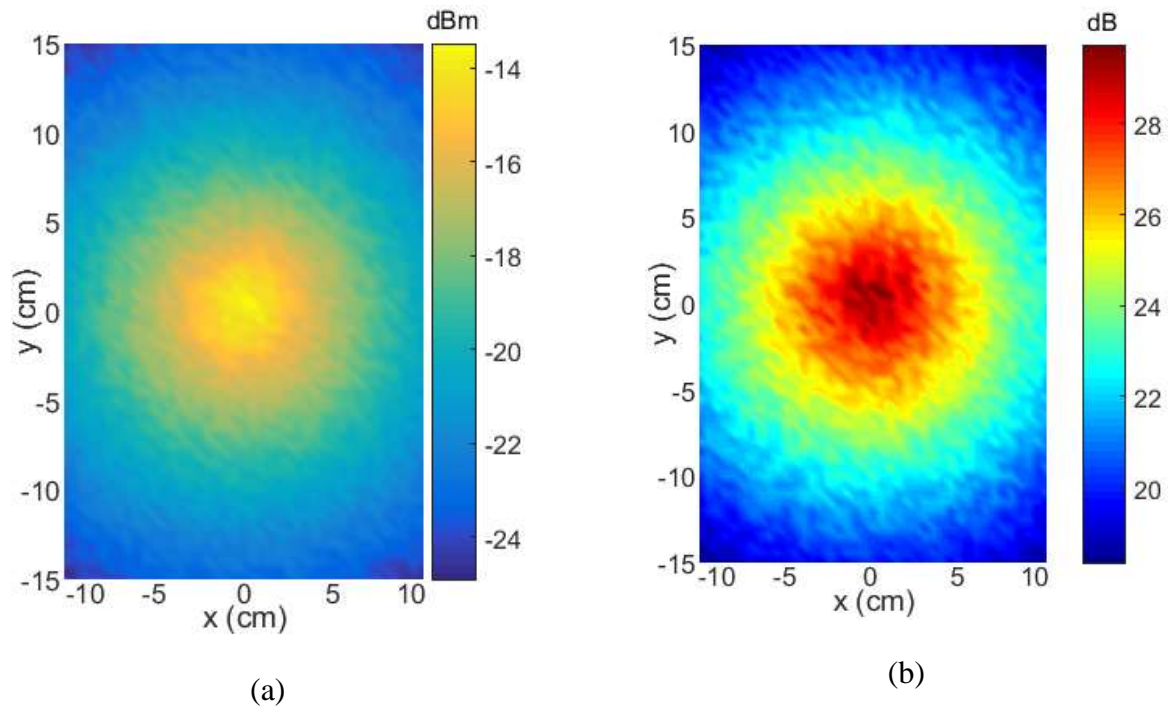


**Figure 5.11:** Distribution of the received power and SNR over the area within which the (isotropic) biosensor antennas are allocated due to a central on-body cylindrical helix antenna fed with input power,  $P_{in} = 4 \text{ dBm}$  at  $f = 2.45 \text{ GHz}$ , (a) Power received by isotropic biosensor antennas, (b) SNR at the receiving biosensor antennas.

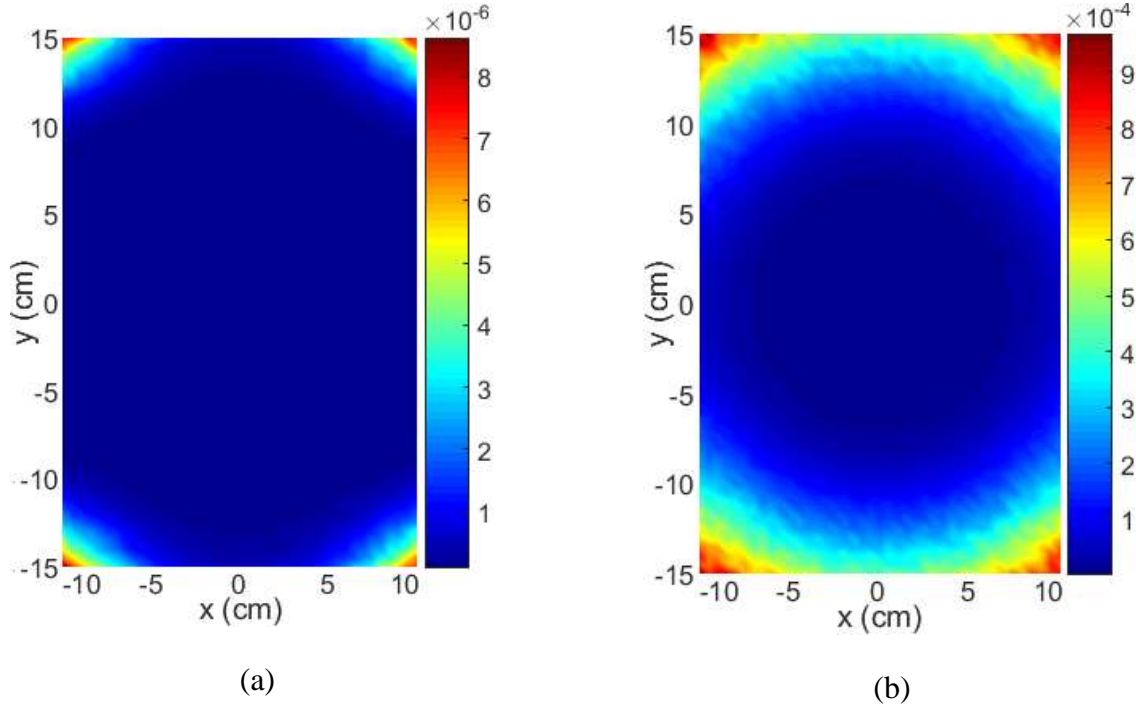


**Figure 5.12:** Distribution of the BER over the area within which the (isotropic) biosensor antennas are allocated due to a central on-body cylindrical helix antenna fed with input power,  $P_{in} = 4$  dBm at  $f = 2.45$  GHz, (a) BER for 8-symbol PSK, (b) BER for 16-symbol PSK.

#### 5.6.4.3. Distribution of the Received Power, SNR and BER due to the Conical Helix Antenna

Assuming isotropic receiving biosensor antennas allocated on the patient body within the area indicated in Figure 4.1 (Chapter 4), the distributions of the received power and SNR over the area of concern on the human body surface due to a central on-body conical helix antenna placed as shown in Figure 3.2 (Chapter 3) and fed with input power,  $P_{in} = 4$  dBm at  $f = 2.45$  GHz, are presented in Figure 5.13. It is shown that SNR over the area of concern on the surface of the human body is high enough for reliable communications despite the on-body conical helix antenna is fed with relatively low power (4 dBm).

The corresponding distributions of the BER over the same area on the body surface are presented in Figure 5.14 assuming that the WBAN is employing  $M$ -ary PSK modulation technique for  $M = 8$ , and  $M = 16$ . Obviously the BER obtained for  $M = 16$  is higher than that obtained for  $M = 8$ . However, the achieved BER seems to acceptable in the two cases, which indicates that the proposed conical helix antenna is quite efficient for reliable on-body

communications of the WBAN as it results in acceptable BER even when it is fed with low value of the input power.

When comparing the BER distributions presented in Figure 5.16 when the conical helix antenna is used as on-body central antenna for WBAN communication system to the BER distributions presented in Figure 5.14 when the cylindrical helix antenna is used for the same purpose, it becomes clear that the conical helix antenna shows higher performance.

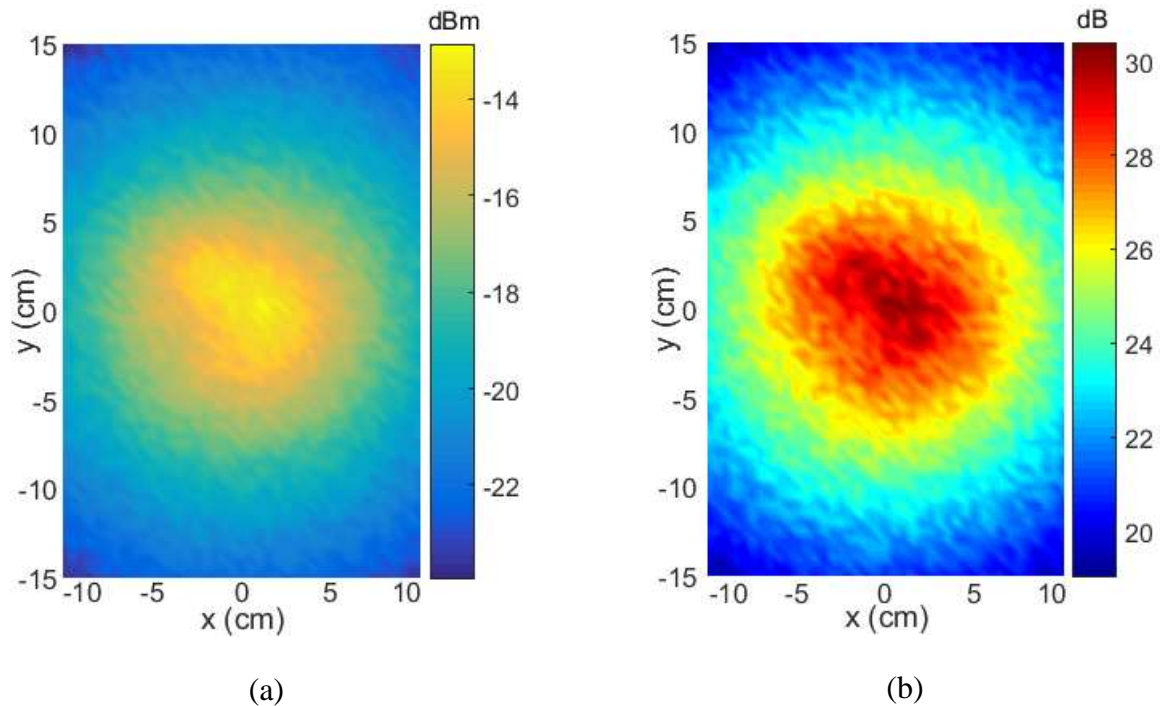


**Figure 5.13:** Distribution of the received power and SNR over the area within which the (isotropic) biosensor antennas are allocated due to a central on-body conical helix antenna fed with input power,  $P_{in} = 4 \text{ dBm}$  at  $f = 2.45 \text{ GHz}$ , (a) Power received by isotropic biosensor antennas, (b) SNR

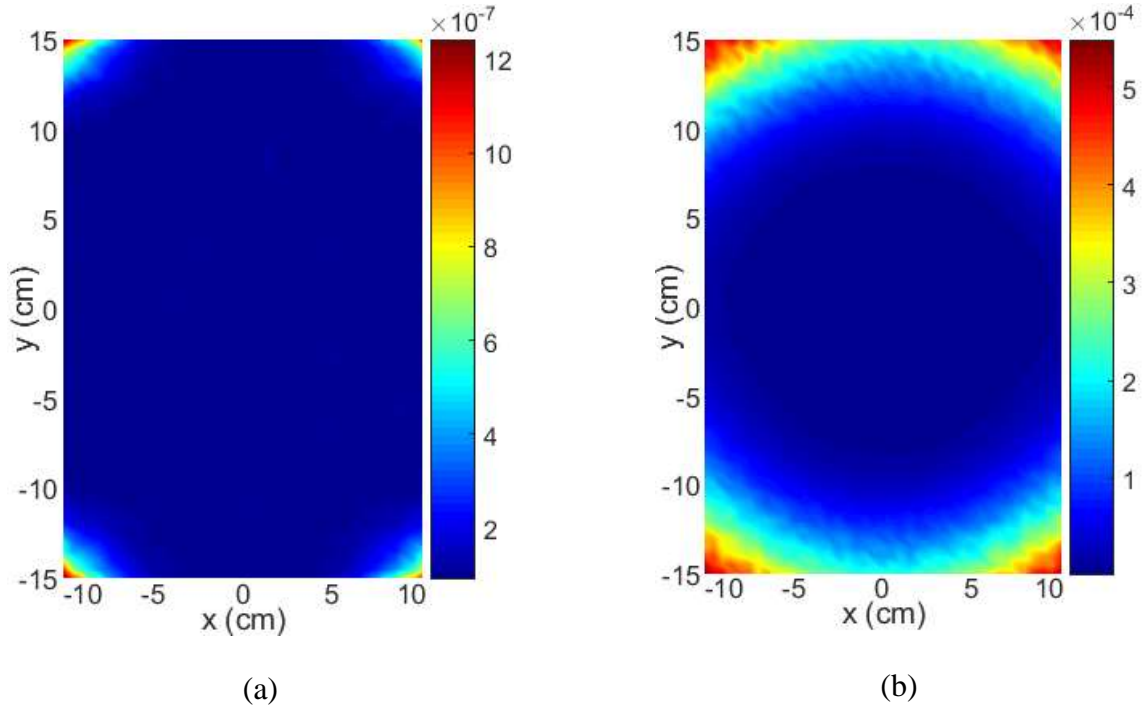


**Figure 5.14:** Distribution of the BER over the area within which the (isotropic) biosensor antennas are allocated due to a central on-body conical helix antenna fed with input power,  $P_{in} = 4$  dBm at  $f = 2.45$  GHz, (a) BER for 8-symbol PSK, (b) BER for 16-symbol PSK.

### 5.6.5. Optimization of the Conical Helix Antenna for Higher Performance of the WBAN Communication System

As the conical helix antenna is shown to be of higher performance when compared to the other two types helical antennas when proposed to work as on-body central antenna for WBAN communications, it is convenient to study the effect of the dimensional parameters and the location of the conical helix antenna relative to the skin surface on the performance of the communication system regarding the SNR and the BER.

#### 5.6.5.1. Dependence of the SNR and BER on the Height of the Conical Helix Antenna

The effects of the height of the conical helix antenna proposed for on-body communications in WBANs on the SNR and the BER are presented in Figures 5.15 and 5.16, respectively, for different values of the input power to the antenna. As shown in the figures, the SNR is increased and hence, the BER is decreased with increasing the height of the conical helix.

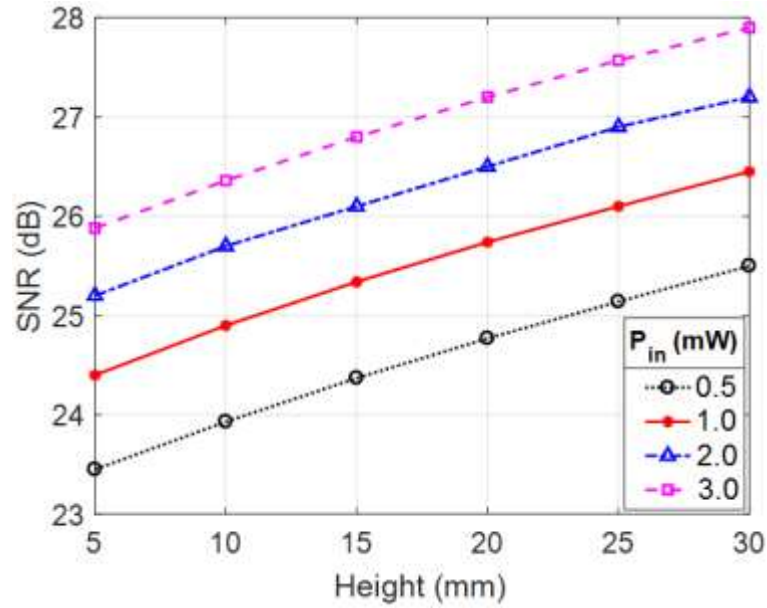


**Figure 5.15:** Dependence of the minimum resulting SNR on the height of the conical helix when used in WBAN as a central on-body antenna fed with different values of the input power at  $f = 2.45$  GHz.

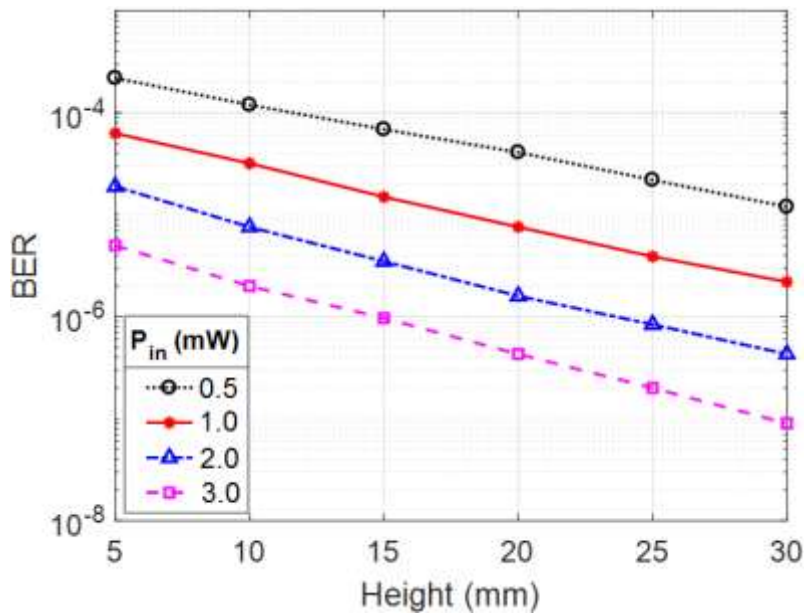


**Figure 5.16:** Dependence of the maximum resulting BER on the height of the conical helix when used in WBAN as a central on-body antenna fed with different values of the input power at  $f = 2.45$  GHz.

### 5.6.5.2. Dependence of the SNR and BER on the Apex Angle of the Conical Helix Antenna

The effects of the apex angle of the conical helix antenna proposed for on-body communications in WBANs on the SNR and the BER are presented in Figures 5.17 and 5.18, respectively. As shown in these figures, the SNR and, hence, the BER seem be constant and independent of the apex angle of the conical helix. This study is considered one of the most important contributions in this thesis.

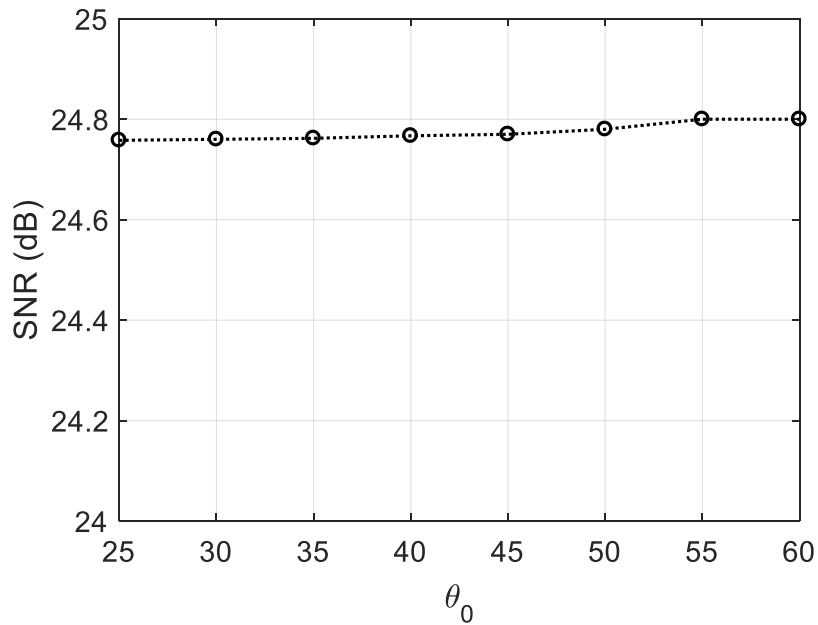


**Figure 5.17:** Dependence of the minimum resulting SNR on the half apex-angle of the conical helix when used in WBAN as a central on-body antenna fed with input power,  $P_{in} = 4 \text{ dBm}$  at  $f = 2.45 \text{ GHz}$ .



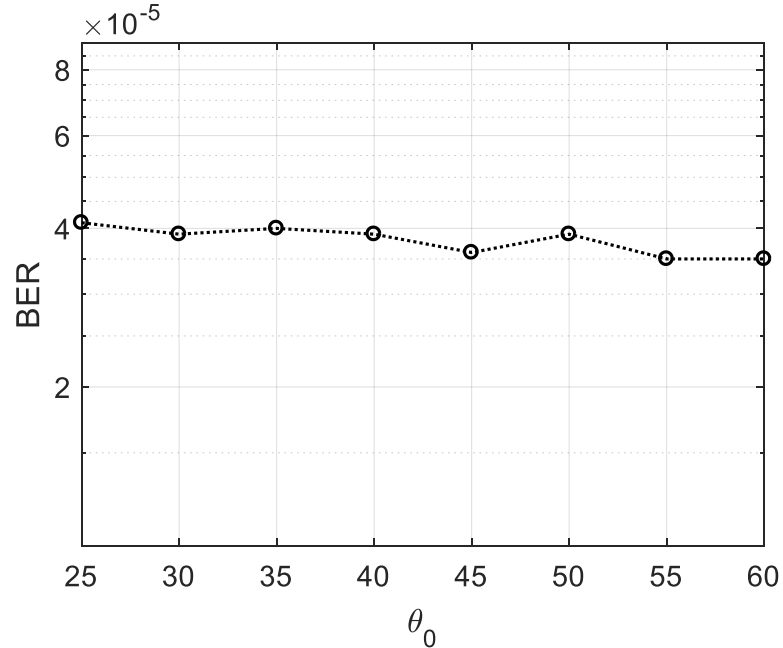


**Figure 5.18:** Dependence of the maximum resulting BER on the half apex-angle of the conical helix when used in WBAN as a central on-body antenna fed with input power,  $P_{in} = 4$  dBm at  $f = 2.45$  GHz.

### 5.6.5.3. Dependence of the SNR and BER on the Height of the Conical Helix Antenna above the Skin of the Human Body

The height at which the conical helix antenna (proposed for on-body communications in WBANs) is placed has a significant effect on the SNR and the BER as shown in Figures 5.19 and 5.20, respectively, for different values of the input power to the antenna. As shown in these figures, the SNR is increased and, hence, the BER is decreased with increasing the height of the conical helix above the surface of the human body.

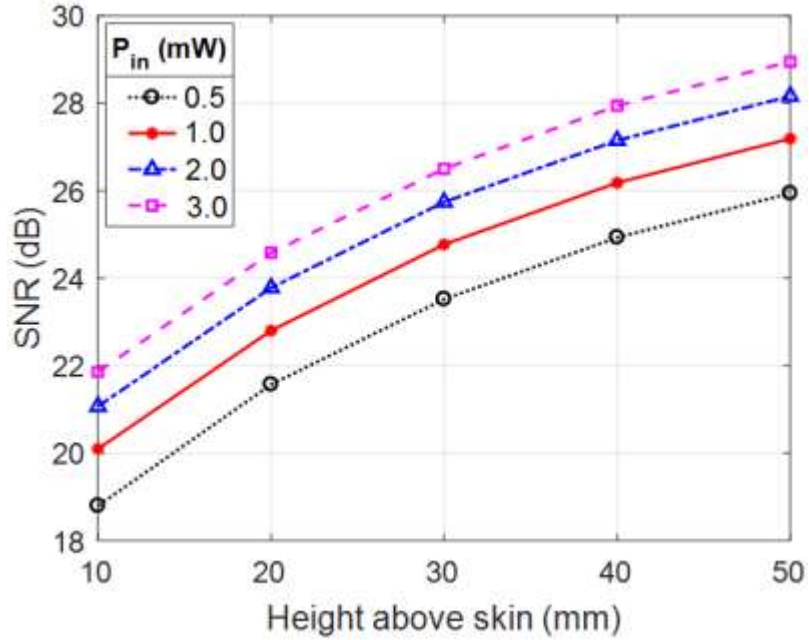


**Figure 5.19:** Dependence of the minimum resulting SNR on the location of the conical helix above the surface of the human body when used in WBAN as a central on-body antenna fed with different values of the input power at  $f = 2.45$  GHz.

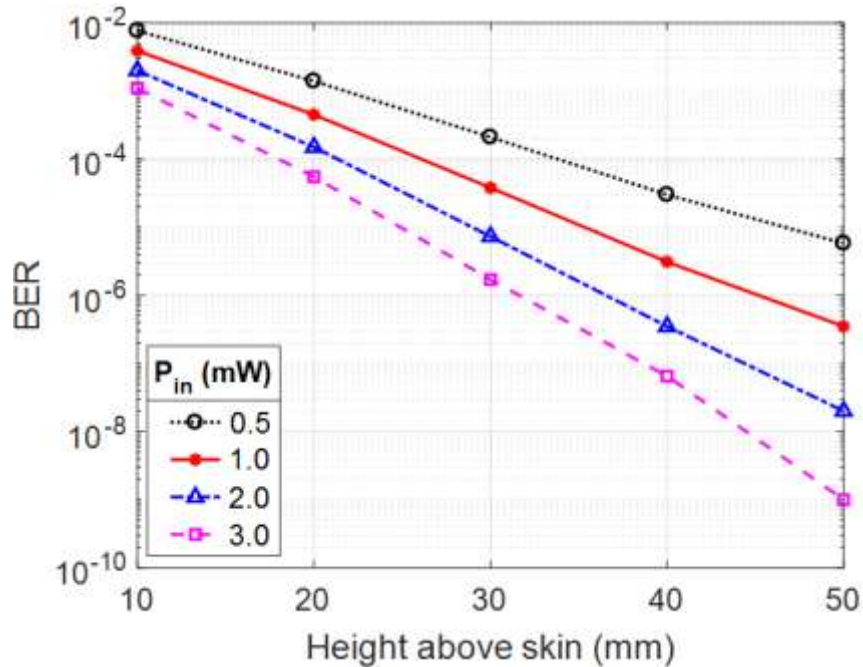


**Figure 5.20:** Dependence of the maximum resulting BER on the location of the conical helix above the surface of the human body when used in WBAN as a central on-body antenna fed with different values of the input power at  $f = 2.45$  GHz.

## 5.7. Conclusion

Quantitative assessment of the WBAN communication system performance is achieved when each of the cylindrical and conical helix antennas is employed as on-body central antenna for the WBAN. For its high immunity to noise, the utilized modulation system is assumed to be  $M$ -ary PSK, with  $M = 8$  and  $M = 16$ . A channel modeling is performed for such a communication system by considering AWGN to evaluate the SNR and, hence, the corresponding BER can be calculated. This enables the calculation of the minimum input power of the proposed on-body WBAN central antenna that achieves the required BER for a specific data rate. On the other hand, the distribution of the microwave power density near the body surface is evaluated by simulation and experimental measurements to ensure the realization of the electromagnetic exposure safety limits. Also, the SAR distribution inside the human tissues of concern is evaluated. It is shown that the conical helix antenna has higher performance than that of the cylindrical helix antenna. The effects of the on-body conical helix antenna dimensional parameters and, also, the antenna height above the human body surface on such performance measures and electromagnetic dose level are numerically studied for the purpose of arriving at the optimum design of the proposed on-body wearable conical helix antenna. It is shown that SNR is increased and, hence, the BER is decreased with increasing the height of the conical helix while being constant and independent of the apex angle of the conical helix.

## Chapter 6

### Low Power Dual-Band Conical-Helix/Monopole and Monopole/Spiral On-Body Antennas

---

#### 6.1. Introduction

Novel dual-band conical-helix/monopole and monopole/spiral antennas are proposed to operate as on-body central antennas for Wireless Body Area Network (WBAN). The proposed antennas communicate in three ways: (i) off-body communication through its end-fire radiation with the ceil-mounted Wi-Fi antenna at 5.8 GHz, (ii) on-body communication through its broadside radiation with the on-skin biosensor antennas at 3.0 GHz, and (iii) in-body communication with the in-body (implanted) biosensor antennas at 3.0 GHz. The characteristics of the proposed antennas are investigated through a semi-analytic technique developed in the present work, the commercially available CST simulator, and the experimental measurements. Prototypes of the proposed antennas are fabricated for experimental assessments. The antennas are matched with  $50\Omega$  coaxial feeder over a wide frequency band, mounted on a copper circular disc, and covered with a very thin dielectric radome for mechanical protection. Such antennas covered by the radome are shaped like a hemispherical button that can be attached to the patient clothes and, hence, can be considered as wearable antennas. The near-field distribution over the surface of human body is presented at 3.0 GHz. The radiation patterns obtained by experimental measurements show good agreement with those obtained by the CST simulator and are shown to be appropriate for communication with the ceil-mounted Wi-Fi antenna and the biosensor antennas at 5.8 GHz and 3.0 GHz, respectively. The distribution of the microwave power densities near the body surface are evaluated by simulation and experimental measurements to ensure the realization of the electromagnetic exposure safety limits. The (Specific Absorption Rate) SAR distribution inside the human tissues of concern is evaluated showing safe level of electromagnetic exposure. Quantitative assessment of the WBAN communication system performance is achieved when the proposed antennas are employed as on-body central antennas

for the WBAN. Thanks to the optimized design of the proposed antennas the Bit-Error-Rates (BER) are shown to be very low even when the input power fed to both antennas is only 1 mW.

## **6.2. The Proposed Conical Helix/Monopole Dual-Band Antenna**

This section is concerned with the description of the conical-helix/dipole antenna proposed to work as on-body central antenna in WBANs. This antenna is dual-band and designed to communicate (through its far-field pattern) with the ceil-mounted Wi-Fi antenna at 5.8 GHz, and to communicate (through its near-field or far-field pattern) with the on-skin and in-body biosensor antennas at 3.0 GHz. The wire monopole antenna is responsible for broadside radiation at 3.0 GHz whilst the wire conical-helix produces end-fire (balloon-like) radiation pattern at 5.8 GHz.

A photograph of a prototype for the proposed antenna with the hemispherical protective dielectric cover is shown in Figure 6.1. The dual-structure wire antenna is mounted on a copper circular disc (representing the ground plane and the board on which the electronic circuit can be embedded) and matched with  $50\Omega$  coaxial feeder over the two frequency bands. The antenna structure is covered with a very thin dielectric radome (almost transparent at the microwave frequencies) to provide mechanical protection. Such an antenna when covered by the radome is shaped like a hemispherical button that can be attached to the patient clothes as shown in chapter three, Figure 3.2(a) and, hence, it can be considered as a wearable antenna.



**Figure 6.1:** Photograph of the proposed antenna with the hemispherical protective dielectric cover.

The geometric model of the dual-structure of the proposed on-body antenna is shown in Figure 6.2. The monopole height is  $H_M$ ; the height, base diameter, and apex half-angle of the conical helix are  $H_H$ ,  $D_H$ , and  $\theta_H$ , respectively.

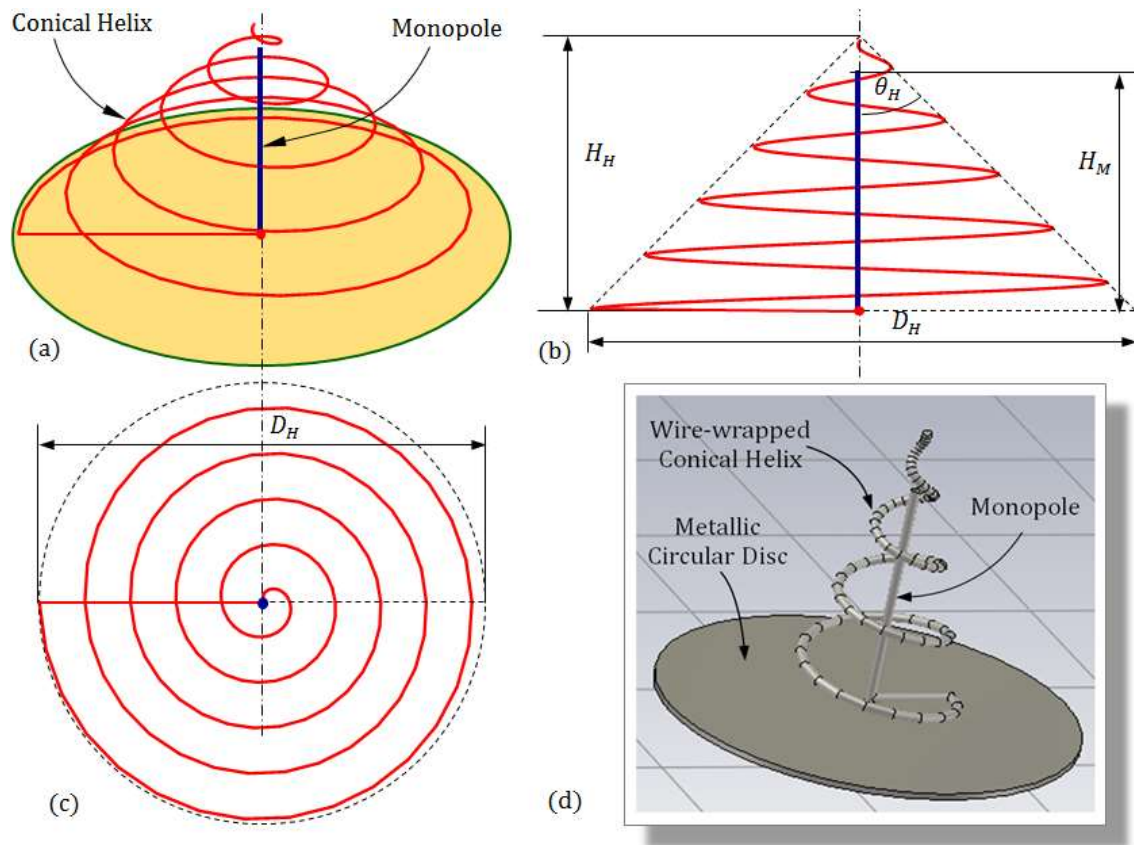


**Figure 6.2:** Geometry of the conical-helix/monopole antenna (a) Three-dimensional view, (b) Elevation view, (c) Top view, (d) Geometric model of the proposed antenna in the CST® simulator

The design of the proposed antenna permits the use of low power (few milli-Watts) while communicating (at 3.0 GHz) with the in-body or on-skin antennas which are connected to in-body biosensors and allows the use of higher level of power while communicating with the Wi-Fi antenna (at 5.8 GHz). The power consumption is, thus, optimized leading to low level of the SAR in the human tissues and long life-time of the batteries required to energize the on-body antenna and the in-body biosensor antennas.

The performance of the proposed antennas in this chapter is accurately assessed through: (i) the semi-analytic technique developed in Chapter 3, (ii) the commercially available CST simulation package and (iii) experimental measurements of the fabricated prototype of the proposed antenna.

### **6.3. Assessment of the WBAN Communication System Performance**

For transmitting information through physical channels in the communication systems, the design of these systems requires to construct mathematical models, which show the most important features of the transmission media. This section is concerned with the quantitative description of shared wireless transmission model of the WBAN explained in Chapter 3. The purpose of building such a channel model is the assessment of the communication system performance regarding the SNR and the corresponding BER assuming that the modulation system is  $M$ -ary PSK.

### **6.4. Results of Electromagnetic Simulation and Experimental Measurements**

This section is concerned with the presentation and discussion of the results of the electromagnetic simulation and experimental measurements to study the characteristics of the dual-structure conical-helix/monopole antenna proposed to work as on-body central antenna for WBAN. The presented results are concerned with investigating the performance of the on/off-body communication systems employing the proposed antenna including the power consumption, the SNR and BER and the associated SAR in the different human tissues near the body surface (skin, fat and muscle).

#### **6.4.1. Antenna-on-Body Model for Electromagnetic Simulation**

For realistic electromagnetic simulation, the human body below the antenna can be replaced by the three-layer (skin-fat-muscle) model shown in Figure 6.3. The electric properties of the three tissue types at 3.0 GHz and 5.8 GHz are listed Table 6.1.



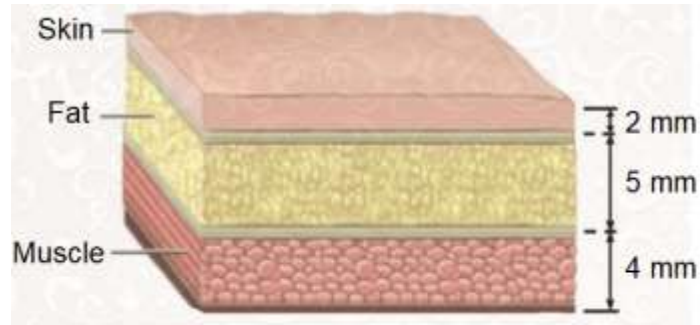


**Figure 6.3:** Three-layer (skin-fat-muscle) model of the human body for the simulation scenario of electromagnetic radiation from on-body antenna radiation

The geometric model of the same conical helix antenna in the commercially available CST simulator is presented in Figure 6.4. The monopole has a length of  $H_H = 18.5$  mm, the height, base diameter, and apex half-angle of the 3-turn conical helix are, respectively,  $H_H = 20$  mm,  $D_H = 20$  mm, and  $\theta_H = 36.5^\circ$ . The diameter of the circular copper plate is 40 mm. The CST simulator is used to evaluate the far-field pattern at 5.8 GHz when the input power to the antenna is 10 dBm. The three-layer planar structure described in Figure 6.3 is placed just below the antenna base as shown in Figure 6.4 to represent the human body.

**Table 6. 1:** Electric properties of the concerned types of the human tissues at 3.0 GHz and 5.8 GHz. [116]

Tissue Type	Mass Density, $\rho(\text{kg/m}^3)$	Dielectric Constant, $\epsilon_r$			
		$f =$ 3.0 GHz	$f =$ 5.8 GHz	$f =$ 3.0 GHz	$f =$ 5.8 GHz
Skin	1109	37	35.11	1.95	3.72
Fat	911	5.1	4.95	0.16	0.29
Muscle	1090	51.2	48.48	2.90	4.96

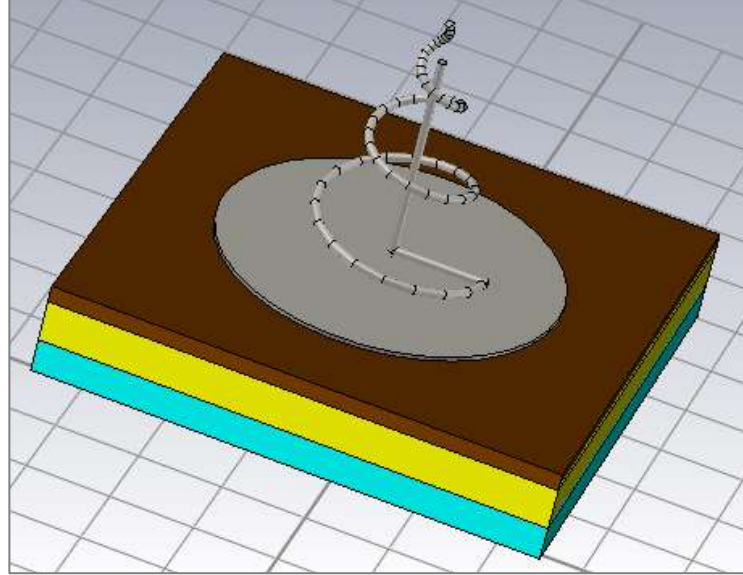


**Figure 6.4:** Model of the proposed conical-helix/monopole on-body antenna placed on the three-layer (skin-fat-muscle) model of the human body in the commercially available CST® simulator; the antenna has the dimensional parameters  $N_T = 3$ ,  $H_H = 20$  mm, and  $D_H = 20$  mm,  $H_M = 1.85$  mm.

The evaluation of the field distribution on the top surface of the skin layer is a necessary requirement for the performance assessment of the on-body communication between the proposed central antenna and distributed on-skin biosensor antennas.

In addition, the calculation of the electric field penetrating the human tissues namely the skin, fat, and muscle tissues is necessary for the evaluation of the SAR in these tissues and for the evaluation of the power received by the in-body biosensor antennas.

## 6.5. Fabrication of the On-Body Conical-Helix/Monopole Antenna Prototype

This section is concerned with the procedure of fabricating a prototype for the proposed conical-helix/monopole antenna.

### 6.5.1. Constructing the Conical-Helix and Monopole Wires

For the fabrication of a prototype of the proposed antenna, a copper wire is wrapped to take the shape of the conical helix with the dimensions given in Section 6.2. A wire wrapped in the right-hand sense produces right-hand circularly polarized field whereas a wire wrapped in the left-hand sense, as that shown in Figure 6.5, produces left-hand circularly polarized field.

The wrapped helix is then, welded near the cone base to a straight wire to form the monopole part of the complete wire antenna as shown in Figure 6.5.



**Figure 6.5:** A copper wire is wrapped to form a conical helix and then welded to a straight wire to form the conical-helix/monopole antenna proposed to play the role of a central on-body antenna for on-body biosensor antenna network

### 6.5.2. Mounting the Wire Structure on the Ground Plate and the Feeding Connector

A ground plane and a feeding coaxial connector are necessary for the operation of such monopole helical antennas. A circular copper disc of 4 cm diameter is prepared for this purpose and an SMA coaxial connector is mounted with its outer conductor welded to the circular disc as shown in Figure 6.6. The entire structure of the wire antenna, shown in Figure 6.7, is mounted on a circular copper plate by welding the monopole extension at the cone base to the inner conductor of the SMA connector as shown in Figure 6.7.

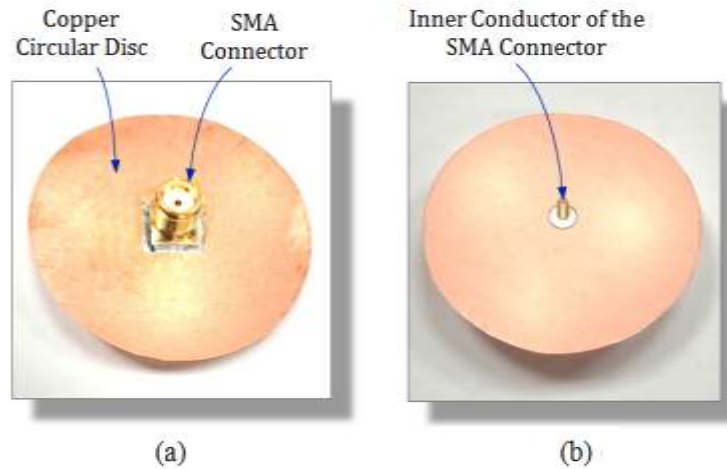


**Figure 6.6:** Fabricated copper circular disc to act as a ground base for the proposed conical-helix/monopole antenna with a mounted SMA connector, (a) Bottom view, (b) Top view.

### 6.5.3. Adding Impedance Matching Elements to the Antenna Structure

The wire antenna should be matched with the  $50\Omega$  SMA coaxial connector. The conical-helix antennas are characterized by an advantage of low imaginary part of the input impedance at the design frequency for end-fire radiations. Unfortunately, they are, also, characterized by a resistive part of the impedance that is much smaller than  $50\Omega$ . The real part of the impedance can be increased to  $50\Omega$  by attaching a small conductive triangular patch to the wire of the antenna near the feed point as shown in Figure 6.8. On the other hand, the quarter-wavelength straight wire monopole antennas are characterized, at resonance, by very low imaginary part of the input impedance and a resistive part that is greater than  $50\Omega$ . The real part of the monopole impedance can be decreased to  $50\Omega$  by attaching a small conductive rectangular patch near the feed point as shown in Figure 6.8. The shape, size and location of such patches for impedance matching can be properly attached to the antenna structure with the aid of a VNA to minimize the reflection coefficient  $|S_{11}|$  over the bandwidth of interest.

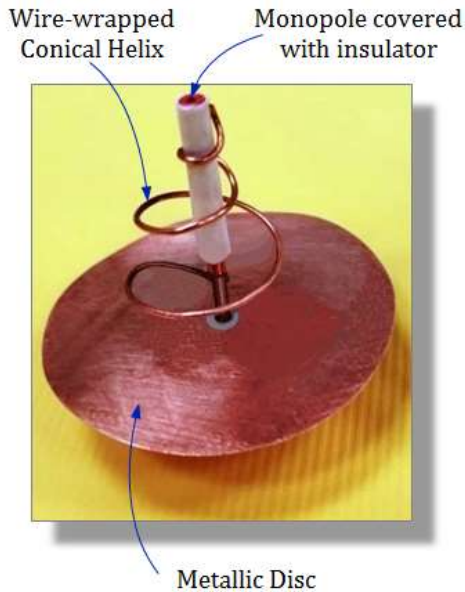


**Figure 6.7:** The conical-helix/monopole structure is mounted on a circular copper disc and connected to the inner conductor of an SMA connector without impedance matching.

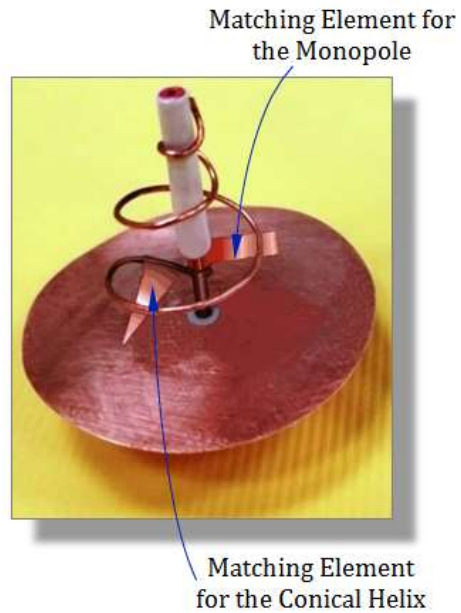
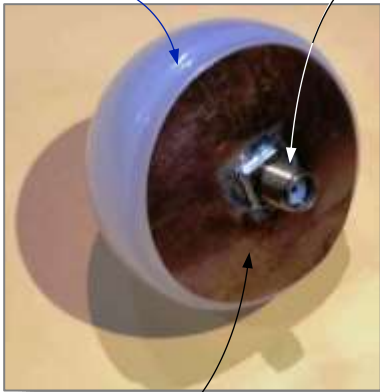


**Figure 6.8:** The conical-helix/monopole antenna with a triangular patch connected to the conical helix and another rectangular patch connected to the monopole near the feed point for impedance matching.

#### 6.5.4. Covering the Wire Antenna with Hemispherical Radom for Mechanical Protection

For protecting the wrapped wires of the fabricated helical antennas from deformation due to unavoidable mechanical stresses, a hemispherical radome of very thin dielectric material is used to cover the antenna structure as shown in Figure 6.9(a). As this radome is made of very thin dielectric material, it is almost electromagnetically transparent at the microwave frequencies and, consequently, has no effect on the antenna characteristics. Finally, for measurement purposes, the antenna is connected to flexible 50Ω coaxial cable as shown in Figure 6.9(b).

Protective Radom



Copper Disc

(a)



(b)

**Figure 6.9:** The final form of the proposed on-body medical antenna (a) covered with hemispherical radome and (b) connected to a coaxial cable for the purpose of experimental measurements.

## 6.6. Return Loss and Impedance Bandwidth of the Proposed On-Body Antenna

The reflection coefficient at the antenna port is measured using vector network analyzer (VNA) of the Agilent Field Fox N9918A. The frequency response of the reflection coefficient  $|S_{11}|$  is measured over a wide range of the frequency. The experimental measurements are compared to the numerical results obtained by electromagnetic simulation using the commercially available CST microwave studio suite.

The experimental setup for measuring the frequency response of the reflection coefficient  $|S_{11}|$  of the cylindrical helix antenna is shown in Figure 6.10. The comparison between measurement curves appearing the screen of the measurement device presented in Figures 6.10(a) and 6.10(b) shows that the reflection coefficient of the conical-helix/monopole antenna is almost unaffected by the placement of the radome to cover the antenna.





(a)



(b)

**Figure 6.10:** Measurement of the reflection coefficient  $|S_{11}|$  of the conical-helix/monopole antenna using the VNA of the Agilent Field Fox N9918A, (a) The uncovered antenna, (b) The antenna covered with the hemispherical radome.

Figure 6.11 presents the measured frequency responses of the reflection coefficient  $|S_{11}|$  of the conical-helix monopole antenna. Both the experimental measurements and the simulation results show that the antenna impedance is matched to  $50\Omega$  over the two frequency bands of interest. The impedance matching bandwidth (for  $|S_{11}| \leq -10$  dB) is about 11% at 3.0 GHz and about 22% at 5.8 GHz. The sharp minimum in the frequency response of  $|S_{11}|$  shows that the antenna is resonant at the frequency 3.0 GHz, which corresponds to the resonance of the quarter-wavelength monopole. However, the bandwidth at 3.0 GHz is fairly acceptable for high-speed data transmission between the biosensor antennas and the proposed central on-body antenna. On the other and, the wider bandwidth at the Wi-Fi frequency 5.8 GHz enables the central on-body antenna to transmit data at much higher speed, which facilitates the transmission of large data records of the patient through the Wi-Fi communication system.

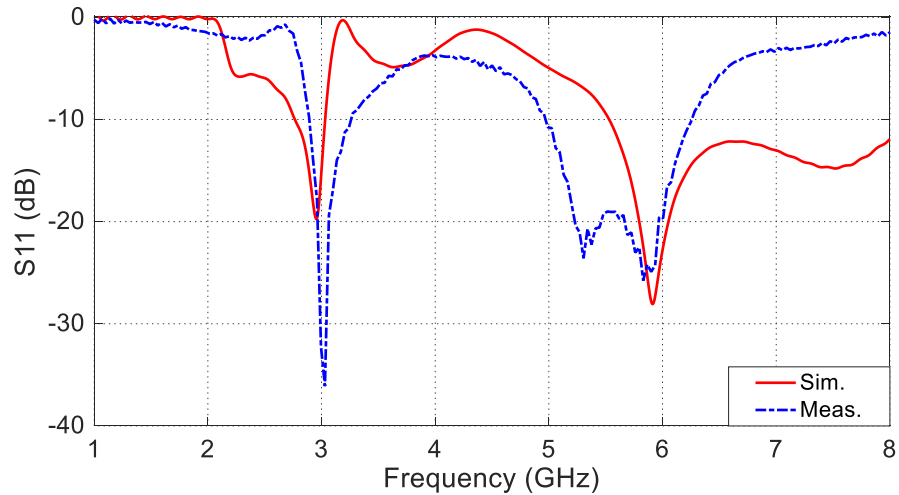


**Figure 6.11:** Comparison between the measured frequency response of the reflection coefficient  $|S_{11}|$  of the proposed conical-helix/monopole antenna and that obtained by electromagnetic simulation using the commercially available CST simulation package.

### 6.7. Simulation and Experimental Assessment of the Radiation Patterns of the Proposed On-Body Antenna

The commercially available CST simulation package is used to evaluate the far-field radiation patterns produced by the conical-helix/monopole antennas at 3.0 GHz and 5.8 GHz using the antenna-on-body model described in Section 6.2.

On the other hand, the experimental setups for measuring the radiation patterns of the proposed antenna using the VNA of the Agilent Field Fox N9918A while being placed in free space and mounted on the human body are shown in Figures 6.12 and 6.13, respectively. A reference right-hand circularly polarized helical antenna is connected to port ‘2’ of the VNA whereas the antenna under test is connected to port ‘1’ to obtain its radiation pattern by measuring the transmission coefficient  $|S_{21}|$  at the frequencies of concern.





**Figure 6.12:** Experimental setup for measuring the radiation pattern of the proposed on-body conical-helix monopole antenna in free space using the VNA of the Agilent Field Fox N9918A.



**Figure 6.13:** Experimental setup for measuring the radiation patterns of the conical-helix/monopole antenna on the human body using the VNA of the Agilent Field Fox N9918A.

### 6.7.1. Radiation Patterns at 3.0 GHz

The CST simulator is used to evaluate the radiation pattern produced at by the conical-helix/monopole antenna 3.0 GHz when the antenna is placed in free space. Also, the experimental setup shown in Figure 6.14 is used to measure the radiation pattern at the same frequency. The two-dimensional radiation patterns obtained by simulation and experimental measurements are presented in Figure 6.14 in comparison to each other showing good agreement. As shown in this figure, the radiation pattern is omnidirectional in the azimuth plane and broadside in the elevation planes with null in the direction parallel to the antenna axis. This shape of the radiation pattern means that monopole is the active part of the composite wire antenna at this frequency and, consequently, it is responsible for the radiation at 3.0 GHz.

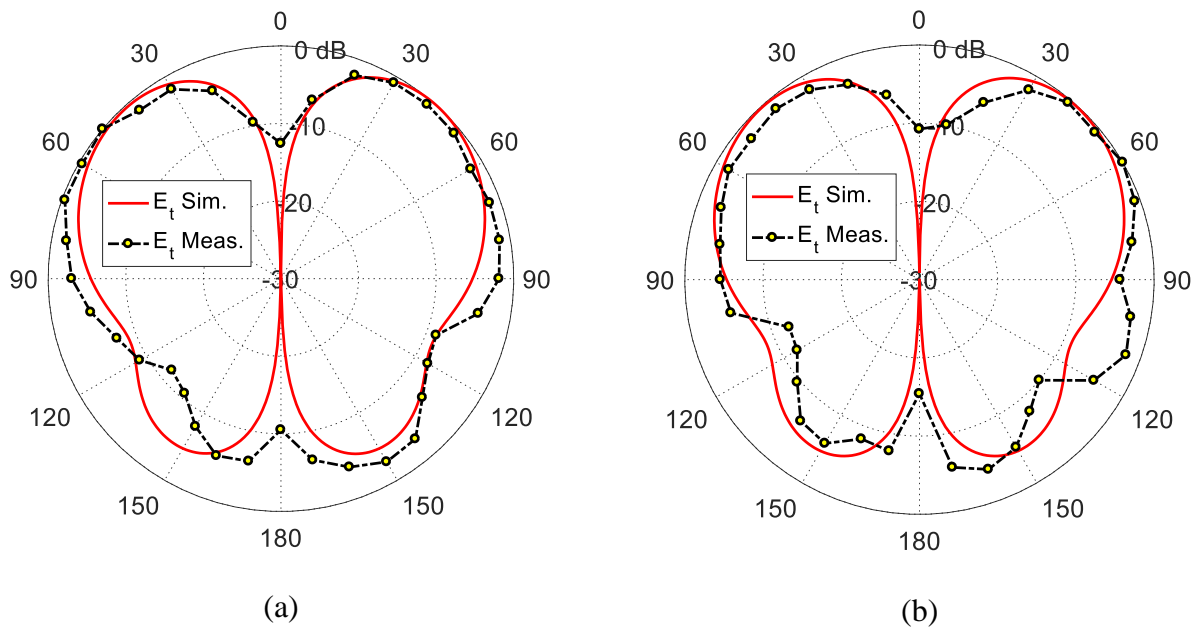


**Figure 6.14:** Comparison between the radiation patterns obtained by experimental measurements and CST simulator for the total field produced by the conical-helix/monopole antenna (placed in free space) in the planes, (a)  $\phi = 0, 180^\circ$ , and (b)  $\phi = 90, 270^\circ$ ,  $f = 3.0$  GHz.

The CST simulator is used to evaluate the far-field pattern produced at 3.0 GHz by the same antenna when mounted on the three-layer model of the human body described in Section 6.2. The resulting three-dimensional radiation pattern of the total radiated field is presented in Figure 6.15. The experimental setup described above, Figure 6.14, is used to evaluate the two-dimensional radiation patterns in the elevation planes that are presented in Figure 6.16 in

comparison with the patterns obtained by the CST simulator. As shown in the figure, the experimental measurements and the simulation results show good agreement. It is clear that the radiation at this frequency is mainly produced by the monopole part of the composite structure of the wire antenna. As shown in this figure, the radiation pattern is omnidirectional in the azimuth plane and broadside in the elevation planes with null in the direction parallel to the antenna axis. Thus, the radiated power at 3.0 GHz is mainly directed towards the body surface or into the human tissues near the body surface, which is appropriate for the conical-helix/monopole antenna to perform on-body and in-body communications with the biosensor antennas. When this pattern is compared to that obtained when the antenna is placed in free space, Figure 6.14, it is shown that the human body has the effect of reducing the backscatter and, thus, increasing the front-to-back ratio of the radiation.

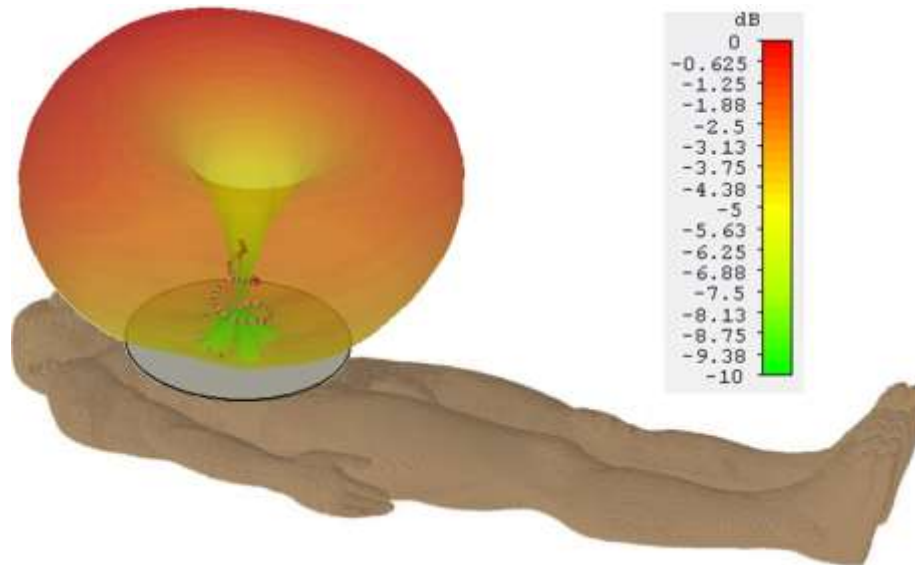


**Figure 6.15:** Three-dimensional far-field radiation pattern of the on-body conical-helix/monopole antenna of dimensions,  $H_M = 20 \text{ mm}$ ,  $H_H = 20 \text{ mm}$ ,  $\theta_H = 36.5^\circ$ ,  $D_H = 20 \text{ mm}$ ,  $f = 3 \text{ GHz}$ .

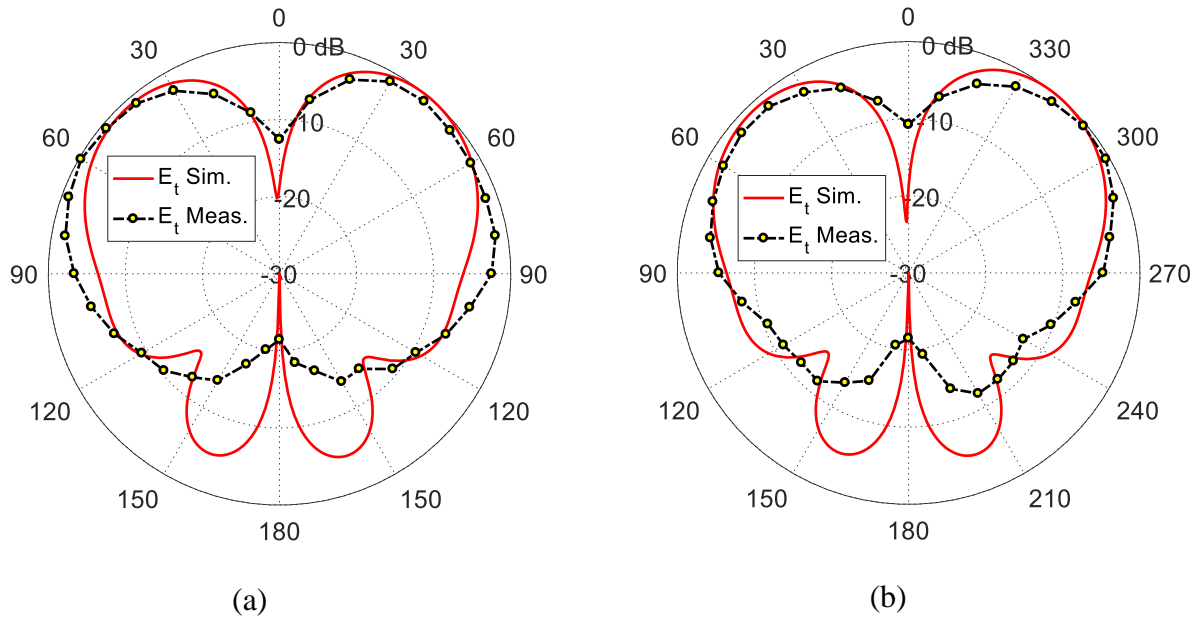


**Figure 6.16:** Comparison between the patterns obtained by experimental measurements and CST® simulator for the total field produced by the conical-helix/monopole antenna (placed on the human body) in the planes, (a)  $\phi = 0, 180^\circ$ , and (b)  $\phi = 90, 270^\circ$ ,  $f = 3.0$  GHz.

### 6.7.2. Radiation Patterns at 5.8 GHz

The CST simulator is used to evaluate the radiation pattern of the circularly polarized fields produced at by the conical-helix/monopole antenna at 5.8 GHz when the antenna is placed in free space. Also, the experimental setup shown in Figure 6.12 is used to measure the corresponding radiation patterns at the same frequency. The two-dimensional radiation patterns obtained by the CST simulator and experimental measurements are presented in Figure 6.17 in comparison to each other showing good agreement. As shown in this figure, the radiation patterns show good circular polarization with omnidirectional radiation in the azimuth plane and end-fire (balloon-like) radiation in the elevation planes. The maximum radiation is obtained in the direction parallel to the antenna axis. This shape of the radiation pattern means that conical helix is the active part of the composite wire antenna at this frequency and, consequently, it is responsible for the radiation at 5.8 GHz.

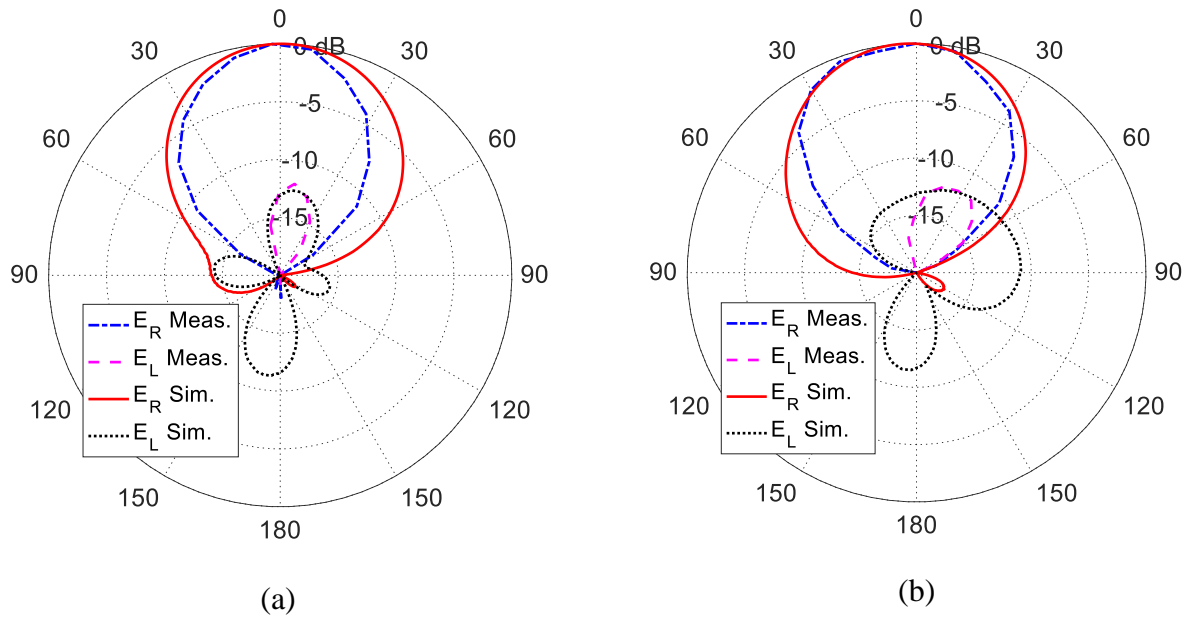


**Figure 6.17:** Comparison between the simulated and measured far-field radiation patterns of the right-hand and left-hand circular polarization for the conical helix antenna in the planes, (a)  $\phi = 0, 180^\circ$ , and (b)  $\phi = 90, 270^\circ$ ,  $f = 5.8$  GHz.

The CST simulator is used to evaluate the far-field pattern produced at 5.8 GHz by the proposed on-body antenna when mounted on the three-layer model of the human body as described in Section 6.2. The three-dimensional radiation pattern of the total radiated field is presented in Figure 6.18. The experimental setup described above, Figure 6.13, is used to evaluate the two-dimensional radiation patterns in the elevation planes that are presented in Figure 6.19 in comparison with the patterns obtained by the CST simulator. As shown in the figure, the experimental measurements and the simulation results show good agreement. It is clear that the radiation at this frequency is mainly produced by the conical helix part of the composite structure of the wire antenna. As shown in this figure, the radiation pattern is omnidirectional in the azimuth plane and end-fire (balloon-like) in the elevation planes with maximum in the direction parallel to the antenna axis. Thus, the radiated power at 5.8 GHz is mainly directed towards the Wi-Fi antenna mounted in the room ceil, which is appropriate for off-body communications intended at this frequency. Moreover, such a radiation pattern is appropriate to keep the main radiation at this frequency far from the human body to reduce the SAR in the human tissues.

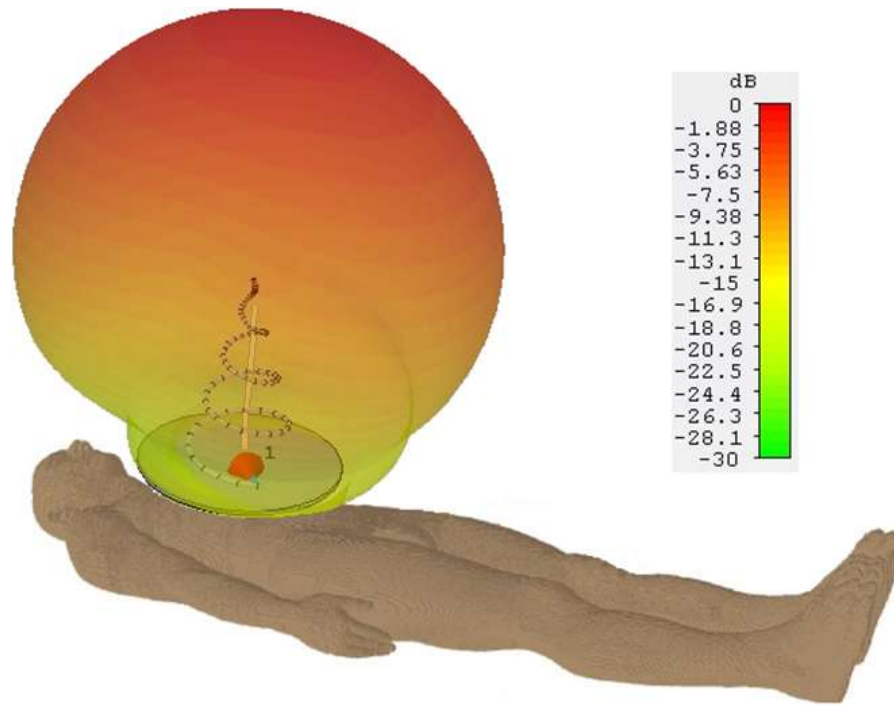


**Figure 6.18:** Three-dimensional radiation pattern of total field produced by the on-body conical-helix/monopole antenna of dimensions,  $N_T = 3$ ,  $H_M = 20$  mm,  $H_H = 20$  mm,  $\theta_H = 36.5^\circ$ ,  $D_H = 20$  mm,  $f = 5.8$  GHz.

The measured radiation patterns of right-hand circularly polarized field of the cylindrical helix antenna in the elevation planes  $\phi = 0, 180^\circ$  and  $\phi = 90^\circ, 270^\circ$  are presented in Figure 6.19 in comparison to the radiation pattern obtained by the CST simulator for the same antenna model. The measured radiation patterns of the cylindrical helix antenna show good agreement with those obtained by simulation.



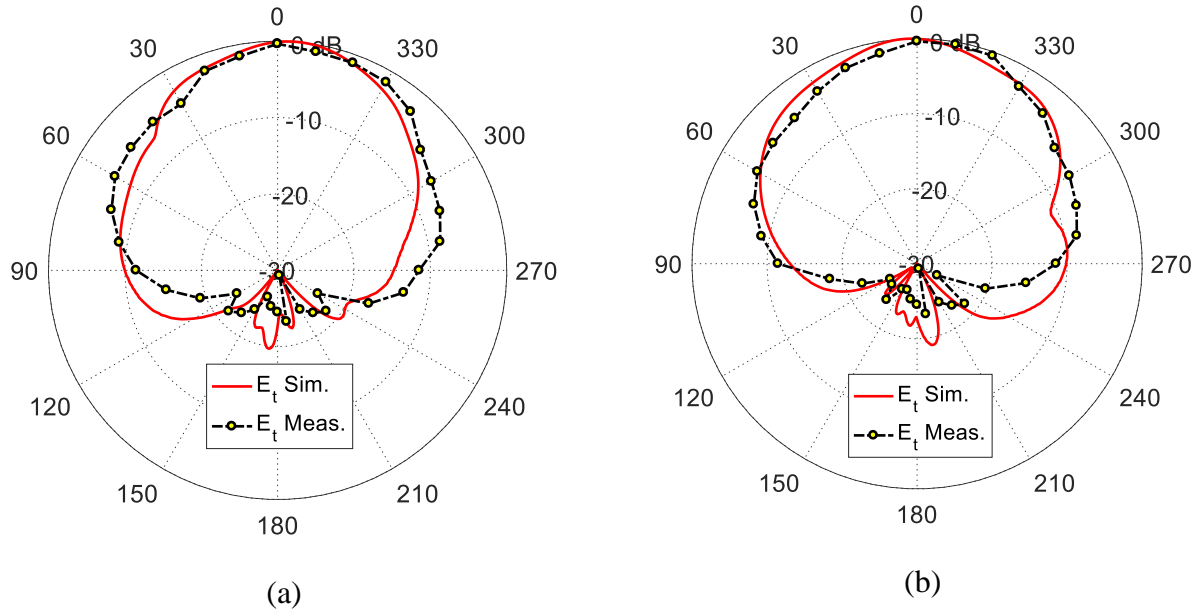


**Figure 6.19:** Comparison between the patterns obtained by experimental measurements and CST simulator for the total field produced by the conical-helix/monopole antenna (placed on the human body) in the planes, (a)  $\phi = 0, 180^\circ$ , and (b)  $\phi = 90, 270^\circ$ ,  $f = 5.8$  GHz.

## 6.8. Power Density and SAR Distribution in the Human Tissues due to Radiation from the Proposed On-Body Antenna

This section is concerned with the experimental measurement and the numerical assessment of the power density distribution on the surface of the human body while the proposed conical-helix/monopole antenna is mounted on the human body and being excited at 3.0 GHz. Also, the SAR distribution in the different tissues of the three-layer human body model described in Section 6.4 using the semi-analytic model explained in Chapter 3.

### 6.8.1. Experimental Assessment of the Power Density Distribution on the Surface of the Human Body

For experimental assessment of the power density distribution on the human body surface, the radiation hazard meter Extech® model 480846 is used with its isotropic probe touching the human body as shown in Figure 6.20 while the conical-helix/monopole antenna (covered with the radome) is placed on the patient chest and excited with input power  $P_{in} = 0$  dBm (1 mW) at

$f = 3.0$  GHz. The power density meter shows a reading of  $0.041 \mu\text{W}/\text{cm}^2$  when antenna is oriented with tip pointing to the power density meter as shown in Figure 6.20(a). When the antenna is oriented with the tip of the conical helix pointing to the room ceil (normal operation) the reading of the power density meter is  $0.276 \mu\text{W}/\text{cm}^2$ . Comparing the two readings of the power density meter taking the orientations of the antenna into consideration indicates that the radiation of the conical helix antenna has mainly broadside radiation at this frequency. However, the power density still ensures safe values of the electromagnetic exposure.

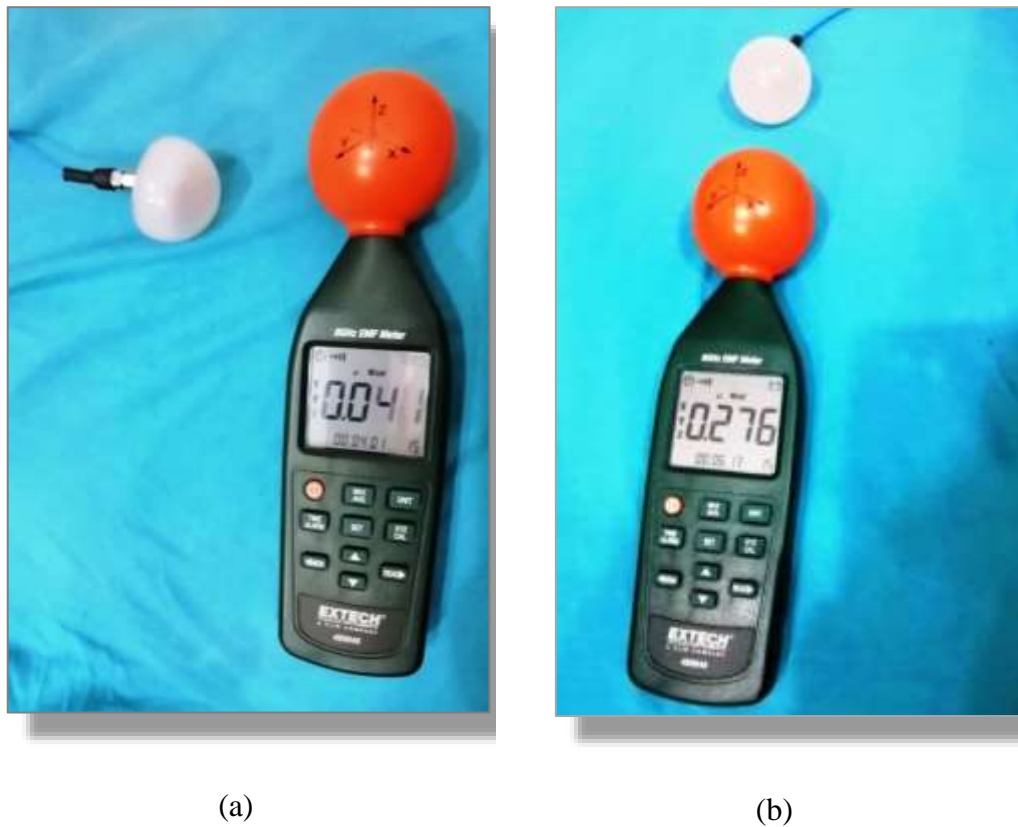


**Figure 6.20:** Measurement of the power density distribution near the skin of the body using the radiation hazard meter Extech® model 480846 when the conical helix antenna is excited with input power  $P_{in} = 0$  dBm at  $f = 2.45$  GHz, (a) The antenna is oriented with tip pointing to the power density meter , (b) The antenna is oriented with tip pointing to the room ceil (normal operation).



### 6.8.2. Semi-Analytic Assessment of the Power Density and SAR Distribution in the Tissues of the Human Body

The geometric model of the proposed conical-helix/monopole antenna shown in Figure 6.2 is generated by a Matlab program. This program applies the semi-analytic technique described in chapter 3 to evaluate the electric field distribution over the body surface within the rectangular area bounded by the dashed rectangle shown in Figure 4.1.

The electric field intensity distribution on the skin surface over the rectangular area (indicated by the dashed rectangle in Figure 4.1) is presented in Figure 6.21 using the shown color code when the operating frequency is 3.0 GHz and the input power to the conical-helix/monopole antenna is 0 dBm (1 mW). It is shown that the electric field magnitude does not exceed 5.5 V/m. Figure 6.22(a) presents the corresponding distribution of the microwave power density just on the skin surface over the rectangular area surrounded by the blue dashed rectangle shown in Figure 4.1 due to the placement of the conical-helix/monopole antenna with its base touching the human body surface while being excited by input power  $P_{in} = 0$  dBm at  $f = 3.0$  GHz. It should be noted that the power density distribution is evaluated using the semi-analytic technique developed in chapter 3. It is shown that the maximum power density on the skin doesn't exceed  $0.035$  mW/cm<sup>2</sup>, which ensures safe level of electromagnetic exposure. The corresponding SAR distributions in the tissues of skin, fat, and muscle over the area of interest are presented in Figures 6.22(b), 6.22(c), and 6.22(d). The SAR is evaluated using (19), where the magnitude of the electric field in the human tissues is evaluated using the semi-analytic technique developed in chapter 3. It is shown that the maximum value of the SAR occurs in the skin tissues whereas the fat tissues has the minimum value of the SAR due to the higher conductivity of the skin tissue and larger depth of the fat tissues inside the human body. The maximum SAR in all the tissues doesn't exceed  $0.3$  W/kg, which ensures safe level of electromagnetic exposure.

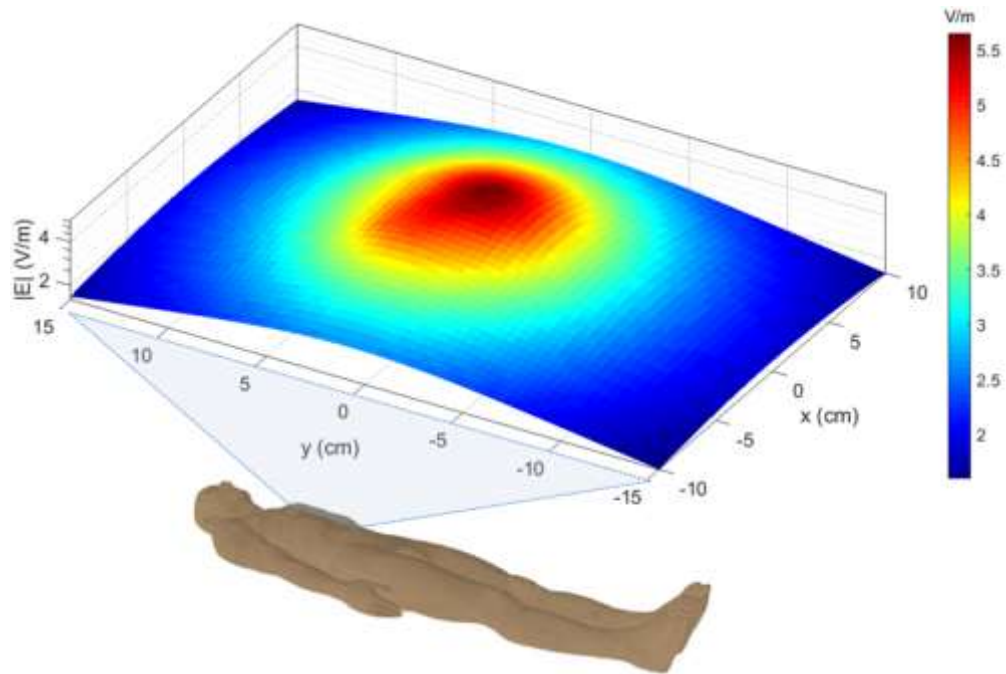
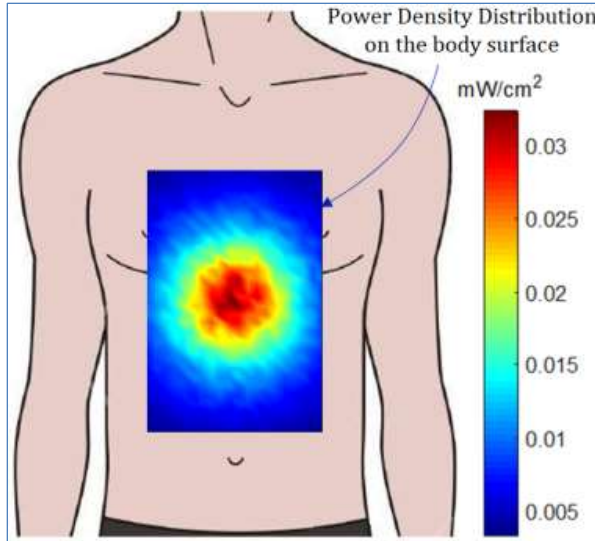
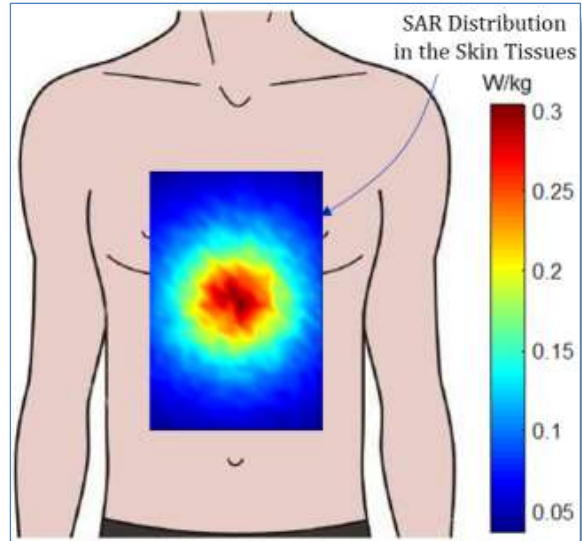


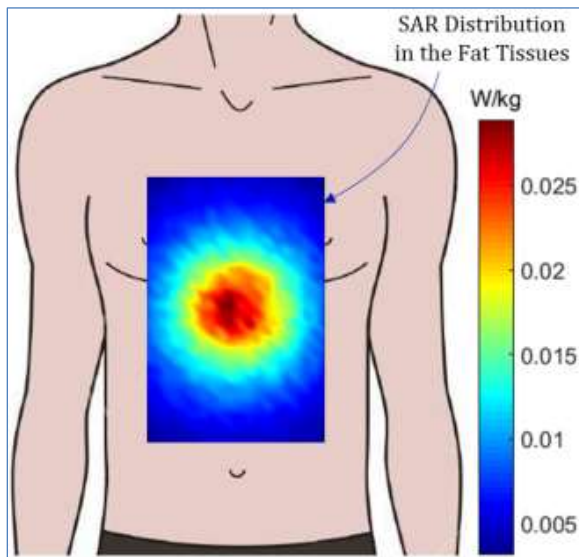
**Figure 6.21:** Electric field distribution in the plane of the biosensor antennas (parallel to the skin of the human body) due to the proposed conical-helix/monopole antenna working as a central on-body antenna,  $N_T = 3$ ,  $H_M = 20$  mm,  $H_H = 20$  mm,  $\theta_H = 36.5^\circ$ ,  $D_H = 20$  mm,  $f = 3.0$  GHz.



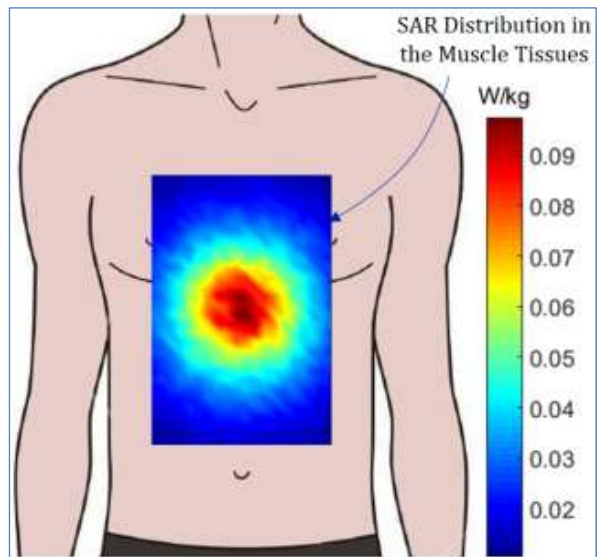
(a)



(b)



(c)



(d)

**Figure 6.22:** Distribution of (a) Microwave power density on the surface of the body, (b) SAR in the skin tissues (c) SAR in the fat tissues, and (d) SAR in muscle tissues, due to conical-helix/monopole antenna fed with input power  $P_{in} = 0 \text{ dBm}$  at  $f = 3.0 \text{ GHz}$ ; the antenna dimensions are  $N_T = 3$   $H_M = 20 \text{ mm}$ ,  $H_H = 20 \text{ mm}$ ,  $\theta_H = 36.5^\circ$ ,  $D_H = 20 \text{ mm}$ ,  $f = 3.0 \text{ GHz}$ .

## **6.9. Assessment of the On/Off-Body Communication System Performance using the Proposed On-Body Antenna**

This section is concerned with the presentation of some numerical results for the assessment of the performance of the WBAN communication system described previously according to the channel model described in chapter 3. It is assumed that all the biosensor antennas (both on-body and in-body) in the WBAN are isotropic and lossless and distributed on the surface of the human body. The losses are caused only by the microwave propagation inside the lossy tissues on the surface of the human body.

### **6.9.1. Distribution of the SNR and BER on the Skin due to the Proposed On-Body Antenna**

The distribution of the SNR due to AGWN of power spectral density  $N_0/2 = 1 \times 10^{-3}$  mW/Hz at isotropic receiving biosensor antennas distributed on the skin surface over the rectangular area (indicated by the dashed rectangle in Figure 4.1) is presented in Figure 6.23(a) using the shown color code when the operating frequency is 3.0 GHz and the input power to the conical-helix/monopole antenna is 0 dBm (1 mW). The corresponding distributions of BER over the same area of the human body surface are presented in Figures 6.23(b) and 6.23(c) under the assumption of using 8-symbol and 16-symbol in the  $M$ -ary PSK modulation technique, respectively. In spite of the low power fed to the proposed on-body conical-helix /monopole antenna (only 1 mW), and thanks to the optimized design of this antenna, the BER doesn't exceed  $1.2 \times 10^{-6}$  and  $5.3 \times 10^{-4}$  for the two modulation schemes.

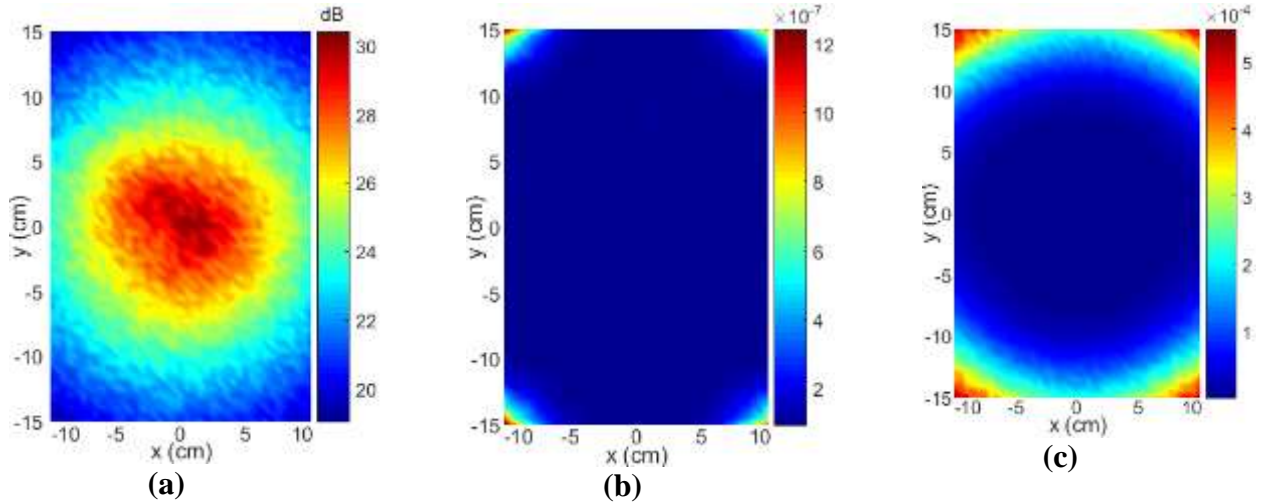


**Figure 6.23:** Distribution of the SNR and the corresponding BER over the area of the skin within which the (isotropic) biosensor antennas are allocated due to a central on-body conical-helix/monopole antenna fed with input power,  $P_{in} = 0$  dBm at  $f = 3.0$  GHz, (a) SNR, (b) BER for 8-symbol PSK, (c) BER for 16-symbol PSK, the antenna dimensions are  $N_T = 3$   $H_M = 20$  mm,  $H_H = 20$  mm,  $\theta_H = 36.5^\circ$ ,  $D_H = 20$  mm,  $f = 3.0$  GHz.

### 6.9.2. Dependence of the SNR and BER on the Height of the On-Body Antenna above the Skin

The height at which the conical helix antenna (proposed for on-body communications in WBANs) is placed has a significant effect on the SNR and the BER as shown in Figures 6.24(a) and 6.24(b), respectively, for different values of the input power to the proposed on-body conical-helix/monopole antenna. As shown in these figures, the SNR is increased and, hence, the BER is decreased with increasing the height of the conical helix above the surface of the human body.

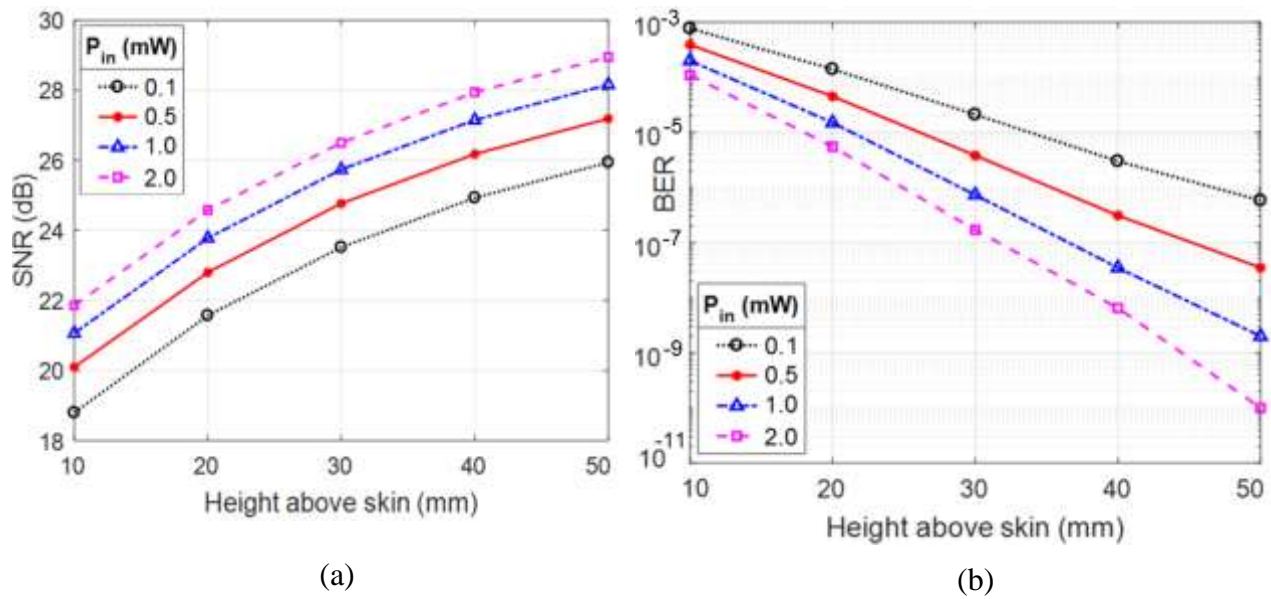


**Figure 6.24:** Dependence of the minimum SNR and the corresponding BER on the height at which the conical-helix/monopole antenna is placed above the surface of the human body when used in WBAN as a central on-body antenna fed with different values of the input power at  $f = 3.0$  GHz, (a) Minimum SNR, (b) Maximum BER.

## 6.10. The Proposed Dual-Band Monopole/Spiral Antenna

This section is concerned with the description of the monopole/spiral antenna proposed to work as on-body central antenna in WBANs. This antenna is dual-band and designed to communicate (through its far-field end-fire pattern) with the ceil-mounted WiMAX antenna at 5.8 GHz, and to communicate (through either its near-field or far-field broadside pattern) with the on-skin and in-body (implanted) biosensor antennas at 3.0 GHz. The monopole is a part of the wire antenna structure that is responsible for broadside radiation at 3.0 GHz whilst the single-arm spiral produces end-fire radiation pattern at 5.8 GHz. The proposed antenna has a small size as shown in Figure 6.25(a) and can be mounted on the human body as a button attached to the clothes as shown in Figure 6.25(b) and (c). Excluding the SMA connector, the antenna diameter is 20 mm and the antenna height is 15 mm.

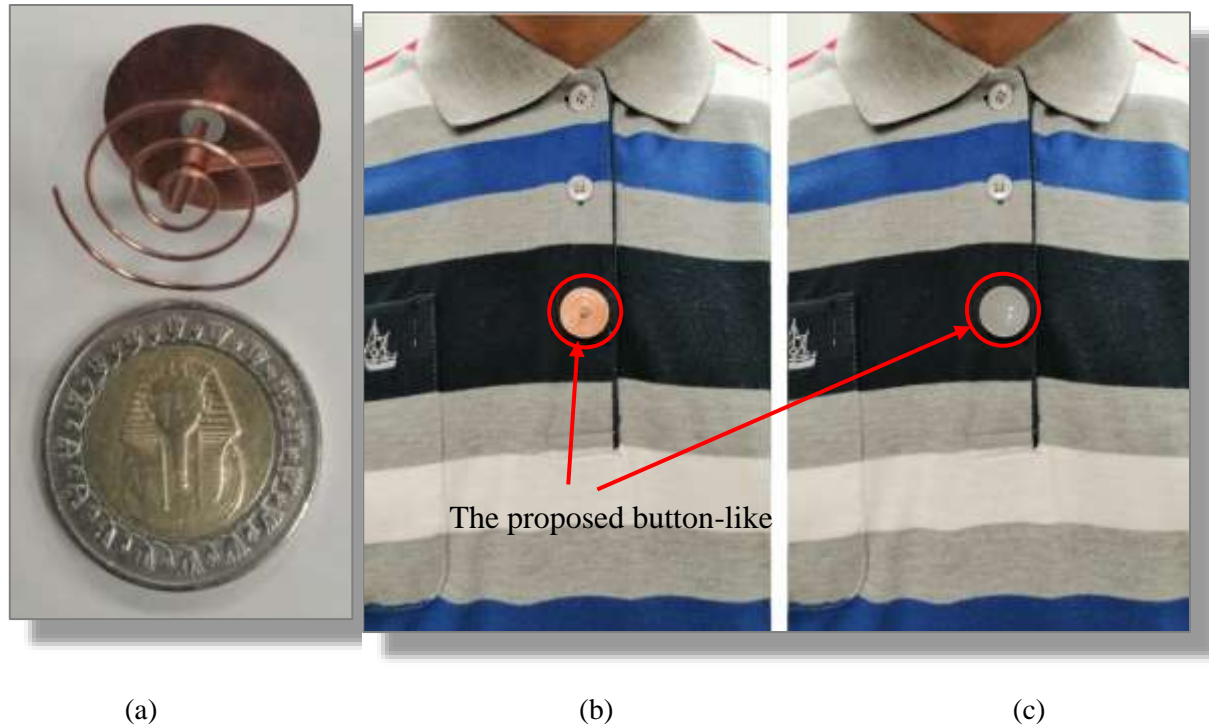


**Figure 6.25:** The fabricated prototype of the proposed monopole/spiral antenna (a) the antenna size compared with the size of a standard one-inch coin, (b) the uncovered antenna attached to the clothes as a button, (c) the antenna covered with the radome and attached to the clothes as a button.

The proposed antenna is designed to have a balloon-shaped radiation pattern to communicate with the Wi-Fi system at 5.8 GHz and to have a figure-of-eight radiation pattern to communicate with the on-body and in-body biosensor antennas at 3.0 GHz. The configuration of the antenna system required for on/off-body communications in the WBANs is illustrated in Figure 6.26, where the monopole/spiral antenna proposed in the present work to play the role of a central on-body antenna can be attached to clothes of the patient as wearable button-like antenna.



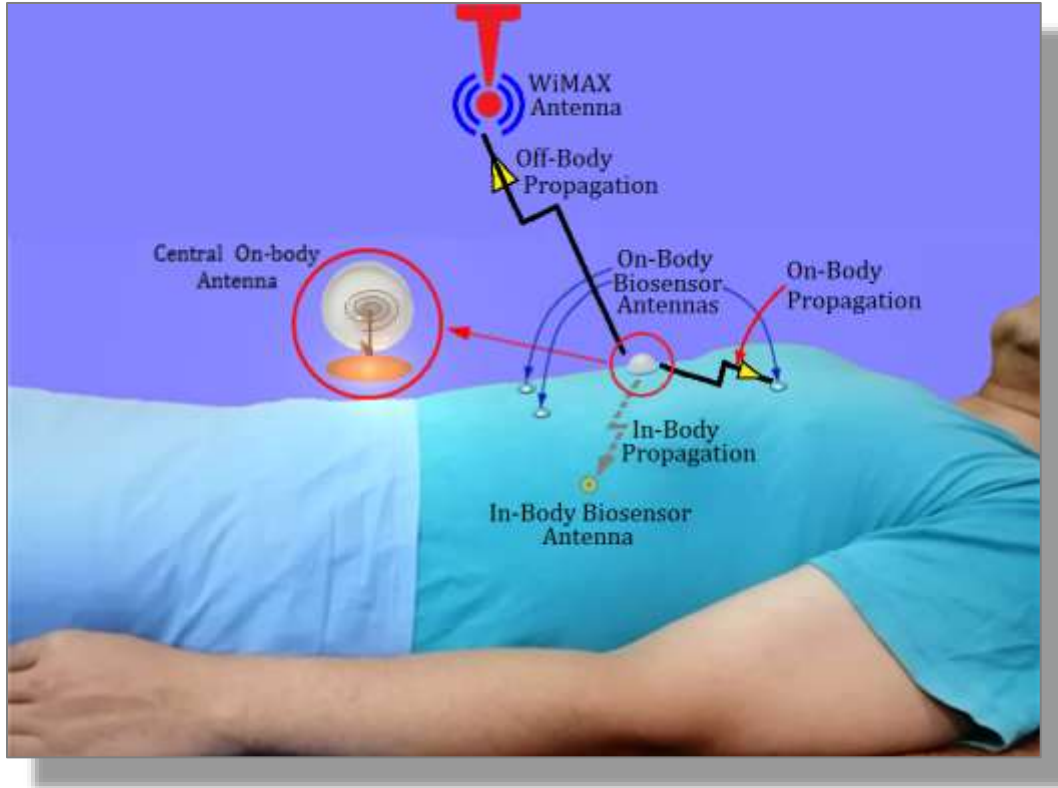


**Figure 6.26:** The monopole/spiral antenna proposed in the present work is attached to clothes of the patient as wearable button antenna. The on-body central antenna communicates with the on-body and in-body biosensor antennas via on-body/in-body microwave propagation. The on-body antenna connects the WBAN to the Wi-Fi through off-body (far-field) radiation into free space.

The geometric model of the dual-structure of the proposed on-body antenna is shown in Figure 6.27. The monopole length is  $H_M$ ; the external diameter of the spiral is  $D_S$ . The equation of the planar single-arm spiral can be expressed as follows.

$$r = \frac{D_S}{N\pi} \phi$$

where  $(r, \phi)$  are the coordinates of a point on the planar spiral.



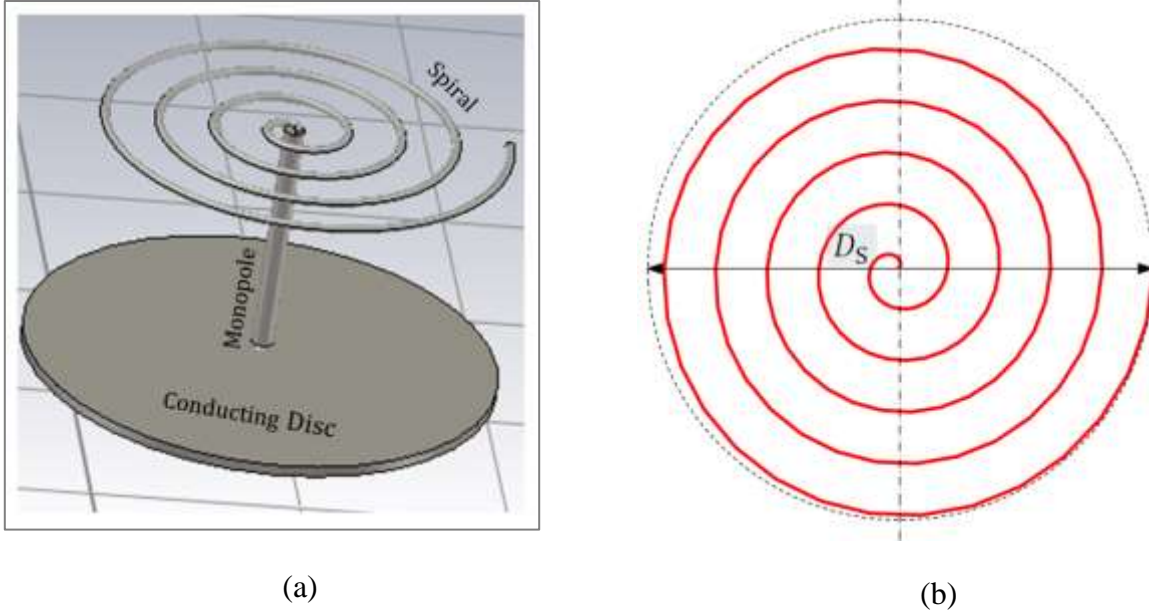


**Figure 6.27:** Geometry of the monopole/spiral antenna (a) Geometric model of the proposed antenna in the CST simulator, (b) Schematic antenna dimensional parameters.

The design of the proposed antenna permits the use of low power (few milli-Watts) for communication with the on-body and in-body biosensor antennas at 3.0 GHz and allows the use of higher level of power while communicating with the Wi-Fi antenna (at 5.8 GHz). The power consumption is, thus, optimized leading to low level of the SAR in the human tissues and long lifetime of the batteries required to energize the transceiver attached to the central on-body antenna and the biosensor antennas.

The geometric model of the proposed monopole/spiral antenna in the commercially available CST simulator when mounted directly on the top layer of the three-layer body model is presented in Figure 6.28. The monopole has a length of  $H_M = 15$  mm, the external diameter of the 3-turn planar spiral is  $D_S = 20$  mm. The diameter of the circular copper plates used for simulation is 20 mm. The CST simulator is used to evaluate the far-field pattern at 5.8 GHz. The three-layer planar model, described in Figure 4.1, is placed just below the antenna base as shown in Figure 6.28 to represent the human body.

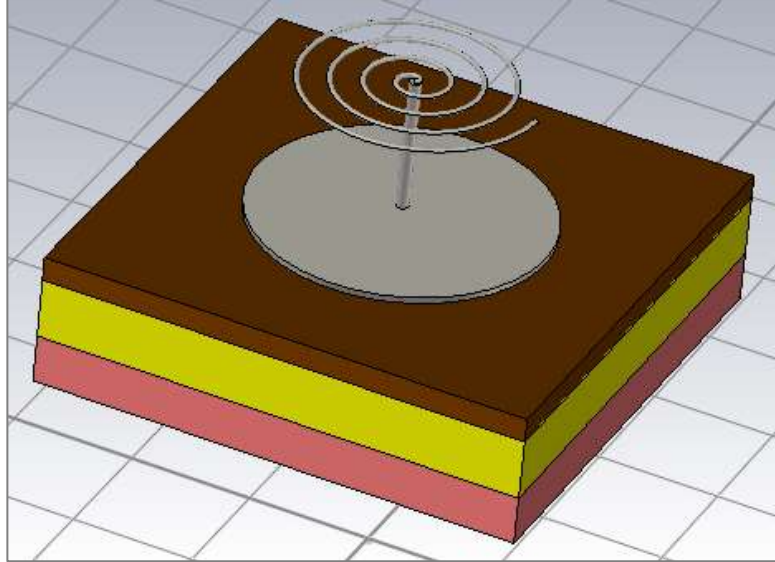


**Figure 6.28:** Model of the proposed monopole/spiral on-body antenna placed on the three-layer (skin-fat-muscle) model of the human body (the dimensions of the model used in the simulator are much larger than those shown in the figure); the antenna has the dimensional parameters  $N = 3$ ,  $H_M = 1.5$  mm, and  $D_S = 20$  mm,.

The evaluation of the field distribution on the top surface of the skin layer is a necessary requirement for the performance assessment of the on-body communications between the proposed central antenna and distributed on-skin biosensor antennas. Also, the calculation of the electric field penetrating the human tissues namely the skin, fat, and muscle tissues is necessary for the evaluation of the SAR in these tissues and for the evaluation of the power received by the in-body biosensor antennas.

It should be noted that the human body region of concern in the present study is the area surrounded by the blue dashed rectangle shown in Figure 4.1. The field distribution over this area is evaluated under the assumption of a flat surface of this region of the body. It should be noted that this rectangular area has the dimensions  $L_x = 20$  cm and  $L_y = 30$  cm; these dimensions are considered throughout the following presentations and discussions of numerical results unless otherwise indicated.

## **6.11. Fabrication of the Monopole/spiral Antenna Prototype**

This section is concerned with the procedure of fabricating a prototype for the proposed monopole/spiral antenna. The antenna is fabricated using a copper wire of 0.5 mm. Two circular copper discs of 40 mm and 20 mm diameters are used for experimental assessment. Due to high conductivity of the copper and the absence of any dielectric parts, the Ohmic losses of this antenna can be negligible.

### **6.11.1. Constructing the Single-Arm Spiral and Monopole Wires**

For the fabrication of a prototype of the proposed antenna, a copper wire is wrapped to take the shape of the single-arm spiral with the dimensions given in the previous section. A wire wrapped in the right-hand sense produces right-hand circularly polarized field whereas a wire wrapped in the left-hand sense, as that shown in Figure 6.29(a), produces left-hand circularly polarized field.

The wrapped planar spiral is then welded at its origin to a straight wire monopole (slightly shorter than a quarter-wavelength at 3.0 GHz) to form the complete wire structure of the antenna as shown in Figure 6.29(a). A ground plane and a feeding coaxial connector are necessary for the operation of such a spiral/monopole antenna. A circular copper disc of 4 cm diameter is prepared for this purpose and an SMA coaxial connector is mounted with its outer conductor welded to the circular disc as shown in Figure 6.29(b). The dual-structure of the wire antenna, shown in Figure 6.29(a), is mounted on a circular copper plate by welding the monopole free terminal to the inner conductor of the SMA connector to form the entire antenna structure shown in Figure 6.30(a). A foam tube can be used to enclose the wire monopole for electric insulation between the monopole and the planar spiral.

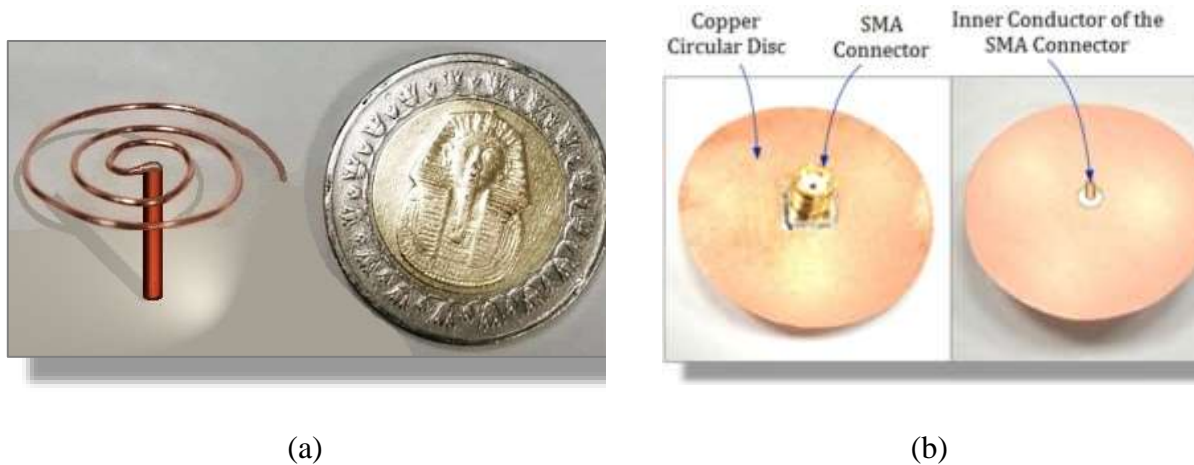


**Figure 6.29:** A copper wire is wrapped to form a single-arm planar spiral and then welded to a straight wire to form the dual wire structure of the monopole/spiral antenna proposed to play the role of a central on-body antenna for WBAN (a) the dual wire structure of the antenna, (b) the circular copper disc on which the wire structure is mounted.

### 6.11.2. Adding Impedance Matching Element to the Antenna Structure

To minimize the return loss, the wire antenna should be matched to the  $50\Omega$  SMA coaxial connector. The single-arm spiral antenna is characterized by an advantage of low imaginary part of the input impedance at the design frequency for end-fire radiations. Unfortunately, it is, also, characterized by a resistive part of the impedance that is much smaller than  $50\Omega$ . The real part of the impedance can be increased to  $50\Omega$  by attaching a small conductive rectangular patch to the wire of the antenna near the feed point as shown in Figure 6.30(b). The size and location of such rectangular and rectangular patches used for impedance matching can be experimentally adjusted while being attached to the antenna structure with the aid of a Vector Network Analyzer (VNA) to minimize the reflection coefficient  $|S_{11}|$  over the frequency bands of interest.

### 6.11.3. Covering the Wire Antenna with Hemispherical Radom for Mechanical Protection

For protecting the wrapped wires of the fabricated antenna from deformation due to unavoidable mechanical stresses, a hemispherical radome of very thin dielectric material is used to cover the antenna structure as shown in Figure 6.30(c). As this radome is made of very thin dielectric material ( $\epsilon_r = 1.5$ ), it is almost electromagnetically transparent at the microwave

frequencies and, consequently, has no effect on the antenna characteristics. Finally, for the purpose of microwave measurement, the antenna is connected to flexible 50Ω coaxial cable through the SMA connector mounted on the circular disc.

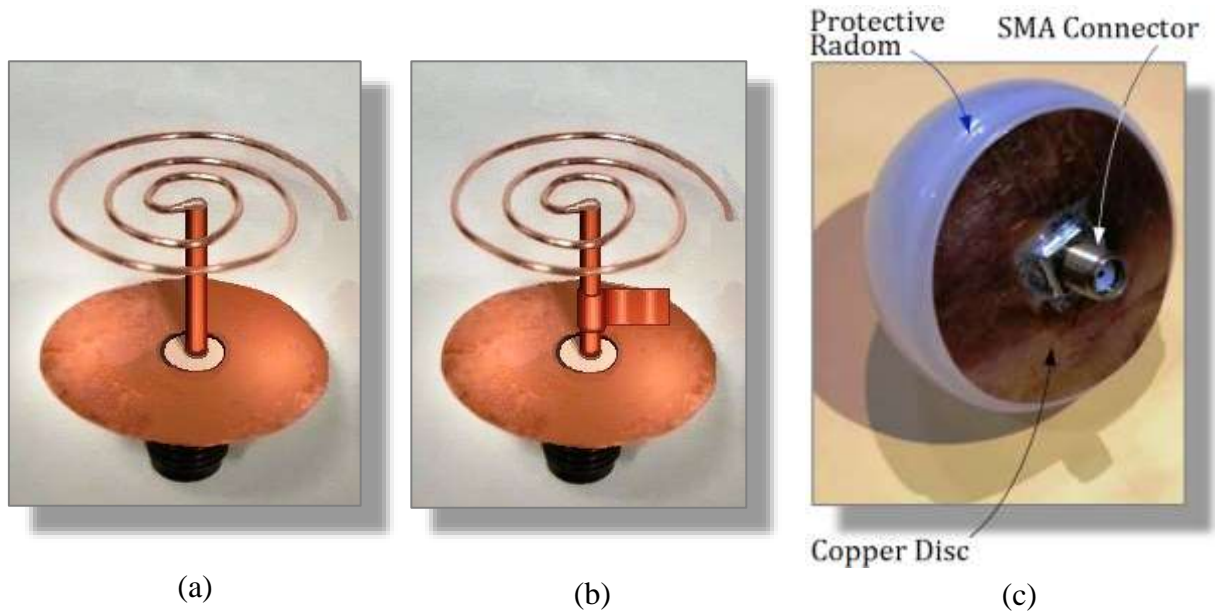


**Figure 6.30:** The wire monopole/spiral structure is mounted on a circular copper disc and connected to the inner conductor of an SMA connector (a) without impedance matching, (b) with a rectangular patch connected to the monopole near the feed point for impedance matching, (c) the matched antenna covered with hemispherical radome for mechanical protection.

## 6.12. Results of Electromagnetic Simulation and Experimental Measurements

This section is concerned with the presentation and discussion of the electromagnetic simulation results and experimental measurements to study the characteristics of the monopole/spiral antenna proposed to work as on-body central antenna for WBAN. The presented results are, also, concerned with investigating the performance of the on/off-body communication system employing the proposed antenna including the power consumption, the SNR and BER and the associated SAR in the different human tissues near the body surface (skin, fat and muscle).

### 6.12.1. Return Loss and Impedance Bandwidth of the Proposed On-Body Antenna

The reflection coefficient at the antenna port is measured using VNA of the Agilent FieldFox N9918A. The frequency response of the reflection coefficient  $|S_{11}|$  is measured over a wide range of the frequency. The experimental measurements are compared to the numerical results obtained by electromagnetic simulation using the commercially available CST microwave studio suite.

The experimental setup for measuring the frequency response of the reflection coefficient  $|S_{11}|$  of the monopole/spiral antenna is shown in Figure 6.31. The comparison between measurement curves appearing on the screen of the measurement device presented in Figures 6.31(a) and 6.31(b) shows that the reflection coefficient of the monopole/spiral antenna is almost unaffected by the placement of the radome to cover the antenna.

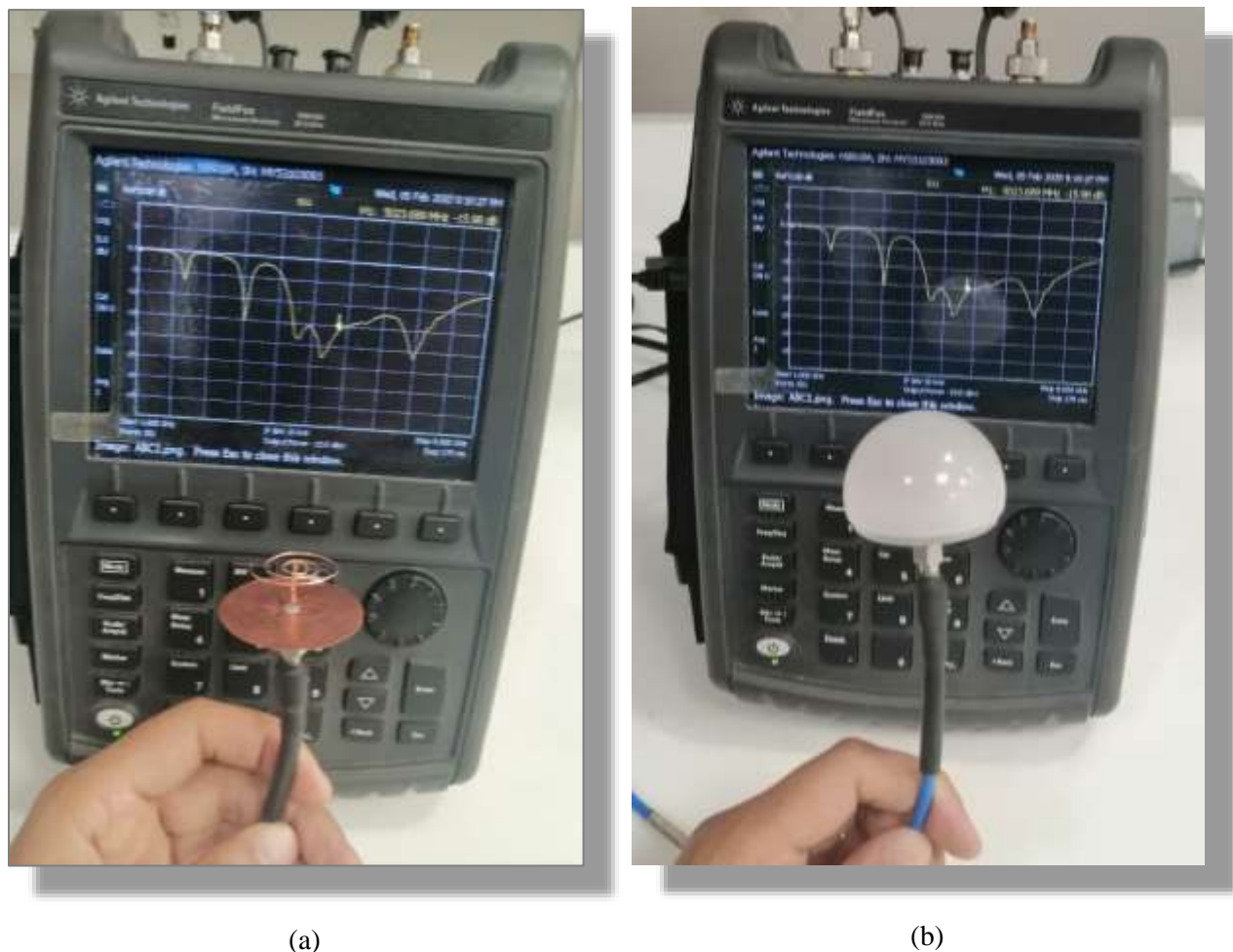


**Figure 6.31:** Measurement of the reflection coefficient  $|S_{11}|$  of the monopole/spiral antenna using the VNA of the Agilent Field Fox N9918A, (a) uncovered antenna, (b) antenna covered with the hemispherical radome.



Figure 6.32 presents the measured frequency responses of the reflection coefficient  $|S_{11}|$  of the monopole/spiral antenna. Both the experimental measurements and the simulation results show that the antenna impedance is matched to  $50\Omega$  over the two frequency bands of interest. The impedance matching bandwidth (for  $|S_{11}| \leq -10$  dB) according to the experimental measurement is about 11% at 3.0 GHz and about 22% at 5.8 GHz. The sharp minimum of the  $|S_{11}|$  frequency response shows that the antenna is resonant at the frequency 3.0 GHz. This corresponds to the first resonance of the quarter-wavelength monopole. However, the bandwidth at 3.0 GHz is fairly acceptable for high-speed data transmission between the biosensor antennas and the proposed central on-body antenna. On the other hand, the bandwidth at the Wi-Fi frequency 5.8 GHz is much wider as this frequency can be considered a travelling-wave antenna, which enables the central on-body antenna to transmit data at much higher speed and, thus, facilitates the transmission of large data records of the patient state through the Wi-Fi communication system.

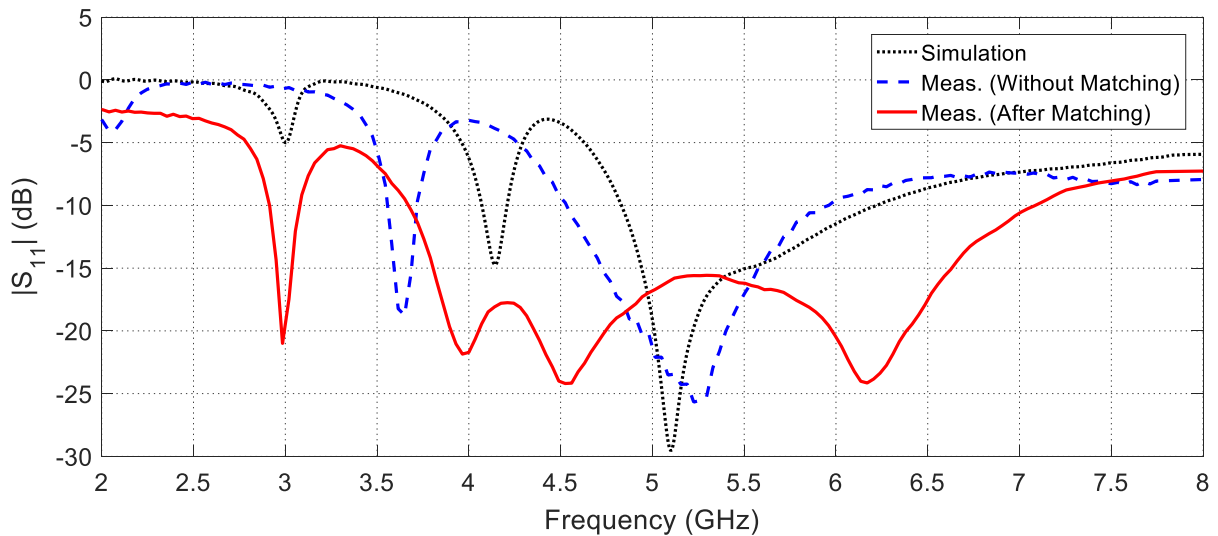


**Figure 6.32:** Comparison between the measured frequency response of the reflection coefficient  $|S_{11}|$  of the proposed monopole/spiral antenna and that obtained by electromagnetic simulation using the commercially available CST simulation package.

### 6.12.2. Simulation and Experimental Assessment of the Radiation Patterns of the Proposed On-Body Antenna

The CST simulation package is used to evaluate the far-field radiation patterns produced by the monopole/spiral antennas at 3.0 GHz and 5.8 GHz using the three-layer model of the human body described in Figure 6.28.

On the other hand, the experimental setups for measuring the radiation patterns of the proposed antenna using the VNA of the Agilent FieldFox N9918A while being placed in free space and mounted on the human body as done for the previous types of antennas in this work as shown in Figure 6.33. A reference right-hand circularly polarized helical antenna is connected to port '2' of the VNA whereas the antenna under test is connected to port '1' to obtain its radiation pattern by measuring the transmission coefficient  $|S_{21}|$  at the frequencies of concern.

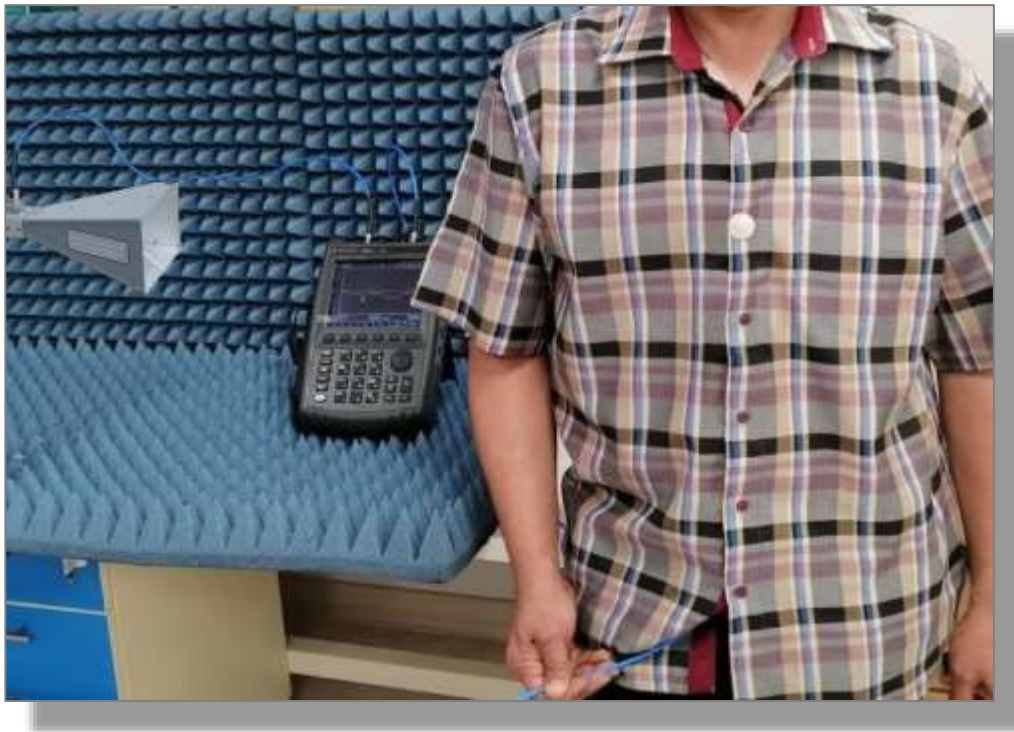


**Figure 6.33:** Experimental setup for measuring the radiation patterns of the monopole/spiral antenna when mounted on the human body using the VNA of the Agilent Field Fox N9918A.

#### 6.12.2.1. Radiation Patterns at 3.0 GHz

The radiation pattern produced at by the monopole/spiral antenna at 3.0 GHz is obtained by electromagnetic simulation when the antenna is placed in free space. Also, the experimental setup shown in Figure 6.33 is used to measure the radiation pattern at the same frequency. The



two-dimensional radiation patterns obtained by simulation and experimental measurements are presented in Figure 6.34 in comparison to each other showing good agreement. As shown in this figure, the radiation pattern is omnidirectional in the azimuth plane and broadside in the elevation planes with null in the direction parallel to the antenna axis (i.e. normal to the human body surface). This shape of the radiation pattern means that the quarter-wavelength monopole is the active part of the composite wire antenna as it is resonant at this frequency and, consequently, it is responsible for the radiation at 3.0 GHz.

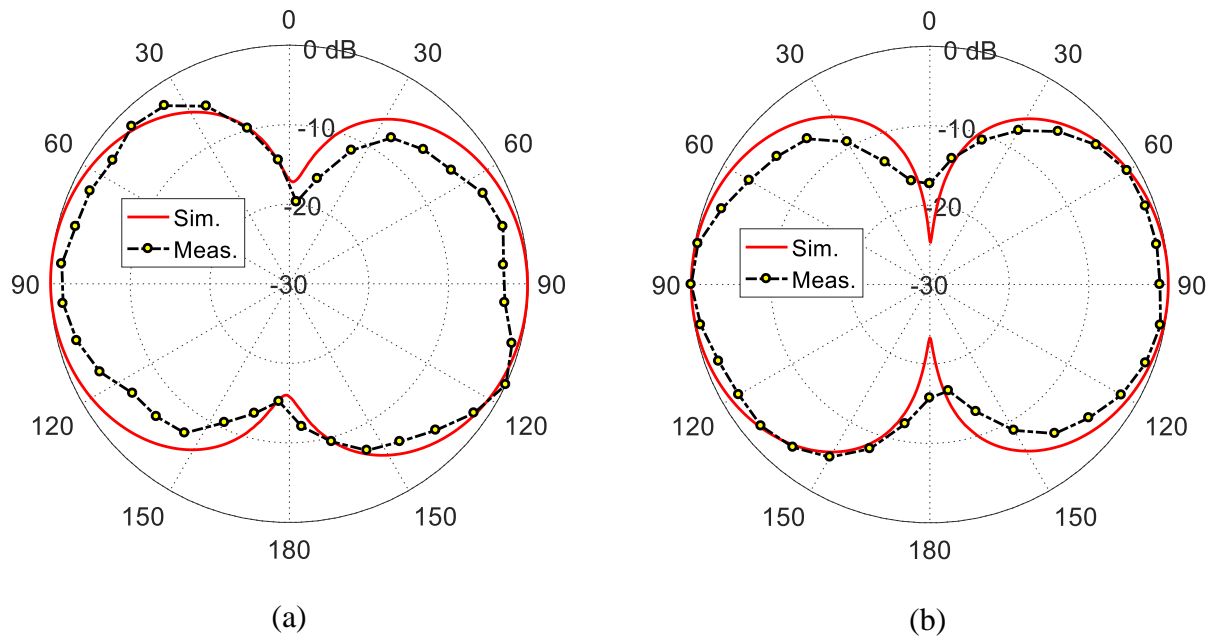


**Figure 6.34:** Comparison between the radiation patterns obtained by simulation and experimental measurements for the total field produced by the monopole/spiral antenna (placed in free space) in the planes, (a)  $\phi = 0, 180^\circ$ , and (b)  $\phi = 90, 270^\circ$ ,  $f = 3.0$  GHz; the antenna dimensions are  $N = 3$ ,  $H_M = 15$  mm, and  $D_S = 20$  mm.

The far-field pattern produced at 3.0 GHz by the on-body antenna when mounted on the three-layer model of the human body is obtained by electromagnetic simulation. The resulting three-dimensional radiation pattern of the total radiated field is presented in Figure 6.35. The experimental setup described in Figure 6.33 is used to evaluate the two-dimensional radiation patterns in the elevation planes when the antenna is mounted on a real human body. These patterns are presented in Figure 6.36 in comparison with the patterns obtained by electromagnetic simulation. As shown in the figure, the experimental measurements and the

simulation results show good agreement. It is clear that the radiation at this frequency is mainly produced by the monopole part of the composite structure of the wire antenna. As shown in this figure, the radiation pattern is omnidirectional in the azimuth plane and broadside in the elevation planes with null in the direction parallel to the antenna axis (normal to the body surface). Thus, the radiated power at 3.0 GHz is mainly directed towards the body surface or into the human tissues near the body surface. Such a radiation pattern makes the monopole/spiral antenna appropriate to perform on-body and in-body communications with the biosensor antennas. When this pattern is compared to that obtained when the antenna is placed in free space, Figure 6.34, it is shown that the human body has the effect of reducing the backscatter and, thus, increasing the front-to-back ratio of the radiation.

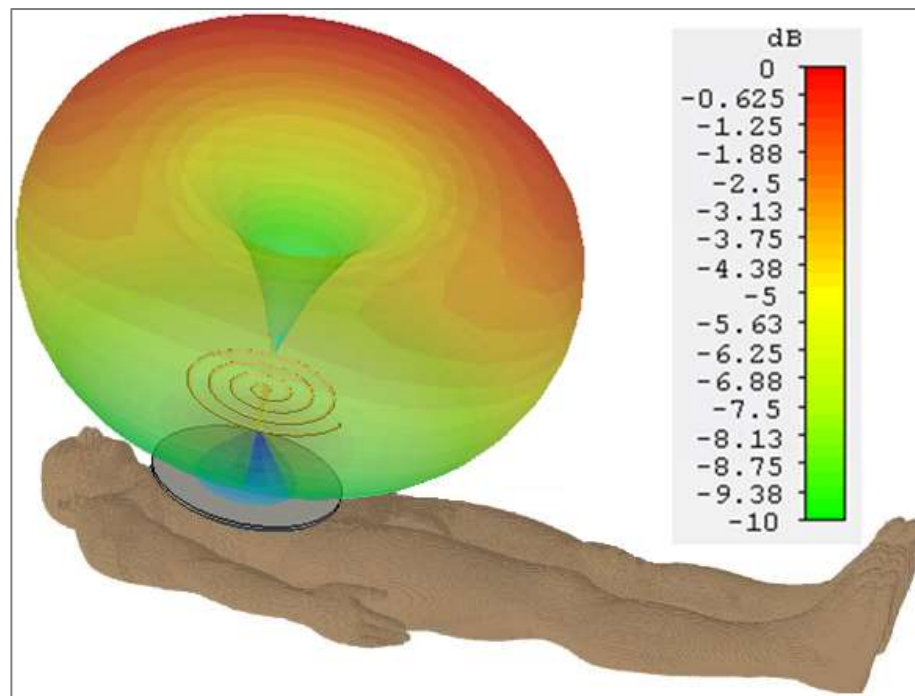


**Figure 6.35:** Three-dimensional far-field radiation pattern of the on-body monopole/spiral antenna of dimensions,  $N = 3$ ,  $H_M = 15 \text{ mm}$ , and  $D_S = 20 \text{ mm}$ ,  $f = 3.0 \text{ GHz}$ .

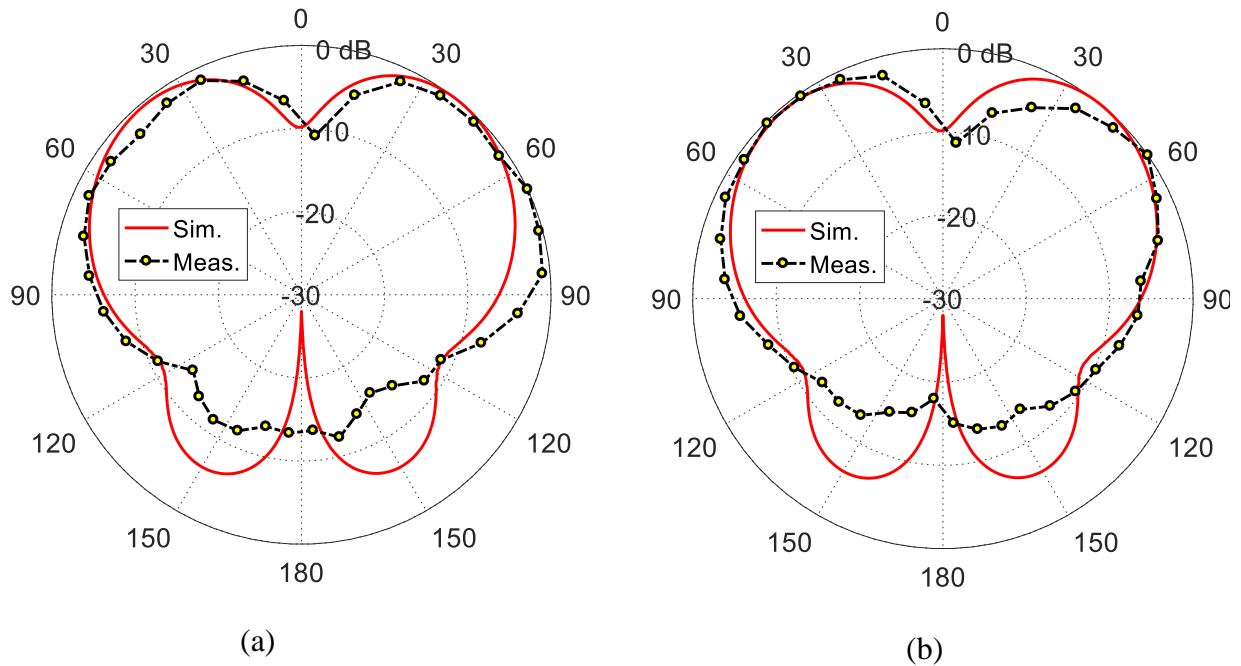


**Figure 6.36:** Comparison between the patterns obtained by simulation and experimental measurements for the total field produced by the monopole/spiral antenna (placed on the human body) in the planes, (a)  $\phi = 0, 180^\circ$ , and (b)  $\phi = 90, 270^\circ$ ,  $f = 3.0$  GHz; the antenna dimensions are  $N = 3$ ,  $H_M = 15$  mm, and  $D_S = 20$  mm.

### 6.12.2.2. Radiation Patterns at 5.8 GHz

The radiation patterns produced at by the monopole/spiral antenna at 5.8 GHz are obtained by electromagnetic simulation when the antenna is placed in free space. Also, the experimental setup shown in Figure 6.33 is used to measure the corresponding radiation patterns at the same frequency. The two-dimensional radiation patterns obtained by electromagnetic simulation and experimental measurements are presented in Figure 6.37 in comparison to each other showing good agreement. As shown in this figure, the radiation patterns show omnidirectional radiation in the azimuth plane and end-fire (balloon-like) radiation in the elevation planes. The maximum radiation is obtained in the direction parallel to the antenna axis. This shape of the radiation pattern means that single-arm spiral is the active part of the composite wire antenna at this frequency and, consequently, it is responsible for the radiation at 5.8 GHz.

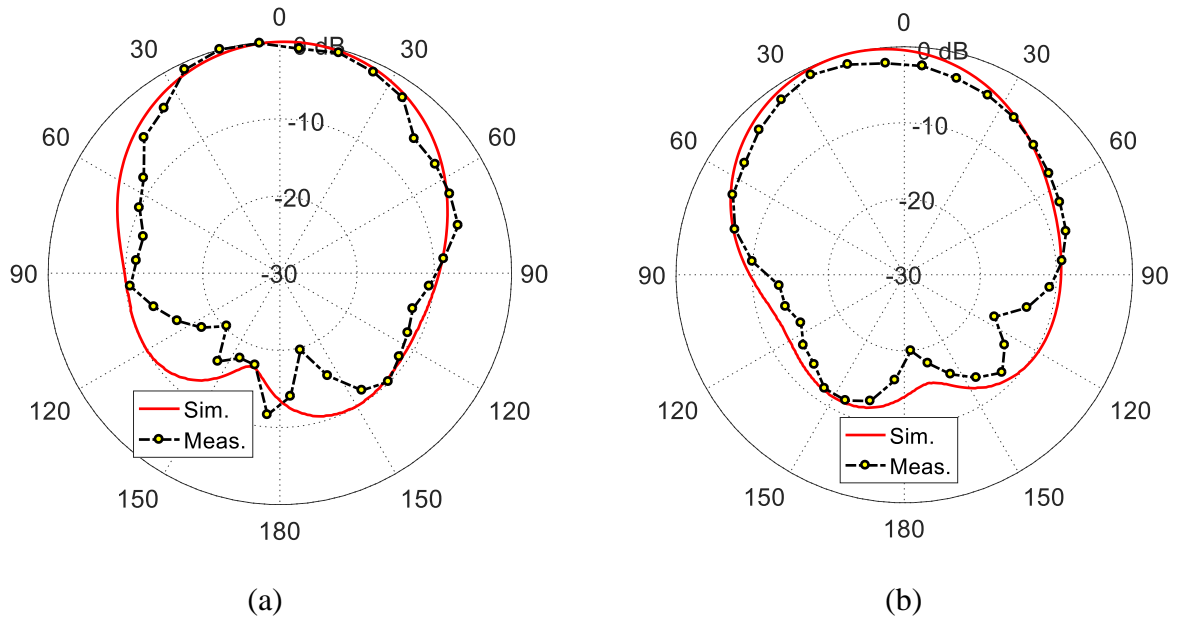


**Figure 6.37:** Comparison between the simulated and measured far-field radiation patterns of the monopole/spiral antenna in the planes, (a)  $\phi = 0, 180^\circ$ , and (b)  $\phi = 90, 270^\circ$ ,  $f = 5.8 \text{ GHz}$ ; the antenna dimensions are  $N = 3$ ,  $H_M = 15 \text{ mm}$ , and  $D_S = 20 \text{ mm}$ .

The far-field pattern produced at 5.8 GHz by the proposed on-body antenna when mounted on the three-layer model of the human body is obtained by electromagnetic simulation. The three-dimensional radiation pattern of the total radiated field is presented in Figure 6.38. The experimental setup described in Figure 6.33 is used to evaluate the two-dimensional radiation patterns in the elevation planes when the antenna is mounted on a real human body. These patterns are presented in Figure 6.39 in comparison with the patterns obtained by electromagnetic simulation. As shown in the figure, the experimental measurements and the simulation results show good agreement. It is clear that the radiation at this frequency is mainly produced by the spiral part of the composite structure of the wire antenna. As shown in this figure, the radiation pattern is omnidirectional in the azimuth plane and end-fire (balloon-like) in the elevation planes with maximum in the direction parallel to the antenna axis. Thus, the radiated power at 5.8 GHz is mainly directed towards the Wi-Fi antenna mounted in the room ceil, which is appropriate for off-body communications intended at this frequency. Moreover, such a radiation pattern is appropriate to keep the main radiation at this frequency far from the human body to reduce the SAR in the human tissues.

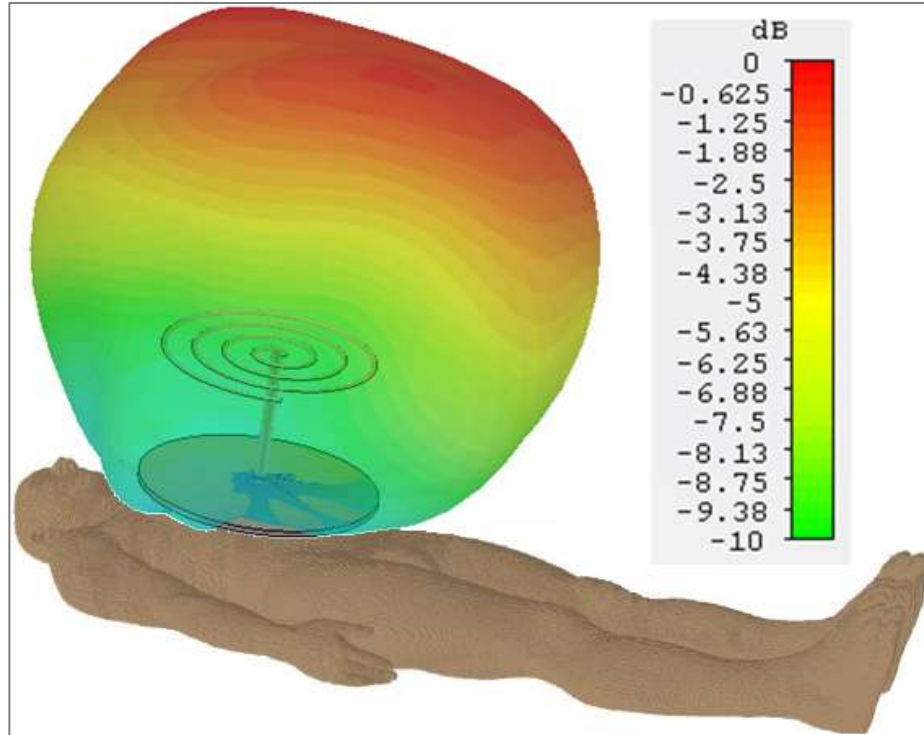


**Figure 6.38:** Three-dimensional radiation pattern of total field produced by the on-body monopole/spiral antenna of dimensions  $N = 3$ ,  $H_M = 15$  mm, and  $D_S = 20$  mm,  $f = 5.8$  GHz.

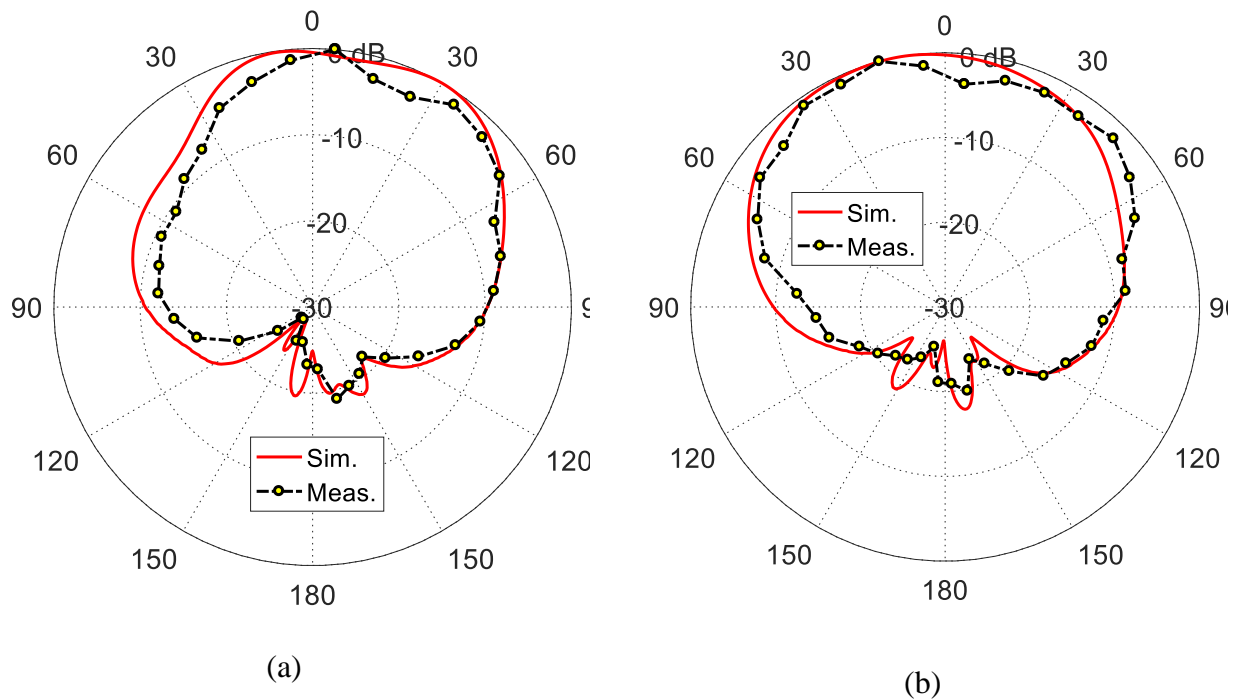


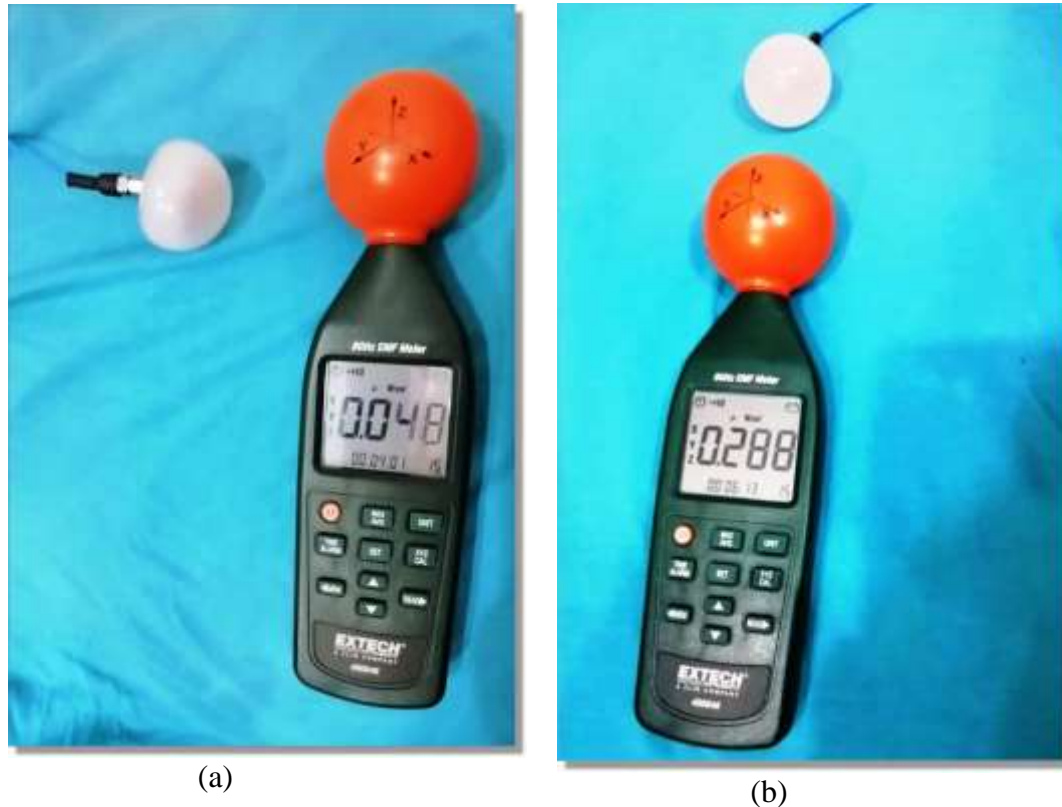
**Figure 6.39:** Comparison between the patterns obtained by simulation and experimental measurements for the total field produced by the monopole/spiral antenna (placed on the human body) in the planes, (a)

$\phi = 0, 180^\circ$ , and (b)  $\phi = 90, 270^\circ$ ,  $f = 5.8$  GHz; the antenna dimensions are  $N = 3$ ,  $H_M = 15$  mm, and  $D_S = 20$  mm.

### **6.13. Power Density and SAR Distribution in the Human Tissues due to Radiation from the Proposed On-Body Antenna**

This section is concerned with the experimental measurement and the numerical assessment of the power density distribution on the surface of the human body at 3.0 GHz when the proposed monopole/spiral antenna is mounted on the human body as shown in Figures 6.26 and 6.34. Also, the numerical results concerned with the SAR distribution in the different tissues of the three-layer human body model are presented and discussed.

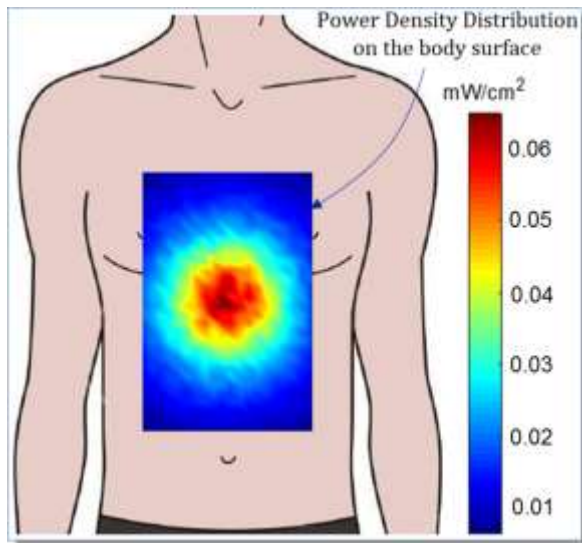
For experimental assessment of the power density distribution on the human body surface, the radiation hazard meter Extech® model 480846 is used with its isotropic probe touching the human body as shown in Figure 6.40 while the monopole/spiral antenna (covered with the radome) is placed on the patient chest and excited with input power  $P_{in} = 0$  dBm (1 mW) at  $f = 3.0$  GHz. The power density meter shows a reading of  $0.048 \mu\text{W}/\text{cm}^2$  when antenna is oriented with the spiral pointing to the power density meter as shown in Figure 6.40(a). When the antenna is oriented with the spiral pointing to the room ceil (normal operation) the reading of the power density meter is  $0.288 \mu\text{W}/\text{cm}^2$  as shown in Figure 6.40(b). The comparison of the two readings of the power density meter, taking the orientations of the antenna into consideration, indicates that the radiation of the monopole/spiral antenna has mainly broadside radiation at this frequency. However, the maximum level of the power density still ensures safe values of the electromagnetic exposure.



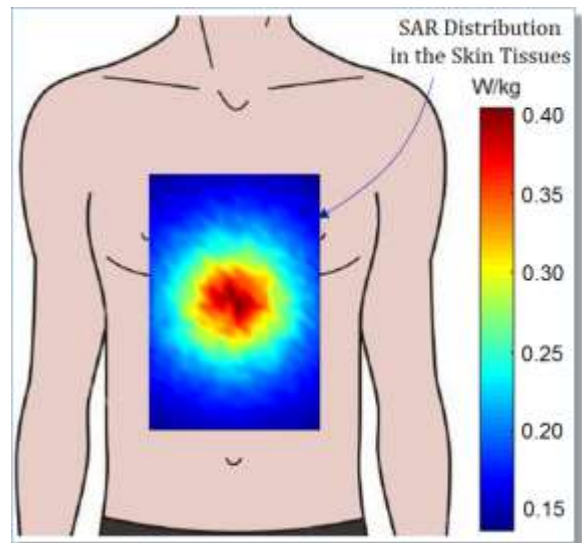
**Figure 6.40:** Measurement of the power density distribution near the skin of the body using the radiation hazard meter Extech® model 480846 when the monopole/spiral antenna is excited with input power  $P_{in} = 0$  dBm at  $f = 3.0$  GHz, (a) The antenna is oriented with tip pointing to the power density meter , (b) The antenna is oriented with tip pointing to the room ceil (normal operation) ; the antenna dimensions are  $N = 3$ ,  $H_M = 15$  mm, and  $D_S = 20$  mm.

Figure 6.41(a) presents the distribution of the microwave power density just on the skin surface over the rectangular area surrounded by the blue dashed rectangle shown in Figure 4 due to the placement of the monopole/spiral antenna with its base touching the human body surface while being excited by input power  $P_{in} = 0$  dBm at  $f = 3.0$  GHz. It is shown that the maximum power density on the skin does not exceed  $0.065$  mW/cm<sup>2</sup>, which ensures safe level of electromagnetic exposure. The corresponding SAR distributions in the tissues of skin, fat, and muscle over the area of interest are presented in Figures 6.41(b), 6.41(c), and 6.41(d). It is shown that the maximum value of the SAR occurs in the skin tissues whereas the fat tissues has the minimum value of the SAR due to the higher conductivity of the skin tissue and larger depth of the fat tissues inside the human body. It is shown that the maximum SAR in all the tissue types does not exceed  $0.4$  W/kg, which ensures safe level of electromagnetic exposure.

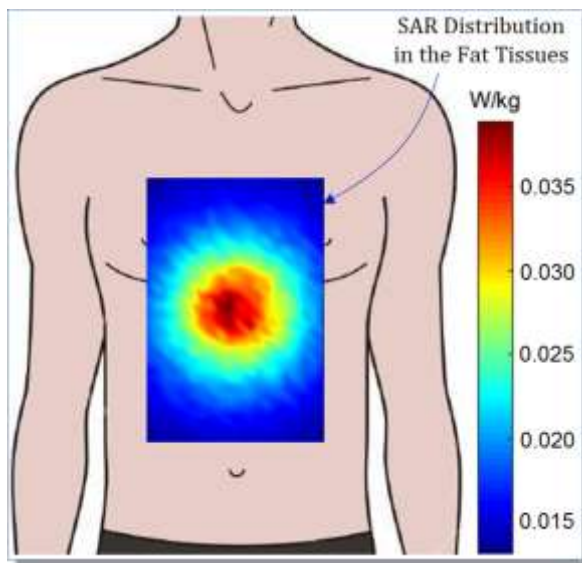




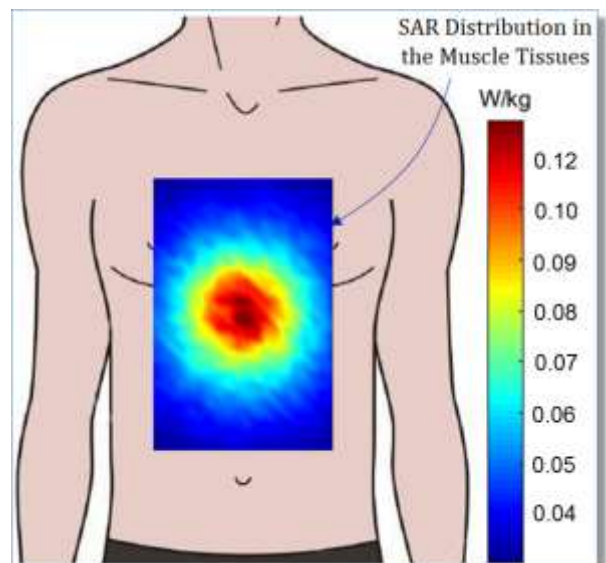
(a)



(b)



(c)



(d)

**Figure 6.41:** Distribution of (a) Microwave power density on the surface of the body, (b) SAR in the skin tissues (c) SAR in the fat tissues, and (d) SAR in muscle tissues, due to monopole/spiral antenna fed with input power  $P_{in} = 0$  dBm at  $f = 3.0$  GHz; the antenna dimensions are  $N = 3$ ,  $H_M = 15$  mm, and  $D_S = 20$  mm.



## **6.14. Assessment of the WBAN Communication System Performance using the Proposed On-Body Antenna**

This section is concerned with the presentation of some numerical results for the assessment of the performance of the WBAN communication system described previously. It is assumed that all the biosensor antennas (both on-body and in-body) in the WBAN are isotropic and lossless and distributed on the surface of the human body. The losses are caused only by the microwave propagation inside the lossy tissues on the surface of the human body.

### **6.14.1. Distribution of the SNR and BER on the Skin due to the Proposed On-Body Antenna**

The distribution of the SNR due to AGWN of power spectral density  $N_0/2 = 1 \times 10^{-3}$  mW/Hz at isotropic receiving biosensor antennas distributed on the skin surface over the rectangular area (indicated by the dashed rectangle in Figure 6.27 is presented in Figure 6.42(a) using the shown color code when the operating frequency is 3.0 GHz and the input power to the monopole/spiral antenna is 0 dBm (1 mW). The corresponding distributions of BER over the same area of the human body surface are presented in Figures 6.42(b) and 6.42(c) under the assumption of using 8-symbol and 16-symbol in the  $M$ -ary PSK modulation technique, respectively. In spite of the low power fed to the proposed on-body monopole/spiral antenna (only 1 mW), and thanks to the optimized design of this antenna, the BER doesn't exceed  $6 \times 10^{-8}$  and  $5.3 \times 10^{-5}$  for the two modulation schemes.

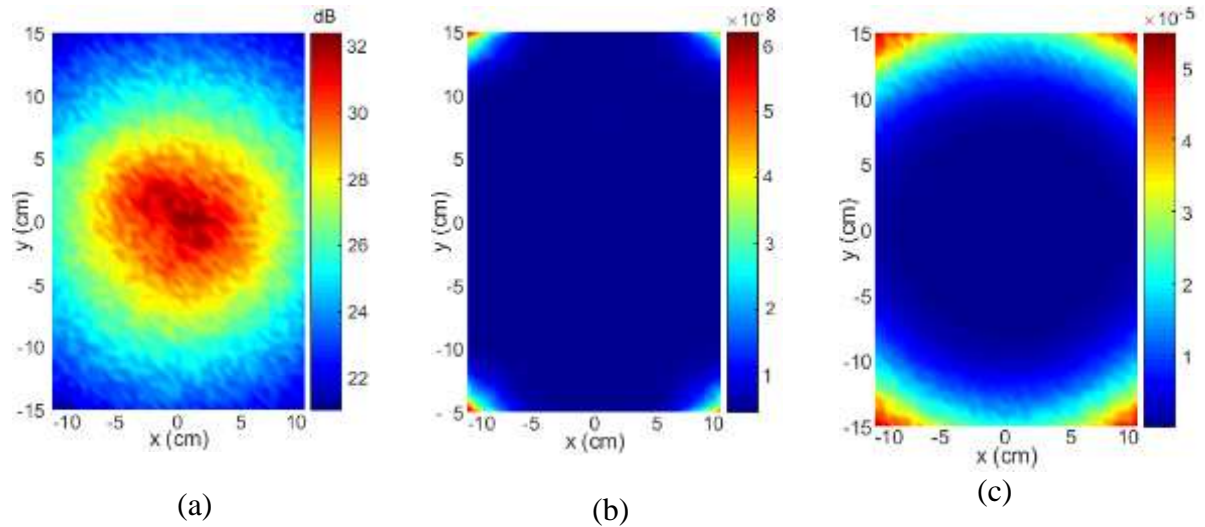


**Figure 6.42:** Distribution of the SNR and the corresponding BER over the area of the skin within which the (isotropic) biosensor antennas are allocated due to a central on-body monopole/spiral antenna fed with input power,  $P_{in} = 0$  dBm at  $f = 3.0$  GHz, (a) SNR, (b) BER for 8-symbol PSK, (c) BER for 16-symbol PSK, the antenna dimensions are  $N = 3$ ,  $H_M = 15$  mm, and  $D_S = 20$  mm.

### 6.14.2. Dependence of the SNR and BER on the Height of the On-Body Antenna above the Skin

The height at which the monopole/spiral antenna (proposed for on-body communications in WBANs) is placed has a significant effect on the SNR and the BER as shown in Figures 6.43(a) and 6.43(b), respectively, for different values of the input power to the proposed on-body monopole/spiral antenna. As shown in these figures, the SNR is increased and, hence, the BER is decreased with increasing the height of the monopole/spiral antenna above the surface of the human body. Thus, it is preferable to place the antenna at a higher level above the surface of the human body for better performance of the communication system (i.e. higher SNR and lower BER).

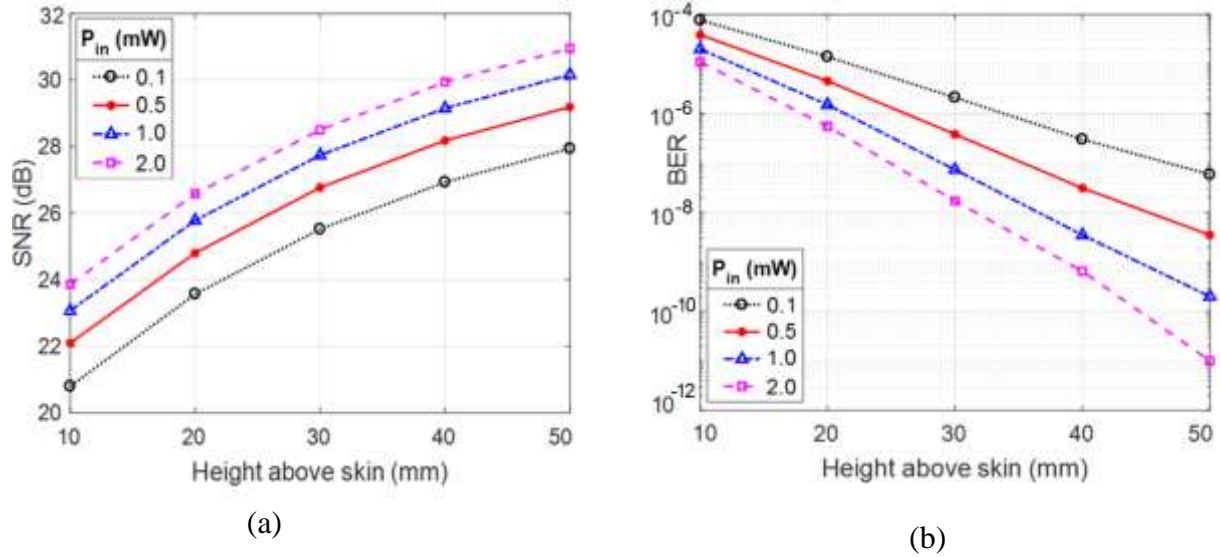


**Figure 6.43:** Dependence of the minimum SNR and the corresponding BER on the height at which the monopole/spiral antenna is placed above the surface of the human body when used in WBAN as a central on-body antenna fed with different values of the input power at  $f = 3.0$  GHz, (a) Minimum SNR, (b) Maximum BER; the antenna dimensions are  $N = 3$ ,  $H_M = 15$  mm, and  $D_S = 20$  mm.

## 6.15. Conclusion

A dual-band conical-helix/monopole and monopole/spiral antennas are proposed to operate as central on-body antennas for WBAN. The characteristics of these antennas are investigated through electromagnetic simulation and experimental measurements. Both antennas are designed to produce in the end-fire (balloon-like) radiation to communicate (through its far-field) with the Wi-Fi antenna at 5.8 GHz, and to produce broad-side (figure of eight) radiation to communicate (through its near or far field) with the on-skin biosensor antennas at 3.0 GHz. Prototypes of the proposed antennas are fabricated for experimental assessments. The antennas are matched to  $50\Omega$  coaxial feeder over the operational frequency bands, mounted on a copper circular disc, and covered with a very thin dielectric radome for mechanical protection. The radiation patterns obtained by experimental measurements show good agreement with those obtained by electromagnetic simulation and are shown to be appropriate for communication with the Wi-Fi antenna and the biosensor antennas at 5.8 GHz and 3.0 GHz, respectively. The SAR distributions inside the human tissues of concern (skin, fat and muscle) are evaluated showing safe level of electromagnetic exposure. Quantitative assessment of the WBAN communication system

performance is achieved when the proposed antennas are employed as on-body central antennas for the WBAN. Owing to the optimized design of the proposed antennas, the BER shown to have very low BER even when the input power fed to the antennas is only 1 mW.

## Chapter 7

### Conclusions and Suggestions for Future Work

---

#### 7.1. Conclusions

Biosensors are mainly designed for the purpose of diagnostic, therapeutic and assistive applications in health-care, active living and sports technology. In WBAN, to monitor a patient's health status, the implanted device collects various physiological data and wirelessly transmits the information to external medical devices in real time. For wearable antennas intended for on/off-body wireless communications, the challenge is to design an antenna with dual operation modes, each mode has its specific radiation characteristics, and to make the antenna input impedance matching less sensitive to potentially varying distance between the antenna and the human body. For the first mode the antenna is used for on-body communications to collect vital information from the human body (i.e. from the in-body and on-body biosensors). This requires the antenna to have wide-beam or omnidirectional radiations in the plane parallel to the human body surface to provide maximum coverage over the body. This can be achieved by minimizing the radiations that are away from the human body (i.e. off-body). By introducing a null in the direction normal to the body, we can suppress off-body radiations and can enhance the on-body radiations. In the second mode of operation the antenna is used to transmit the collected information towards the outside Wi-Fi for example. In this case, the radiated beam can be directed towards the receiving device placed away of the patient's body.

The present thesis aims to arrive at the optimum design of the on-body antenna to operate as a central antenna for WBAN. This antenna should have dual-frequency operation; the lower frequency band is at 2.45 GHz for the on-body communications (WBAN) whereas the higher frequency band is as 5.8 GHz for the off-body communications (Wi-Fi).

Furthermore, several studies were made to develop the dependence of the SNR and BER on the height and the apex angle of the conical helix antenna. These studies resulted in that with increasing the height of the conical helix, the SNR is increased and the BER is decreased, while when increasing the apex angle the SNR and BER stay constant.

An overview of the types of the medical implant biosensors is presented showing the difference between the in-body, on-body, and off-body biosensors and the uses of each type. The WBAN architecture is illustrated with the associated network problems and design considerations. The wireless communication protocols used in the WBAN is reviewed. Finally, the antenna design considerations for the on/off body biosensor are investigated. The most important factors affecting the antenna design include antenna detuning, impedance matching, radiation pattern, SAR, size compactness, space constraints, low cost, light weight, multi-band operation, interference mitigation, reconfigurability, positioning, bending and stable performance with the variation of the gap between the antenna and the human body. The details of each design parameter is presented with some examples for antennas designed to work as an on/off body biosensor.

A semi-analytic rigorous technique for the assessment of microwave propagation on the medium equivalent to the human body is developed to evaluate the near field radiated from arbitrarily shaped wire antennas at the possible locations of on-skin antennas connected to implantable (in-body) biosensors. Three types of helical antennas are proposed to be employed as central antennas for WBAN. Each of the proposed antennas is a dual-band of the helical wire type. It is designed to operate in the end-fire (axial) mode to communicate with the Wi-Fi communication system (5.0 – 6.0 GHz). Also, it is designed to operate in the broad-side (normal) mode to communicate with the on-skin biosensor antennas at 2.45 GHz. The radiated fields from the proposed on-body antenna helical antenna types in the near zone are evaluated using the proposed semi-analytic technique.

The cylindrical helix, conical helix, and inverted conical helix antennas proposed to operate as central antennas for WBAN are investigated through semi-analytic technique, CST® simulator, and experimental measurements. Each of the proposed helical antennas is a dual-band that is designed to produce in the end-fire radiation to communicate (through its far-field) with the Wi-Fi antenna at 5.8 GHz, and to produce broad-side radiation to communicate (through its near field) with the on-skin biosensor antennas at 2.45 GHz. Three prototypes of the proposed helical antennas are fabricated. Each antenna is matched with  $50\Omega$  coaxial feeder over a wide frequency band, mounted on a copper circular disc, and covered with a very thin dielectric radome for protecting the wire antenna. Such an antenna when covered by the radome is shaped

like a hemispherical button that can be attached to the patient clothes and, hence, it can be considered as wearable antenna. The near-field distribution over the surface of human body is presented at 2.45 GHz. The radiation patterns obtained by experimental measurements for the three fabricated prototypes show good agreement with those obtained by the CST® simulator and are shown to be appropriate for communication with the Wi-Fi antennas at 5.8 GHz.

Quantitative assessment of the WBAN communication system performance is achieved when each of the cylindrical and conical helix antennas is employed as on-body central antenna for the WBAN. For its high immunity to noise, the utilized modulation system is assumed to be  $M$ -ary Phase-Shift Keying (PSK), with  $M = 8$  and  $M = 16$ . A channel modeling is performed for such a communication system by considering Additive White Gaussian Noise (AWGN) to evaluate the SNR and, hence, the corresponding BER can be calculated. This enables the calculation of the minimum input power of the proposed on-body WBAN central antenna that achieves the required BER for a specific data rate. On the other hand, the distribution of the microwave power density near the body surface is evaluated by simulation and experimental measurements to ensure the realization of the electromagnetic exposure safety limits. Also, the SAR distribution inside the human tissues of concern is evaluated. It is shown that the conical helix antenna has higher performance than that of the cylindrical helix antenna. The effects of the on-body conical helix antenna dimensional parameters and, also, the antenna height above the human body surface on such performance measures and electromagnetic doze level are numerically studied for the purpose of arriving at the optimum design of the proposed on-body wearable conical helix antenna. It is shown that SNR is increased and, hence, the BER is decreased with increasing the height of the conical helix while being constant and independent of the apex angle of the conical helix.

Several studies were made and resulted in obtaining power density distribution of about (0.03-0.06) mW/cm<sup>2</sup>, SAR distribution of about (0.3-0.4) W/kg. The optimized BER did not exceed  $1.2 \times 10^{-6}$  and  $5.3 \times 10^{-4}$ .

## **7.2. Suggestions for Future Work**

It is proposed to design an ultra-wideband antenna with band notches to operate as on-body central antenna for WBAN. In addition to the requirements that should be fulfilled by an on-body antenna, the frequency locations of the band notches shall be unique for each antenna and shall be used as identifier of the patient's body on which this antenna is mounted.

It is, also, suggested to extend the semi-analytic technique developed in Chapter 3 of the present thesis to account for an exact three-dimensional geometric model of the human body instead of the simplified flat model of the human body surface used in the present work.

In addition, further tests will be held considering other sources of interference from other mediums operating in similar frequencies.

## **7.3. Reflection**

This research was done by digging deep into WBAN, sensors, antenna designs, safety regulations and impacts on the human body. Developing a mathematical model and de-embedding for the on-body antennas in order to obtain the electric field parameters have improved my analytical techniques.

The practical and experimental work in this thesis have built up so much knowledge and experience for me. Furthermore, experimentally testing the helix windings, apex angle, number of turns and test them using the power density meter, the radiation patterns and the SAR inside the laboratory.



## References

- [1] S. Zhang, Y. Qin, J. Kuang, P. U. Mak, S. H. Pun, M. I. Va, and Y. Liu, “Development and prospect of implantable intra-body communication technology,” in *Journal of Computers*, vol. 9, no. 2, pp. 463–473, 2014
- [2] R. Warty, M.-R. Tofighi, U. Kawoos, and A. Rosen, “Characterization of implantable antennas for intracranial pressure monitoring: Reflection by and transmission through a scalp phantom,” *IEEE Transactions on Microwave Theory and Techniques*, vol. 56, no. 10, pp. 2366–2376, 2008.
- [3] U. Kawoos, X. Meng, M.-R. Tofighi, and A. Rosen, “Too much pressure: Wireless intracranial pressure monitoring and its application in traumatic brain injuries,” *IEEE Microwave Magazine*, vol. 16, no. 2, pp. 39–53, 2015.
- [4] E. Johannessen, O. Krushinitskaya, A. Sokolov, P. Häfliger, A. Hoogerwerf, C. Hinderling, K. Kautio, J. Lenkkeri, E. Strömmer, V. Kondratyev et al., “Toward an injectable continuous osmotic glucose sensor,” *Journal of diabetes science and technology*, vol. 4, no. 4, pp. 882–892, 2010.
- [5] E. Moradi, T. Björninen, L. Sydänheimo, J. M. Carmena, J. M. Rabaey, and L. Ukkonen, “Measurement of wireless link for brain–machine interface systems using human-head equivalent liquid,” *IEEE Antennas and Wireless Propagation Letters*, vol. 12, pp. 1307–1310, 2013.
- [6] S. Reichelt, J. Fiala, A. Werber, K. Forster, C. Heilmann, R. Klemm, and H. Zappe, “Development of an implantable pulse oximeter,” *IEEE Trans. Biomed. Eng.*, vol. 55, no. 2, pp. 581–588, 2008.
- [7] S. Goldstein, J. Peterson, and R. Fitzgerald, “A miniature fiber optic ph sensor for physiological use,” *Journal of biomechanical engineering*, vol. 102, no. 2, pp. 141–146, 1980.
- [8] D. Panescu, “An imaging pill for gastrointestinal endoscopy”, *IEEE Engineering in Medicine and Biology magazine*, vol. 24, no. 4, pp. 12–14, 2005.

- [9] D. B. Shire, S. K. Kelly, J. Chen, P. Doyle, M. D. Gingerich, S. F. Cogan, W. A. Drohan, O. Mendoza, L. Theogarajan, J. L. Wyatt et al., “Development and implantation of a minimally invasive wireless subretinal neurostimulator,” *IEEE Trans. Biomed. Eng.*, vol. 56, no. 10, pp. 2502–2511, 2009.
- [10] T. Abell, R. McCallum, M. Hocking, K. Koch, H. Abrahamsson, I. LeBlanc, G. Lindberg, J. Konturek, T. Nowak, E. M. Quigley et al., “Gastric electrical stimulation for medically refractory gastroparesis,” *Gastroenterology*, vol. 125, no. 2, pp. 421–428, 2003.
- [11] B. B. Yellen, Z. G. Forbes, D. S. Halverson, G. Fridman, K. A. Barbee, M. Chorny, R. Levy, and G. Friedman, “Targeted drug delivery to magnetic implants for therapeutic applications,” *Journal of Magnetism and Magnetic Materials*, vol. 293, no. 1, pp. 647–654, 2005.
- [12] W. F. House, “Cochlear implants,” *Annals of Otology, Rhinology & Laryngology*, vol. 85, no. 3\_suppl, pp. 3–3, 1976.
- [13] P. M. Lewis, H. M. Ackland, A. J. Lowery, and J. V. Rosenfeld, “Restoration of vision in blind individuals using bionic devices: a review with a focus on cortical visual prostheses,” *Brain research*, vol. 1595, pp. 51–73, 2015.
- [14] F. Lotte and C. Guan, “Regularizing common spatial patterns to improve bci designs: unified theory and new algorithms,” *IEEE Trans. Biomed. Eng.*, vol. 58, no. 2, pp. 355–362, 2011.
- [15] Qin. Y. Howlader, M.M.R. Deen, M.J. Haddara, Y.M. Selvaganapathy, P.R. “Polymer integration for packaging of implantable sensors”. *Sens. Actuators B Chem.*, vol. 202, pp. 758–778, 2014
- [16] Clausen, I. Glott, T. “Development of Clinically Relevant Implantable Pressure Sensors: Perspectives and Challenges”, *Sensors*, 14, 17686–17702, 2014
- [17] A. Cavallini, C. Baj-Rossi, S. Ghoreishizadeh, G. De Micheli, S. Carrara, “Design, fabrication, and test of a sensor array for perspective biosensing in chronic pathologies”, In *Proceedings of the 2012 IEEE Biomedical Circuits and Systems Conference (BioCAS)*, Hsinchu, Taiwan, 28–30; pp. 124–127, November 2012

- [18] S. W. Hwang, H. Tao, D. H. Kim, H. Cheng, J. K. Song, E. Rill, M. A. Brenckle, B. Panilaitis, S. M. Won, Y. S. Kim “A physically transient form of silicon electronics”, *Science*, 337, 1640–1644, 2012
- [19] A. Blau, A. Murr, S. Wol, E. Sernagor, P. Medini, G. Iurilli, C. Ziegler, F. Benfenati, “Flexible, all-polymer microelectrode arrays for the capture of cardiac and neuronal signals”, *Biomaterials*, 32, 1778–1786, 2011
- [20] S. Vaddiraju, I. Tomazos, D. J. Burgess, F. C. Jain, F. Papadimitrakopoulos, “Emerging Synergy between Nanotechnology and Implantable Biosensors: A Review”, *Biosens. Bioelectron.*, 25, 1553–1565. 2010
- [21] K. Bazaka, M. Jacob, “Implantable Devices: Issues and Challenges”, *Electronics*, 2, 1–34. 2012
- [22] V. Kochkodan, N. Hilal, “A comprehensive review on surface modified polymer membranes for biofouling mitigation”, *Desalination*, 356, 187–207. 2015
- [23] I. Jeerapan, S. Poorahong, “Review—Flexible and Stretchable Electrochemical Sensing Systems: Materials, Energy Sources, and Integrations”, *J. Electrochem. Soc.*, 167, 037573. 2020
- [24] S. H. Lee, C. K. Jeong, G. T. Hwang, K. J. Lee, “Self-powered flexible inorganic electronic system. *Nano Energy*”, 14, 111–125, 2015
- [25] D. H. Kim, R. Ghaari, N. Lu, S. Wang, S. P. Lee, H. Keum, R. Dangelo, L. Klinker, Y. Su, C. Lu, “Electronic sensor and actuator webs for large-area complex geometry cardiac mapping and therapy”. *Proc. Natl. Acad. Sci. USA*, 109, 19910–19915, 2012
- [26] <https://spectrum.ieee.org/the-human-os/biomedical/devices/what-is-neural-implant-neuromodulation-brain-implants-electroceuticals-neuralink-definition-examples>
- [27] <https://www.peptest.co.uk/endostim-reflux/>
- [28] Mohammad H. Behfar, Toni Björninen, ElhamMoradi, Lauri Sydänheimo, and Leena Ukkonen, “Biotelemetric Wireless Intracranial Pressure Monitoring: An In Vitro Study”, *International Journal of Antennas and Propagation*, Hindawi, 2015

- [29] D. H. Kim, N. Lu, R. Ma, Y. S. Kim, R. H. Kim, S. Wang, J. Wu, S.M. Won, H. Tao, A. Islam, “Epidermal electronics”, *Science*, 333, 838–843. 2011
- [30] A. J. Bandodkar, W. Jia, J. Wang, “Tattoo-Based Wearable Electrochemical Devices: A Review”, *Electroanalysis*, 27, 562–572. 2015
- [31] M. Bertini, L. Marcantoni, T. Toselli, R. Ferrari, “Remote monitoring of implantable devices: Should we continue to ignore it?”, *Int. J. Cardiol.*, 202, 368–377, 2016
- [32] K. Bazaka, M. Jacob, “Implantable Devices: Issues and Challenges”, *Electronics*, 2, 1–34. 2012
- [33] M. N. Dakurah, C. Koo, W. Choi, Y. H. Joung, “Implantable bladder sensors: A methodological review”, *Int. Neurorol. J.*, 19, 133–141, 2015
- [34] S. Tsujimura, H. Yamagishi, Y. Sankai, “Development of a bidirectional data communication system using ultra high frequency radio wave for implantable artificial hearts”, In *Proceedings of the TENCON 2010–2010 IEEE Region 10 Conference*, Fukuoka, Japan, 21–24 November 2010.
- [35] European Telecommunication Standard Institute (ETSI), “Electromagnetic compatibility and radio spectrum matters (ERM); short range devices (SRD); ultra low power active medical implants (ULP-AMI) and peripherals (ULP-AMI-P) operating in the frequency range 402 MHz to 405 MHz; part 1: Technical characteristics and test methods,” in *European Standard (Telecommunications series)*, vol. V1.3.1, 2009.
- [36] G. J. Suaning and N. H. Lovell, “Cmos neurostimulation asic with 100 channels, scaleable output, and bidirectional radio-frequency telemetry,” *IEEE Trans. Biomed. Eng.*, vol. 48, no. 2, pp. 248–260, 2001.
- [37] J. D. Weiland and M. S. Humayun, “A biomimetic retinal stimulating array,” *IEEE engineering in medicine and biology magazine*, vol. 24, no. 5, pp. 14–21, 2005.
- [38] A. K. Teshome, B. Kibret, and D. T. Lai, “Galvanically coupled intrabody communications for medical implants: A unified analytic model,” *IEEE Trans. Antennas Propag.*, vol. 64, no. 7, pp. 2989–3002, 2016.

- [39] F. Mazzilli and C. Dehollain, “184 \_w ultrasonic on–off keying/amplitude-shift keying demodulator for downlink communication in deep implanted medical devices,” *Electronics Letters*, vol. 52, no. 7, pp. 502–504, 2016.
- [40] G. E. Santagati and T. Melodia, “Experimental evaluation of impulsive ultrasonic intra-body communications for implantable biomedical devices,” *IEEE Trans. Mobile Comput.*, vol. 16, no. 2, pp. 367–380, 2017.
- [41] J. L. Abita and W. Schneider, “Transdermal optical communications,” *Johns Hopkins APL Techn. Dig.*, vol. 25, no. 3, pp. 261–268, 2004.
- [42] M. Faria, L. N. Alves, and P. S. de Brito André, “Transdermal optical communications,” *Visible Light Communications: Theory and Applications*, p. 309, 2017.
- [43] M. Mujeeb-U-Rahman, D. Adalian, C.-F. Chang, and A. Scherer, “Optical power transfer and communication methods for wireless implantable sensing platforms,” *Journal of biomedical optics*, vol. 20, no. 9, pp. 095 012–095 012, 2015.
- [44] D. Malak and O. B. Akan, “A communication theoretical analysis of synaptic multiple-access channel in hippocampal-cortical neurons,” *IEEE Trans. Commun.*, vol. 61, no. 6, pp. 2457–2467, 2013.
- [45] O. B. Akan, H. Ramezani, T. Khan, N. A. Abbasi, and M. Kuscu, “Fundamentals of molecular information and communication science,” *Proceedings of the IEEE*, vol. 105, no. 2, pp. 306–318, 2017.
- [46] E. Balevi and O. B. Akan, “A physical channel model for nanoscale neuro-spike communications,” *IEEE Trans. Commun.*, vol. 61, no. 3, pp. 1178–1187, 2013.
- [47] S. Gabriel, R. Lau, and C. Gabriel, “The dielectric properties of biological tissues: Iii. Parametric models for the dielectric spectrum of tissues,” *Physics in medicine and biology*, vol. 41, no. 11, p. 2271, 1996.
- [48] S. Pandey, P. K. Tiwari, and T.-Y. Byun, “Integration of bio-sensing with information and communication to provide improved health-care services,” in *Embedded and Multimedia Computing Technology and Service*. Springer, pp. 509–516, 2012

- [49] Jovanov E, Milenkovic A. Body area networks for ubiquitous healthcare applications: Opportunities and challenges. *J Med Syst*;35: 1245–1254, 2011
- [50] Warren S, Jovanov E. The need for rules of engagement applied to wireless body area networks. *IEEE Consumer Communications and Networking Conference CCNC2006*. Piscataway, NJ: IEEE, 979–983, 2006
- [51] Vullers R, Schaijk R, Visser H, Penders J, Hoof C. Energy harvesting for autonomous wireless sensor networks. *IEEE Solid-State Circuits Mag* 2(2):29–38, 2010
- [52] Perpetua Power Source Technology, Inc. [www.perpetuapower.com/press01142010.htm](http://www.perpetuapower.com/press01142010.htm)
- [53] Wu Y, Chaudhari Q, Serpedin E. Clock synchronization of wireless sensor networks. *IEEE Signal Processing Mag* (28):124–138, 2011
- [54] Khan M, Rahman Md, Talha Md and Mithila T. “Wearable Antenna for Power Efficient On-Body and Off-Body Communications ”, *Journal of Electromagnetic Analysis and Applications*, pp. 238-243, 2014.
- [55] EE times. Medical electronics: From hospital and clinics to home. [www.eetimes.com/design/medicaldesign/4211247/Medical-electronics-fromhospitaland-clinic-to-the-home](http://www.eetimes.com/design/medicaldesign/4211247/Medical-electronics-fromhospitaland-clinic-to-the-home)
- [56] Cao H, Leung V, Chow C, Chan H. Enabling technologies for wireless body area networks: A survey and outlook. *IEEE Communications Mag* 47(12):84–93, 2009
- [57] Georgakakis E, Nikolidakis S, Vergados D, Douligeris C. An analysis of Bluetooth, ZigBee and Bluetooth low energy and their use in WBANs. In: Lin C, Nikita K, eds. *Wireless mobile communication and healthcare*. Berlin: Springer Verlag, 168–175, 2010
- [58] Bluetooth low energy technology. <http://bluetooth.com/Pages/low-energytech-info.aspx>
- [59] IEEE 802.15.4d–2009, Part 15.4: Wireless medium access control (MAC) and physical layer (PHY) specifications for low-rate wireless personal area networks (WPANs). New York: IEEE, 2009.
- [60] Memsic. Iris sheet. [www.memsic.com/support/documentation/wireless-sensornetworks/category/7-datasheets.html?download=135%3Airis](http://www.memsic.com/support/documentation/wireless-sensornetworks/category/7-datasheets.html?download=135%3Airis)

- [61] Liu H, Krishnamachari B. Energy optimization for upstream data transfer in 802.15.4 beacon enabled star formulation. *Advanced Signal Processing Algorithms, Architectures, and Implementations XVIII*. Proceedings of SPIE, San Jose, CA. 70740I–70740I-9, 2008
- [62] A. Brizzi, A. Pellegrini, and Y. Hao, "Design of a cylindrical resonant cavity antenna for BAN applications at V band," in *IEEE International Workshop on Antenna Technology (iWAT)*, pp. 152-155, 2012
- [63] S. M. Abbas, Y. Ranga, K. P. Esselle, and S. G. Hay, "Recent Developments in Antennas with Full Ground Planes for Wireless Body Area Networks," in *International Symposium on Antennas and Propagation (ISAP)*, Hobart, Tasmania, Australia, November 9-12, 2015.
- [64] S. M. Abbas, Y. Ranga, and K. P. Esselle, "A Printed Antenna with a Ground Plane and Electromagnetically Coupled Feed for 2.45GHz Body Area Networks", in *IEEE International Symposium on Antennas and Propagation*, Orlando, Florida, USA, July 7- 13, 2013.
- [65] S. M. Abbas, K. P. Esselle, and Y. Ranga, "A Printed Dual Band Antenna with a Ground Plane and Electromagnetically- Coupled Feed for Wireless Body Area Networks," in *IEEE International Workshop on Antenna Technology (iWAT)*, Sydney, Australia, March 4-6, 2014.
- [66] S. M. Abbas, K. P. Esselle, and Y. Ranga, "An arm band wearable printed antenna with a full ground plane for body area networks," in *IEEE International Symposium on Antennas and Propagation*, Memphis, Tennessee, USA, July 6-11, 2014.
- [67] S. M. Abbas, Y. Ranga, and K. P. Esselle, "Sensitivity of a Wearable Printed Antenna with a Full Ground Plane in Close Proximity to Human Arm " in *9th European Conference on Antennas and Propagation*, Lisbon, Portugal, 2015.
- [68] Q. Bai and R. Langley, "Wearable EBG antenna bending and crumpling," in *Loughborough Antennas & Propagation Conference (LAPC)*, pp. 201-204, 2009
- [69] P. S. Hall and Y. Hao, *Antennas and Propagation for Body-Centric Wireless Communications*, Artech House, Norwood, Mass, USA, 2006.

- [70] Kyeol Kwon, Jaegeun Ha, Soonyong Lee, and Jaehoon Choi, “Design of a Dual-Band On-Body Antenna for a Wireless Body Area Network Repeater System”, Hindawi Publishing Corporation, International Journal of Antennas and Propagation, ID 350797 , 2012
- [71] J. Ha, K. Kwon, and J. Choi, “Compact zeroth-order resonant antenna for implantable biomedical service applications,” Electronics Letters, vol. 47, no. 23, pp. 1267–1269, 2011.
- [72] J. Lee, S. I. Kwak, and S. Lim, “Wrist-wearable zeroth-order resonant antenna for wireless body area network applications,” Electronics Letters, vol. 47, no. 7, pp. 431–433, 2011.
- [73] U. Kim and J. Choi, “Design of a microstrip patch antenna with enhanced F/B for WBAN applications,” IEICE Transactions on Communications, vol. E94-B, no. 5, pp. 1135–1141, 2011.
- [74] Mohd Noor Islam, Mehmet R. Yuce, “Review of Medical Implant Communication System (MICS) band and network”, ScienceDirect, ICT Express 2 , pp. 188–194, 2016
- [75] Seonghun Kang and Chang Won Jung, “Wearable Fabric Reconfigurable Beam-Steering Antenna for On/Off-Body Communication System”, Hindawi Publishing Corporation, International Journal of Antennas and Propagation, ID 539843, 2015.
- [76] Dumanli, S., Sayer, L., Mellios, E., Fafoutis, X., Hilton, G., & Craddock, I., “Off-Body Antenna Wireless Performance Evaluation in a Residential Environment,” IEEE Transactions on Antennas and Propagation, pp. 6076-6084, 2017.
- [77] Sarmad M., Asnor I., Alyani I., Azura S., Zahriladha Z. and Sameer A., “ON-OFF Body Ultra-wideband (UWB) Antenna for Wireless Body Area Networks (WBAN): A Review,” IEEE Access, 2020.
- [78] Amira M., Jocelyne E. and Ahmed M., “Moving Towards Body-to-Body Sensor Networks for Ubiquitous Applications: A Survey”, Journal of sensor and Actuator Networks, 2019.
- [79] Chen Z. and Wen G., “Design of a dual band dual mode antenna for on/off body communications,” Wiley Periodicals, Inc., 2019.
- [80] Rahat A. K. and Al-Sakib K. P., “The state-of-the-art wireless body area sensor networks: A survey,” International Journal of Distributed Sensor Networks, Vol. 14(4), 2018.



- [81] G.S., Anderson and C.G., Sodini, "Body Coupled Communication: The Channel and Implantable Sensors," *IEEE International Conference on Body Sensor Networks*, pp. 1-5, May 2013.
- [82] J., Lee et al., "A 60 Mb/s Wideband BCC Transceiver with 150 pJ/b Rx and 31 pJ/b Tx for Emerging Wearable Applications," *IEEE International Solid-State Circuits Conference Digest of Technical Papers (ISSCC)*, pp. 498-499, Feb. 2014.
- [83] C., Oliveira; M., Mackowiak and L.M., Correia, "Challenges for Body Area Networks Concerning Radio Aspects," *the 11th European Wireless Conference - Sustainable Wireless Technologies*, pp. 1-5, Apr. 2011.
- [84] H., Alemdar and C., Ersoy, "Wireless Sensor Networks for Healthcare: A Survey," *Computer Networks Journal, ELSEVIER*, vol. 54, no. 15, pp. 2688-2710, Oct. 2010.
- [85] W.J., Yi and J., Saniie, "Smart Mobile System for Body Sensor Network," *IEEE International Conference on Electro/Information Technology (EIT)*, pp. 1-4, May 2013.
- [86] B.H., Calhoun et al., "Body Sensor Networks: A Holistic Approach from Silicon to Users," *Proceedings of the IEEE*, vol. 100, no. 1, pp. 91-106, Jan. 2012.
- [87] R., Saeedi; B., Schimert and H., Ghasemzadeh, "Cost- Sensitive Feature Selection for On-Body Sensor Localization," *UbiComp' 14 ADJUNCT*, pp. 833-842, Sep. 2014.
- [88] A., Bideaux et al., "A Personalized and Reconfigurable Cyberphysical System to Handle Multi-Parametric Data acquisition and Analysis for Mobile Monitoring of Eplieptic Patients," *The 11th International Conference on Wearable and Implantable Body Sensor Networks*, 2014.
- [89] H., Permana; Q., Fang and S., Lee, "A Microstrip Antenna Designed for Implantable Body Sensor Network," *IEEE International Conference on Orange Technologies (ICOT)*, pp. 103-106, Mar. 2013.
- [90] Q., Bonds et al., "A Tunable Cavity Backed-Slot Antenna (CBSA) for Close Proximity Biomedical Sensing Applications," *IEEE International Conference on Microwaves, Communications, Antennas and Electronics*, pp. 1-5, Nov. 2009.
- [91] H., Huang et al., "RFID Tag Helix Antenna Sensors for Wireless Drug Dosage Monitoring," *IEEE Journal of Translational Engineering in Health and Medicine*, vol. 2, Mar. 2014.
- [92] S., Zhao; C., Fumeaux and C., Coleman, "Optimal Helical Antenna with Continously varying Radius using Evolutionary Optimizers," *IEEE International Symposium on Antennas*

*and Propagation (APSURSI)*, pp. 757-760, Jul. 2011.

[93] S.H., Zainud-Deen; H.A., Malhat and K.H., Awadalla, "Octafilar Helical Antenna for Portable UHF-RFID Reader," *International Journal of Engineering Business Management*, vol. 4, no. 24, pp. 13-20, 2012.

[94] H., Huang et al., "Dual Band Electrically Small Non-Uniform Pitch Ellipsoidal Helix Antenna for Cardiac Pacemakers," *IEEE Topical Conference on Wireless Sensors and Sensors and Sensor Networks (WiSNet)*, pp. 121-123, Jan. 2013.

[95] R.C., Santiago et al., "Experimental Path Loss Models for In-Body Communications within 2.36-2.5 GHz," *IEEE Journal of Biomedical and Health Informatics*, vol. 19, no. 3, pp. 930-937, May 2015.

[96] A., Celebi; T., Wong and M., Kenkel, "Bifilar Transverse Bilateral Helical Antenna for Bandwidth Enhancement," *IEEE International Symposium on Antennas and Propagation and USNC/URSI National Radio Science Meeting*, pp. 1414-1415, Jul. 2015.

[97] A., Khaleghi and I., Balasingham, "Wireless Communication Link for Capsule Endoscope at 600 MHz," *37th Annual International Conference of the IEEE Engineering in Medicine and Biology Society (EMBC)*, pp. 4081-4084, Aug. 2015.

[98] C., Liu; Y., Guo and S., Xiao, "Circularly Polarized Helical Antenna for ISM-Band Ingestible Capsule Endoscope Systems," *IEEE Transactions on Antennas and Propagation*, vol. 62, no. 12, pp. 6027-6039, Nov. 2014.

[99] F.A., Ghaffar and A., Shamim, "A Ferrite LTCC Based Dual Purpose Helical Antenna Providing Bias for Tunability," *IEEE Antennas and Wireless Propagation Letters*, vol. 14, pp. 831-834, 2015.

[100] R., Omar and S.I.S., Hassan, "Analyzing and Designing of a Dual Band Active Antennas," *IEEE Conference on Research and Development Proceedings*, pp. 136-140, 2002.

[101] S., Iqbal; M., Amin and J., Yousaf, "Switchable dual-mode helix antenna," *IEEE 10<sup>th</sup> International Conference on Applied Sciences and Technology*, pp. 377-380, Jan 2013.

- [102] N.P.I., Kammersgaard et al., "In-The-Ear Spiral Monopole Antenna for Hearing Instrument," *Electronics Letters*, vol. 50, no. 21, pp. 1509-1511, Oct. 2014.
- [103] A.P., George and M., Sujatha, "Imbedded Spiral Antenna for Endoscope," *International Conference on Information Communication and Embedded Systems (ICICES)*, pp. 1-5, Feb. 2014.
- [104] M.A., Youssef and A.M.M.A., Allam, "Implanted Antenna on Human Breast," *IEEE International Conference on Engineering and Technology*, pp. 1-4, Apr. 2014.
- [105] T., Yilmaz et al., "Wearable Wireless Sensors for Healthcare Applications," *IEEE International Workshop on Antenna Technology*, pp. 376-379, Mar. 2013.
- [106] R.B.V.B., Simorangkir; S.M., Abbas and K.P., Esselle, "A Printed UWB Antenna with Full Ground Plane for WBAN Applications," *IEEE International Workshop on Antenna Technology (iWAT)*, pp. 127-130, Mar. 2016.
- [107] H., Abufanas et al., "New Approach for Design and Verification of a Wideband Archimedean Spiral Antenna for Radiometric Measurement in Biomedical Applications," *IEEE German Microwave Conference (GeMic)*, pp. 127-130, Mar. 2015.
- [108] S., Zhang et al., "On-Body Measurements of Embroidered Spiral Antenna," *IEEE Loughborough Antennas and Propagation Conference (LAPC)*, pp. 1-5, Nov. 2015.
- [109] B., Shankar, M, Santanu & B. C., Sekhar & M., Monojit, "A Compact Dual Band Dual Polarized Omnidirectional Antenna for ON Body Applications", *IEEE Transactions on Antennas and Propagation*, pp. 1-1, 2019.
- [110] M.S.R., Bashri, T., Arslan, W., Zhour and N., Haridas, "A Compact RF Switching for Wearable Microwave Imaging", *IEEE Loughborough Antennas and Propagation Conference (LAPC)*, pp. 1-4, 2016.
- [111] Dhakad, S.K., Dwivedi, U.K., & Bhandari, T., "Design and Analysis of Reconfigurable Antenna using PIN Diodes for Multi Band WLAN Applications", *International Conference on Wireless Communications, Signal Processing and Networking (WiSPNET)*, pp. 1705-1708, 2017.
- [112] C.H., Lin and K., Ito, "A Compact Dual-Mode Wearable Antenna for Body-Centric Wireless Communications," *Electronics Journal*, vol. 3, pp. 398-408, Jul. 2014.

[113] Y., Oya; K., Ito and K., Saito, "Design of Dual-mode Antenna at 21 MHz and 2.45 GHz for Medical Applications," *International Symposium on Antennas and Propagation (ISAP)*, pp. 587-588, Dec. 2014.

[114] Grimm, M., Manteuffel, D., Thomä, R., Knöchel, R.H., Sachs, J., Willms, I. and Zwick, T., 2013. Antennas and Propagation for On-, Off-and In-Body Communications. In *Ultra-Wideband Radio Technologies for Communications, Localization and Sensor Applications*. InTech.

[115] CVallejo, Mónica, Joaquín Recas, Pablo García Del Valle, and José L. Ayala. "Accurate human tissue characterization for energy-efficient wireless on-body communications." *Sensors* 13, no. 6 (2013): 7546-7569.